


Julie Wee

**Glacier-permafrost
interactions and
interrelation: dynamics of
Little Ice Age glacier
forefields in alpine
permafrost environments**



DOI : <https://doi.org/10.51363/unifr.sth.2025.065>

Julie Wee  <https://orcid.org/0000-0001-7210-793X>

© Julie Wee, 2025



This work is published under the Creative Commons Attribution 4.0 International license (CC BY 4.0): <https://creativecommons.org/licenses/by/4.0/>

Department of Geosciences
University of Fribourg (Switzerland)

Glacier-permafrost interactions and interrelation: dynamics of Little Ice Age
glacier forefields in alpine permafrost environments

THESIS

Presented to the Faculty of Science and Medicine of the University of Fribourg (Switzerland) in
consideration for the award of the academic grade of
Doctor of Philosophy in Geography

by

Julie Wee

from

Marsens and Sorens

Thesis No: 4662

Printed at UniPrint, Fribourg

2025

Accepted by the Faculty of Science and Medicine of the University of Fribourg (Switzerland) upon the recommendation of Dr. Isabelle Gärtner-Roer, Prof. Christian Hauck, Dr. Christophe Lambiel and Dr. Marcia Phillips

Fribourg, 3 December 2024

Thesis supervisors

Prof. Christian Hauck



.....

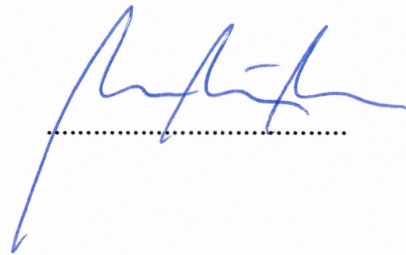
Dr. Christophe Lambiel



.....

Dean

Prof. Ulrich Ultes-Nitsche



.....

"What we call the present is given shape by an accumulation of the past."

- Haruki Murakami, 1Q84

Summary

Little Ice Age glacier forefields in alpine permafrost environments are characterized by complex past or current glacier-permafrost interactions. These environments, sitting astride the fields of glaciology, geomorphology, hydrology, paleo-climatology and natural hazard assessment, are the result of a wide and interconnected spectrum of glacial, periglacial, nival, hydrological, gravitational, and mass-wasting processes. Glacier-permafrost relationships in high mountain environments give rise to the coexistence of a diverse range of landforms, such as glaciogenic debris, glacier ice masses, including debris-covered ice and buried dead glacier ice, but also thermally controlled (permafrost-related), viscous creeping debris-masses (rock glaciers) disturbed and sometimes partly displaced by the loading of glacial-stress (glaciotectonic). These interactions thus contribute to the development of morphologies beyond simple either-or-type landform classification. The consideration of interactions between glaciers and permafrost is fundamental to understanding the long-term evolution of high-mountain landscape. Due to their thermal inertia, viscous-permafrost creep landforms can develop over millennial timescales and may act as archives of past climatic oscillations. Repeated sequences of glacial and interglacial periods throughout the Holocene and recent historical glacier advances have driven the multi-phased geomorphic processes in glacier forefields and contributed to the morphology of present-day glacier forefields in permafrost environments. The driving processes contributing to the dynamics of the systems in which glaciers and permafrost interacted remain understudied by the scientific community.

This thesis presents and synthesises five years of research on Little Ice Age glacier forefields in alpine permafrost environments. Their internal structure, thermal evolution, and kinematic behaviour across temporal and spatial scales were investigated at three sites, located in the western and southern Swiss Alps. The extensive dataset gathered from field campaigns, combined with a thorough literature review, has enhanced the understanding of the driving processes behind the post-LIA morphodynamical evolution of these systems.

Throughout the different investigations carried out in the scope of this thesis, we were able to emphasize the value of applying a multi-method approach, which provided new insights on the dynamics of these systems across varying spatio-temporal scales. On all three sites, we were able to highlight the heterogeneous distribution of the ground ice content and origin within the glacier forefields and their associated landforms. The variability of ground ice content and properties is reflected through the varying degrees of sensitivity to thermally-driven processes. It was also revealed that the spatial heterogeneity of the kinematic behaviour of the investigated landforms – such as glacitectonized perennially frozen landforms and debris-covered glaciers – can be largely attributed to the landform origin and development, as well as the debris coverage and the topographical slope. Key processes driving surface changes include ice melt-induced subsidence and downslope permafrost (back-)creep deformation, both of which exhibit seasonal signals due to their thermal drivers. The magnitude of ice melt-induced subsidence was the highest in areas where massive ice lenses (or debris-covered glacier ice) were found. This study also revealed the resilience of the ground ice to a warming atmosphere, in particular in the permafrost of perennially frozen landforms with a coarse debris mantle. This was also found for the glacier ice beneath the thickening debris-cover of the glaciers' terminus, which is in complete disequilibrium with the current climate.

Résumé

Les marges proglaciaires du Petit Âge Glaciaire situées dans un contexte de pergélisol alpin se caractérisent par des interactions complexes entre glaciers et pergélisol. Ces environnements, situés à la croisée des domaines de la glaciologie, de la géomorphologie, de l'hydrologie, de la paléoclimatologie et de la gestion des risques naturels, sont le résultat d'un large spectre de processus glaciaires, périglaciaires, nivaux, hydrologiques et gravitationnels. Dans les environnements de haute montagne, les relations entre les glaciers et le pergélisol donnent lieu à la coexistence de diverses formes de relief, telles que des sédiments glaciogéniques, des glaciers, notamment des glaciers couverts, mais aussi des formations de glace morte, ainsi que des glaciers rocheux mécaniquement et thermiquement perturbés par l'avancée glaciaire. Ces interactions contribuent ainsi au développement de morphologies qui vont au-delà des classifications de formes de relief simples. La prise en compte des interactions entre glaciers et pergélisol est fondamentale pour comprendre l'évolution à long terme des paysages de haute montagne. En raison de leur inertie thermique, les formes du relief découlant du fluage du pergélisol peuvent se développer sur des échelles temporelles millénaires et constituer des archives des oscillations climatiques passées. Les séquences répétées de périodes glaciaires et interglaciaires tout au long de l'Holocène et les avancées glaciaires historiques récentes ont fortement influencé les processus géomorphologiques multi-phasés dans les marges proglaciaires et ont contribué à la morphologie des marges proglaciaires actuels dans les environnements de pergélisol. Les processus moteurs contribuant à la dynamique des systèmes dans lesquels glaciers et pergélisol ont interagi restent peu étudiés par la communauté scientifique.

Cette thèse présente et synthétise cinq années de recherche sur les marges proglaciaires du Petit Âge Glaciaire situées dans les environnements de pergélisol alpin. Leur structure interne, leur évolution thermique et leur comportement cinématique à travers les échelles temporelles et spatiales ont été étudiés sur trois sites situés dans les Alpes suisses occidentales. L'importante base de données recueillie lors de campagnes de terrain, combinée à une revue approfondie de la littérature, a permis d'améliorer la compréhension des processus à l'origine de l'évolution morphodynamique post-Petit Âge Glaciaire de ces systèmes.

Grâce aux investigations menées dans le cadre de cette thèse, nous avons pu relever les avantages d'une approche multi-méthodes, qui a fourni de nouvelles perspectives sur la dynamique de ces systèmes à travers différentes échelles spatio-temporelles. Nous avons pu mettre en évidence la distribution hétérogène du contenu et de l'origine de la glace dans les marges proglaciaires. La variabilité du contenu et des propriétés de la glace se reflète dans les différents degrés de sensibilité aux processus thermiques. Il a également été révélé que l'hétérogénéité spatiale du comportement cinématique des morphologies étudiées – telles que les moraines de poussées et les glaciers couverts – peut être largement attribuée à l'origine et au développement du relief, ainsi qu'à la couverture de débris et à la pente topographique. Les processus à l'origine des changements de surface sont l'affaissement induit par la fonte et la déformation par (rétro-)fluage du pergélisol, qui présentent tous deux des signaux saisonniers en raison de leurs facteurs thermiques. L'ampleur de l'affaissement induit par la fonte de la glace était la plus élevée dans les zones où l'on a trouvé des lentilles de glace massives (ou de la glace de glacier recouverte de débris). Cette étude a également révélé la résilience de la glace malgré le réchauffement de l'atmosphère, en particulier dans le pergélisol des reliefs gelés de façon permanente. Cela a également été constaté pour la glace de glacier sous la couverture de débris de plus en plus épaisse du terminus des glaciers, qui est en complet déséquilibre avec le climat actuel.

Acknowledgements

What a journey! Not only across the Alps, but also through time. From the Little Ice Age to the last five years. These last five years have been quite hectic, yet many different people were here along the way to make this happen. This thesis is the result of a collective effort, bringing people together – on the field, at an excursion, around a table discussing the latest data collected – and sharing a fascination for the alpine environments and landscapes.

Through these few lines, I would like to thank many (*many*) people.

First of all, Christian Hauck and Christophe Lambiel who agreed to jump in the supervision of this thesis. Your positive attitude, encouragements and ideas inspired me to push my research always a little step further... sometimes a little too far. Thank you for helping me keep the steering wheel in the right direction. With both of you as supervisors, I had the chance to see and experience my research from a geophysicist's perspective, but also from a geomorphologist's perspective. Having new visions in the middle of my thesis, gave a slightly different turn to my research, which I am thankful for. It allowed me to explore techniques and concepts, which gave a lot of value to this thesis.

I would like to thank Marcia Phillips, as a member of my *jury d'accompagnement* and jury member of this thesis. Thanks for the constructive exchanges that often helped me gain some perspective about the research that I was conducting. Your kindness and understanding during times of doubt, helped me get the head out of the water and continue this journey. To the other jury member of this thesis, Isabelle Gärtner-Roer. Our discussions about Gruben and glacier-permafrost interactions in general were very insightful. Thank you for sharing your expertise in permafrost research.

To everyone involved in bits and pieces of my research. Thanks to Coline Mollaret and Tamara Mathys for sharing their knowledge on the PJI scheme. To Sebastián Vivero and Hanne Hendrickx for being the photogrammetry maestros and for pushing me do some cool analysis with the Ritord dataset. To Jan Beutel for sharing your thoughts on permanent dGNSS stations during a day out running in the mountains. To Wilfried Haerberli, for opening the breach of research on glacier-permafrost interactions in the Alps. It is inspiring. Thank you for the fascinating discussions and your far-reaching insights on Gruben.

To all the people who accompanied me on the field. Without you, this thesis would have not been the same... or simply been. To Armando (el zio), Pato, Nicholetta, Alex, Hanne, Baptiste, Eliane for experiencing with me my first “big” fieldwork campaign. To Tania, Dim, Ale, Martina, Beni, Eric, Jessica, Bastien, Aldo, Grégoire, Noalie, Clément, Tifenn, Paula, Gaëlle, Andrew, Thomas, Eva-Maria for helping me carry heavy backpacks in coarse blocky terrains and for helping me do some alpine gardening – planting electrodes and water them, hoping for a fruitful result. To Cécile, Dominik and Gaëlle for braving the cold in Ritord and for the coffee up there. To Nicole, for joining me on spontaneous field campaigns to just go and check if the permanent dGNSS station is still there, but most importantly to check the skiability of the snow conditions on the field site. To Lucien for our botanical quest of *génépi* and temperature loggers.

To Jonathan, Elisa and Chantal. Thanks for being such great Young Geomorphologists. I am super grateful for all the nice (and cloudy-rainy) days spent together analysing the landscape and talking about life and a bit of geomorphology.

A big thank you to all fellow PhD colleagues at the University of Fribourg. For the shared lunches, babyfoot games, discussions and complaints around beers and chips, the creative hat-making sessions. I really enjoyed this time with you.

To Nicole, Sylvie, Astrid, David and Alex. Thank you for the huge support solving technical and sometimes administrative issues, but also to remind me to do backups of my work.

Thanks to all the collaborators at the department for the discussions shared during (sometimes very long) coffee breaks. For the fruitful exchanges about science during pre-lunch seminars, but also for the moments spent on the field in the Alps or elsewhere.

To the Girls* on Ice team. For being a source of inspiration – to me but also to many others. To Kathrin, Lena, Maud, Natalie, Jane, Marijke, Léa, Nathalie, Nicole, Laura, Yvonne for all the work and passion invested in this programme.

To all my friends who supported me throughout this journey, but also to the ones who accompanied me to this journey. Nato, un grand merci d'être une amie de vie. Aux Babes, merci pour tous les moments partagés – de nos premières sorties alors qu'adolescentes à nos p'tites crêpes-party. A mes copains et copines avec qui je peux partager un paquet de chips ou une glace. A tous les ami.e.s avec qui j'ai tapé du pied ou fait du hoola-hoop à Chatalette. A Chloé, Reminem, Camille, Laeti, Antoine, Emilien, Del, Pia, Emilie, Valou, Mathilde, Jan, Lulu, et toute la clique. Merci d'être des ami.e.s plus qu'en or. A la colloc' de la Prairie, M^e Kolly, Paul, Baptiste, Remi, et Jean-Marc, merci de m'avoir accueilli dans votre havre de paix et sérénité où fleurissent les petites marguerites. A Laure, pour ta positivité et douceur. A Manon et James, pour les soupers spontanés, pour les cafés-jardin, pour votre positivité. A Nicole et les co-équipières du super attelage : Julie, Manon, Maëlle, Aline, Mathilde et Camille (bis). Merci de nous faire vivre de telles aventures. Parlant d'aventure, merci à toi Martina de m'avoir emmené découvrir de nouvelles montagnes en Asie centrale. A Anouk, d'avoir été là pendant un peu près tout le temps (même à Neuch') et pour les thés chez Baechler. A Eliane, de m'accompagner dans mes idées folles et d'être une amie si précieuse. A Flo, Res, Marlene, Jonas pour tous ces moments partagés. Ces journées sans fin sur les skis, dans des locaux d'hiver au fin fond du Tessin, pour les journées blanches où la légèreté de la neige nous remplissait de joie, pour mon immersion totale au suisse-allemand, pour le partage de ces repas gargantuesques sans que le dessert soit de trop, pour ces journées ensoleillées au pied d'une falaise, au plus grand désespoir de Beni. A Mirta, merci d'égayer la vie et de la rendre si douce. A ma famille, merci, tout simplement. A ma grand-maman Agnès, merci de m'avoir rappelé de temps à autre qu'il reste encore des jours derrière le Moléson et d'avoir été ma deuxième maman au cœur d'or. A ma maman, d'avoir été une source de force et d'inspiration.

Finalement, merci à toi Beni. Pour tout.

Contents

Summary	i
Résumé	ii
Acknowledgements	iii
Contents	v
Abbreviations	vii
Part I Synopsis	1
1 Introduction	3
1.1 Sate of knowledge on glacier–permafrost interactions	3
1.1.1 Permafrost and rock glaciers	3
1.1.2 Holocene glacier variations in the Alps	5
1.1.3 Little Ice Age glaciers in alpine permafrost environments	6
1.1.4 Glacier-permafrost interactions	9
1.2 Motivation and relevance	12
1.3 Aims and research questions	15
1.4 Structure of the thesis	16
2 Study sites	17
2.1 Aget	18
2.2 Ritord	20
2.3 Gruben	23
2.4 Climatic setting	25
3 Methodology	27
3.1 Geodetic approaches	28
3.1.1 In-situ continuous geodetic measurements	28
3.1.2 In-situ seasonal and annual geodetic measurements	29
3.1.3 Structure-from-Motion photogrammetry	29
3.2 Geophysical methods and applications	31
3.2.1 Geoelectrical surveys in permafrost environments	31
3.2.2 Refraction seismic tomography (RST)	35
3.2.3 Petrophysical joint inversion	36
3.2.4 Ground penetrating radar	37
3.3 Ground surface temperature	37
4 Key findings and discussion	39

4.1	Evolution of ground ice and its influence on long-term permafrost creep dynamics – case study of Aget (<i>Publication I</i>)	39
4.1.1	Ground ice content distribution and evolution	40
4.1.2	Contribution of ground ice content evolution on the kinematic behaviour of the Aget GFL A	42
4.2	Ground ice content and origin and its influence on seasonal surface dynamics – case study of Gruben (<i>Publication II</i>).....	46
4.2.1	Characterization and estimation of ground ice content	47
4.2.2	Seasonal surface dynamics.....	49
4.3	Post-glacial dynamics of a glacier forefield and its components in the context of mountain permafrost across spatial and temporal scales – case study of Ritord (<i>Publication III</i>)	53
4.3.1	Characterization of the internal structure of the glacier forefield	53
4.3.2	Evolution of ground ice through changes in electrical resistivity	55
4.3.3	Pluri-decadal surface lowering and displacement	56
4.3.4	Influence of ground thermal regime on sub-seasonal kinematic behaviour.....	61
5	Synthesis	65
5.1	Methodological approach.....	65
5.2	Main system components and their associated dynamics	67
5.3	Internal structure and dynamics	69
5.3.1	Glacitectonized perennially frozen landforms (push-moraines).....	69
5.3.2	Debris-covered glaciers.....	70
6	Conclusions and outlook.....	73
6.1	Conclusions	73
6.2	Outlook	74
7	References.....	77
	Part II Research publications.....	89
	Publication I: Wee and Delaloye (2022), Permafrost and Periglacial Processes	91
	Publication II: Wee et al. (2024), The Cryosphere	109
	Publication III: Wee et al. (in review)	137
	Curriculum vitae	193

Abbreviations

AG	Aget
AGNES	Automated GNSS Network for Switerland
a.s.l.	above sea level
BTS	Bottom Temperature of the Snowcover
CORS	Continuously Operating Reference Station
DCG	Debris-Covered Glacier
DEM	Digital Elevation Model
dGNSS	differential Global Navigation Satellite System
DoD	DEM of Difference
ELA	Equilibrium Line Altitude
ERT	Electrical Resistivity Tomography
GCP	Ground Control Point
GFI	Ground Freezing Index
GFL	Glaciotectonized Frozen Landform
GPS	Global Positioning System
GRU	Gruben
GSB	Col du Grand St-Bernard Meteorological Station
GST	Ground Surface Temperature
GTI	Ground Thawing Index
GTN-P	Global Terrestrial Network Permafrost
IPA	International Permafrost Association
LIA	Little Ice Age
LiDAR	Light Detection and Ranging
LoD	Limit of Detection
MAAT	Mean Annual Air Temperature
MAGST	Mean Annual GST
MPA	Mountain Permafrost Altitude
NCC	Normalized Cross-Correlation
PERMOS	Swiss Permafrost Monitoring Network
PJI	Petrophysical Joint Inversion
RGIK	Rock Glacier Inventories and Kinematics
RIT	Ritord
RMSE	Root Mean Square Error
RST	Refraction Seismic Tomography
RTK	Real-Time Kinematics
TGS	Terrestrial Geodetic Survey
SAE	Säntis Meteorological Station
SfM	Structure from Motion
Swipos	Swiss Positioning Service
Swisstopo	Swiss Federal Office of Topography
UAV	Uncrewed Aerial Vehicle
UTL	Universal Temperature Logger
VBH	Virtual Borehole
VES	Vertical Electrical Sounding
VRS	Virtual Reference Station
WEqT	Winter Equilibrium Temperature

Part I Synopsis

1 Introduction

Sitting astride the fields of glaciology, geomorphology, hydrology, paleo-climatology and natural hazard assessment, environments and their associated landforms subject to glacier-permafrost interactions and interrelations reach beyond clear and linear research frontiers. Being part of a wide and interlaced spectrum of processes and complex interconnected systems, glacier-permafrost relationships in high mountain environments tend to breach research frontiers, fostering interdisciplinary research. The first part of this introductory chapter provides an overview of the current state of research. The second part discusses the motivation and relevance of advancing research on glacier-permafrost interactions, and defines the main research questions guiding this thesis. The last part presents the structure of the thesis.

1.1 State of knowledge on glacier–permafrost interactions

Historically, research on glaciers and permafrost has evolved along separate lines. Permafrost research has its principal origins in glacier-free, high-latitude lowlands, while glaciology emerged in high-mountain environments where permafrost is heterogeneously distributed and difficult to recognize. Descriptions of glacier-permafrost interactions were first documented in the sub-Arctic and Arctic lowlands from the early decades of the 20th century (Bersier, 1954; Carlé, 1938; Hopkins, 1923; Kälin, 1971; Kupsch, 1962), whereas their identification and description in the high-mountain context were published in the latter half of the 20th century (Evin, 1992; Haeberli, 1979; Käab et al., 1997; King et al., 1987; Kneisel, 1998; Ribolini et al., 2007). These first scientific insights on glacier-permafrost interactions and the environments in which they occur have opened a door to expand the knowledge on their genesis, on their evolution, and on the driving processes behind their dynamics, as well as in defining their geomorphological significance under a changing climate (Bosson et al., 2015; Cusicanqui et al., 2023; Gärtner-Roer et al., 2022; Haeberli et al., 2024; Kunz et al., 2022; Kunz and Kneisel, 2020; Vivero et al., 2021). This sub-chapter provides a brief overview of the current knowledge from the scientific literature on glacier-permafrost interactions in high-mountain environments, which will allow the definition of key terms encountered in this thesis.

1.1.1 Permafrost and rock glaciers

Permafrost is thermally defined as ground material (i.e. rock, sediments or soil) that remains continuously at or below 0°C for at least two consecutive years (Harris et al., 1988). Considering exclusively temperature as a defining parameter, permafrost does not necessarily contain frozen water. Rather, it encompasses any substrate that is subject to specific thermal conditions. Permafrost is found in regions where the mean annual air temperature (MAAT) is below 0°C (Péwé, 1983). Permafrost is widespread in the Arctic and affects most of the Subarctic, and a great part of high mountain regions, underlying approximately one-fifth of the global land surface (Gruber, 2012; Obu, 2021). The distribution of permafrost can vary from being continuous in the coldest regions, where 90-100% of the area is affected by permafrost, to discontinuous or sporadic in

warmer or mountainous regions, where the occurrence of permafrost is 50-90% or 10-50%, respectively. In the Alps, permafrost is mostly sporadic or discontinuous, reflecting its complex and heterogeneous spatial distribution, with respect to the different surface and near-surface characteristics and properties governing its existence and evolution (Haeberli and Gruber, 2009). In the Swiss Alps it is generally found at elevations above around 2500 m a.s.l. on north-facing slopes, covering about 3-5 % of the area of Switzerland (Boeckli et al., 2012; Keller et al., 1998; Kenner et al., 2019).

As a thermal phenomenon, permafrost is usually invisible from the surface. However, various direct and indirect methods enable its detection and characterization (Hauck and Kneisel, 2008; Noetzli et al., 2021). In the alpine context, permafrost generally occupies barren terrain above the tree line, such as rock walls and coarse debris-covered slopes, amongst which rock glaciers are the most discernible evidence of past and present permafrost occurrence (Barsch, 1992; Waharftig and Cox, 1959). Because of their distinct appearance and their thermo-dynamical response to the warming climate (Kellerer-Pirklbauer et al., 2024), rock glaciers have received increasing attention from the scientific community. Nevertheless, the dynamic response of these phenomena and landforms to this warming trend is not uniform in space nor in time as their occurrence in high mountain environments can be found under a wide spectrum of possible conditions, origins, landform settings and assemblages (Bosson and Lambiel, 2016; Monnier et al., 2014; Navarro et al., 2023). Moreover, in a context of growing interest to coordinate the development of rock glacier inventories as part of large scale approaches to quantify the impact of climate change on permafrost, efforts have been undertaken to create clarity in order to better interpret and analyse the climatic, hydrological and geomorphological significance of rock glaciers, in particular where complex geomorphological contexts (e.g. glacier-permafrost interactions) hamper simple and straightforward “either-or” classification (Haeberli et al., 2024).

Rock glaciers are defined by the former or current viscous creep of ice-rich frozen ground (Haeberli et al., 2006). They are recognizable in the landscape by their steep lateral and frontal margins and their surface topography characterised by a successive pattern of ridges and furrows, reflecting a cohesive flow behaviour. The movement of rock glaciers, when in their thermally and kinematically active state, occurs essentially at the shear horizon (Arenson et al., 2002; Arenson and Springman, 2005). Internal thermally-driven deformation in the ice-rich core and displacements due to sliding or tilting boulders at the surface of the active layer also account for their movement. The dynamic behaviour of rock glaciers is highly dependent on the properties of the latter and former structural components, which in turn influence the mechanical processes taking place at the shear horizon (Cicoira et al., 2019).

Being the uppermost layer of viscous-creep landforms (i.e. rock glaciers), the active layer is composed of coarse blocky seasonally frozen material of a few meters. The active layer is by definition the interface between the atmosphere and the perennially frozen and ice-rich rock glacier core. This ground thermal regime is owed to complex thermodynamic processes between the atmosphere and ground surface properties, governing its energy balance (Amschwand et al., 2024; Hoelzle et al., 2001; Scherler et al., 2014; Wicky and Hauck, 2020) and consequently affecting the processes occurring in the ice-rich permafrost layer and in the shear horizon with a thermal lag. As a buffer layer between the atmosphere and the ground ice, the active layer insulates the ground ice, reducing the thawing process occurring at the permafrost table. Nevertheless, the strength of the insulation effect depends on the active layer thickness. The influence of increasing air temperatures can significantly contribute to enhanced ice melt-induced subsidence in cases of supersaturated ice-rich permafrost conditions or embedded

glacier-ice lenses within the permafrost body, or permafrost thaw. The presence of ice of glacial origin within perennially frozen rock glacier bodies, can occur in contexts of former or current glacier-permafrost interactions (Haeberli, 1979; Kunz and Kneisel, 2020). Such interactions can largely modify the thermal regime of rock glaciers, but also their thermo-mechanical behaviour, thereby fundamentally influencing their general kinematic behaviour. Many aspects of how the coexistence and interaction between glaciers and pre-existing perennially frozen landforms influence their post-interaction internal structure and subsequent processes remain largely unknown. This thesis aims to assess the extent of the impact of former glacier-permafrost interactions on glacitectonized frozen landforms. Specifically, we will address the following questions: Is there embedded ice of glacial origin within these landforms? If so, where is it located? Is the thickness of the active layer or the debris cover influenced by these interactions? Lastly, how do these structural changes in viscous-creep glacitectonized frozen landforms influence their dynamics?

1.1.2 Holocene glacier variations in the Alps

The Holocene experienced repeated sequences of glacial and interglacial periods with differing intensities. In the Alps, the strongest glacier advances likely occurred during the Little Ice Age (ca. 1350–1850 in the Alps), as during most of the Holocene, alpine glaciers were never significantly larger than they were during this last significant period of glacier expansion (Ivy-Ochs et al., 2009; Nussbaumer et al., 2011). The LIA underwent a general temperature depression of about one or two degrees (Grove, 2008), mainly due to large explosive volcano eruptions causing radiative summer cooling, increased summer precipitations, and altered circulation patterns (Lüthi, 2014; Wegmann et al., 2014). Reconstructed alpine mean annual temperatures revealed alternating warm and cold periods (Casty et al., 2005), reflected by episodic and rapid glacier length fluctuations (Figure 1.1; Nussbaumer et al., 2011; Zumbühl et al., 2008). In general, glacier advances during the period of maximum extent were within a few hundred metres. The precise timing and amplitude of these fluctuations varies between glaciers, depending on factors such as glacier size and slope, as well as topographic conditions and mass balance sensitivity (Paul and Bolch, 2019). Maximal glacier extents were documented in the 1600s, 1650s and 1850s (Lüthi, 2014; Nussbaumer et al., 2011), and were preceded by periods of particularly harsh winters with low temperatures and high precipitation (Casty et al., 2005; Vincent, 2005). The fluctuations of LIA glaciers, with their maximal extent reached in the 1850s, exerted a strong influence on the multi-phased geomorphic processes contributing to the past- and present morphodynamical evolution of the alpine landscape (Maisch et al., 2003).

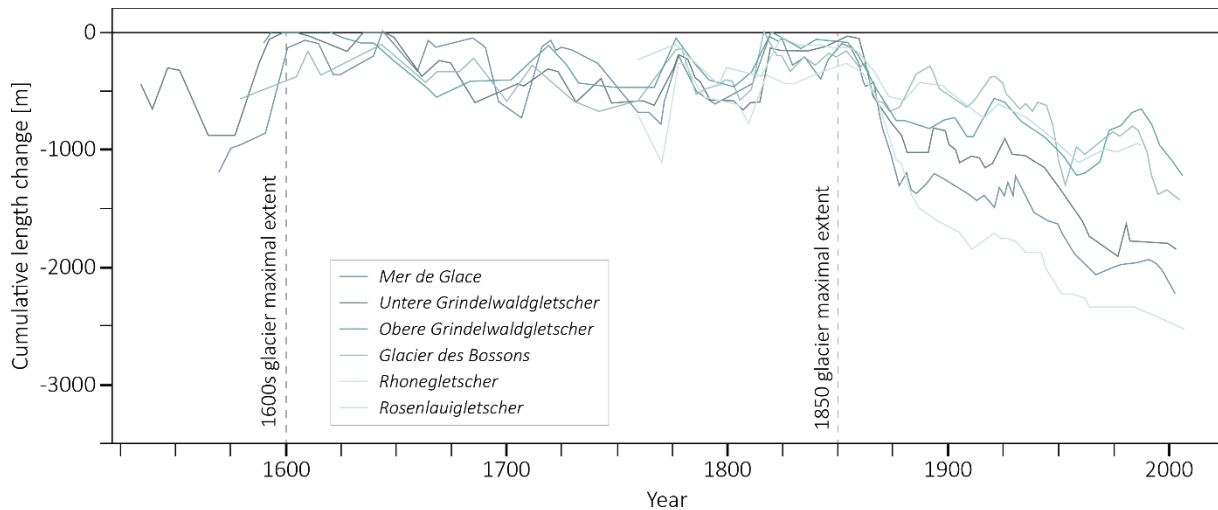


Figure 1.1: Reconstructed and measured cumulative glacier front variation in the Alps since the LIA. The zero value on the y-axis corresponds to the most extensive front position of glaciers during the LIA. Modified after Zemp et al. (2011).

1.1.3 Little Ice Age glaciers in alpine permafrost environments

The distribution of glaciers and permafrost is highly dependent on the degree of continentality in climate conditions, being a function of mean annual air temperature and annual precipitation (Haeberli and Burn, 2002; Kenner and Magnusson, 2017). In regions with humid-maritime climate, active glaciers whose extent often reach permafrost-free area tend to predominate (Pfeffer et al., 2014). In contrast, regions with too dry-continental climate hamper the formation of glaciers in cold environments and are rather characterized by widespread permafrost (Azócar and Brenning, 2010). Nevertheless, in some dry-continental climatic contexts, polythermal to cold glaciers can form where permafrost conditions occur (Bosson, 2016; Etzelmüller and Hagen, 2005; Haeberli and Burn, 2002). The dry topo-climatic conditions of the inner Swiss Alps allowed, during the LIA, the development of relatively small cirque glaciers confined within the belt of discontinuous permafrost (see Figure 1.2; also Bosson, 2016), as one can assume that the reasonably small climatic oscillations of the Holocene could potentially mean that the lower altitudinal limit of permafrost did not differ significantly from the current one throughout the last 10000 years or so (Ivy-Ochs et al., 2009).

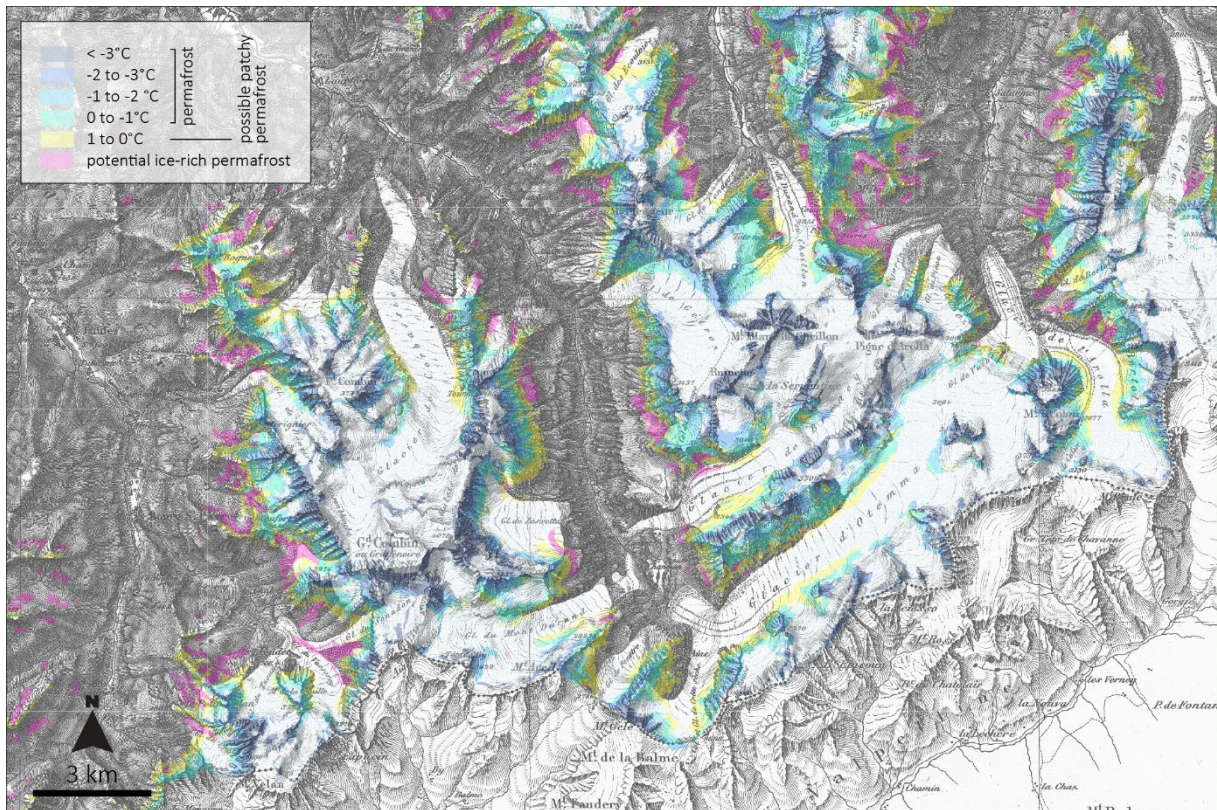


Figure 1.2: Little Ice Age glacier maximal extent in the western Swiss Alps based on the historical Dufour map (1864) and current permafrost distribution (Kenner et al., 2019). Swisstopo (2024).

In the Swiss Alps, glaciers that extended exclusively within the belt of discontinuous permafrost were mainly small (cirque) glaciers, as larger valley glaciers extended beyond the lower limit of mountain permafrost (Figure 1.2). Small cirque glaciers are commonly found where the maximal altitude of the surrounding relief is slightly higher than the regional equilibrium line altitude (ELA) or at lower elevations where the topography enables higher accumulation rates (Colucci, 2016; González Trueba et al., 2008; Huss and Fischer, 2016; Oliva et al., 2018). Small glaciers develop under climatically-dominant processes or topographically-dominant processes. For instance, small glaciers are often situated in cirques, bellow rock walls, where wind-drift and avalanches in steep topographical settings may locally multiply winter accumulation by a larger factor (Helfricht et al., 2015; Kuhn, 1995). Because of their size and micro-climatic regulation, small glaciers are very responsive to climatic changes (Colucci and Guglielmin, 2015). However, some of these small cirque glaciers are often debris-covered, as the presence of steep rock walls enables important sediment production (Capt et al., 2016). The thickness of supraglacial debris controls how glaciers respond to climatic fluctuations, as a thin layer (less than a few centimetres) enhances melting, while a thick layer insulates the underlying ice, making them more resilient to climate change (Østrem, 1959; Pellicciotti et al., 2015; Rounce et al., 2021). Nevertheless, understanding the influence of larger scale climatic changes on their evolution can be seen as a challenge as their mass balance is mainly governed by complex advective processes of snow and small-scale effects (Huss and Fischer, 2016; Scotti et al., 2014).

The majority of glaciers present in permafrost environments are either cold-based or polythermal (Etzelmüller and Hagen, 2005). This is due to the fact that the temperature of glacier ice is dependent on the energy exchanges with the climate and the Earth's surface (Cuffey and

Paterson, 2010). Etzelmüller and Hagen (2005) identified three main spatial configurations of thermal regime for these glaciers. At high elevation or in very cold and dry climatic conditions, when the equilibrium line altitude (ELA) of glaciers is well above the mountain permafrost altitude (MPA), glacier ice is likely to be below the temperature of the pressure melting point, making the glacier cold (Figure 1.3a). Whereas in slightly warmer and wetter, but still dry-continental conditions, where limited summer melting occurs, the glacier can be polythermal when the basal layer is temperate (at the pressure melting point) due to latent heat release by meltwater refreezing or by internal deformation (Figure 1.3b-c; Aschwanden and Blatter, 2005). Alternatively, the glacier can be polythermal when cold ice is present only in the marginal glacier zones, while the central part is temperate (Figure 1.3d-e).

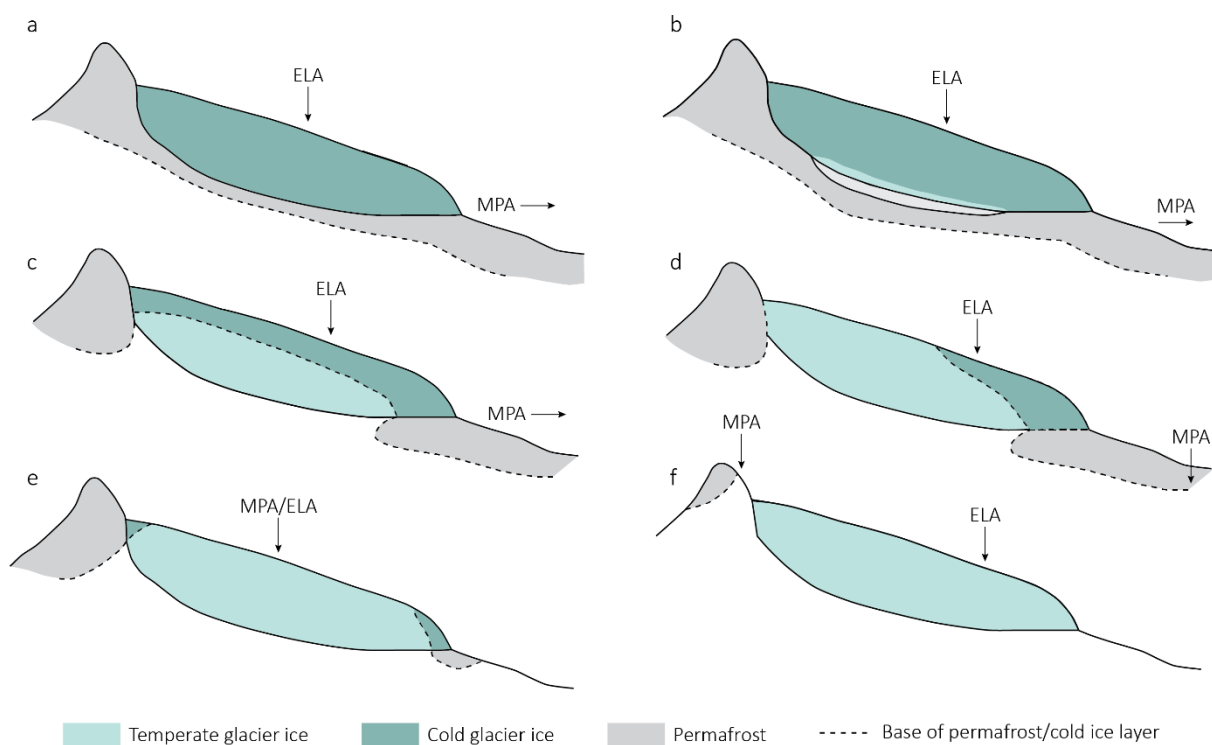


Figure 1.3: Schematic profiles of glaciers showing the distinct thermal regimes that possibly occur in mountain permafrost conditions. ELA and MPA refers to the equilibrium line altitude and to the mountain permafrost altitude, respectively. In the (a) situation, the glacier is entirely cold. For (b-c), temperate ice occurs at the glacier-ground interface, and for (d-e), cold ice is located at the margins of the glacier and temperate ice at its central part. Modified after Etzelmüller and Hagen (2005).

The thermal regime of a glacier is influenced by a multitude of factors, including the spatial and temporal variations in the snow cover thickness, the glacier thickness, the energy fluxes related to water circulation and phase changes, as well as geothermal heat fluxes (Cuffey and Paterson, 2010; Gilbert et al., 2012). The thermal structure of a glacier exerts a critical influence on its mechanical and hydrological properties (Cuffey and Paterson, 2010; Irvine-Fynn et al., 2011). Hydrological processes are prevalent in temperate ice, whereas they are scarce or absent in cold ice, given that it acts as an impermeable layer. The presence of water within a temperate glacier and at its bed exerts a significant influence on the deformation properties of the ice, thereby enhancing the glacier's dynamics. Conversely, cold ice is less subject to internal deformation as the cooling of ice increases its viscosity (Cuffey and Paterson, 2010). As a consequence, cold

glaciers are immobile and bed erosion is usually very limited. Found at the interface between temperate and cold glaciers, polythermal glaciers present a certain complexity in terms of their hydro-dynamical dichotomy.

In polythermal glaciers, the occurrence of temperate ice in the accumulation zone is driven by the release of latent heat, which is caused by the refreezing of percolating meltwater in firn areas. Conversely, the presence of cold ice in the marginal zones is partly owed to the more efficient cooling of the ice during periods of low air temperature in winter. This is because the snow cover on the ablation zone sets on later in the season and is often thinner than in the accumulation zone, thus diminishing its insulating effect. Furthermore, englacial meltwater circulation, which contributes to the warming of ice, are generally uncommon or absent in glacier margins (Cuffey and Paterson, 2010; Gilbert et al., 2012). Because of their thermal structure (i.e. extensive cold ice content), polythermal glaciers can exhibit limited rates of ice deformation (Etzelmüller et al., 1993; Irvine-Fynn et al., 2011). In cases where the proportion of temperate ice is greater than cold ice in polythermal glaciers, increased effective glacial stress and ice deformation may be induced. Nevertheless, cold ice remains frozen to its bed and compressive stresses can be transmitted by the glacier into proglacial frozen sediments that may locally result in their deformation through thrusting (Etzelmüller and Hagen, 2005). These glacitectonized frozen sediments, also known as push-moraines or glacier forefield-connected rock glaciers, are the visible expression of glacier-permafrost interactions. While this thesis primarily focuses on the glacitectonized frozen landforms within Little Ice Age glacier forefields, it also examines the internal structure and dynamics of two adjacent polythermal debris-covered glacier tongues at Ritord and Gruben. These two glaciers are directly connected to the investigated forefields, making them relevant to the study. Although few studies (Bosson, 2016; Capt et al., 2016) have explored the processes associated with small debris-covered glacier systems in alpine permafrost environments, this research aims to further our understanding of the dynamics these systems through geodetic and geophysical investigations. By doing so, we hope to enhance our understanding of how these particular glacier types respond to recent climatic fluctuations within permafrost regions.

1.1.4 Glacier-permafrost interactions

Glacier-permafrost interactions in the Alps have been investigated in pioneering studies half a century ago (Haeberli, 1979; Haeberli and Röthlisberger, 1976). Early studies have mainly focussed on investigating thermal conditions and permafrost occurrences in recently exposed LIA alpine glacier forefields located within the belt of mountain permafrost by using geomorphological mapping, ground surface temperature measurements, and geophysical soundings (Evin, 1992; Haeberli, 1979; Kääb et al., 1997; King et al., 1987; Kneisel, 1998; Reynard et al., 2003; Ribolini et al., 2010). These first scientific insights on glacier-permafrost interactions in the Alps established a general typology of these systems and their components.

LIA glacier forefields in alpine permafrost environments provide insight into the role of Holocene glaciers in the production, transfer, deposition, and reworking of unfrozen and frozen sediments, which contribute to their development (Bosson, 2016). Holocene glacier fluctuations, occurring at varying rates over time, created conditions conducive to the continuous production of sediments within the glacier catchment, thus contributing to the development of multi-phased and polygenic permafrost-related landforms, but also glaciogenic landforms (Bosson, 2016;

Maisch et al., 2003). Moreover, as geomorphological and glaciological systems, environments in which glacier-permafrost interactions have occurred are the result of a wide and interconnected spectrum of glacial, periglacial, nival, hydrological, gravitational, and mass-wasting processes (Ballantyne, 2018; Etzelmüller and Hagen, 2005). Such interactions give rise to the coexistence of a diverse range of landforms, such as glaciogenic debris, glacier ice masses, including debris-covered ice and buried dead glacier ice, but also thermally controlled (permafrost-related), viscous creeping debris-masses (rock glaciers) disturbed and sometimes partly displaced by the loading of glacial-stress (glaciotectonics). Besides geometrical alteration, these glacitected frozen landforms (push-moraines or glacier forefield-connected rock glaciers) may encompass sporadic embedding of glacier ice (sedimentary ice) into frozen rock debris. In such systems, the occurrence of ice can be found within a wide spectrum of possible conditions, processes, materials, origins, landform settings and assemblages (Bosson and Lambiel, 2016; Cusicanqui et al., 2023; Monnier et al., 2014; Navarro et al., 2023). The origin and spatial distribution of ice within these systems predominantly reflects the thermal and mechanical impacts of the most recent glaciation, as well as the complexity of their dynamic response to the current warming trend, which is not uniform in space nor in time. In line with the questions raised in section 2.1, this thesis also examines the significance and impact of glacier-permafrost interactions on the spatial configuration of the investigated systems through the establishment of an (non-exhaustive) inventory of glacitected frozen landforms in LIA glacier forefields permafrost environments in the Swiss Alps.

1.1.4.1 Thermal influences of glaciers on permafrost

During the LIA, the advance of glaciers induced a thermal buffer effect between the atmosphere and the ground surface. Despite the cooling of the atmosphere during this cold period, warming of the overridden sub-glacial permafrost system can occur. The ice layer can exert an insulating effect by reducing heat exchange between the cold atmosphere and the ground (Etzelmüller and Hagen, 2005). Simultaneously, the glacier can facilitate advective heat transport through the movement of ice masses and through meltwater flow (Cuffey and Paterson, 2010). Ice flow can redistribute heat stored within the glacier from warmer accumulation zones to colder ablation zones, while meltwater transport within and beneath the glacier enhances heat transfer due to its high thermal capacity. This meltwater, originating from temperate zones of the glacier, can warm the underlying ground, especially as it releases latent heat upon refreezing in subglacial permafrost. Nevertheless, a reduction in the ground temperature gradient reduces the thermal response of permafrost to the presence of a polythermal glacier. Consequently, the longevity of permafrost can be sustained even in the presence of a temperate-based glacier (Etzelmüller and Hagen, 2005). However, it was often found that the central zones of glacier forefields are deprived of permafrost, due to warming effect of the temperate base of the polythermal glacier, often expressed by the presence of fluted moraines (Kneisel, 2003; Reynard et al., 2003; Figure 1.4). Fluted moraines are defined as a set of low ridges formed on the basal moraine surface, parallel to the glacier's flow direction (Hoppe and Schytt, 1953). The formation of fluted moraines is essentially due to the compression exerted on a water-saturated basal moraine following a basal detachment of the glacier when it surpasses an obstacle (such as a large boulder, outcrop of bedrock) (Delaloye, 2004). The presence of such patterns indicates that the glacier rested on saturated sediments and, thereby indicating that it was temperate at the base (Haeberli, 1979).

1.1.4.2 Mechanical influences of glaciers on permafrost

Cold ice is often present in the marginal zones of polythermal glaciers, which can allow the preservation of permafrost conditions (Gilbert et al., 2012). The marginal distribution of permafrost in glacier forefields where glacier-permafrost interactions occurred not only reflects the thermal impact, but also the mechanical influence of advancing polythermal glaciers on the frozen terrain. Rather than overriding the frozen sediments, the cold glacier margins can bind to the frozen debris. The loading of ice onto the frozen debris, induces the geometrical deformation of the latter, which is expressed by glaciotectionic landforms (compressive ridges and furrows perpendicular to the stress exerted by the LIA advancing glacier; Figure 1.4). The perennially frozen landforms (partly) derived from glaciotectionics are thus referred to as glacitected frozen landforms, push-moraines (Haerberli, 1979), thrust-moraines (Kunz and Kneisel, 2020), glacier forefield-connected rock glaciers (RGIK, 2023), or complex (former) contact zones (Gärtner-Roer et al., 2022; Haerberli et al., 2024b). The geometrical changes induced by glacial pressures also induce changes in stress transmission and reoriented stress fields, which are often expressed by a back-creeping behaviour (in the direction of the topographic thalweg formerly occupied by the glacier) following the glacial unloading. During the process of their formation, push moraines are frequently displaced towards a counter-slope. The glacier's retreat initiates a process of debuttressing, which results in slope instability (Deline et al., 2021). To offset this disequilibrium, the back-creeping of push-moraines is a common kinematic and geometrical response to glacier retreat, which also indicates the frozen state of the landform. In addition, enhanced surface elevation changes mainly due to ice melt-induced subsidence of embedded glacier ice lenses can also be observed. During the contact phase between the cold glacier margins and the frozen debris, glacier ice lenses can be embedded within the perennially frozen landform (Figure 1.4). Results from the very few existing studies revealed the presence of sporadic lenticular frozen bodies with a high electrical resistivity, often found in the proximal side of the investigated landforms (Cusicanqui et al., 2023; Delaloye, 2004; Kunz et al., 2022; Kunz and Kneisel, 2020; Reynard et al., 2003; Ribolini et al., 2010). This thesis aims to refine the two-dimensional characterization of the ground ice content at the study sites through geophysical investigations in order to better understand the distribution of permafrost and glacier ice in glacitected frozen landforms.

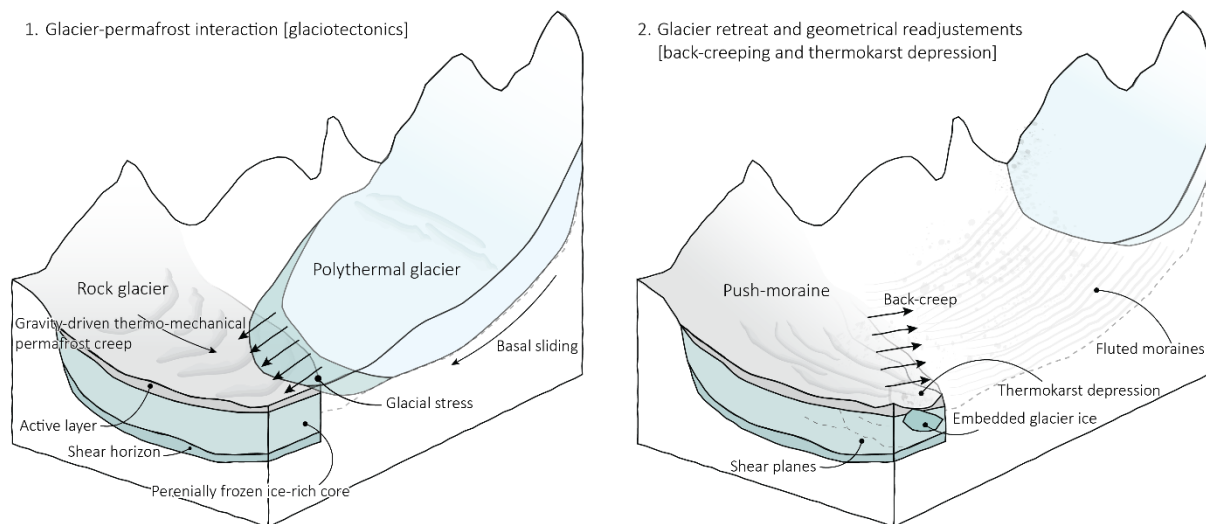


Figure 1.4: Schematic description of glacier-permafrost interactions contributing to the formation of a glacitected frozen landform (or push-moraine). Light blue corresponds to temperate ice and dark blue corresponds to cold ice.

1.2 Motivation and relevance

The high alpine environment is characterized by glacial and periglacial processes and landforms, which express varying degrees of sensitivity to the current warming trend (Carturan et al., 2020; Huss and Fischer, 2016; Kellerer-Pirklbauer et al., 2024; Mollaret et al., 2019a). The increase of temperature initiated at the end of the Little Ice Age (LIA; ca. 1350-1850 in the Alps; (Ivy-Ochs et al., 2009)) has largely contributed to the alteration of alpine environments, partly illustrated by a degrading cryosphere, and symbolized by the shrinkage of glaciers (Hock et al., 2019; Hugonnet et al., 2021). In the process of deglaciation, the forefields of glaciers are gradually enlarged, exposing unconsolidated sediments and ice of various origins, and forming a transitional landscape which may be subject to rapid geomorphic activity and evolution (Bosson et al., 2015; Carrivick et al., 2013; Carrivick and Heckmann, 2017; Gärtner-Roer and Bast, 2019; Figure 1.5). However, the dynamic response of these new landscapes and associated landforms to this shift from glacial towards periglacial or even post-periglacial (in cases of advanced permafrost degradation) conditioning can vary widely in space and in time as the occurrence of ice in such environments can be found under a wide range of possible conditions, processes, materials, origins, landform settings and assemblages (Bosson and Lambiel, 2016; Cusicanqui et al., 2023; Monnier et al., 2014; Navarro et al., 2023). It is particularly the case in environments subject to glacier-permafrost interactions, such as glacier forefields in alpine permafrost environments.

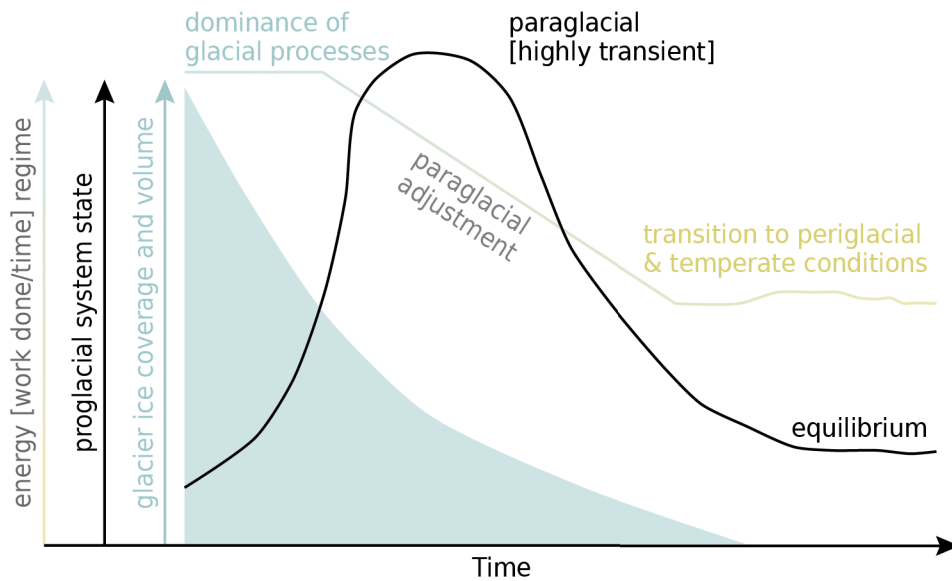


Figure 1.5: Conceptual model of glacier forefield systems in their transitional stages: from glacial-dominant processes, through a paraglacial phase, towards a periglacial-dominant processes, and perhaps ultimately a temperate landscape (modified after Carrivick and Heckmann, 2017).

Situated within a broad and continuous spectrum of glacial, periglacial, nival, hydrological, gravitational, and mass-wasting processes, these systems – as wholes – and their associated landforms have been overlooked by the fields of glaciology and geomorphology due to their complexity and the necessity to deconstruct research boundaries. The motivation behind this work is **to foster a better understanding of the morphodynamical response of these systems under transitioning climate conditions** and their **evolution across different timescales and spatial extents**. Further research in the dynamics of glacier forefield in alpine permafrost environments can lead to significant advances in research fields such as periglacial geomorphology, glaciology, mountain hydrology and natural hazard management.

In high-mountain regions, ice- and debris-dammed periglacial lakes are found at the front or margins of glaciers, as well as in permafrost areas. Outbursts of such proglacial, ice marginal or thermokarst lakes represent a significant natural hazard and can be associated with extreme discharge events (Kääb and Haeberli, 2001). Glacier shrinkage and permafrost degradation contribute to the development of potential hazardous proglacial lakes or thermokarstic periglacial lakes. Investigating and understanding the full spatio-temporal complexity of relations and interactions between surface and subsurface ice contributing to the evolution of the landscape is essential in a context of applied hazard management purposes (Cusicanqui et al., 2023; Haeberli and Röthlisberger, 1976; Kääb and Haeberli, 2001; Lliboutry et al., 1977).

In a context of growing interest and effort to coordinate the development of rock glacier inventories as part of large-scale approaches to quantify the impact of climate change on permafrost, such as the Global Terrestrial Network-Permafrost (GTN-P) and IPA Action Group Rock Glacier Inventories and Kinematics (IPA Action Group RGIK, 2023; Streletskiy et al., 2021), there is a need to create clarity in order to better interpret and analyse the climatic, hydrological and geomorphological significance of rock glaciers, in particular where complex geomorphological contexts such as glacier-permafrost interactions hamper simple and straightforward “either-or” classification (Haeberli et al., 2024). The characterisation of these

landforms is even more so important in a context where glaciers and viscous-permafrost creep landforms are subject to environmental laws whose purpose is to protect surface and subsurface perennial ice reservoirs (Arenson et al., 2022; Azócar and Brenning, 2010; Brenning, 2008; Vivero et al., 2021). This is why their correct characterisation through process understanding and ground truth data have become a highly relevant environmental matter.

The consideration of interactions between glaciers and permafrost (Kenner, 2018) is undoubtedly fundamental to the understanding of high-mountain landscape long-term evolution. Due to their thermal inertia, viscous-permafrost creep landforms can develop over millennial timescales and may act as archives of past climatic oscillations (Haeberli, 2000; Kääb, 2013). Repeated sequences of glacial and interglacial periods throughout the Holocene and recent historical glacier advances have strongly orchestrated the multi-phased geomorphic processes in glacier forefields and contributed to the morphology of present-day glacier forefields in permafrost environments (Ivy-Ochs et al., 2009; Maisch et al., 2003). During periods of glacier advances, permafrost was probably glacitectonically deformed and pushed upslope by the cold-based margins of advancing glaciers (Etzelmüller and Hagen, 2005). This interaction is often associated with the resulting morphologically distinctive ice-marginal landforms such as push-moraines at the former line of contact between the glacier and the pre-existing frozen debris. A deeper understanding of the genesis of push-moraines (or glacitectonized frozen landforms) as the visible expression of glacier-permafrost interactions, as well as the typology of their ice content and their associated morphodynamical processes can further their potential as indicators of past and future landscape evolution, contributing to estimations of mountain sediment fluxes and of their hydrological significance under different climatic conditions.

1.3 Aims and research questions

This thesis aims to explore the driving processes behind the dynamics of glacitected frozen landforms in three alpine Little Ice Age glacier forefields, as well as their adjacent debris-covered glaciers, and to study their variation over different spatial and temporal scales. From a geomorphological perspective, this thesis lies within the scope of a multi-method approach, whose overarching goal is to gain further insight into glacier-permafrost interactions and their contribution to kinematic and mass-wasting processes in such environments. This will be addressed in the form of site-specific case studies, through the following research questions:

Research question I:

What are the driving mechanisms behind the dynamics of viscous-creep features in LIA glacier forefields in mountain permafrost environments?

The viscous-creep of ice-rich mountain permafrost features (rock glaciers) shows strong inter-annual variations in velocities. The continuous ground and permafrost warming over the last two decades caused a general increase in creep rates of rock glaciers in the Alps. Nevertheless, decelerating creep rates have been observed in some cases. The objective of *Publication I* is to identify and assess the underlying driving processes responsible for such kinematic behaviour in permafrost creep formerly affected by glacier-permafrost interactions through the analysis of long-term geodetic, temperature and geophysical datasets.

Research question II:

To what extent do ground ice properties and origins influence the surface dynamics of landforms where glacier-permafrost interaction occurred?

The post-glacial dynamics of systems where glacier-permafrost interactions occurred comprise spatio-temporally complex and interlaced glacial, periglacial, nival, hydrological, gravitational, and mass-wasting processes. The full understanding of these systems requires high-resolution, quantitative, multi-method and interdisciplinary approaches. *Publication II* proposes an extensive data coverage to facilitate the interpretation and analysis of the climatic, hydrological, and geomorphological significance of landforms where glacier-permafrost interaction occurred.

Research question III:

How do LIA glacier forefields in alpine permafrost environments respond to climatic variations from pluri-decadal to seasonal timescales?

Inter-disciplinary investigations in the context of permafrost monitoring contribute to the understanding of the recent dynamics of viscous-creep landforms in mountain permafrost. However, the dynamic variations across the long-term evolution of complex systems in the context of glacier-permafrost interactions remains sparse. The assessment of the morphodynamical evolution of glacitected frozen landforms and a debris-covered glacier within a LIA glacier forefield in mountain permafrost across timescales ranging from decades to days is proposed in *Publication III*.

1.4 Structure of the thesis

This thesis is divided into two main parts. **Part I** provides a detailed synopsis of the research project, while **Part II** presents the scientific publications on which the work is based.

Part I – Synopsis

This section provides a comprehensive overview of the research conducted within the framework of this thesis. It begins with a detailed review of the current state of knowledge on glacier–permafrost interactions, followed by an identification of key knowledge gaps, which in turn leads to the motivation and relevance of the study, and the formulation of the main research questions. The study sites and the climatic context are then introduced, providing the geographical context in which the research is set. The methodological framework is subsequently outlined and detailed. The main findings are then presented through three case studies, each corresponding to a research publication, and are discussed in a broader context. A synthesis of the results is then given, integrating the findings from the individual case studies to identify common system components and dynamics across sites. A summary of the main outcomes and an outlook on future research directions closes the first part of this thesis.

Part II – Research Publications

This section contains the three scientific publications that constitute the core of this dissertation. All three are based on original research conducted during the thesis work and focus on different aspects of glacier forefield dynamics and glacier–permafrost interactions:

- Wee and Delaloye (2022), *Permafrost and Periglacial Processes*
- Wee et al. (2024), *The Cryosphere*
- Wee et al. (submitted), *Geomorphology*

Each publication is preceded by a short summary, a list of the main findings, a statement of author contributions, information on data availability, and the journal in which it is published or submitted.

The combination of these two parts provides an integrated and multi-method perspective on the evolution, structure, and surface dynamics of glacier forefields in alpine permafrost environments.

2 Study sites

This dissertation investigates the driving processes behind the dynamics of frozen landforms in Little Ice Age glacier forefields in mountain permafrost environments. As a first step in this research, an inventory of LIA glacier forefields in mountain permafrost environments, where mass movements of landforms subject to glacier-permafrost interactions occur, was undertaken to gain some familiarity with the systems under study (Figure 2.1). This was achieved using existing inventories of moving landforms in periglacial environments in the Swiss Alps (Barboux et al., 2014; Delaloye et al., 2010) and the LIA glacier inventory (Maisch, 2000) as a baseline for the inventory of the extent of the glaciers forefields, delimited by the LIA moraines. It allowed the identification of LIA glacier forefields and their associated glactectonized viscous-creep landforms in mountain permafrost, which were found under various spatial configurations. From this non-exhaustive inventory, the sites of Aget, Ritord and Gruben, located between the western and southern Swiss Alps were selected. Their choice relied essentially on their long-term permafrost monitoring history (Delaloye, 2004; Gärtner-Roer et al., 2022; Haeberli, 1976; Reynard et al., 2003), but also because of their different spatial configurations and site characteristics, which outline specific processes occurring in LIA glacier forefields in mountain permafrost environments.

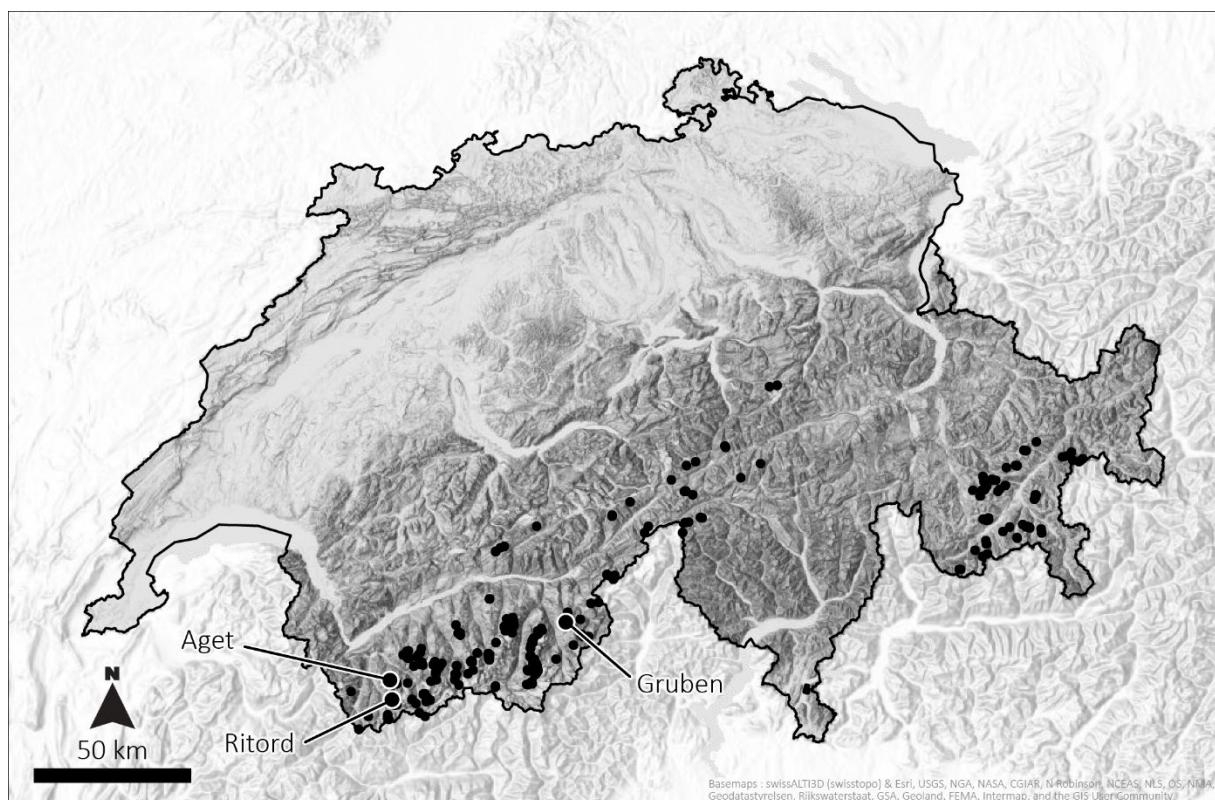


Figure 2.1: Non-exhaustive inventory of glactectonized viscous-creep landforms in mountain permafrost environments established on the basis of existing inventories of mass movements in periglacial environments in the Swiss Alps (Delaloye et al., 2010; Barboux et al., 2014).

2.1 Aget

Aget is a LIA glacier forefield located in the Bagnes valley in the western Swiss Alps (46°00'32"N, 7°14'20"E; Figure 2.2; Figure 2.3; Delaloye, 2004; Reynard et al., 2003; Wee and Delaloye, 2022). The area where the Aget glacier developed is dominated by the Grand-Aget (3133 m a.s.l.) and the Mont Rogneux (3084 m a.s.l.) summits in its uppermost western part and extends northeast down to the LIA frontal moraine at 2770 m a.s.l. Potential permafrost conditions occur in most of the forefield, as characterized by the occurrence of a south-east facing push-moraine complex in the orographic left of the LIA glacier forefield. It is likely that during its advance, the Aget LIA glacier was mostly free of debris and temperate at its base, as attested by widespread fluted moraines, whereas cold-based conditions were likely towards the glacier margins, which could explain the presence of permafrost conditions in the margin of the forefield (Reynard et al., 2003). Tiny remnants of the glacieret were still present in 2020 but occupied less than a hectare at the foot of the Grand-Aget headwall and were entirely covered by a thin layer of debris. Following the retreat of the Aget glacier, paraglacial readjustments such as lateral back-creeping in the direction of the topographic thalweg formerly occupied by the glacier of the push-moraine complex were initiated as indicated by geomorphological evidence of permafrost creep features such as ridges and furrows.

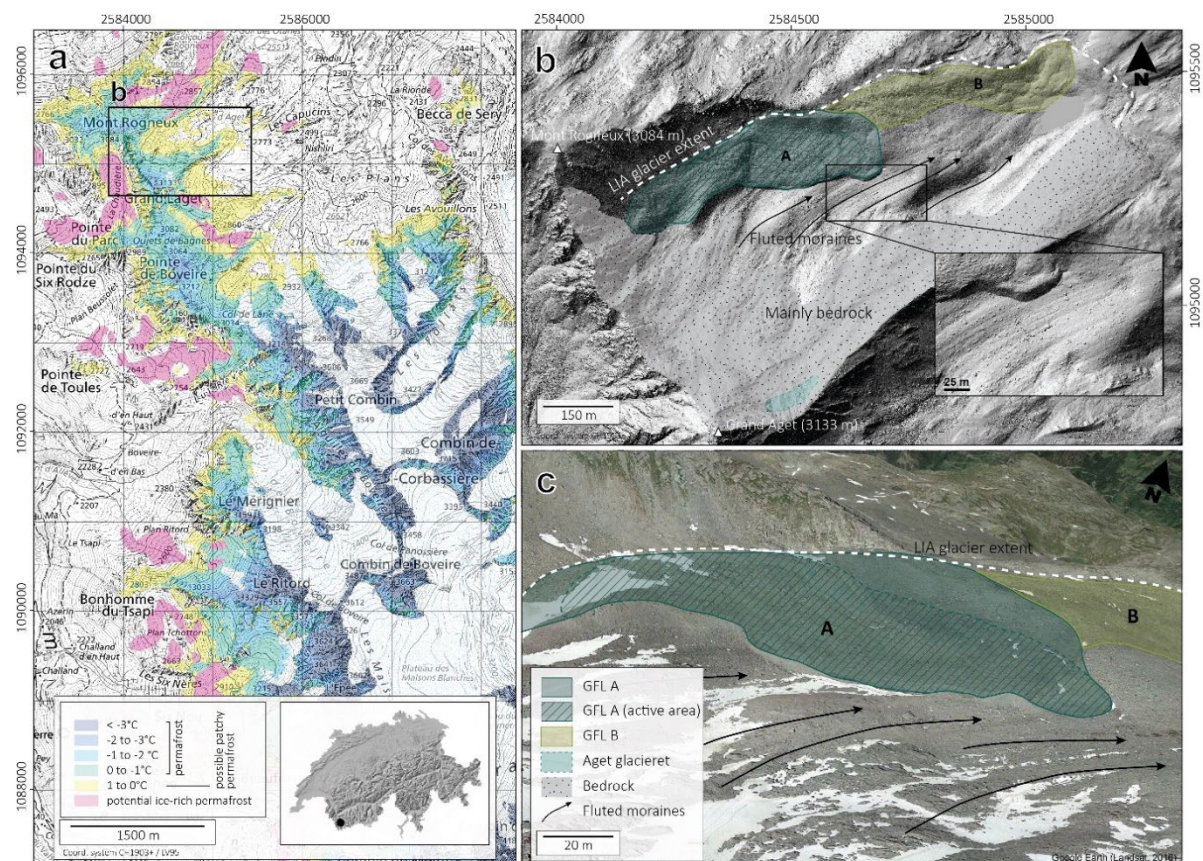


Figure 2.2: General description of the Aget LIA glacier forefield (b, c) and its location within the western Swiss Alps (a) and indicative permafrost distribution (Kenner et al., 2019). The dark blue polygon represents the investigated glacitectorized frozen landform (GFL) A, and the hatched lines highlight its actively back-creeping area. The green polygon represents the no longer active GFL B. The black arrows represent fluted moraines and the LIA extent of the Aget glacier is highlighted by the white dashed lines (base map a: Swisstopo, digital elevation model b: Flotron AG 2019, aerial image c: Google Earth, Landsat 2016).

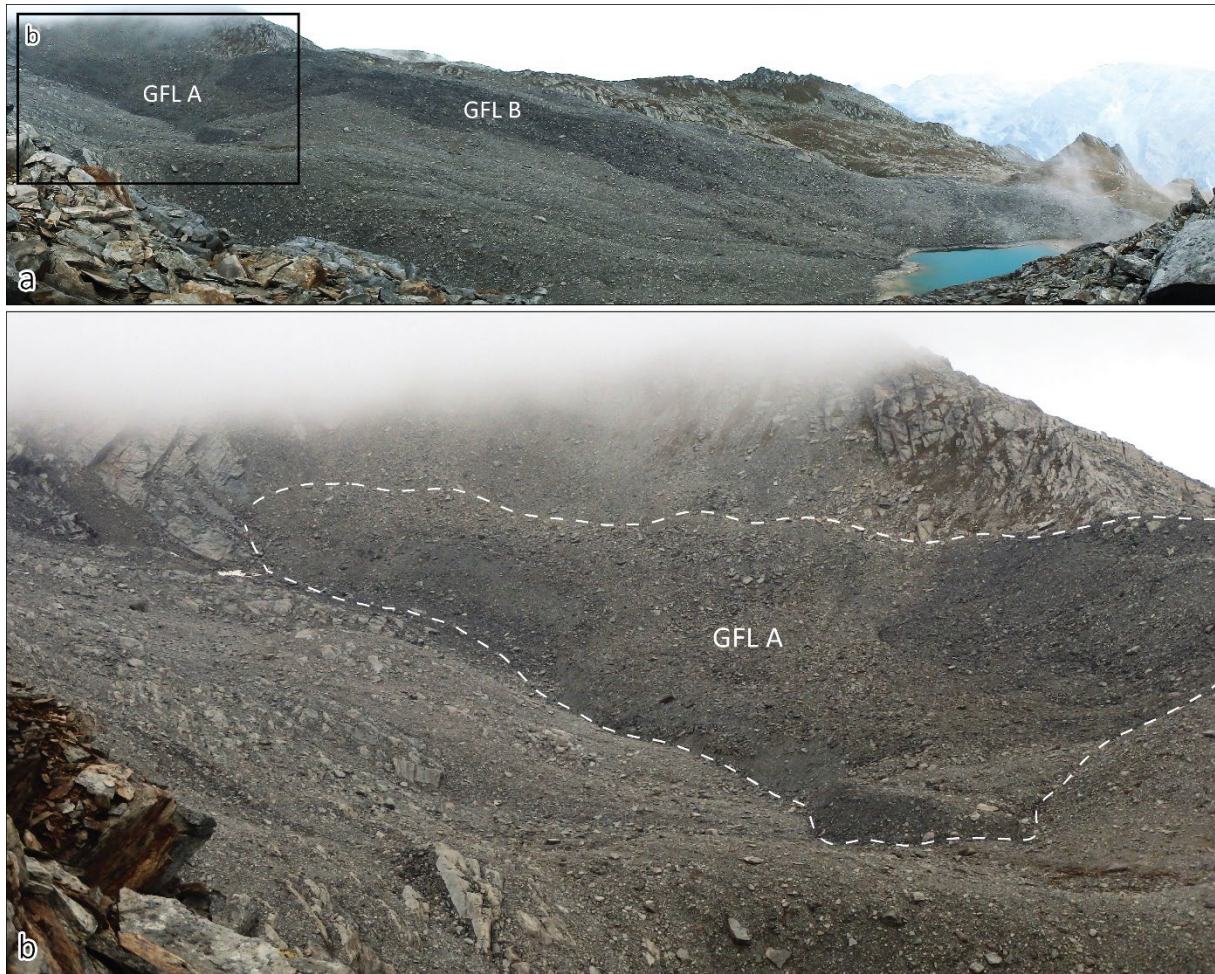


Figure 2.3: Panoramic view of the Aget Little Ice Age glacier forefield (a) and close-up photograph of the Aget glacetectonized frozen landform (push-moraine) A, highlighted by the white dashed lines (b). The lower part of the forefield is occupied by the no longer kinematically active GFL B, while the upper part of the forefield is occupied by the kinematically active and back-creeping GFL A (b).

To gain deeper insights into the driving mechanisms behind the dynamics of viscous-creep features within Little Ice Age glacier forefields in mountain permafrost environments, the following key measurements (detailed in *Publication I*) were conducted at the Aget field site (Table 2.1):

Table 2.1: Key measurements carried out at the Aget field site.

Method	Purpose
Repetition of historical vertical electrical soundings (2017)	To assess the evolution of permafrost through the analysis of resistivity changes and the implications on the morphodynamic
Electrical resistivity tomography (2021)	To characterize in two-dimension the internal structure of the Aget GFL A and determine the current state of permafrost within the landform
In-situ annual dGNSS surveys (2001 – ongoing)	To assess the long-term (decadal scale) kinematic behaviour of the Aget GFL A
Ground surface temperature measurements (1998 – ongoing)	To assess the evolution of the thermal state of the ground surface and its implication on the dynamics of the Aget GFL A

2.2 Ritord

The Ritord site (45°57'10.671"N 7°14'46.078"E; Figure 2.4; Delaloye, 2004) is located in the Entremont valley in the western Swiss Alps. It is enclosed by the Ritord (3557 m a.s.l.), the Pointe de Challand (3623 m a.s.l.) and the Grande Aiguille (3681 m a.s.l.) summits on its eastern part and its western boundary extends down to the Little Ice Age (LIA) morainic bastion of the Challand and Epée glaciers (2800 m a.s.l.). The study site is characterized by the remnants of the Challand glacieret and the vanishing Epée debris-covered glacier and its adjacent partly disconnected debris-covered tongue (now considered as dead-ice), two perennially frozen back-creeping push-moraines, and two glacier forefield-connected rock glaciers. During its LIA maximal extent, the polythermal debris-covered Epée glacier mainly occupied the southern zone of the study site, while the polythermal debris-free Challand glacier occupied the northern zone. A medial moraine indicates where both glaciers converged. During their advance, the cold-based margins of both glaciers partly thrust and overrode pre-existing perennially frozen debris landforms occupying the margins of the area. This former glacier-permafrost interaction altered the spatial distribution of ground ice, the thermal regime, and the surface morphology of the Challand and Epée glacier forefields. Both push-moraines show morphological proof of glaciotectonics (compressive ridges and furrows perpendicular to the stress exerted by the LIA advancing glacier) and reveal embedded lenses of ice, while the rooting zone of both rock glaciers is characterized by a topographical depression. A clear mechanical response following the shrinkage of both glaciers and consequent release of glacier-induced stress, expressed as back-creeping (flow field in the direction of the topographic thalweg formerly occupied by the glacier) dominates as the kinematic behaviour of the two push-moraines. The forefield of the Challand glacier is partly occupied by widespread fluted moraines, indicating that the glacier lay on saturated sediments and was temperate at its base. In contrast to this ice-free forefield, the forefield of the Epée debris-covered glacier is occupied by its partly disconnected debris-covered glacier tongue.

At Ritord, we seek to better understand the dynamics of the different landforms within the area of interest, namely the lateral glaciectonized frozen landforms (push-moraines), the glacier forefield-connected rock glacier, and the debris-covered glacier tongue, across different spatial and temporal scales. The following key measurements (detailed in *Publication III*) were conducted at the Ritord field site (Table 2.2):

Table 2.2: Key measurements carried out at the Ritord field site.

Method	Purpose
Repetition of historical vertical electrical soundings (2020)	To assess the evolution of permafrost through the analysis of resistivity changes
Electrical resistivity tomography (2021)	To characterize in two-dimension the internal structure of the two lateral push-moraines and the Epée debris-covered glacier tongue
Ground penetrating radar (2021)	To delineate the internal structure of the Epée debris-covered glacier tongue and the northern push-moraine
In-situ seasonal dGNSS surveys (2020 – 2023)	To assess the seasonal kinematic behaviour of the investigated push-moraines and the Epée debris-covered glacier tongue
In-situ continuous dGNSS measurements (2020 – 2024)	To assess the daily kinematic evolution of one push-moraine (northern-most) and the Epée debris-covered glacier tongue, and in particular the kinematic response to ground surface temperature changes
UAV-surveys (2022 – 2023)	To obtain a high spatial and temporal resolution of the surface changes
Historical aerial images analysis (1964 – 2005)	To assess the long-term kinematic and geomorphological evolution of the area of interest and the kinematic responses to different climatic settings (from 1960s to present)
Ground surface temperature measurements (1998 – <i>ongoing</i>)	To assess the evolution of the thermal state of the ground surface and its implication on the dynamics of the push-moraines and debris-covered glacier tongue

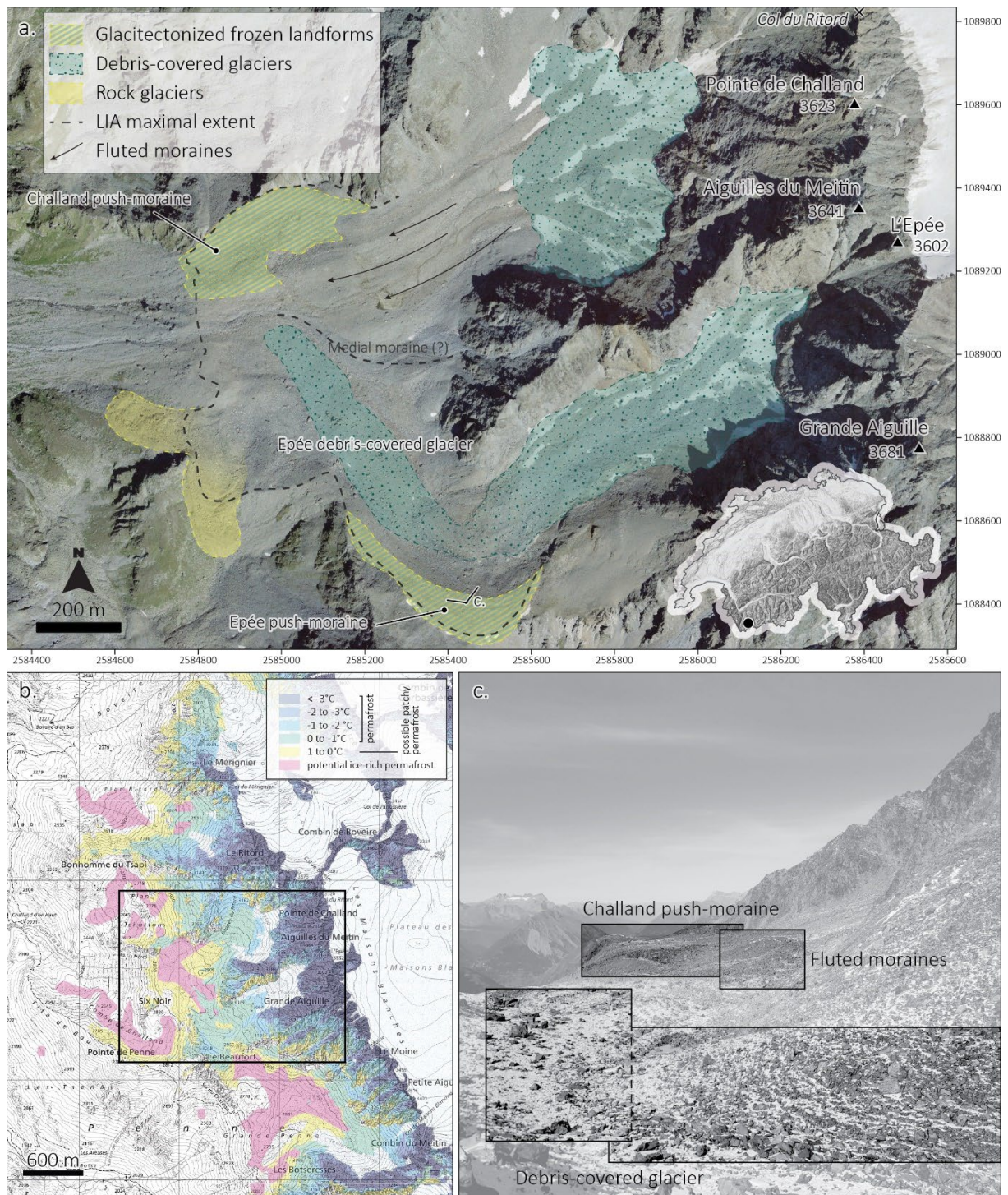


Figure 2.4: General geomorphological description of the Ritord site (a, c) and the general distribution of permafrost (Kenner et al., 2019) in the study area (b). The Ritord glacitected frozen landforms (or push-moraines) are highlighted by alternating yellow and blue dashed lines. The rock glaciers are highlighted in yellow. The Epée and Challand (-now) debris-covered glaciers are highlighted in blue. Black dashed lines indicate part of the LIA maximal extent of the Challand and Epée glaciers. Fluted moraines indicate the flow direction of the Challand debris-free glacier. Location and direction of picture (c) is marked by a symbol on map (a). Background map (a): SWISSIMAGE 2017 (Swisstopo).

2.3 Gruben

The Gruben site (46°10'22"N 7°58'09"E; Figure 2.5) is located in the Saas Valley in the southern Swiss Alps. It is characterized by the rapidly shrinking debris-covered cold tongue of the polythermal Gruben glacier below the western face of the Fletschhorn (3985 m a.s.l.), the continuously advancing, perennially frozen Gruben glacier forefield-connected rock glacier below the south-eastern flank of the Rothorngrat (3104 m a.s.l.), and a complex contact zone of the previously more extended Little Ice Age glacier and the rock glacier permafrost (Haeberli et al., 2024). During its LIA maximal extent, the margins of the Gruben polythermal glacier overrode the uppermost zone of the pre-existing Gruben rock glacier (Gärtner-Roer et al., 2022; Käab et al., 1997), consequently altering the thermal regime, spatial distribution of ground ice and morphology of this zone. The morphological signature of this glacier-permafrost contact and interaction is expressed by glaciotectonics (compressive ridges and furrows perpendicular to the stress exerted by the LIA advancing glacier) and thermokarst features, the latter inferring the presence and degradation of buried massive ground ice. Geometrical changes and reoriented stress fields in this zone are expressed by lateral back-creeping (in the direction of the topographic thalweg formerly occupied by the glacier) and enhanced surface elevation changes mainly due to ice melt-induced subsidence. In contrast to the complex contact zone, the rock glacier displays longitudinal ridges and furrows, parallel to its extending flow field.

The debris-covered glacier tongue of the polythermal Gruben glacier (south-eastern part in Figure 2.5) is characterized by a rather chaotic surface morphology, in which a pattern of somewhat subdued transverse ridges and furrows from compressing flow is discernible. Earlier borehole temperature investigations (Haeberli, 1976) revealed ice temperatures of -1°C to -2°C within the tongue of the glacier, which was frozen to its bed at the margins (i.e. cold-based glacier margins) but was temperate at its upglacier base (cf. Etzelmüller and Hagen, 2005). Surface elevation changes express strong signs of downwasting: the central zone shows important rates of ice melt-induced subsidence, gradually decreasing towards the margins, inferring the rapid thinning and vanishing of (cold) glacier ice (Gärtner-Roer et al., 2022).

At Gruben, the following investigations (Table 2.3) have been conducted to determine the extent to which ground ice properties influence the surface dynamics of landforms where glacier-permafrost interaction occurred (detailed in *Publication II*):

Table 2.3: Key measurements carried out at the Gruben field site.

Method	Purpose
Petrophysical joint inversion (electrical resistivity tomography and refraction seismic tomography) (2022; 2023)	To quantify and characterize the volumetric fraction of ice, water, air and rock content of the Gruben rock glacier and its complex contact zone
In-situ seasonal dGNSS surveys (2012 – ongoing)	To assess the seasonal kinematic behaviour of the investigated landforms
In-situ continuous dGNSS measurements (2018; 2022 – 2024)	To assess sub-seasonal (daily) kinematic response to ground surface temperature changes on the complex contact zone, the intact rock glacier and the debris-covered glacier tongue
UAV-surveys (2022 – 2023)	To obtain a high spatial and temporal (seasonal) resolution of the surface changes
Ground surface temperature measurements (2012 – ongoing)	To assess the evolution of the thermal state of the ground surface and its implication on the dynamics of the glacier forefield-connected Gruben rock glacier

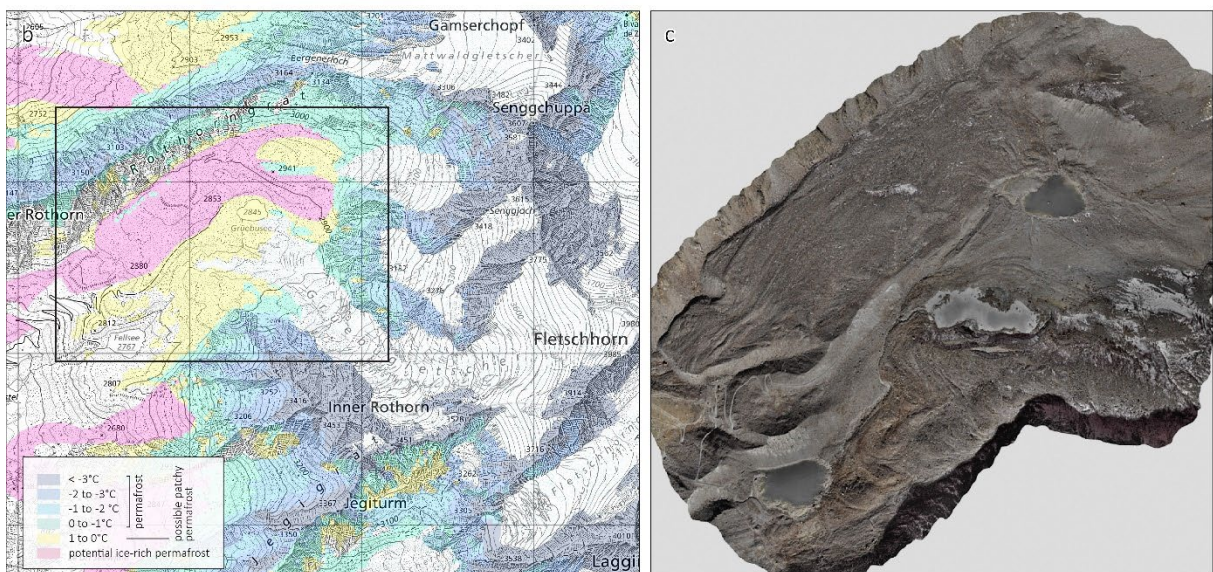
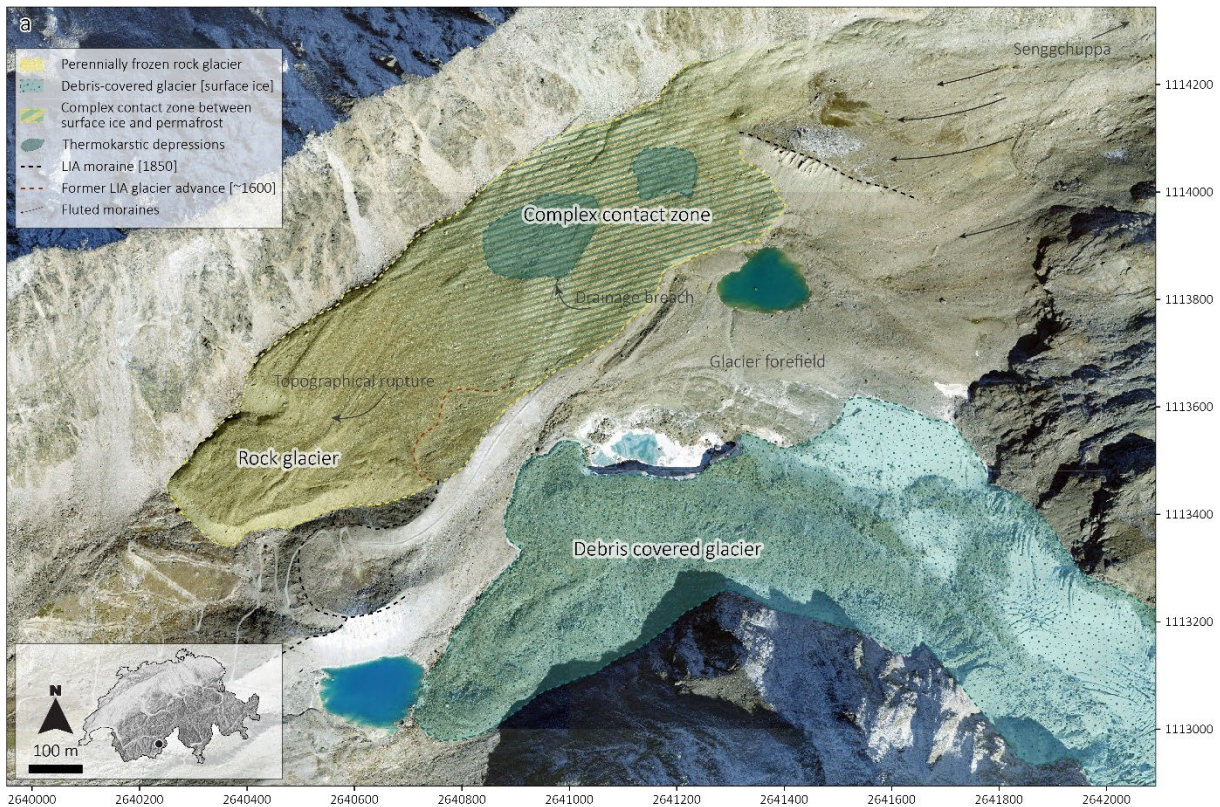


Figure 2.5: General geomorphological description of the Gruben site. The Gruben rock glacier is highlighted by the yellow dashed lines. The complex contact zone is highlighted by alternating yellow and blue dashed lines. The delineation between the rock glacier and the complex contact zone (faded hatched lines) is here not clearly defined but based on geomorphological knowledge and prior studies (Kääb et al., 1997; Gärtner-Roer et al., 2022). The Gruben debris-covered glacier terminus is highlighted in blue. Black dashed lines indicate part of the LIA maximal extent of the Gruben glacier. Red dashed lines indicate a probable former (~1600) LIA glacier advance. Fluted moraines indicate the flow direction of the adjacent Senggchuppa glacier (a). Background (a): SWISSIMAGE 2017 (Swisstopo). Permafrost distribution map (Kenner et al., 2019) of the Gruben area (b), and UAV-derived orthoimage of the Gruben site taken on the 6 October 2022 (c) (S. Vivero 2022).

2.4 Climatic setting

The Aget and Ritord glacier forefields are located in the western Swiss Alps, while the Gruben glacier forefield is located in the southern Swiss Alps. The general climate of the three study areas is characterized by inner-alpine continental climatic conditions, predominantly influenced by high-relief topography. Being shielded by the high-mountain topography of the surrounding mountain ranges, the mean annual precipitation at the study sites in the western part of the Swiss Alps (Aget and Ritord) ranges between 1300 – 1500 mm/y, while the study site located in the southern Swiss Alps (Gruben) receives less precipitation, as it is shielded by mountain ranges to its west and south (MeteoSwiss, 2024; Figure 2.6a).

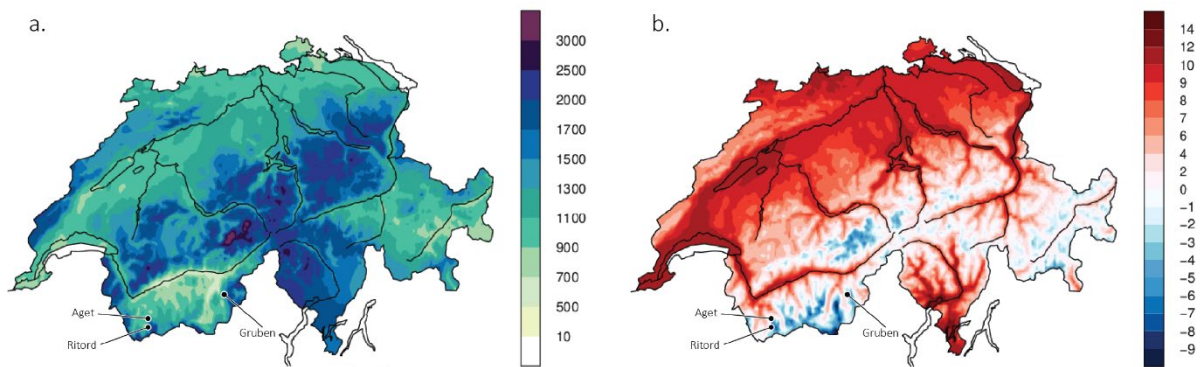


Figure 2.6: Mean annual precipitation (mm) based on the reference period of 1991-2020 (a) and mean annual temperature (°C) based on the reference period of 1991-2020 (b) (MeteoSwiss, 2022).

The mean annual air temperature for the reference period of 1981-2010 measured at the meteorological station Col du Grand St-Bernard (GSB) located at 2472 m a.s.l. (45°52'09.01"N 7°10'14.57"E) is -0.6 °C, which infers that at the elevation of the sites of Aget and Ritord (around 2800-2900 m a.s.l.), the mean annual temperature, when considering an environmental lapse rate of -0.65°C per 100 m, is approximately between -2 to -3°C. Temperatures measured since 1864 reveal a clear warming trend of 1.44°C/100 years, particularly marked by the temperature rise of the last forty years (MeteoSwiss, 2024; Figure 2.6b).

3 Methodology

Improving the understanding of processes governing the dynamics of LIA glacier forefields in mountain permafrost environments and their associated frozen landforms necessitates the collection of detailed observations of the various processes and changes occurring on and within these systems. The acquisition of such datasets in high mountain terrain can be a challenging endeavour. The nature of the setting presents researchers with challenging working conditions, including limited accessibility to the field sites, unpredictable and rapidly changing weather conditions, and field logistics that rely on human-power, which can collectively pose significant safety concerns. For the acquisition of such datasets, meticulous preparation is required prior to any measurement campaigns, as well as the consideration of alternative methodologies. In the scope of this thesis, we were able to apply a multi-method and interdisciplinary approach to gain the most comprehensive understanding of the driving processes contributing to the dynamics of the studied systems (Figure 3.1). For instance, the compilation of previously existing datasets on which novel observations from in-situ and remote sensing techniques were built allowed to continue the monitoring and, consequently, the comprehension of the investigated sites across different spatial and temporal dimensions. The following chapter provides details of the methods applied to investigate the dynamics and evolution of LIA glacier forefields in mountain permafrost environments and their associated frozen landforms.

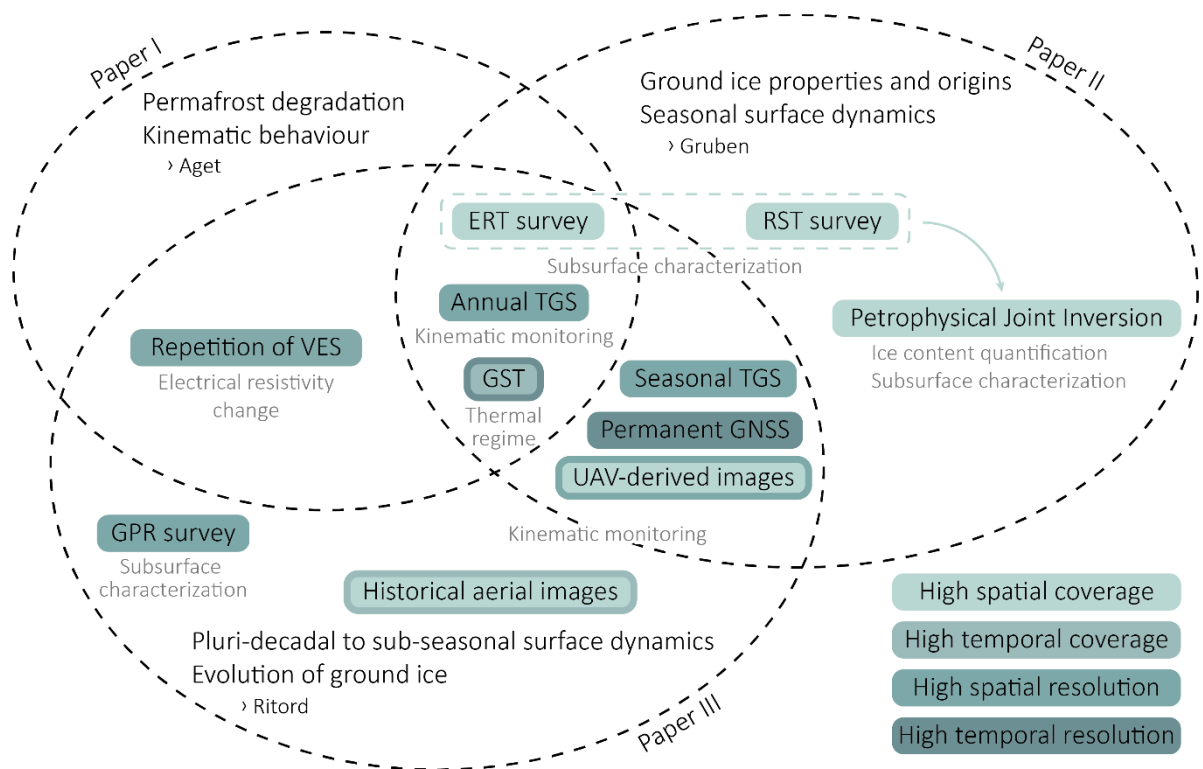


Figure 3.1: Schematic overview of the different methods, their spatial and temporal coverage and resolution, and their application to each of the study sites (corresponding individual publication).

Surface dynamics were assessed at different spatial and temporal scales using in-situ geodetic methods and remote-sensing approaches. Annual, seasonal and hourly differential global navigation satellite system (dGNSS) acquisitions allowed high-temporal resolution observations, while UAV-based and historical aerial-based imagery acquisitions combined with structure-from-motion (SfM) three-dimensional (3D) reconstruction allowed high-resolution topographic analysis. The general characterization of the frozen ground was qualitatively assessed based on the application of geoelectrical measurements such as vertical electrical soundings (VES) and electrical resistivity tomography (ERT). In addition, refraction seismic tomography (RST) was carried out at one site, enabling the application of the newly developed petrophysical joint inversion (PJI) scheme to quantitatively estimate the fraction of ice in the subsurface. Ground penetrating radar (GPR) measurements were also carried out at one of the three sites investigated to identify structures in the frozen ground. Ground surface temperature measurements were equally used to strengthen the analysis of thermally-driven processes. The combination of thermal, geodetic, and geophysical measurements enabled to discern spatially variable ground ice contents over time.

3.1 Geodetic approaches

Geodetic observation techniques allow to accurately determine positions on the Earth's surface. The geodetic methods applied here are commonly used in the context of mass movement monitoring. The aim of their application is to assess the kinematic behaviour and surface changes of the studied landforms at different temporal and spatial scales. The following sub-chapters give a brief description of the geodetic techniques used in this thesis.

3.1.1 In-situ continuous geodetic measurements

Two permanent dGNSS stations were installed at Ritord in 2020 and three at Gruben in 2022, enabling a very high-temporal resolution of surface displacements, as they yield continuous displacement data for single point locations, allowing to follow the sub-seasonal variations affecting the velocity and surface dynamics of the landforms. Hourly positions are determined in real-time kinematics with a cm-range accuracy based on (1) a continuously operating reference station (CORS) installed on stable terrain, but can also be based on (2) the Swiss Positioning Service (swipos) which provides data from the automatic GNSS network Switzerland (AGNES) CORS network as virtual reference stations via GSM, enabling the differential GNSS measurements of high accuracy. The first approach is applied for the stations at Ritord, while at Gruben a combination of the two approaches was applied. At Gruben, a fourth permanent dGNSS station installed in 2012 (Beutel et al., 2021) was used to complete the already dense dataset. For all data hourly positions were averaged to obtain daily positions. A Gaussian kernel smoothing approach was applied to the daily positions to reduce noise and improve the data signal quality.

To avoid repetition, the further applications of this technique and the data that it has yielded are presented in detail in *Publication II*, and *Publication III*.

3.1.2 In-situ seasonal and annual geodetic measurements

Within the framework of Swiss Permafrost Monitoring Network (PERMOS), rock glacier surface displacement rates are being measured on a regular basis by terrestrial geodetic surveys (TGS) at Aget and Gruben, while a monitoring network based on the PERMOS standards was put in place at Ritord in the context of this thesis. At Aget, geodetic campaigns have been carried out on a yearly basis since 2001 and bi-annually from 2004 to 2013, however only the annual measurements are considered here. At Gruben, seasonal in-situ geodetic surveys in early-July and early-October have been carried out since 2012, and at Ritord the bi-annual monitoring of surface displacements was initiated in mid-July 2020. At each site a network of 50 – 80 marked boulders are measured once or twice a year with real-time kinematics (RTK) dGNSS surveys, following the measurement set-up described by Lambiel and Delaloye (2004). From these acquisitions, annual and seasonal horizontal, vertical, and three-dimensional surface displacement vectors and rates are calculated. The dGNSS technique is based on the use of a static reference receiver placed at a known point, which is assumed to be stable. The reference GNSS calculates its position continuously and determines the difference to its attributed point coordinate. It then sends this bias value to correct the position measured by another receiver at individual points marked on the rock glacier surface. The Real Time Kinematic (RTK) technique, which involves a permanent state of observation, enables the precision of the measured point position to be enhanced to a level of less than 3 cm (Lambiel and Delaloye, 2004).

More details about this method are given in the respective methodological section of *Publication I*, *Publication II*, and *Publication III*.

3.1.3 Structure-from-Motion photogrammetry

Accurate, precise and rapid acquisition of topographic data is fundamental to the analysis and understanding of landscape evolution at different spatial and temporal scales (Smith et al., 2015). For geomorphological research, Structure-from-Motion (SfM) photogrammetry is a technique that offers high-resolution topographic data, which is fundamental to the qualitative and quantitative analysis of surface changes, particularly in systems of complex morphologies (Eltner and Sofia, 2020; Westoby et al., 2012). The SfM method shares the same fundamental principles as stereoscopic photogrammetry. Both techniques rely upon the ability to resolve three-dimensional structures from a series of overlapping, offset images. However, the approach of SfM differs from conventional photogrammetry, as the geometry of the scene, camera positions and orientation are solved in an automated process without the need to specify a priori a network of target points with known 3D positions. In contrast, these are obtained through the application of a highly redundant, iterative bundle adjustment procedure, based on the automatic identification of matching features extracted from a set of multiple overlapping images (Snively et al., 2008; Westoby et al., 2012). Unlike conventional photogrammetry, the 3D point clouds generated by SfM are given in relative image-space coordinates. The transformation of relative image-space coordinates to an absolute coordinate system can be achieved using known ground-control points (GCPs) with known 3D coordinates, finally yielding high-resolution orthoimages and digital elevation models (DEMs). The latter and former can be used to quantify surface changes in the terrain's topography and mass movements through DEM differencing and image correlation, respectively. These approaches are further explained in *Publication II* and *Publication III*.

3.1.3.1 UAV-SfM photogrammetry

A spatially and temporally (seasonal) high-resolution coverage of the geomorphic changes in the Gruben and Ritord glacier forefields was obtained through the use of uncrewed-aerial-vehicle (UAV) imagery or drone imagery. The operation of UAV systems can often be challenging in mountainous terrain. The topographical setting often requires the device to fly at elevations that are high enough to avoid collision with obstacles yet low enough to obtain a high-quality ground sampling density (Vivero et al., 2022).

Seasonal UAV surveys carried out in Ritord and Gruben were conducted with a DJI Phantom 4 RTK device, equipped with a GNSS L1 and L2 frequency antenna, providing real-time kinematics (RTK) differential corrections using a virtual reference station (VRS) based on the automated GNSS reference stations network for Switzerland (AGNES). Flight missions were planned with the built-in DJI GS RTK application. All missions were designed with the same parameters: side and forward overlap were set to 70% and 80%, respectively and flown at a constant height of 70 m, based on the swissALTI3D DEM loaded in the Terrain Awareness module to cover the entire area of interest. This resulted in approximately 2000 images with a geotagging accuracy between 1-2 cm (horizontally) and 1.5-3 cm (vertically) per survey. The UAV images were processed following Vivero et al. (2021) using the software PIX4Dmapper Pro version 4.7 to derive digital elevation models (DEMs) and orthomosaics, which were sampled at a resolution of 2.5 cm × 2.5 cm.

3.1.3.2 Historical aerial photogrammetry

Historical aerial photographs taken by the Swiss Federal Office of Topography (Swisstopo) for the period 1964 to 2005 were used for the analysis of the long-term evolution of the Ritord glacier forefield. To reference the aerial photographs, the coordinates of a network of GCPs were retrieved from the reference Swiss digital surface model (swissSURFACE3D Raster), derived from airborne LiDAR data with a grid mesh size resolution of 0.5 m. For a high accuracy, it is essential that the selected GCPs remain stable throughout the observation period, are evenly distributed throughout the images, and are identifiable on the images. Due to varying image quality and contrast, it was not always possible to retrace all GCP locations with high accuracy and confidence. This explains the importance of having as many GCPs as possible distributed evenly across the photographs.

To reconstruct historical digital elevation models (DEMs) and orthomosaics, we apply Structure-from-Motion (SfM) and Multi-View-Stereo (MVS) using commercial software Agisoft Metashape (v 2.0.1). To orient the multiple epochs of historical aerial photos, we use multi-temporal tie points which can be tracked over several epochs, originally introduced as Time-SIFT method (Feurer and Vinatier, 2018), further generalized as the co-alignment method (Blanch et al., 2021; Cook and Dietze, 2019; Hendrickx et al., 2020, 2022) and recently also tested and applied for historical aerial data (Genzano et al., 2024). This way, GCPs are only used in the common SfM project to compute image orientation and camera calibration for all the epochs at once. Moreover, the relative accuracy is also improved by the automatic extraction of tie points in stable areas. A sub-pixel reprojection error, indicative of the overall performance of the bundle adjustment, was obtained for the area of interest. After the common tie point reconstruction, dense point clouds are reconstructed for every epoch separately, using high resolution settings with moderate depth

filtering (Cusicanqui et al., 2021). These are subsequently used for the creation of DEMs and orthomosaics.

3.2 Geophysical methods and applications

Geophysical methods allow to image the subsurface in an indirect and non-invasive way. Initially, their development and application has served for the exploration of underground resources such as fossil fuels, geothermal reservoirs, and groundwater reservoirs. Since several decades, permafrost research has made use of geophysical techniques to characterize the distribution and occurrence of ground ice. Geophysical methods applied in the context of permafrost research are based on the contrasting properties between ice and other materials, allowing the qualitative or quantitative estimation of ground ice content. The following sub-chapters briefly describe the geophysical methods used in the scope of this thesis to interpret the extent and properties of the frozen ground.

3.2.1 Geoelectrical surveys in permafrost environments

Geoelectrical measurements are commonly used to detect the occurrence of permafrost and ground ice in mountainous regions (Hauck and Vonder Mühll, 2003). This method is well-suited for imaging the subsurface distribution of mountain permafrost and ground ice due to its ability to distinguish between materials with contrasting electrical properties. Unfrozen ground, ice-rich permafrost, and massive sedimentary ice each exhibit distinct electrical characteristics, making geoelectrical measurements a sensitive and effective technique for imaging varying subsurface properties (e.g. (Bosson et al., 2015; Haeberli and Vonder Mühll, 1996; Halla et al., 2021; Hauck and Kneisel, 2008; Herring et al., 2023; see Table 3.1).

Table 3.1: Range of electrical resistivity for different materials (Hauck and Kneisel, 2008).

Material	Range of resistivity (Ωm)
Groundwater	10 – 30
Topsoil	50 – 500
Clay	1 – 100
Sand/Gravel	100 – 5000
Sandstone	10 – 3000
Limestone	50 – 5000
Granite	5000 – 10^6
Ice	10^6 – 10^8
Air	infinity

Geoelectrical resistivity measurements are conducted by generating a continuous electrical current of intensity I into the ground through one pair of steel electrodes (A and B). The electrical voltage V (or potential difference) is measured between a pair of potential electrodes (M and N). The current I and potential difference ΔV are used to determine the electrical apparent resistivity (ρ_a) of the subsurface as follows (Eq. 3.1):

$$\rho_a = K \frac{V}{I} \quad (\text{Eq. 3.1})$$

where K the geometric factor is defined by the geometry of the configuration of the electrodes.

In the context of this thesis, two distinct geoelectrical resistivity measurement techniques were applied. One-dimensional vertical electrical soundings (VES) were conducted at Aget in Ritord for the purpose of repeating historical VES surveys, and for a robust comparative analysis. Electrical resistivity tomography (ERT) measurements were conducted at all three sites, as this method has the advantage of yielding a two-dimensional image of the distribution of the electrical resistivity of the subsurface, and therefore provide a more accurate interpretation of the distribution of permafrost. Moreover, ERT measurements carried out at Gruben were used for the application of the petrophysical joint inversion scheme (explained in section 3.2.3) in order to quantify the fraction of ground ice in the subsurface.

3.2.1.1 Vertical electrical soundings

The investigation of the evolution of ground ice distribution required the repetition of geoelectrical measurements. In order to achieve a robust comparative analysis of changes in the frozen subsurface, repetitions of vertical electrical soundings (VES) were carried out at Ritord in 2020 and Aget in 2017, based on existing VES datasets from 1997 and 1998 (Delaloye, 2004), respectively. The approach applied in 2017 and 2020 followed Delaloye (2004), regarding the timing of the campaign period in August, and using the same measuring device (McOhm 2115 resistivity-meter), and electrode configuration. Because of the heterogeneity of the subsurface, both the symmetrical Schlumberger and asymmetrical Hummel arrays were applied to all VES in both campaigns. Hummel and Schlumberger arrays require a gradual increase of spacing between electrodes M and N as the spacing between the current electrodes increases. This configuration generates three to four segments, where each segment corresponds to the measurements carried out with the given spacing of MN. Shifting between the segments often occurs in this process (Figure 3.2).

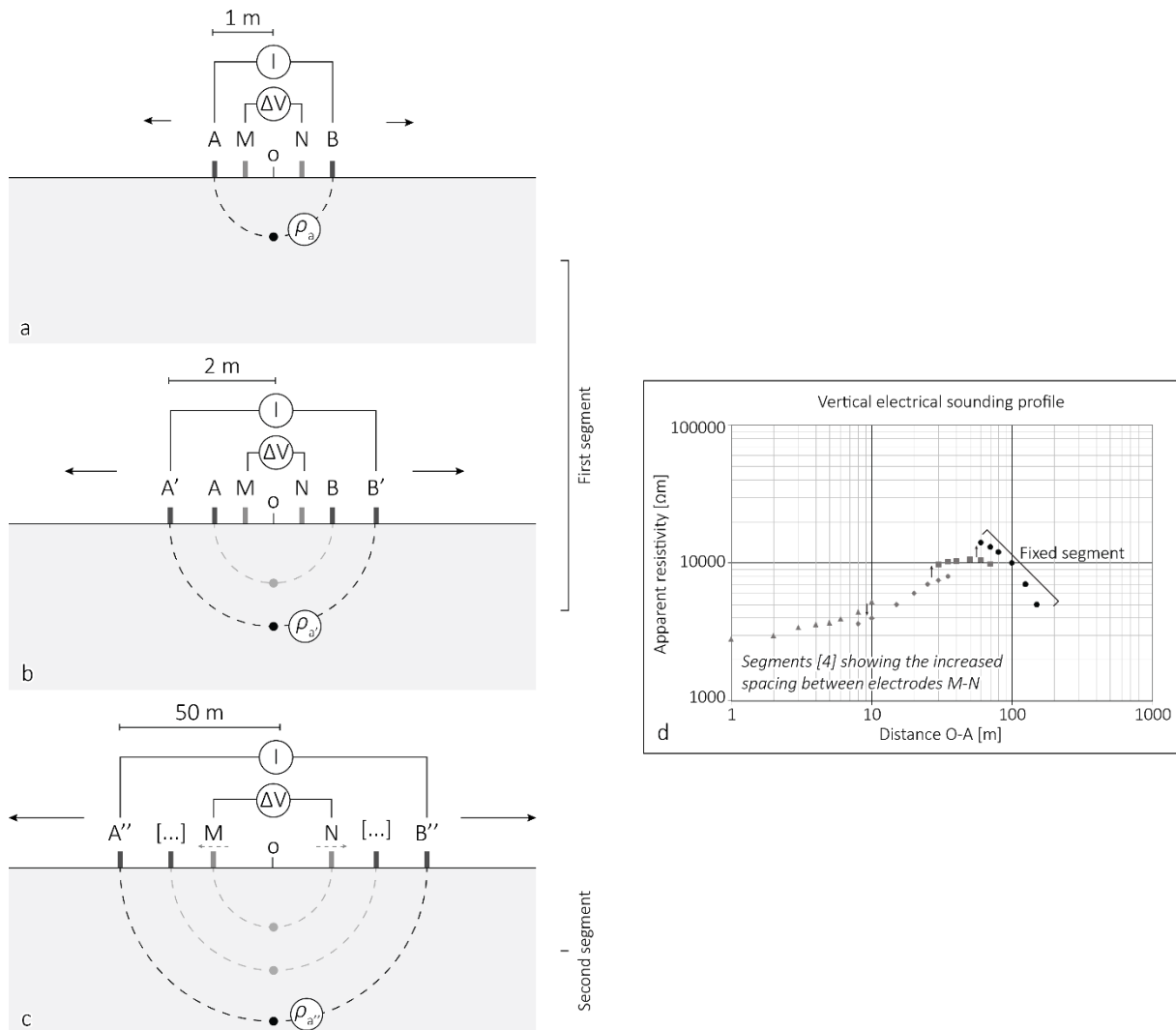


Figure 3.2: Scheme of a Schlumberger array with a gradual increase of the spacing of the current electrode (A-B) (a-b) and as the spacing increases the spacing between the potential electrodes (M-N) is increased (c), consequently increasing the depth of investigation. Example of the resulting profile of a vertical electrical sounding, showing the different segments due to the increased spacing between the potential electrodes M-N (d).

To determine the importance of the shift between two segments, two measurements with the first electrode spacing of MN are systematically repeated with the new electrode spacing of MN. The segments are corrected and adjusted (logarithmic translation) to a fixed segment. To determine the fixed segment, the segments were once adjusted to the second segment, as suggested by Vonder Mühl (1993) and repeated by Delaloye (2004) and were also adjusted to the last (third or fourth) segment, as the margin of error caused by the electrode configuration is potentially smaller with an increased electrode spacing (Figure 3.2d). The values obtained from the adjustment of the segments on the second and on the last segment were compared to each other in order to determine the amplitude of the shift between an adjustment on the second segment or on the last segment (Figure 3.3). The amplitude between the different adjustments (shift of all segments on the second fixed segment or on the last (third or fourth) segment) varied from one sounding to another. This can be explained by the different amplitude ranges of the shifts between each segment, which is partly controlled by the measurement conditions (electrode configuration, topography, conductivity, etc.).

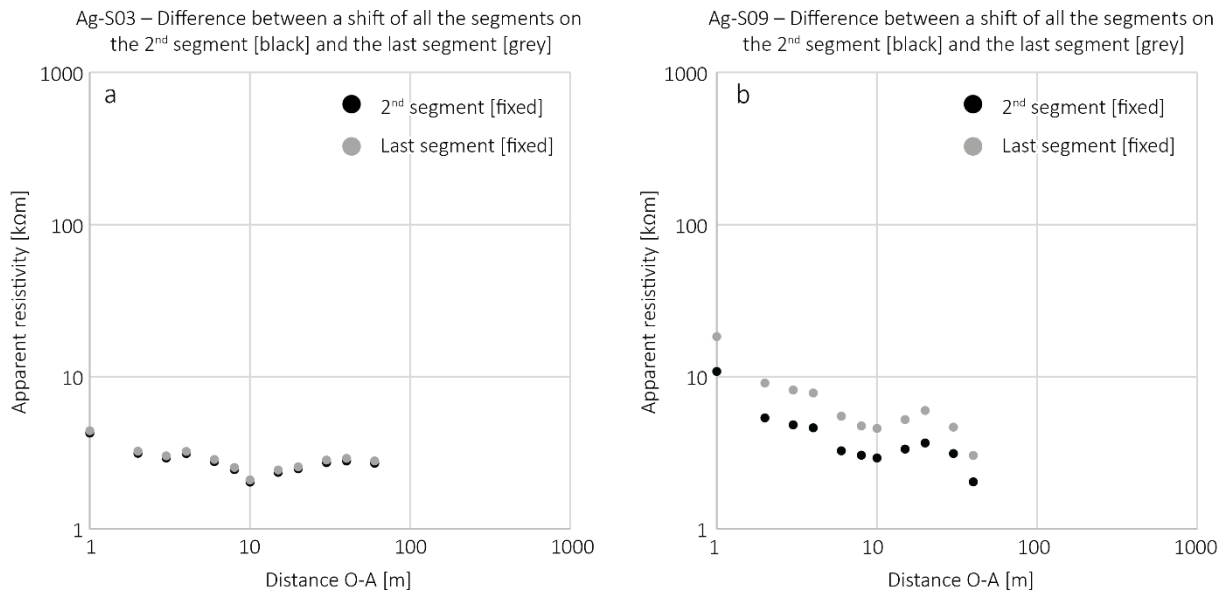


Figure 3.3: Variability of the amplitude of the shifts based on the amplitude between each segment of a profile. The profile Ag-S03 shows a difference of 3.4% between the profile fixed on the second (black) and last (grey) segment (a) and the profile Ag-S09 shows a difference of 63.6% between the profile fixed on the second (black) and last (grey) segment (b).

The calibrated measured apparent resistivity values were inverted to determine the thickness and specific resistivity of the layers of a 1-dimensional model to produce a model response that best-fits the measured values using the programme RES1D ver. 1.0, where the least-square optimisation method is applied (Loke, 2001). A simple initial model of the subsurface is prescribed, and the optimisation subroutine modifies the thickness and resistivity of the layers in order to reduce the discrepancy between the calculated and measured apparent resistivity values. The measured apparent resistivity values were used for the comparative analysis between the historical and repeated datasets, as the model was not able to grasp the oversteepening effect, consequently yielding relatively high root-mean-square (RMS) error values for each individual inversion.

3.2.1.2 Electrical resistivity tomography

Characterizing the internal structure of the landforms present in the investigated glacier forefields was an essential aspect of this thesis as it enabled to link visible processes occurring at the surface with the properties of the subsurface. Electrical resistivity tomography (ERT) is a well-established method to image the two-dimensional distribution of electrical properties of subsurface mountain permafrost and ground ice due to its sensitivity and suitability to distinguish unfrozen material, ice-containing permafrost (excess ice), and massive sedimentary ice due to their contrasting electrical properties (e.g. Bosson et al., 2015; Haeberli and Vonder Mühll, 1996; Halla et al., 2021; Hauck and Kneisel, 2008; Herring et al., 2023).

The Wenner-Schlumberger configuration was applied in the scope of this research as it provides a compromise between the depth of investigation and its horizontal resolution. Tomographic

measurements yield several hundreds of quadrupole (pairs of current and potential electrodes) combinations measurements in an automated process. The apparent resistivity is then inverted to obtain a two-dimensional image of the spatial distribution of the specific resistivity of the subsurface.

3.2.2 Refraction seismic tomography (RST)

RST makes use of the differences in the elastic properties of subsurface materials, such as unfrozen sediments, supersaturated permafrost, and buried surface ice, which are quantified in terms of their different P-wave velocities and their spatial variability. Seismic P-waves are refracted when they encounter subsurface layers with velocity contrasts and are especially well suited to delineate quasi-horizontal subsurface layers and to differentiate between air- and ice-filled pores space, which may both exhibit similarly high electrical resistivities (Draebing, 2016; Halla et al., 2021; Hauck, 2001; Hilbich, 2010).

The RST method is based on the principle that when a seismic wave impinges upon layers with contrasting velocities, a change in direction of the wave occurs. The amount of change of direction is governed by the contrast in seismic velocity across the layer boundary, according to the physical principle of Snell's law (Eq. 3.2):

$$\frac{\sin\theta_i}{\sin\theta_r} = \frac{V_1}{V_2} \quad (\text{Eq. 3.2})$$

where θ_i and θ_r are the angles of incidence and refraction respectively, and V_1 and V_2 are the velocities of the P-wave propagation in the upper layer and lower layer, respectively. When the angle of incidence reaches a particular value, known as the critical angle, the refraction angle becomes 90° , where the refracted wave travels parallel to the boundary layer with a velocity V_2 . This relies on the principle that the propagation velocity increases with depth (i.e. $V_2 > V_1$), which infers that waves travelling at a greater depth can reach the sensor earlier than the direct wave. The refracted wave therefore provides information of deeper layers based on their contrasting velocities (Table 3.2).

Table 3.2: Range of P-wave velocity for different materials (Schrott and Sass, 2008).

Material	Range of P-wave velocity (m/s)
Groundwater	1400 – 1600
Topsoil	100 – 600
Clay	550 – 2700
Sand/Gravel	100 – 2000
Sandstone	800 – 4500
Limestone	2000 – 6200
Granite	3000 – 5800
Ice	3000 – 4500
Air	300 – 330

RST measurements are based on the controlled generation of seismic signals, generally induced by a sledgehammer or explosives, which are recorded by geophones or seismometers. P-waves are the first waves to arrive at the sensor and correspond to the first onset of the seismic signal. The associated arrival travel-time can be identified and picked manually.

3.2.3 Petrophysical joint inversion

A petrophysical joint inversion (PJI) approach (Mollaret et al., 2020; Wagner et al., 2019) was applied to jointly invert the measured apparent resistivities and seismic travel-times to quantify the volumetric fraction of ice, water, air, and rock contents. Following Hauck et al. (2011), the PJI approach is based on petrophysical equations that relate bulk electrical resistivities and seismic velocities to the fractions of the four phases in the subsurface, based on the resistivities and P-wave velocities of ice, water, air and the rock matrix. The sum of all fractions has hereby to adhere to (Eq. 3.3):

$$f_r + f_w + f_a + f_i = 1 \quad (\text{Eq. 3.3})$$

with the indices r , w , a , i indicating rock, water, air and ice, respectively.

The petrophysical equation for P-wave velocities follows the approach of (Timur, 1968) and its extension to four phases by (Hauck et al., 2011) linking the slowness and volumetric content of the four fractions to the measured bulk slowness as follows (Eq. 3.4):

$$\frac{1}{v_p} = \frac{f_r}{v_r} + \frac{f_w}{v_w} + \frac{f_a}{v_a} + \frac{f_i}{v_i} \quad (\text{Eq. 3.4})$$

with the velocities v_r , v_w , v_a and v_i for rock, water, air and ice, respectively.

In the 4PM as well as in the original PJI formulation of Wagner et al. (2019) and in many ERT applications on permafrost, Archie's Law (Archie, 1942) is used to link measured resistivity to material properties such as saturation and porosity (cf. (Herring et al., 2023)), which can then be related to f_w and f_r . Archie's law is generally recognized as valid when electrolytic conduction is the dominant conduction process. However, this is unlikely to be the case for coarse, blocky materials and supersaturated permafrost conditions, limiting its applicability in the context of this study. Thereby, following Mollaret et al. (2020), the geometric mean model (Eq. 3.5; Glover, 2010) was applied here instead, as it has the advantage to include all fractions of the four phases (and not only rock and water as in Archie's Law), and consequently yield realistic and well-constrained ice content estimations also in cases where the water content is potentially low (as in rock glaciers, Mollaret et al., 2020):

$$\rho = \rho_r^{f_r} \cdot \rho_w^{f_w} \cdot \rho_a^{f_a} \cdot \rho_i^{f_i} \quad (\text{Eq. 3.5})$$

where ρ_r , ρ_i , ρ_w and ρ_a are the resistivities for rock, water, air and ice, respectively.

The results of the PJI depend on different sets of parameters in addition to the measured apparent resistivities and seismic travel-times. A range of resistivity [Ωm] and P-wave velocity [m/s] values was attributed to each of the four phases (ρ_w , ρ_i , ρ_a , ρ_r , v_r , v_i , v_w , v_a) in Eq. 3.4. These were based on estimated resistivities and velocities obtained from the ERT and RST datasets as well as on standard ranges found in the literature (Hauck and Kneisel, 2008). A physically plausible range (i.e. 0.2-0.8) of initial porosity ($=1-f_r$) values was prescribed through an iterative process to define the most adequate initial porosity value of each profile, which influences the distribution of the four phases. Regularisation parameters for the inversion were attributed according to the suggested values by Mollaret et al. (2020). Because of the varying sensitivity of the model to prescribed resistivities of the four phases and initial porosity, a looping process was used to systematically test different combinations of parameters (ρ_w , ρ_i , ρ_a , ρ_r and initial porosity) with different sets of prescribed values. The goal was to identify the optimal combination that most closely matched the model's χ^2 (where $\chi^2 = 1$ indicates a perfect fit to the data, given the data error, following the method outlined by Günther and Rucker (2023) and prior site knowledge.

3.2.4 Ground penetrating radar

Ground penetrating radar (GPR) is based on the propagation of high-frequency electromagnetic waves into the ground and their reflection at interfaces between materials with different dielectric permittivity and electrical conductivity. The propagation velocity is determined by the permittivity of the subsurface material, whose values range between 1 (air) and 80 (water). Due to contrasting properties between air, ice, and rock, this method enables the delineation of subsurface layers with velocity contrasts. A GPR campaign was held at the Ritord study site in mid-April 2021. A longitudinal profile (Ri-R08), co-located to the VES and ERT profiles, and two transversal profiles (Ri-R08a and Ri-R08b) were carried out on the debris-covered tongue of the Epée glacier. A profile (Ri-R04) co-located to the VES and ERT profile Ri-S04 was performed on the Challand push-moraine. Being complementary to the other applied geophysical techniques (Kunz and Kneisel, 2020), this allowed to image the internal structure of the debris-covered glacier tongue and the Challand push-moraine. Further details on this method can be found in the respective methodological sections of *Publication III*.

3.3 Ground surface temperature

The thermal state of the ground surface is commonly assessed through the monitoring of ground surface temperature (GST), which result from the energy balance at the ground surface, which is predominantly influenced by solar radiation and air temperature during snow-free periods, but also by the snow cover timing and duration (Hoelzle et al., 2022). Temperature loggers are buried a few decimetres under the ground surface to avoid the GST signal to be disturbed by solar radiation, thereby slightly damping its diurnal temperature amplitude. This allows to analyse the state and changes of the ground thermal regime and the snow cover with relatively little noise in the data. Spatially distributed continuous GST measurements allow to assess the spatial and temporal variability related to varying topographic settings or ground surface characteristics throughout the monitoring period. To maintain consistency in the long-term monitoring of the

ground surface thermal regime, of the positions of the temperature loggers must be kept identical, since the terrain-specific micro-climatic conditions have to be maintained over the monitoring period.

The GST data is used to assess the influence of the ground thermal regime on surface changes in glacier forefields. At Ritord, 20 GST loggers have logged ground surface temperatures in the glacier forefield and on the adjacent debris-covered glacier since 1997. At Aget, 7 GST loggers were installed within the glacier forefield in 1998. At Gruben, 5 loggers were installed in 2012. Since their installation, all temperature loggers have recorded ground surface temperatures at a two-hour frequency. Until 2016, GST data were collected using UTL-1 data loggers (accuracy of $\pm 0.2^{\circ}\text{C}$) and from 2016 onwards UTL-3 data loggers have been used (accuracy of $\pm 0.02^{\circ}\text{C}$). In case of drift, time series are adjusted to match with the zero-curtain temperature during autumn freezing and spring melt periods.

4 Key findings and discussion

The response of systems where glacier-permafrost occurred over varying temporal scales – from intra-seasonal to decadal – has been investigated and evaluated in relation to the corresponding climatic context, using a multi-method and interdisciplinary approach. The joint analysis of different datasets provided insights into the driving processes contributing to the morphodynamical evolution of such systems. The interactions between glaciers and permafrost have resulted in the formation of complex landforms and combinations of landforms. The characterization of these landforms is not straightforward as they are characterized by complex, interacting morphodynamical processes. The complexity of the processes occurring in glacier-affected perennally frozen landforms is inherited from the interaction phase between glacier ice and permafrost. This results in highly variable spatial and temporal variations of their post-glacial dynamic regime, which are closely influenced by the extent of the glacial load exerted during the contact phase, the ground ice content and origin, and the active layer or debris-cover thickness. Furthermore, their dynamical behaviour is primarily driven by key factors, including air and ground temperature, the input of surface liquid water (snowmelt or precipitation), and debris input, which may fluctuate according to the temporal scale and relative climatic conditions under consideration.

The following section presents the principal findings of each of the three case studies, preceded by a brief introduction and summary of their main achievements in the context of the research questions.

4.1 Evolution of ground ice and its influence on long-term permafrost creep dynamics – case study of Aget (*Publication I*)

The dynamics behind the viscous creep-deformation and displacement rate of perennally frozen landforms is mainly driven by complex thermo-hydro-mechanical processes (Arenson et al., 2002; Buchli et al., 2018; Cicoira et al., 2019; Haeblerli et al., 1988; Ikeda et al., 2008), whose variations appear to reflect climate-related fluctuations (Kellerer-Pirklbauer et al., 2024). Nevertheless, local environmental factors such as the topography, geometry, hydrology, and ice content can exert a significant influence on permafrost creep dynamics, to the extent that creep behaviour patterns may be considered to diverge from regional environmental signals. To better understand the driving processes contributing to the kinematic behaviour of perennally frozen landforms, and consequently to answer the *Research Question I*, we investigate the post-glacial dynamics of a glacitected perennally frozen landform (hereby referred as GFL) at Aget. To this aim, the evolution of the extent and properties of ground ice over a twenty-year period is assessed through the analysis of repeated historical geoelectrical measurements (see Figure 4.1 for the location of the geoelectrical profiles). Thereafter, the kinematic behaviour of a mass-wasting GFL is investigated, with an emphasis on the contribution of ice melt-induced subsidence to surface elevation changes, through the combination of the analysis of 20-year of in-situ geodetic and ground surface temperature monitoring surveys. Our observations underline the importance of decadal-scale and multi-method approach in understanding the driving processes contributing to changes in the kinematic behaviour of glacier-affected perennally frozen landforms in the alpine context. The detailed analysis of the results are presented in *Publication I*.

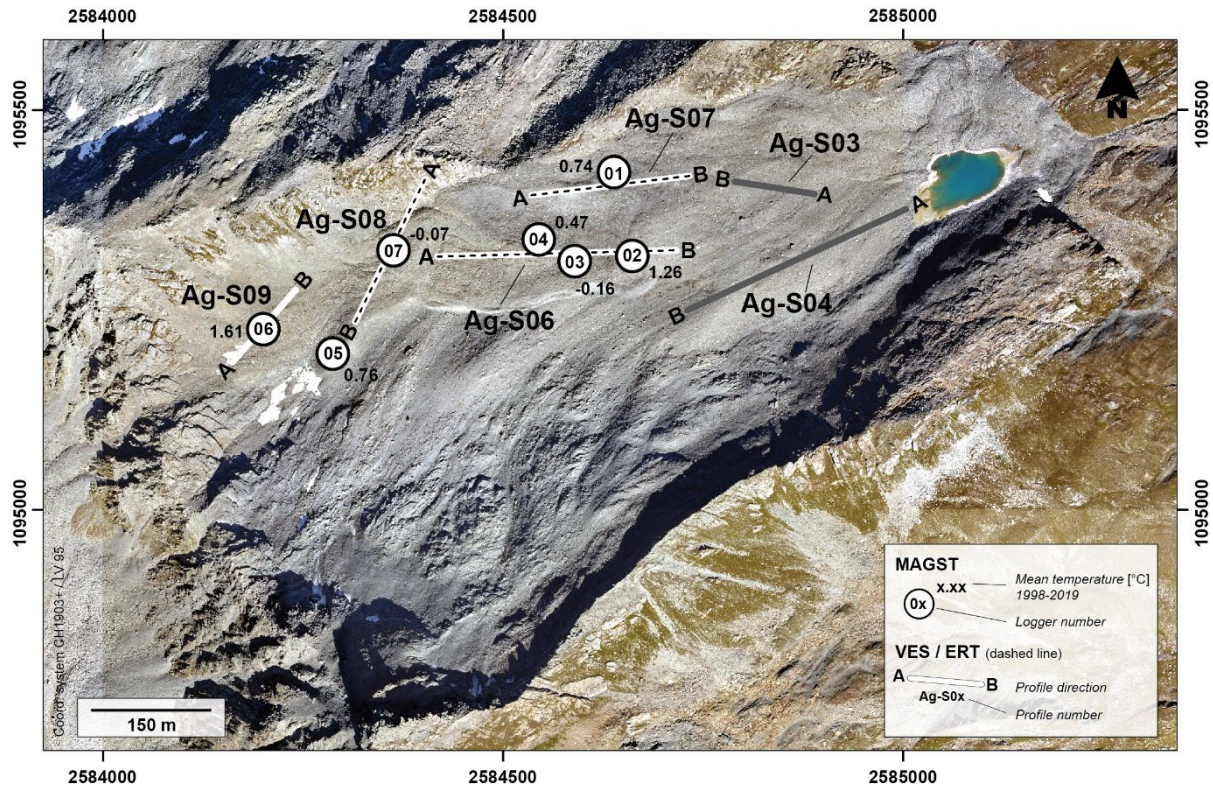
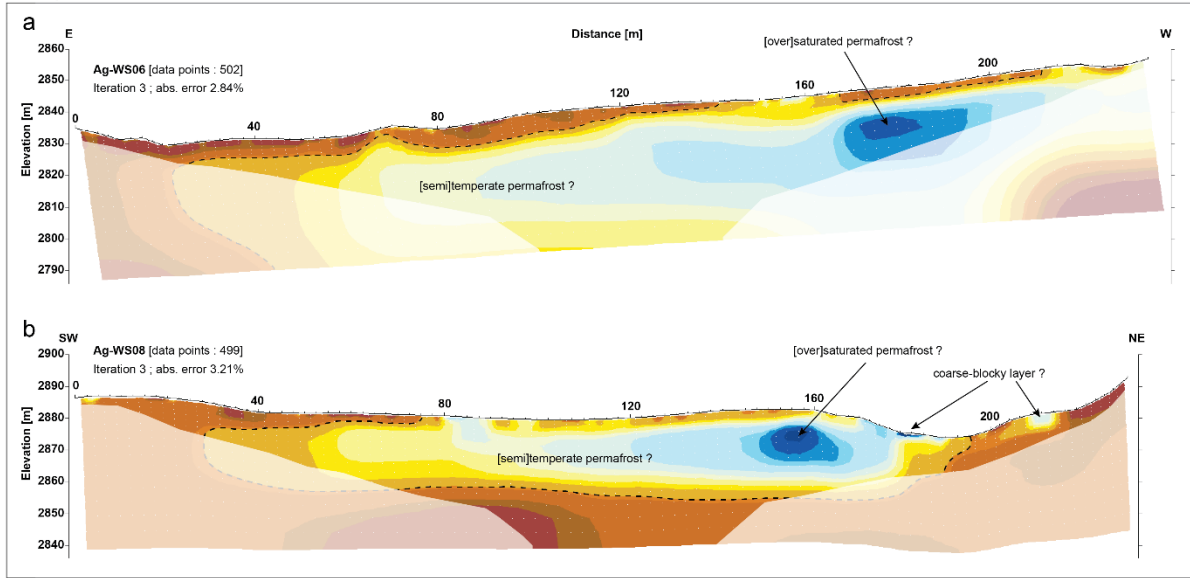


Figure 4.1: Overview of distribution of the GST sensors throughout the site and the location of the geoelectrical profiles. The location of the GST sites is marked by white dots. The geoelectrical profiles at the site are marked by a continuous segment (VES) and by a dashed line (ERT). Profiles marked in white represent permafrost-prone areas, and in grey permafrost-deprived areas (orthorectified aerial image: Flotron AG 2019).

4.1.1 Ground ice content distribution and evolution

The geoelectrical surveys at Aget allowed to characterize a heterogeneous distribution of ground ice within the investigated glactectonized frozen landform (push-moraine) (Figure 4.2). Low electrical resistivity values suggests that the kinematically inactive downstream section of the landform is either experiencing an advanced state of permafrost degradation or is partly unfrozen, which corroborates with the positive ground surface temperature measurements and our geomorphological interpretation. In the still active, yet decelerating section of the landform, permafrost conditions are widespread and local patches of high electrical resistivity values are discernible. From the measured electrical resistivity values, we cannot fully exclude the presence of remnants of buried glacier ice, which could have been embedded during the glacier-permafrost interaction phase.

Creep motion zone



No creep motion zone (transition zone to GFL B)

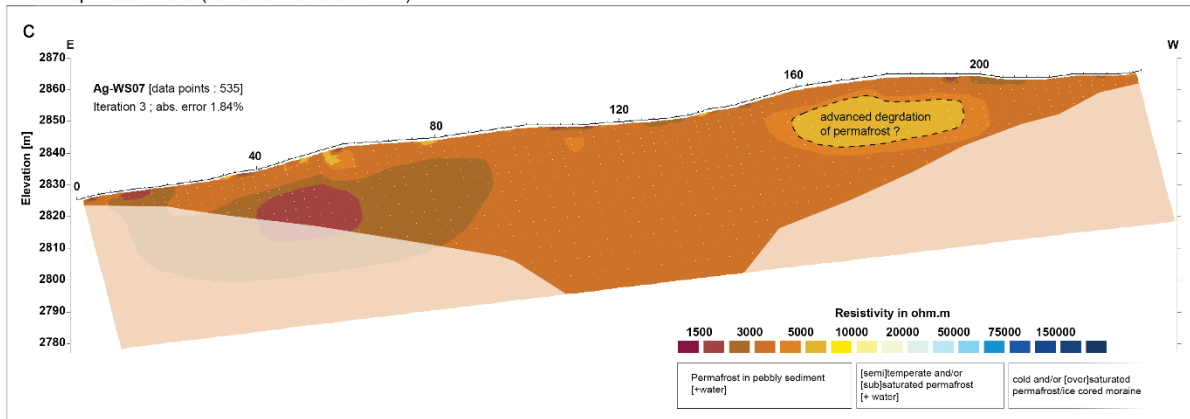


Figure 4.2: ERT profiles Ag-WS06 (a), Ag-WS08 (b), and Ag-WS07 (c). The whited-out sections represent low-sensitivity data at the edges of the tomograms. The dashed line represents the threshold for permafrost occurrence (5 kΩm).

Through the repetition in 2017 of the 1998 historical geoelectrical surveys, we quantified the changes in resistivity values. Because of the heterogeneous spatial distribution of ground ice and the varying ground ice properties, the amplitude of the observed changes are not uniform. As the warming of ground ice induces an increase in the liquid water-to-ice content ratio, a notable decrease in resistivity is expected in interstitial frozen layers as the melt water can fill the pores or build up a thin layer at the contact of ice and rock particles. Smaller changes in resistivity within layers of more massive ice can be attributed to their limited ability to retain additional liquid water, as the structure of massive ice lacks the pore spaces or interfaces present in interstitial frozen ground that facilitate water storage.

In the back-creeping part, where interstitial ice is present, the degradation (here, expressed by change in resistivity) is the strongest (Ag-S06 BC, -44% change in ρ_a ; Figure 4.3). Conversely, in the highly resistive patches observed in the tomograms Ag-W06 and Ag-W08, where a supersaturated ice content is likely to occur, the change in resistivity between 1998 and 2017 is relatively low (Ag-S08 AC, -14% change in ρ_a). Despite the heterogeneity in resistivity changes in

layers containing ground ice, our observations lie within the trend of resistivity decrease due to warming permafrost observed in the Alps (Mollaret et al., 2019; Buckel et al., 2023).

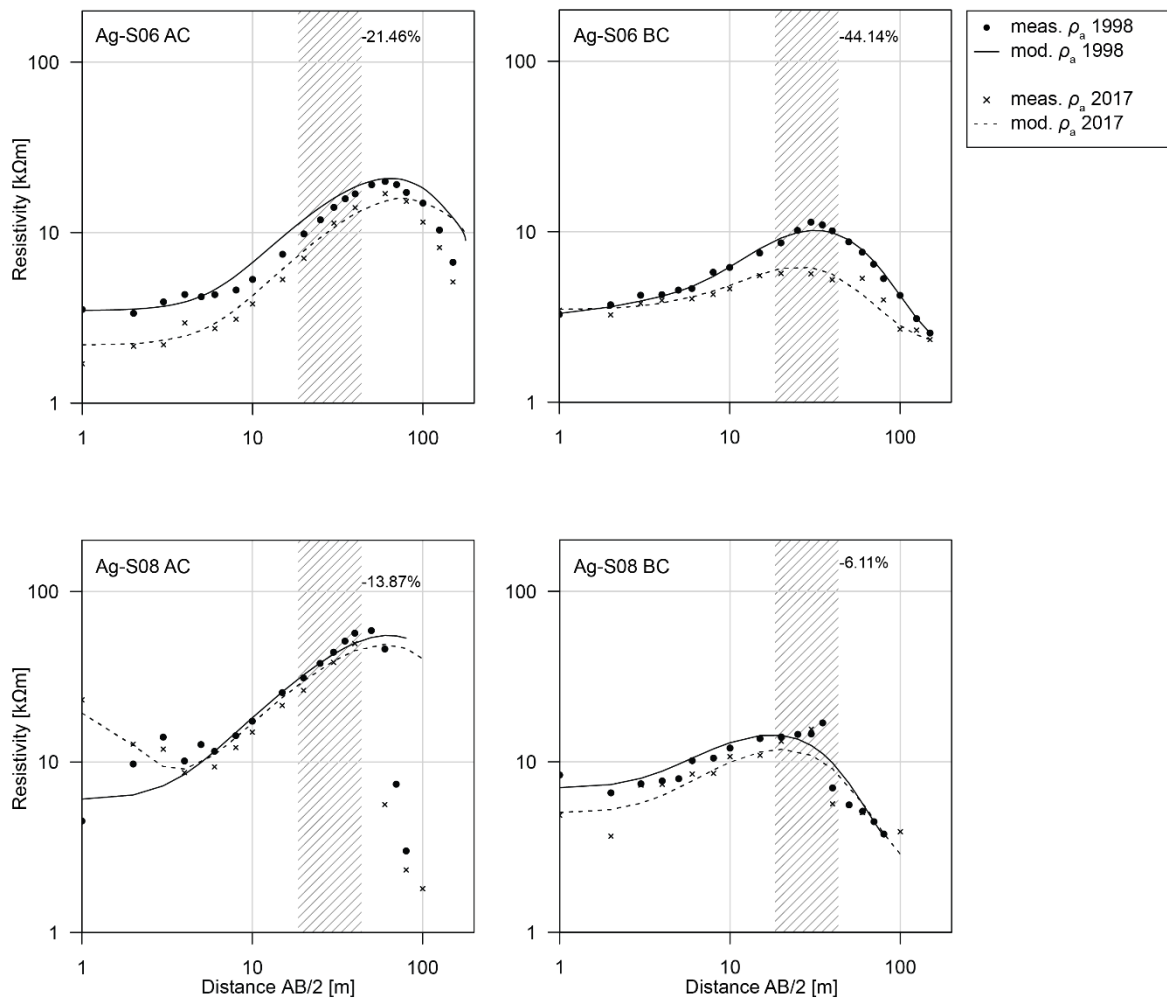


Figure 4.3: Change in resistivity from 1998 to 2017 of VES Ag-S06 and Ag-S08. Both branches AC and BC (Hummel array) of each profile are presented. The data points (measured ρ_a between 20 and 40 m, distance AB/2 [m]) used to calculate the relative change in apparent resistivity are highlighted by the hatched lines.

4.1.2 Contribution of ground ice content evolution on the kinematic behaviour of the Aget GFL A

Along with a decrease in electrical resistivity, permafrost degradation is also expressed by geometrical adjustments such as ice melt-induced subsidence, i.e. the subsidence observed at the surface caused by the gradual melting of ice and corresponding volume change. To address the extent to which ice melt-induced subsidence contributes to surface changes, we first calculated the estimated thickness changes of the GFL related to compressing and extending flow patterns. As the related change in elevation is dependent on the thickness of the moving mass, we prescribed it according to geomorphological observations and the results of the geoelectrical surveys. The measured horizontal displacement, vertical displacement, and topographical slope

angle are considered in the estimation of ground ice melt. A complete overview of this approach is available in *Publication I*.

In the central zone of GFL A, average surface displacements ranging from 0.15 to 0.30 m/year have been measured from 2001 to 2020 (Figure 4.4). In contrast, only small surface movements (mainly between 0.05 and 0.10 m/year) have been observed on the southeastern terminal lobe. The direction of the surface movement follows the slope aspect towards the southeast. The mean slope angle of GFL A is approximately 15°. The slope angle decreases towards the frontal zone (between 5° and 10°), contributing to a reduction in velocity. In the vicinity of the uppermost topographical rupture of the back-creeping GFL section, the slope angle gradually changes from 15° to 30°, resulting in velocities exceeding 0.20 m/year in the area. Throughout the investigated GFL, an extending flow pattern is observed, especially in the uppermost part near the topographical rupture, where values up to +13% are found over the 19-year observation period. For the rest of the surface, the extension rate remains relatively low with values ranging between 0 and +5% (subsidence of up to 1.0 ± 0.25 m). Compression is restricted to the lowermost frontal zone of GFL, where the topography flattens and surface displacements are the slowest, and locally at the foot of the topographical rupture in the upper central zone due to some convergence of the flow field (Figure 4.4). As a geometric response to compressive flow, a relative gain in surface elevation above the initial topography in the order of 0.5 m up to more than 1.0 m on the southeastern front can be expected.

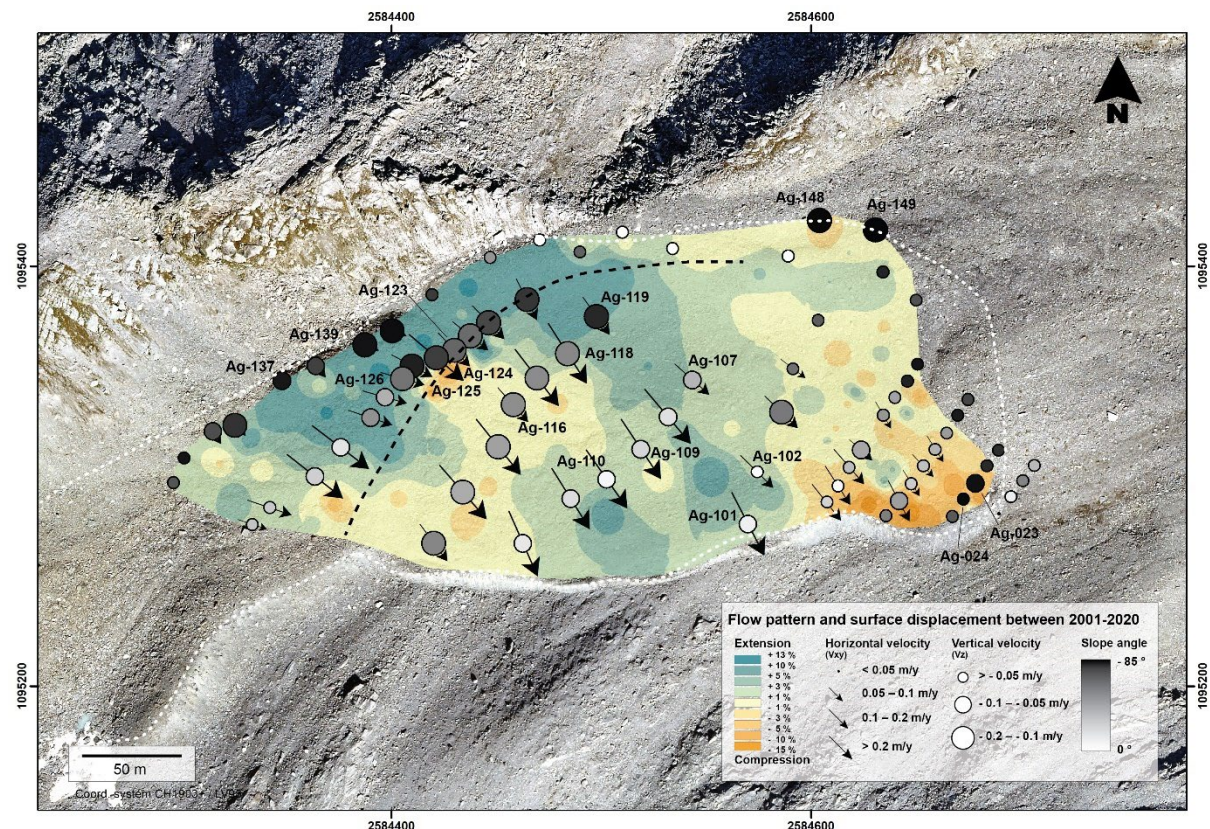


Figure 4.4: Contribution of extensive and compressive flow patterns and surface displacements to thickness variations obtained by an inverse distance weighting (IDW) interpolation. Arrows show the annual horizontal velocity, circles the annual vertical velocity, and the different shades of grey indicate the displacement slope angle of each point. The black dashed line represents the topographical rupture. The white dotted line represents the outline of the investigated GFL.

In areas where topographical changes are the highest, we have observed that surface elevation changes are essentially caused by the gravity-driven downslope permafrost creep along the topographical slope and enhanced by surface thinning due to an extending flow pattern, which could probably favour the deepening of the permafrost table as a thermal response. This is particularly evident in the uppermost zone of the GFL and close to the topographical rupture. Throughout the rest of the landform, ice melt-induced subsidence contributes more or less significantly to surface elevation changes, as expressed by pronounced vertical displacements with almost no horizontal movement (Figure 4.5).

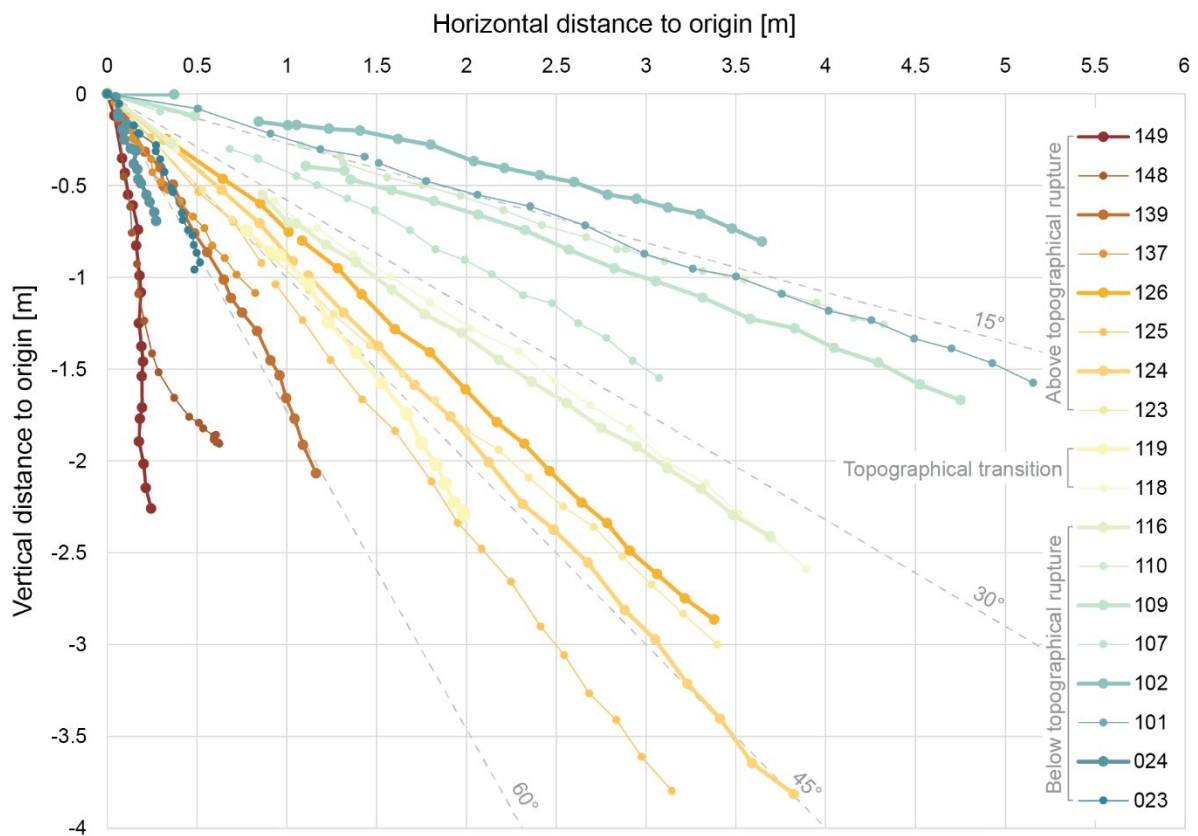


Figure 4.5: Displacement profiles for the period 2001–2020 of selected points distributed throughout the actively back-creeping GFL A.

In areas where the flow pattern is not pronounced (i.e. absence of horizontal movement), or a compression flow pattern dominates, the contribution of the melt of excess ice to surface elevation loss has been the highest, with values ranging between 0.06 and 0.12 m/year, while the surface elevation loss of points in the steeper zone of the landform is mainly driven by the extension flow pattern (refer to Table 1 in *Publication I*). To evaluate the influence of ground surface summer heating on the vertical displacement rates of the measured points, we compared the annual vertical displacements with the annual ground thawing index (GTI) for selected points located in different flow pattern zones (Figure 4.6). In the extension flow pattern zone, characterized by steeper topography, we observed a strong correlation between the GTI and elevation changes. This indicates that ground ice melting, primarily occurring at the permafrost

table and driven by summer ground surface heating, contributes to permafrost warming and accelerates creep rates. In areas of flatter topography with minimal horizontal displacement, a clear but more variable correlation between the GTI and annual vertical displacement suggests that ice melt-induced subsidence dominates the process. Conversely, in the compression flow pattern zone, the correlation is less distinct, likely due to heave resulting from compression, which counterbalances the signal of vertical displacement.

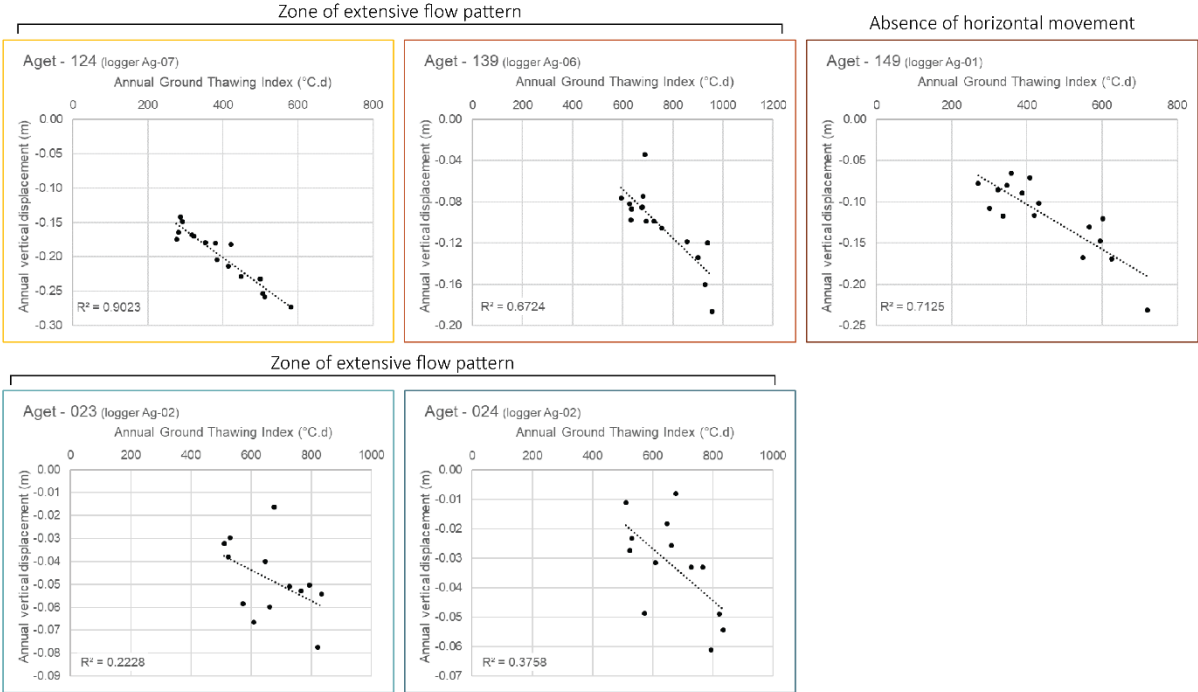


Figure 4.6: Contribution of the GTI to annual vertical displacement for selected points located in the different flow pattern zones from 2006 to 2018. Points Ag-124 and Ag-139 are located in the zone of extensive flow pattern, points Ag-023 and Ag-024 are located in the zone of compressive flow pattern and point Ag-149 is located in a zone where an absence of horizontal movement is observed.

The ongoing melt of ground ice leads to a progressive decrease in the thickness of the frozen column above the shear horizon. This melting increases the liquid water content within the permafrost, initially raising intrapermafrost pore pressure, which can temporarily reduce shear strength and enhance kinematic activity. However, as the frozen column thins further, pore pressure progressively decreases due to drainage and redistribution of meltwater, leading to a reduction in driving stress at the shear horizon. In advanced states of permafrost degradation, as should probably occur at the lowermost section of GFL A, the shear resistance is expected to increase as interlocking between particles becomes more significant, consequently and progressively leading the landform to a state of inactivity. The kinematic data also illustrates a loss of surface elevation, which is essentially driven by extensive flow patterns. This is explained by a topographical step and the divergent flow at the lateral margin of the GFL. The overall thinning of landforms in these areas yields a decrease in stresses exerted at the shear horizon. This contributes to a progressive reduction in its kinematic activity. It can be anticipated that the ongoing deterioration of permafrost and thinning of the GFL will result in its transition from a kinematic active to an inactive state. A similar process likely occurred in the lowermost part of the glacier forefield.

4.2 Ground ice content and origin and its influence on seasonal surface dynamics – case study of Gruben (*Publication II*)

The typology of the ice content and associated processes of the resulting phenomena and landforms can be delicate to assess, given that they are the product of complex interconnected glacial and periglacial processes (Vivero et al., 2021). In chapter 4.1 we have demonstrated that perennially frozen landforms that were subject to interactions with glacier ice can be characterized by a heterogeneous spatial distribution of ground ice and varying ground ice properties. This led us to investigate the influence of the subsurface properties of the Gruben rock glacier and its complex contact zone, a system where glacier-permafrost interactions occurred, on their seasonal dynamics, which we addressed through *Research Question II*. Numerous studies have evidenced the variability of permafrost creep dynamics at a seasonal temporal scale, which is characterized by an acceleration in early summer with flow velocity maxima occurring between summer and early winter, and a deceleration leading to a late-spring minima (Cicoira et al., 2019; Delaloye et al., 2010; Kääb et al., 2007; Wirz et al., 2016). This seasonal velocity signal typically exhibits a temporal lag of a few months with respect to both air and ground surface temperatures (Wirz et al., 2016). This phase lag may be attributed to the time for the temperature signal and water to propagate from the surface to the shear horizon, consequently affecting permafrost creep. Through the application of geophysical surveys, geodetic measurements and ground temperature measurements (Figure 4.7), we aim to understand the impact of subsurface properties on the kinematic behaviour of complex systems where glacier-permafrost interactions occurred, and the driving processes contributing to the morphodynamical expression of the latter. The detailed analysis of the results are presented in *Publication II*.

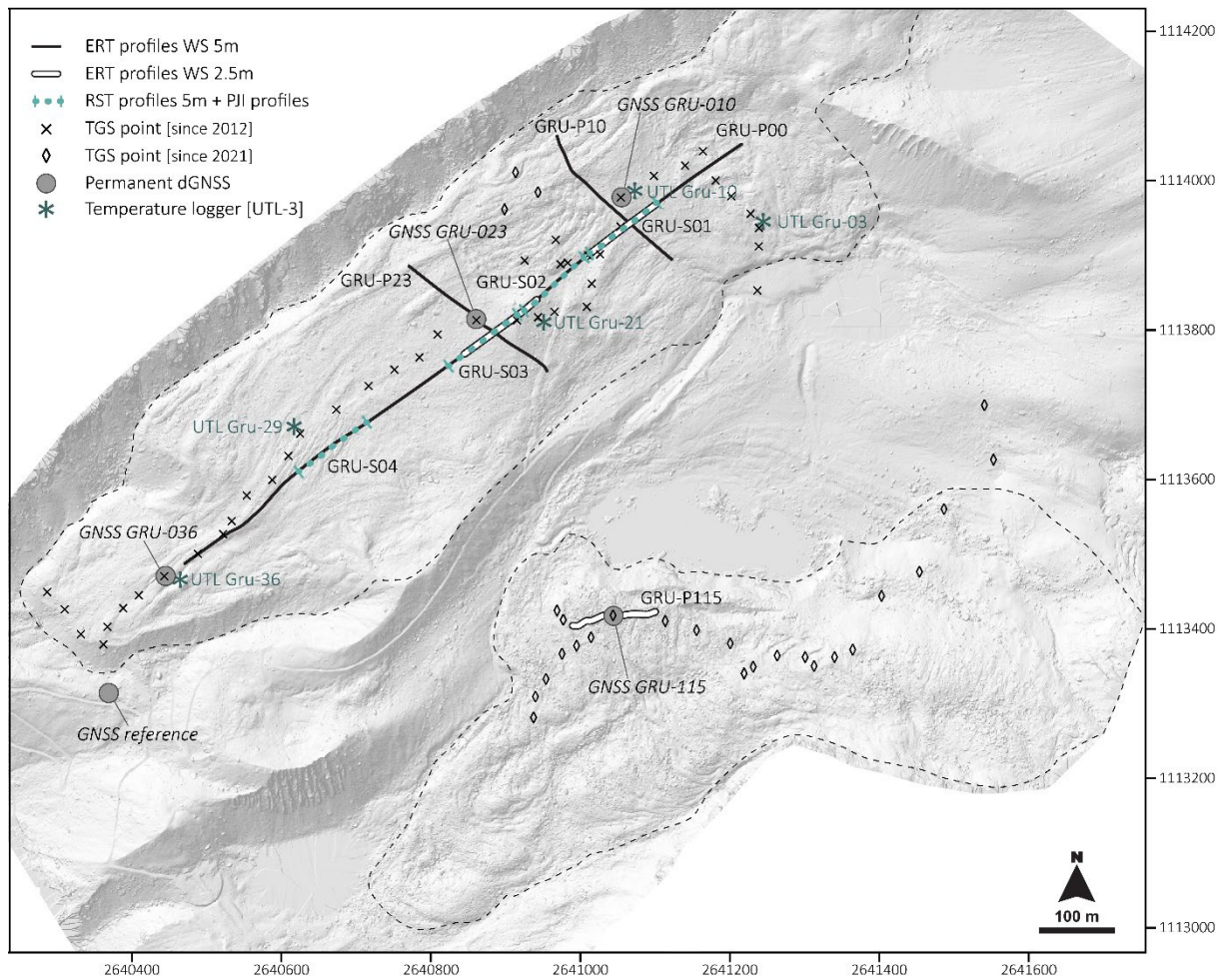


Figure 4.7: Overview of the distribution of the geodetic survey points (crosses are the points monitored since 2012 and diamonds are the points monitored since 2021) and the location of the four permanent dGNSS stations and the reference station. The location of the electrical resistivity tomography (ERT) and refraction seismic tomography (RST) profiles is also presented. The continuous black line indicates ERT profiles with a 5m electrode spacing, and the white lines indicate ERT profiles with a 2.5m electrode spacing (see Sect. 4.1). The distribution of temperature loggers (UTL-3) is also presented. Background: UAV-derived hillshade (6 October 2022).

4.2.1 Characterization and estimation of ground ice content

The characterization of frozen ground is quantitatively assessed using the petrophysical joint inversion (PJI) approach (Mollaret et al., 2020; Wagner et al., 2019), where the measured apparent resistivity and seismic travel-times are jointly inverted to quantify the volumetric fractions of air, water, ice, and rock within the subsurface (Figure 4.8). We prescribe a physically plausible range of initial porosity to the model, and we attribute a range of resistivity and P-wave velocity values to each of the four phases, based on measured values obtained from geoelectrical and refraction seismic surveys. Because of the coarse-blocky and expected ice-rich permafrost conditions, we used the geometric mean model to relate the measured electrical resistivities to the subsurface components (Glover, 2010) as it has the advantage of including all fractions of the four phases, and consequently yield realistic and well-constrained ice content estimations also in cases where the water content is potentially low, such as rock glaciers or push-moraines (Mollaret et al., 2020).

The results confirmed the occurrence of a layer of ice-rich permafrost at depth in the frontal zone of the Gruben rock glacier (Figure 4.8d) and demonstrate the resilience of debris covered, ice-rich permafrost to the increasing air temperatures in the past four decades. The current conditions infer that the Gruben rock glacier was already under permafrost conditions before the LIA advance of the Gruben glacier. In the upslope section of the rock glacier, geomorphological indicators point to a former contact zone between the permafrost of the Gruben rock glacier and the polythermal Gruben glacier during its LIA maximal extent (Gärtner-Roer et al., 2022; Haeberli et al., 2024; Käab et al., 1997). During the interaction phase between the polythermal glacier and the rock glacier, debris-covered glacier ice was locally embedded within, and primarily on top of the frozen debris, as evidenced by the geomorphological imprint of thermokarst in the former contact zone, but also by the extremely resistive and widespread ground ice (Figure 4.8b-c), originating from buried cold surface ice. However, the uppermost section of the contact zone is characterized by a high water-to-ice ratio (Figure 4.8a), which can be explained by the presence at the surface of fine-grained glaciogenic sediments (till), where more capillary action occurs, but also by ground ice affected by the former presence of a thermokarst lake, where the energy exchanges between the lake water and the ground surface could have partly contributed to its thermal degradation.

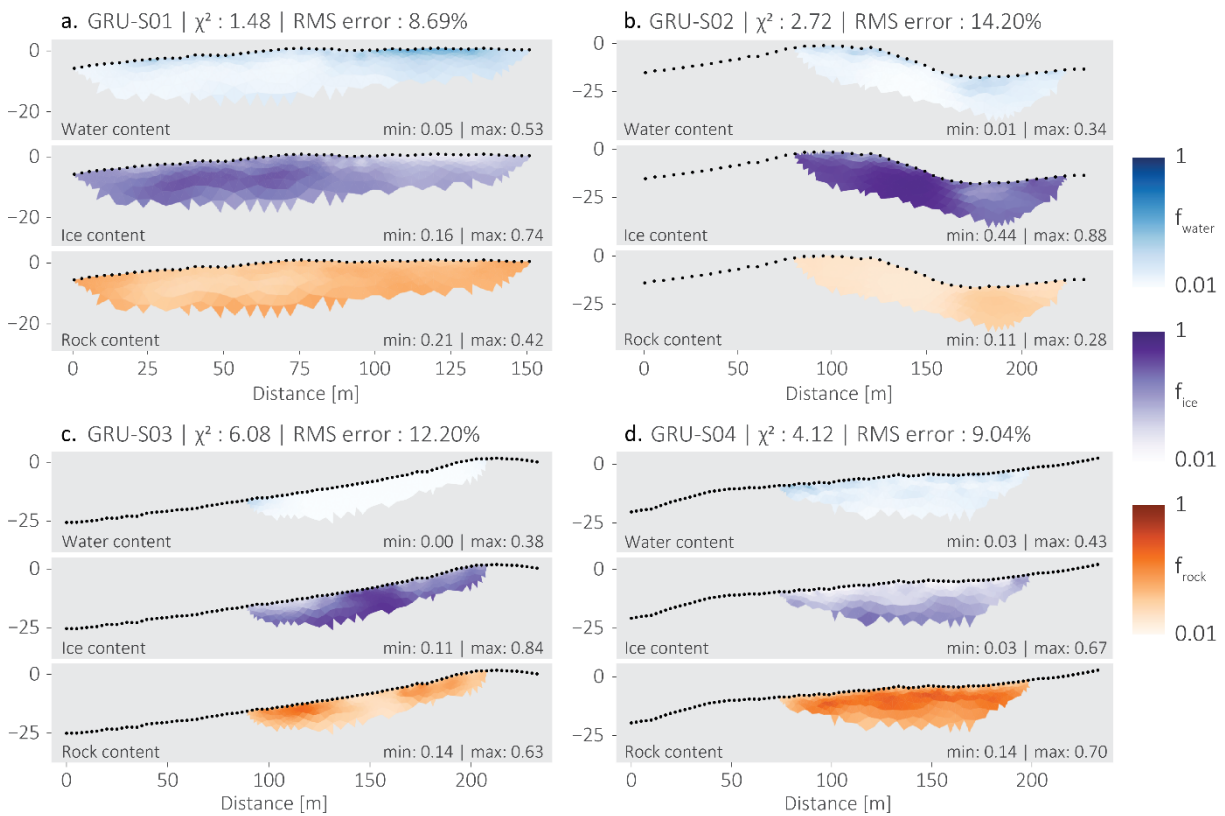


Figure 4.8: Volumetric fractions of water (f_w), ice (f_i) and rock (f_r) estimated by the petrophysical joint inversion of profiles GRU-S01 (uppermost section of former glacier-permafrost contact zone), GRU-S02, GRU-S03 (complex contact zone) and GRU-S04 (rock glacier).

4.2.2 Seasonal surface dynamics

The seasonal kinematic regime of the Gruben rock glacier and its complex contact zone, and the Gruben debris-covered glacier is assessed through the application of different geodetic approaches, allowing to capture both the spatial and temporal extent of morphodynamical changes. These include UAV-derived photogrammetry, seasonal terrestrial geodetic surveys, and continuous automatic geodetic observations. The information yielded by the latter allowed us to grasp the intra-seasonal dynamic variations in relation to seasonal meteorological changes (Figure 4.9), thus enabling a better understanding of the thermo-hydro-mechanical processes contributing to the morphodynamical changes of the rock glacier and complex contact zone.

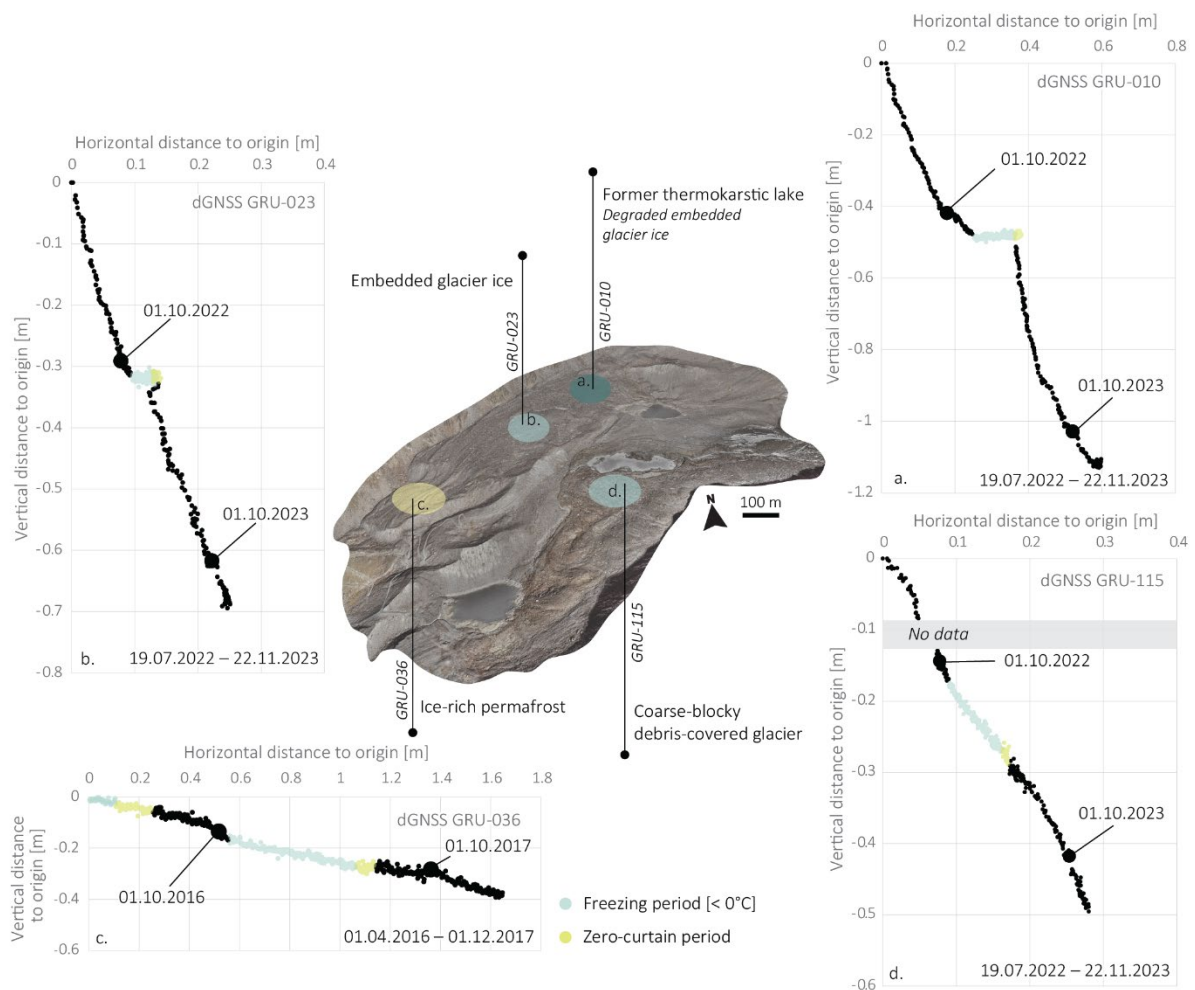


Figure 4.9: Displacement profiles measured by the four permanent dGNSS stations on the Gruben rock glacier (a–c) and the Gruben debris-covered glacier (d). Each marker represents a daily position, with wider markers indicating positions measured on October 1st of each year. Blue markers represent positions measured during the freezing period, while light green markers correspond to positions measured during the zero-curtain period.

Where ground ice content is widespread within a rock matrix with excess ice, surface lowering is mainly interpreted as the expression of ice melt and thaw subsidence. The magnitude of the latter is highly dependent of the ground ice properties, the surface debris thickness and coarseness,

and the temperature of the ground surface. The results from the geodetic and temperature measurements show direct and high-magnitude responses in the form of subsidence to summer ground surface heating in the complex contact zone, the highest temperatures are hereby associated with the largest subsidence (Figure 4.10a). Surface lowering is thus dominated by ice melt, a thermally driven process occurring from the permafrost or ground ice table downwards (Staub et al., 2016; Wee and Delaloye, 2022).

On the rock glacier, elevation loss is primarily driven by internal continuous creep deformation, with slight accelerations in the early summer, peak velocities observed in autumn, followed by deceleration in the winter (Figure 4.10c). Ice melt-induced subsidence has a minimal effect on surface lowering (Gärtner-Roer et al., 2022). However, increased water content from snowmelt and permafrost thaw enhances deformation, suggesting that seasonal increases in extensive flow patterns also contribute to surface lowering (Cicoira et al., 2019).

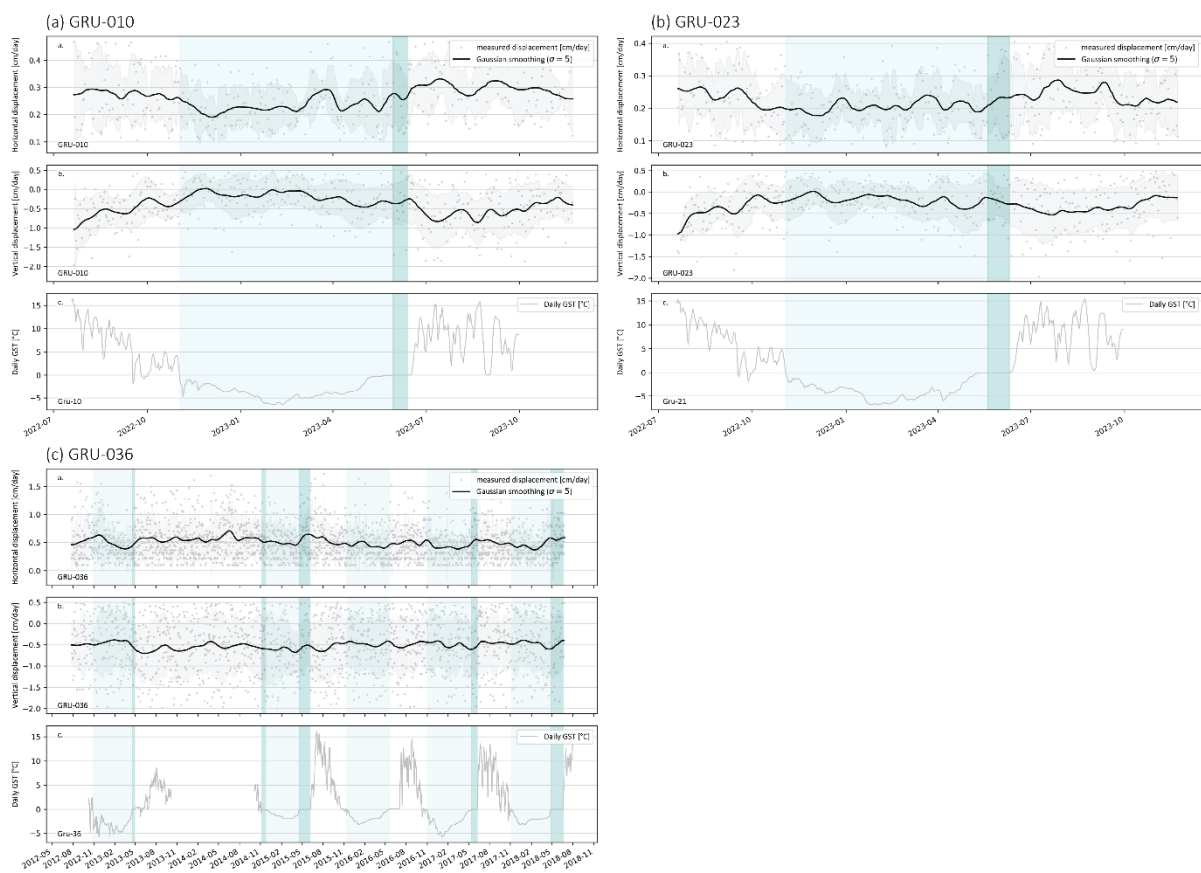


Figure 4.10: Horizontal velocity time series, vertical velocity time series and daily ground surface temperature, respectively from top to bottom plots in the complex contact zone GRU-010 (a) and GRU-023 (b), and in the rock glacier zone Gru-036 (c). The time series recorded by the stations GRU-010 and GRU-023 span from July 2022 to early October 2023, whereas the time series recorded by the station GRU-036 spans from July 2012 to June 2018.

In the area located down-valley of the topographical rupture, the mechanical behaviour of the perennially frozen body remained unchanged from its state prior to the advance of the LIA glacier, as it is likely that large-scale stress transmission did not occur. This is evidenced by coherent flow fields and longitudinal ridges and furrows, which indicate gravity-, hydrologically, and thermally-driven internal permafrost creep deformation and extending flow. In the area up-valley of the

topographical rupture and to the western boundary of the thermokarst depression, it is likely that stress from the Gruben glacier during its LIA advances caused internal and surface deformation, as evidenced by flow trajectories and compression ridges. It is also possible that an earlier glacier advance may have contributed to this mechanical deformation (Figure 4.11). The detailed description of the flow field trajectories and general seasonal kinematic observations obtained from Structure-from-Motion photogrammetry is available in *Publication II*.

In the complex contact zone up-valley, less coherent flow fields converging towards the glacier forefield indicate that there have been geometrical adjustments following the interaction between the Gruben rock glacier and the debris-covered glacier (Figure 4.11). Lateral back-creeping motion dominates this former contact zone. In the vicinity of the thermokarst depression, the flow pattern becomes locally much less coherent as the topography is relatively chaotic, favouring the stochastic displacement of the blocky surface.

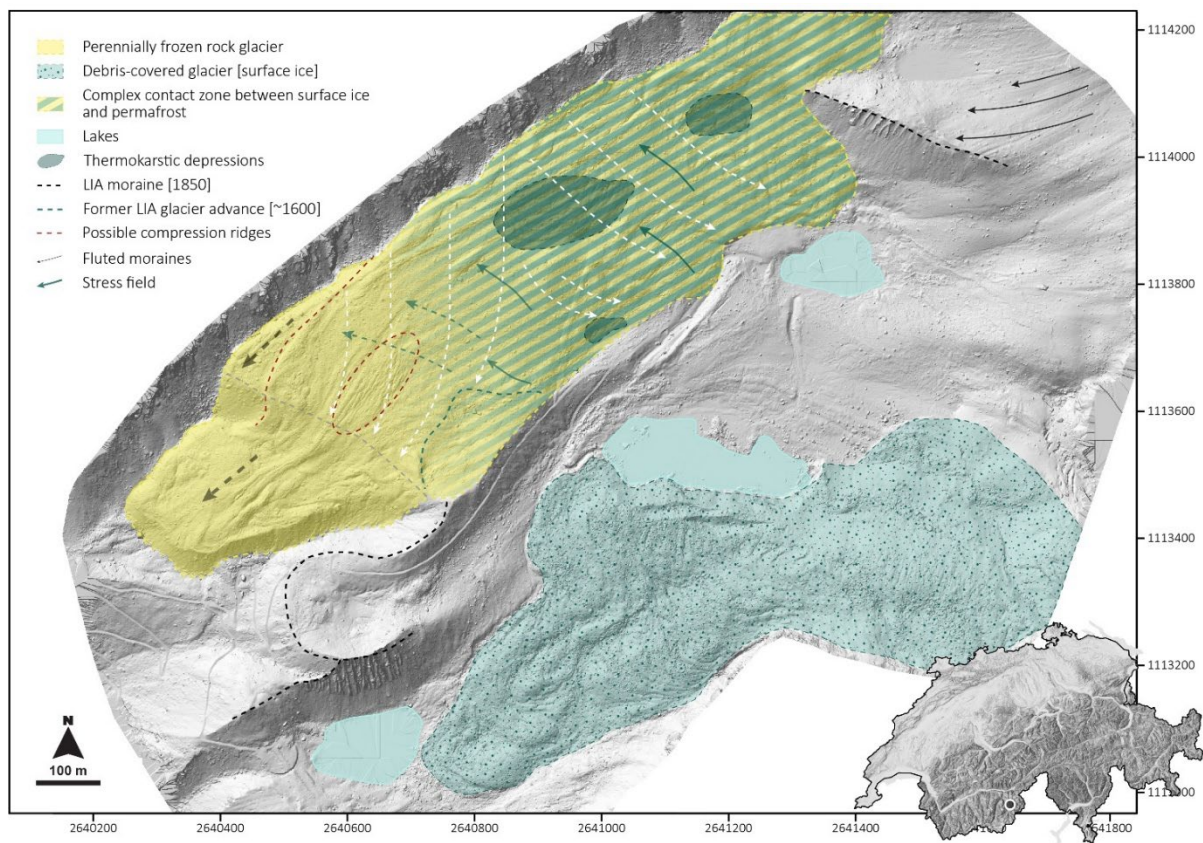


Figure 4.11: Interpretation of the influence of the LIA glacier-permafrost interaction on the mechanical behaviour of the rock glacier and its adjacent complex contact zone based on the analysis of high-resolution photogrammetry. The dashed grey line represents the topographical rupture. The dark blue arrows represent the stress exerted by the glacier onto the rock glacier. The white dashed arrows show the reoriented flow trajectories of the rock glacier and complex contact zone as a response to the stress exerted by the LIA glacier, while the grey dashed arrows show the unchanged flow trajectory of the rock glacier. The blue dashed line shows the probable extent of a prior stage (~1600) of LIA glacier advance. The dark red dashed line on the orographic right side of the rock glacier and the dashed ellipse show compression ridges likely due to the glacier stress. Background: UAV-derived hillshade (06.10.2022).

The kinematic signature of the two morphological zones described in *Publication II* attests of their geomorphological heritage from the Holocene and LIA and highlights the interrelation between glacial and periglacial processes occurring in the so-called complex contact zone. This underlines the complexity in capturing a complete and thorough understanding of the driving processes contributing to the morphodynamical evolution of such systems. This study also revealed the resilience of the ground ice to a warming atmosphere, in particular in the ice-rich permafrost of the rock glacier.

4.3 Post-glacial dynamics of a glacier forefield and its components in the context of mountain permafrost across spatial and temporal scales – case study of Ritord (*Publication III*)

In the previous chapters 4.1 and 4.2, corresponding to *Publication I* and *Publication II*, respectively, we addressed the influence of ground ice content, origin and spatial distribution of ground ice on the surface dynamics within the Aget and Gruben glacier forefields, including the debris-covered glacier tongue of the Gruben glacier. Here, we extend our previous investigation across different spatial and temporal scales, using the study site of Ritord. Very few studies have addressed the long-term evolution of such systems (Capt et al., 2016; Cusicanqui et al., 2023; Gärtner-Roer et al., 2022). Through the analysis of historical aerial images and recent UAV-derived images, we investigate the post-glacial morphodynamical evolution from 1964 to 2023 of the different landforms within the glacier forefield, which includes the glaciers of Challand and Epée. In addition to photogrammetry techniques, we apply geophysical, terrestrial geodetic measurements, and long-term ground surface measurements to capture the full understanding of the past and current dynamics within the Ritord glacier forefield. The kinematic evolution of the landforms within the forefield is investigated with an emphasis on the processes contributing to surface lowering. The evolution of the extent and properties of ground ice and debris-covered surface ice is assessed by geophysical surveys and ground surface temperature measurements. This study, presented in further detail in *Publication III*, seeks to foster the use and application of a multi-method approach to capture the multi-decadal evolution of glacier-permafrost interactions in a high-mountain alpine environment.

4.3.1 Characterization of the internal structure of the glacier forefield

Figure 4.12 presents a synthesis of the inverted electrical resistivity tomograms (ERT) and ground-penetrating radar (GPR) profiles, providing a detailed characterization of the subsurface conditions of the study area. The ERT profiles RIT-P04 and RIT-P12 were carried out on the lateral push-moraines, while RIT-P08 was taken on the debris-covered glacier tongue in the centre. Results from the GPR profiles (Ri-R08, Ri-R08a, and Ri-R08b) are well-aligned with the ERT findings, particularly in the case of profile RIT-P08.

In profile RIT-P04 (Challand push-moraine), the resistivity values at the extremities range from 1 to 5 k Ω m, suggesting a high water-to-ice ratio or permafrost loss. The central section shows a 20 m thick patch with resistivities between 200 and 350 k Ω m, beneath a more conductive 10-15 m thick layer (50 k Ω m). In profile RIT-P12 (Epée push-moraine), resistivity values range from 300 to 600 k Ω m in the lower section, while the upslope area shows a decrease to between 100 and 300 k Ω m, with the uppermost layer exhibiting a conductive zone of around 10 k Ω m, likely reflecting finer-grained sediments.

The ERT profile RIT-P08, which was measured on the Epée debris-covered glacier tongue, reveals high resistivity values (~2500 k Ω m) in the core, indicating massive cold glacier ice. These values gradually decrease downslope to 20-50 k Ω m, delineating the glacier tongue terminus. The upper conductive layer likely corresponds to the debris cover, while resistivity values (~350 k Ω m) near the profile's edges could be artefacts due to reduced sensitivity at the tomogram's margins.

The GPR profiles (Ri-R08, Ri-R08a, and Ri-R08b) further support the ERT findings for RIT-P08. In the uppermost layer of GPR profile Ri-R08, a continuous surface-parallel reflector was identified, interpreted as the boundary between the debris cover and the ice of the partly disconnected glacier tongue. A strong linear reflector observed across all GPR profiles indicates the interface between the ice and bedrock at around 40 m depth in the central zones, thinning towards the extremities. The cross-profiles (Ri-R08a and Ri-R08b) also show reflectors in their eastern and northeastern extremities, respectively, which are interpreted as shear planes, possibly linked to internal ice deformation or impurities.

Together, the ERT and GPR results offer a comprehensive understanding of the subsurface, identifying ice-rich zones, glacier ice-bedrock interfaces, and areas of internal ice deformation, as well as highlighting variations in permafrost conditions and debris cover.

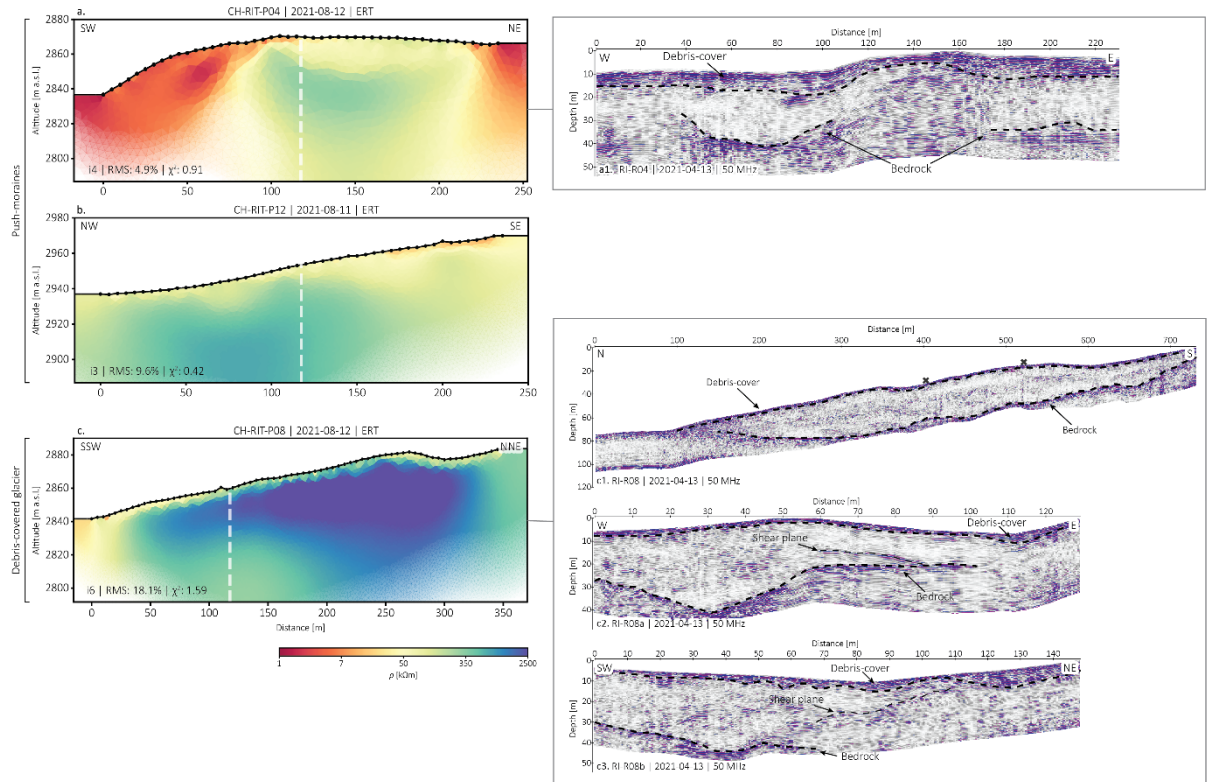


Figure 4.12 : ERT profiles carried out on the two push-moraines and the partly disconnected Epée debris-covered glacier tongue. Profile RIT-P04 corresponds to the Challand push-moraine (a), profile RIT-P12 corresponds to the Epée push-moraine (b), and profile RIT-P12 corresponds to the Epée debris-covered glacier tongue (c). The black dots represent the electrodes. The white dashed line represents the approximate location of the vertical electrical sounding. GPR profiles carried out on the partly disconnected debris-covered glacier tongue (c1-3) and the Challand push-moraine (a1). Ri-R08 corresponds to the longitudinal profile performed on the DCG (c1). The cross at around 510 m represents the intersection of the cross-profile Ri-R08a (c2), and the cross at around 400 m represents the intersection of the cross-profile Ri-08b (c3). Ri-R04 corresponds to the profile carried out on the push-moraine. Dashed lines mark the main reflectors.

4.3.2 Evolution of ground ice through changes in electrical resistivity

The vertical electrical soundings repeated in 2020 show coherent apparent resistivity curves, similar to those observed in 1997, but with a systematic decrease in resistivity values across all profiles. This reduction likely indicates the gradual melting of embedded ice and thawing of permafrost (Figure 4.13).

For the profiles measured on the push-moraines (Ri-S04, Ri-S07, and Ri-S12), the resistivity curves suggest the presence of ice lenses of varying thicknesses embedded within less resistive layers. The resistive cores of the push-moraines are overlain by a 4-6 m thick less resistive layer, likely representing the active layer. The observed decrease in resistivity between 1997 and 2020, ranging from 43.73% to 59.50%, points to the gradual melting and thinning of ice, as well as permafrost thaw.

On the Epée debris-covered glacier, profile Ri-S08 shows very high resistivity values, indicating the presence of cold glacier ice, with a decrease of 28.83%, likely due to ice thinning. In contrast, profile Ri-S09, located near the glacier terminus, exhibits lower resistivity values and an 86.55% decrease since 1997, suggesting faster melting of thinner ice and increased water saturation as the ice-covered surface diminishes.

In the rock glacier rooting zone, profile Ri-S16 measured in 1997 indicated a resistive layer, likely a buried glacier ice lens at a depth of 4-5 m. The significant 96.56% decrease in resistivity suggests the complete melt of this layer, leading to an increase in water content at depth. Profile Ri-S10, located closer to the glacier's margins, shows thick frozen sediments in 1997, where the presence of embedded glacier ice cannot be entirely excluded.

Overall, the observed changes in resistivity across all profiles reflect ongoing ice melt and permafrost thaw, particularly in areas with thinner ice or closer to glacier margins.

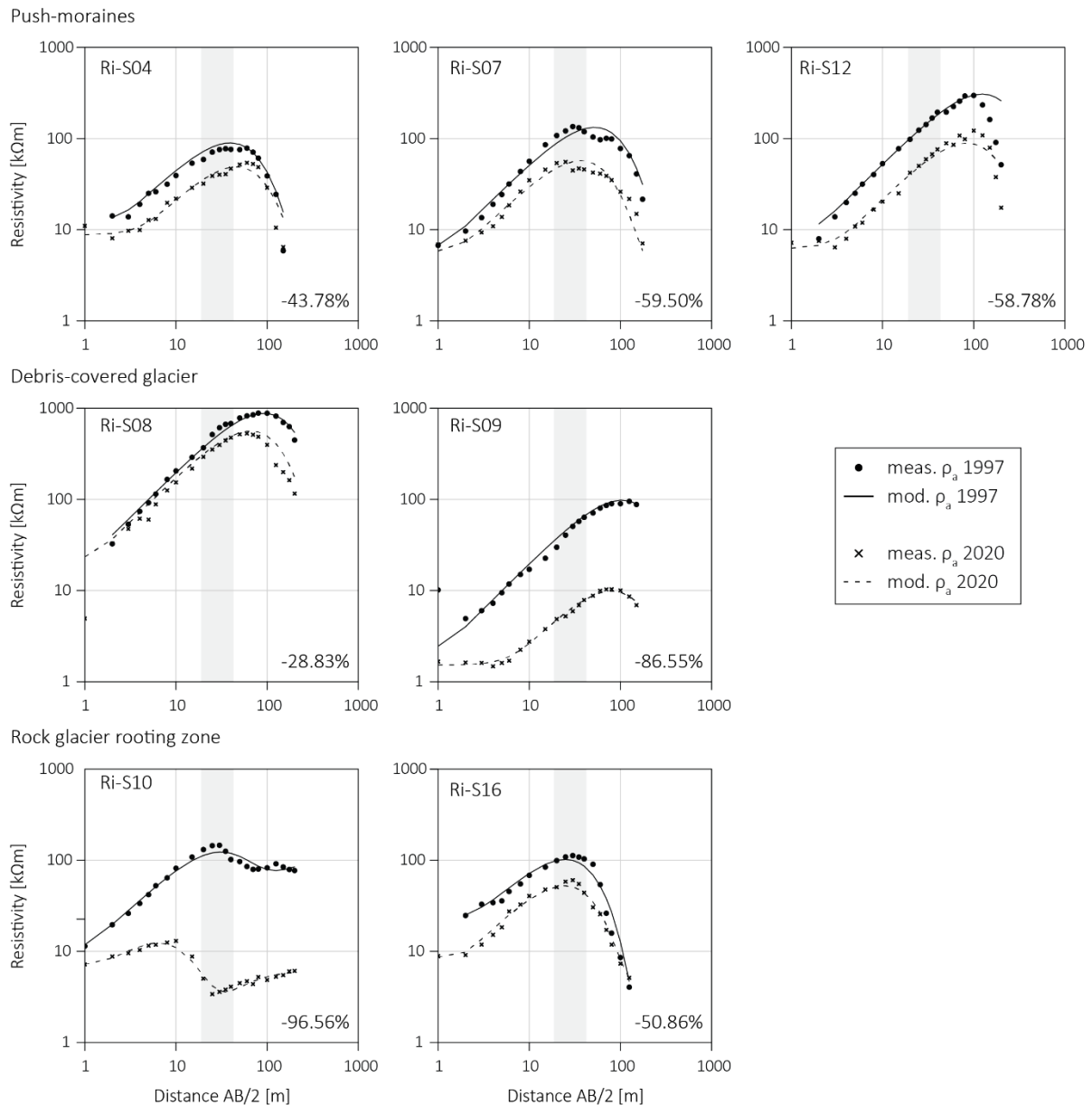


Figure 4.13: Change in apparent electrical resistivity between 1997 and 2020 of vertical electrical soundings Ri-S04, Ri-S07, Ri-S12 (on the northern push-moraine, medial push-moraine and southern push-moraine, respectively), Ri-S08, Ri-S09 (along and across the debris-covered glacier tongue, respectively), Ri-S10, and Ri-S16 (in the rooting zone of the glacier forefield-connected rock glacier). The measured apparent resistivity highlighted in grey (between 20 and 40 m, corresponding to an investigation depth of roughly 10-15 m) were used to calculate the change in resistivity as in Wee and Delaloye (2022).

4.3.3 Pluri-decadal surface lowering and displacement

Surface elevation changes in the Ritord Glacier forefield between 1964 and 2023 were reconstructed using historical aerial photographs, UAV surveys, and existing airborne laser scanning (ALS) data (Figure 4.14). The results show strong spatial and temporal variability across the study area, shaped by several processes: (i) melt-induced subsidence of buried glacier ice within glacier-affected, perennally frozen landforms (such as push moraines, rock glaciers, and

the debris-covered glacier tongue), (ii) thawing of ice-rich permafrost, (iii) downslope displacement, and (iv) thermokarstic erosion.

In the debris-covered tongue of the Epée Glacier (zone 1, Figure 4.14a), surface lowering was already evident from 1964 to 1982, averaging -0.33 m/year. This rate increased slightly to -0.37 m/year between 1982 and 1988 and accelerated further to -0.74 m/year from 1988 to 1999. Particularly high rates of lowering, up to -0.90 m/year, were observed along the orographic right lateral margin, where thermokarstic erosion likely contributed to the development of a lateral gully. Surface lowering continued in subsequent periods with varying intensity: -0.51 m/year (1999–2005), -0.59 m/year (2005–2016), and -0.69 m/year (2016–2019). A temporary slowdown was recorded from 2019 to 2022 (-0.42 m/year), followed by a renewed acceleration to -0.71 m/year between 2022 and 2023, suggesting intensified ice melt in recent years.

The Challand push-moraine (zone 2, Figure 4.14a) showed relatively low rates of surface change in the earlier decades. Between 1964 and 1982, mean surface lowering was -0.16 m/year, dropping to -0.05 m/year between 1982 and 1988. A slight increase was observed between 1988 and 2005, with rates ranging from -0.17 m/year to -0.22 m/year. These values remained close to the detection threshold, indicating limited geomorphic activity. However, more pronounced changes occurred after 2016: -0.28 m/year (2016–2019), -0.11 m/year (2019–2022), and -0.27 m/year (2022–2023). Significant morphological transformations were documented on the south-facing inner flank of the northern push moraine, where surface lowering reached -3.6 m/year (2019–2022) and up to -6 m/year (2022–2023), driven by the melt of outcropping glacier ice embedded in the moraine.

In the rock glacier rooting zone (zone 3, Figure 4.14a), surface elevation changes were negligible prior to 1988. From 1988 to 1999, surface lowering became more noticeable, with a mean rate of -0.41 m/year. This rate declined in subsequent periods: -0.23 m/year (1999–2005), -0.20 m/year (2005–2016), and -0.21 m/year (2016–2019). A significant decrease in lowering occurred from 2019 to 2022 (-0.09 m/year), but the trend reversed between 2022 and 2023, with rates increasing to -0.18 m/year.

In summary, the analysis highlights long-term surface lowering across all glacier-affected landforms, with the strongest changes linked to buried glacier ice melt and permafrost degradation. Surface changes intensified significantly after the late 1980s and have fluctuated in recent years, with a clear resurgence in the most recent period (2022–2023), pointing to increased climatic sensitivity of these high-mountain periglacial systems.

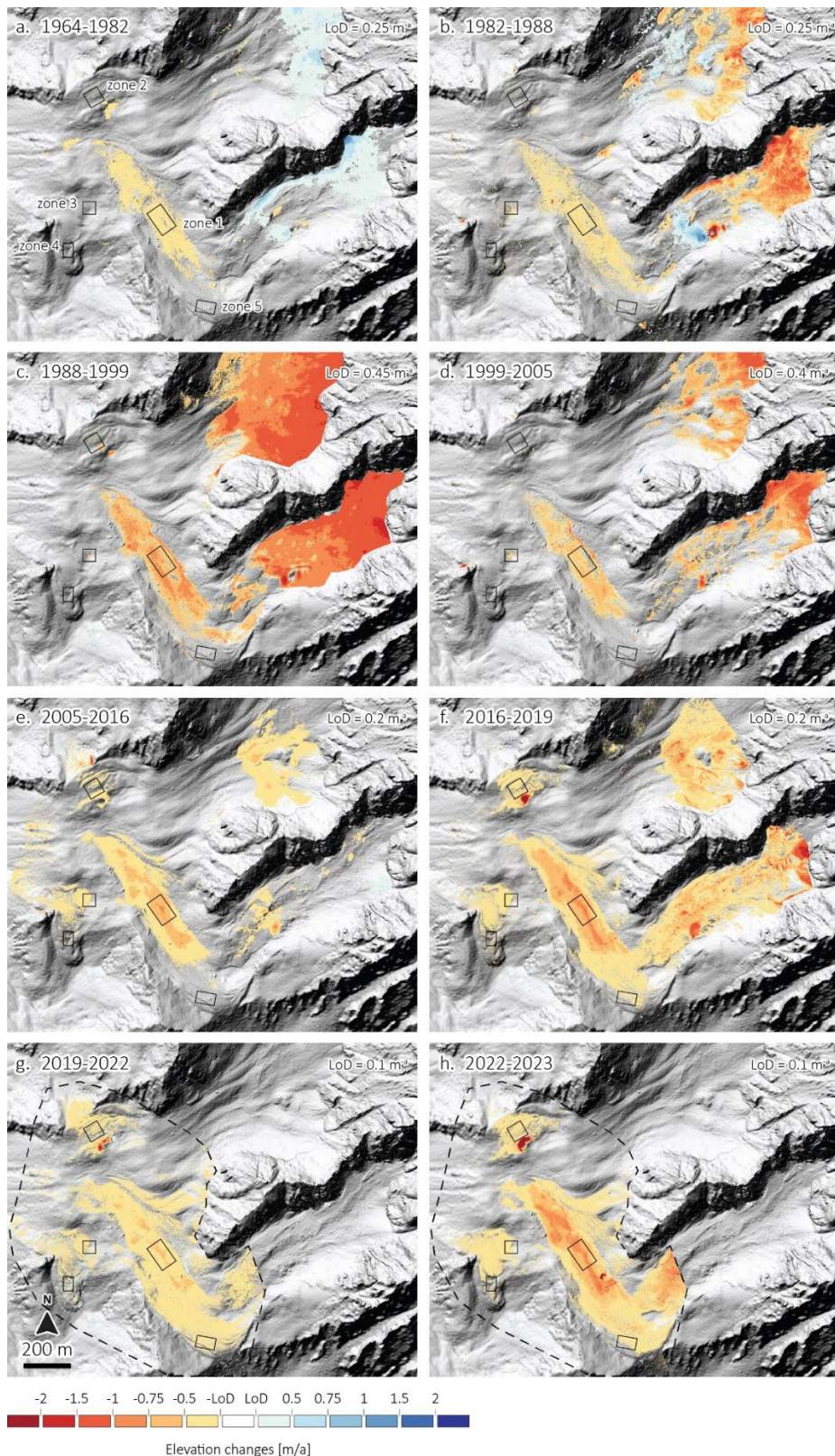


Figure 4.14: Surface elevation changes in the Ritord glacier forefield, including the Epée debris-covered glacier and the Challand glacier, between 1964 and 2023. The DEMs used to calculate surface elevation changes between 1964 and 2005 are derived from historical aerial images of Swisstopo (a-d). The DEMs used for the more recent years are derived from ALS surveys (2016 and 2019) and UAV-derived datasets (2022-2023). The black dashed polygons in panels g) and h) represent the area covered by the UAV surveys. The black boxes correspond to the areas used to calculate the mean surface elevation changes for the different zones detailed in panel a) (zone 1: debris-covered glacier tongue; zone 2: Challand push-moraine; zone 3: rock glacier rooting zone; zone 4: rock glacier; zone 5: Epée push-moraine). Background: swissSURFACE3D (Swisstopo, 2021).

Horizontal surface velocities in the Ritord Glacier forefield reveal spatially and temporally variable dynamics from 1964 to 2023, reflecting the interplay between ice flux, permafrost degradation, and geomorphic processes (Figure 4.15).

On the Epée debris-covered glacier, velocities remained generally low over the entire period, indicating dynamic (partial) disconnection from the glacier's accumulation area. From 1964 to 1982, average velocities were 0.08 m/year, increasing slightly to 0.14 m/year between 1982 and 1988, likely due to a positive mass balance (Capt et al., 2016). A decrease to 0.07 m/year occurred from 1988 to 1999. However, the orographic right lateral margin showed significantly higher movement during this time (0.7 m/year), increasing to 1.4 m/year between 1999 and 2005, likely due to lateral thermokarstic erosion. The overall glacier tongue velocity increased slightly to 0.17 m/year in this period, then stabilized at lower values in recent years (0.08 m/year in 2020–2021 and 2022–2023), confirming its ongoing dynamic stagnation.

From 1964 to 1982, velocities averaged 0.15 m/year (Challand) and 0.07 m/year (Epée). Both increased from 1982 to 1988, reaching 0.19 m/year and 0.16 m/year, respectively, possibly reflecting warmer conditions. The Challand push-moraine continued accelerating through 1999 (0.31 m/year) and peaked at 0.44 m/year in 2005, whereas the Epée push-moraine showed more moderate increases. Recent dGNSS data indicate stable velocities around 0.30 m/year, with a clear back-creep displacement pattern concentrated along the inner flanks of both moraines.

From 1964 to 1982, velocities were 0.19 m/year on the rock glacier and 0.13 m/year in its rooting zone, both decreasing by 1988. A strong acceleration occurred between 1988 and 1999, peaking at 0.31 m/year on the rock glacier in 1999–2005. Meanwhile, the rooting zone saw a sharp drop to 0.09 m/year. Between 2020 and 2023, the rock glacier showed moderate activity (0.24–0.19 m/year), while the rooting zone remained slower (0.12–0.07 m/year), indicating stable yet differentiated dynamics.

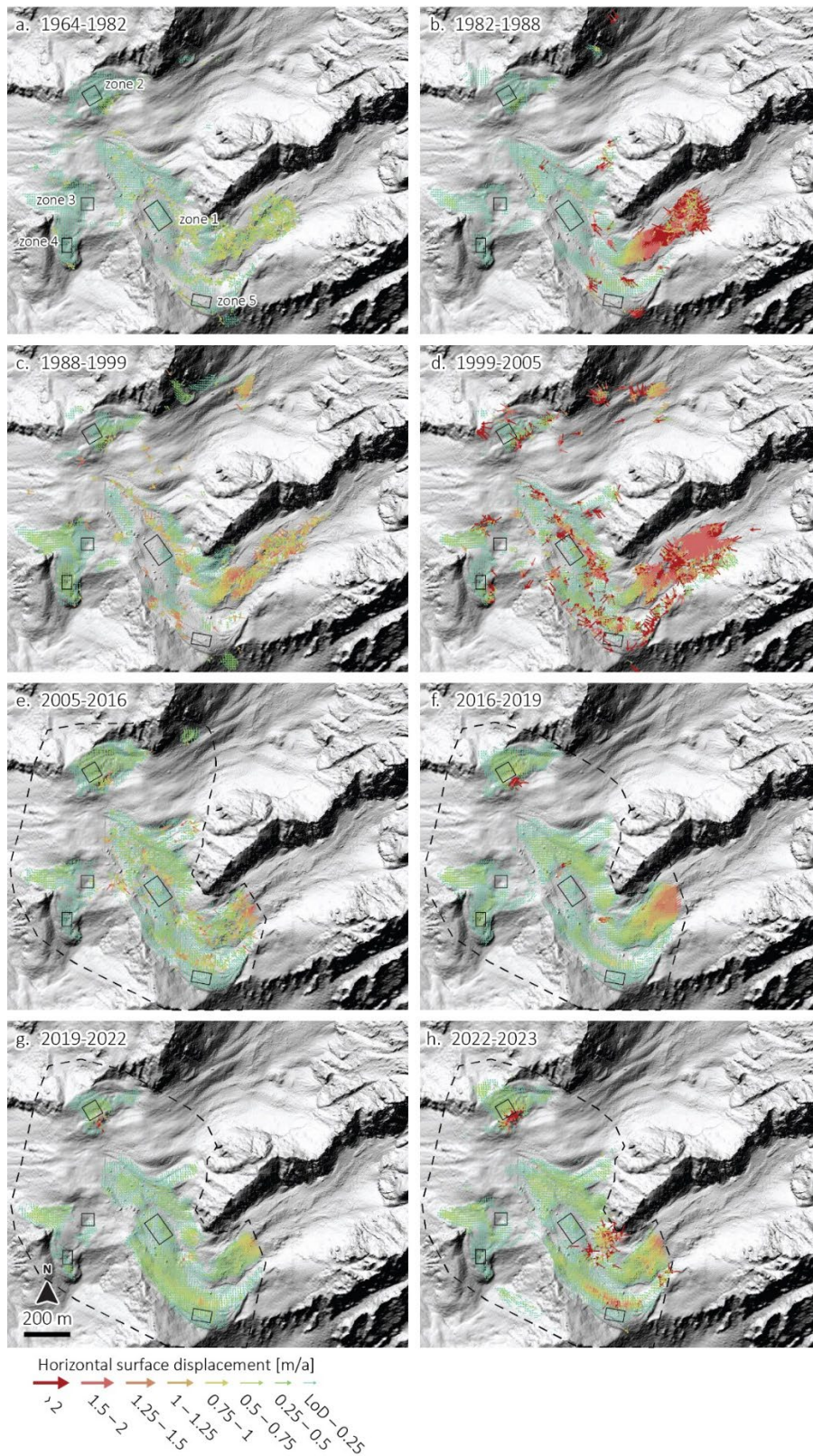


Figure 4.15: Horizontal surface velocities between 1964 and 2023 at the Ritord glacier forefield, comprising the Challand and Epée glaciers. The orthoimages used to calculate the horizontal surface displacement between 1964 and 2005 are from historical aerial image of Swisstopo (a-e). The orthoimages used for the more recent years are derived from Flotron aerial images (2016 and 2019) and UAV-derived images (2022-2023). The black dashed polygons in panels e) to h) represent the area covered by the surveys. The black boxes correspond to the areas used to calculate the mean surface displacements for the different zones (zone 1: debris-covered glacier tongue; zone 2: Challand push-moraine; zone 3: rock glacier rooting zone; zone 4: rock glacier; zone 5: Epée push-moraine; Figure 7a). Background: swissSURFACE3D (Swisstopo, 2021).

Figure 4.16 presents the mean horizontal velocities and surface elevation changes for the different zones outlined in Figure 4.14 and Figure 4.15, covering the period from 1964 to 2023. The results highlight distinct kinematic signatures among the studied landforms. The dynamically disconnected debris-covered glacier tongue is characterized by slow horizontal velocities and significant vertical lowering, reflecting ongoing downwasting driven by intensified ice melt. Glacier-affected landforms containing embedded glacier ice, such as the lateral push-moraines and the rock glacier rooting zone, exhibit more pronounced vertical changes, particularly evident in the Epée push-moraine and the rock glacier rooting zone between 1988 and 1999. In contrast, the rock glacier tongue, likely unaffected by the Epée LIA glacier, shows less vertical change.

In recent years (2020–2023), the kinematic contrast between glacier-affected landforms and the intact rock glacier has become increasingly marked. While the rock glacier shows a morphodynamic signature consistent with permafrost creep, glacier-affected landforms reflect a combined influence of permafrost creep and melt-induced subsidence due to the degradation of embedded glacier ice, especially in the lateral push-moraines.

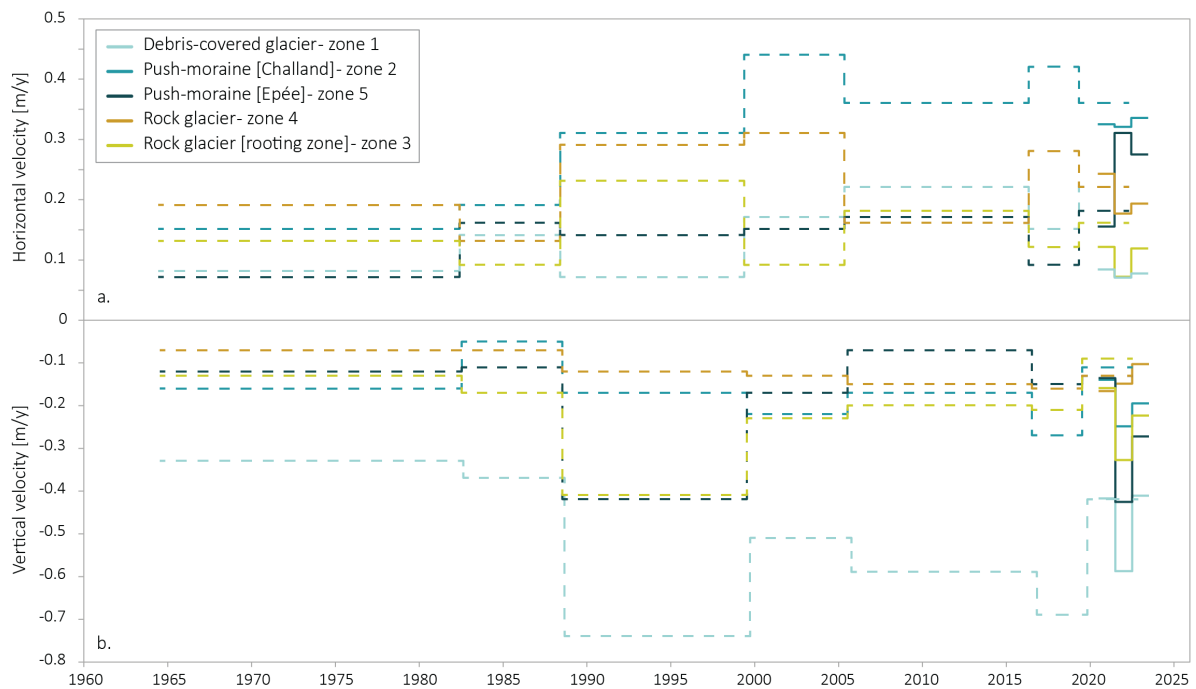


Figure 4.16: Mean horizontal (a) and vertical (b) surface velocity of the different landforms present in the Ritord glacier forefield. Dashed lines represent velocity time series derived from aerial imagery spanning from 1964 to 2022, while continuous lines correspond to terrestrial geodetic surveys conducted between July 2020 and October 2023. Velocity values for each landform are calculated based on the data from the zones delineated in Figure 4.14 and Figure 4.15.

4.3.4 Influence of ground thermal regime on sub-seasonal kinematic behaviour

The driving processes contributing to the intra-annual horizontal surface displacements and elevation changes were assessed through the comparison of daily position measurements by permanent dGNSS stations with the closest daily ground surface temperature measurements (Figure 4.17 and Figure 4.18).

The station BSP-01 (Figure 4.17) is located on the partly disconnected debris-covered glacier tongue, where the surface topography is relatively flat. The horizontal surface velocity tends to increase at the end of the spring zero-curtain period. The acceleration phase starts when the ground surface temperatures measured a few hundred metres from the station (still on the debris-covered glacier tongue) gradually increase in late winter – early spring. The inter-annual horizontal velocity is variable as in 2021, when the peak velocity was reached in autumn, while in 2022 and 2023, the peak velocities were reached in early summer. The vertical velocity systematically reaches its annual peak in summer when the ground surface temperatures are the highest. The maximal summer vertical velocity ranges between -0.80 cm/day to -1.20 cm/day, which corresponds to a summer (01.07. – 01.10.) elevation loss of ± 1 meter. Both the winter periods 2020–2021 and 2022–2023, when the ground surface temperatures are below 0°C, the horizontal displacement stabilizes to ± 0.10 cm/day, while the vertical displacement is close to 0 cm/day. The horizontal displacement during winter period 2021–2022 is characterized by horizontal velocities fluctuating between ± 0.18 – 0.24 cm/day. Similarly to the other winter periods, the vertical displacement during winter 2021–2022 were almost non-existent.

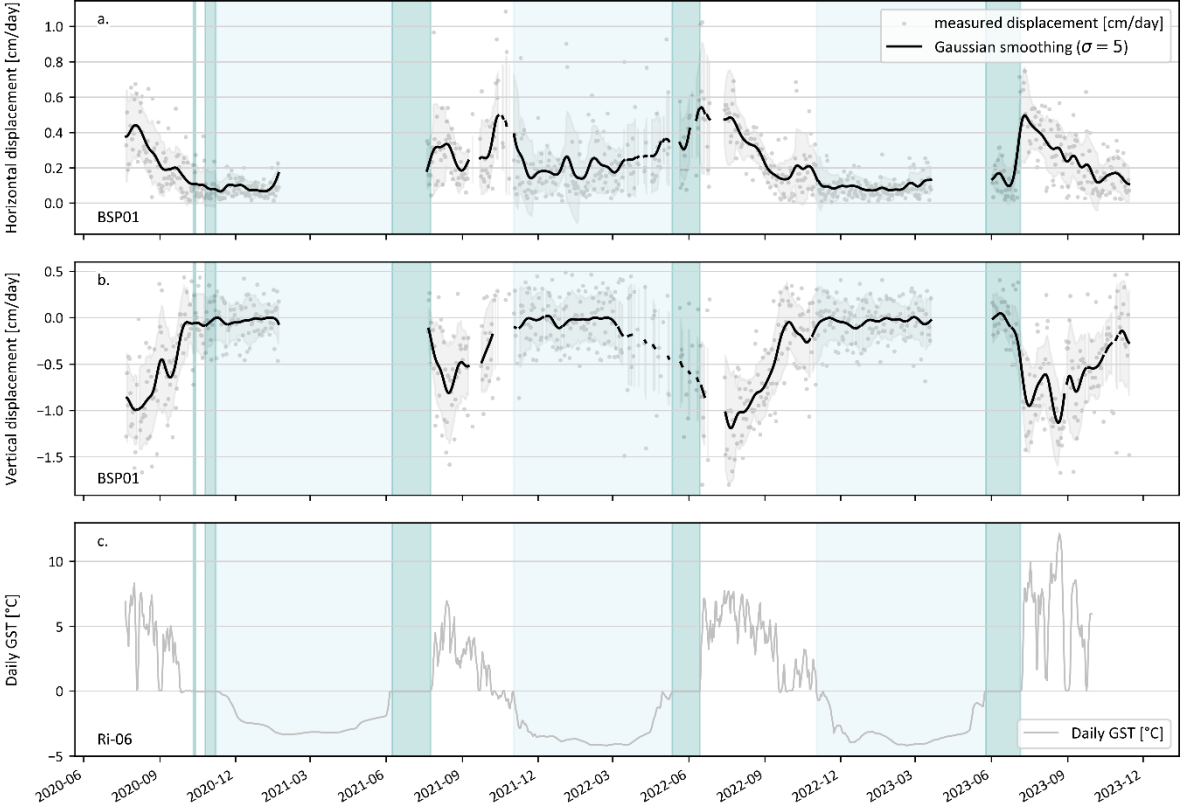


Figure 4.17 : Daily horizontal and vertical surface displacement measured by the permanent dGNSS BSP-01 (a) and (b), respectively. Daily ground surface temperature measured by the logger UTL-06 (Ri-06) (c). The light blue shaded area represents the period when ground surface temperatures are below 0°C for at least 20 days. The dark blue shaded area represents of the zero-curtain period. Discontinuities in the dGNSS data are explained by data gaps caused by the burial of the station by snow or other technical issues in data transfer.

The dGNSS station BSP-02 (Figure 4.18) is located on the Challand push-moraine, where glacier ice is buried within the frozen landform, and where the kinematic behaviour of the landform is

mainly characterized by back-creep. Horizontal velocities tend to reach their peak in autumn and are around 0.25 - 0.35 cm/day. A peak of 0.45 cm/day in horizontal velocity was reached in early summer 2022, which was followed by a deceleration in horizontal displacement (0.30 cm/day) towards the end of the summer. However, the vertical displacement in summer 2022 was more important than in the other years. This can be explained by the particularly high ground surface temperatures, which probably contributed to enhanced ground ice melt-induced subsidence. In winter 2021 – 2022, the horizontal displacement oscillated between 0.15 and 0.35 cm/day, while the vertical displacement was mainly around 0 cm/day, aside from an event in December where the displacement was -0.35cm/day, likely induced by the tilting of the station’s mast. In winter 2022 – 2023, as soon as the ground surface cooling was initiated, the horizontal displacement began to gradually decelerate from early September to early March. Meanwhile, the vertical displacement exhibited a gradual stabilization to 0 cm/day, suggesting a continuous creep behaviour, and an absence of ice melt-induced vertical changes.

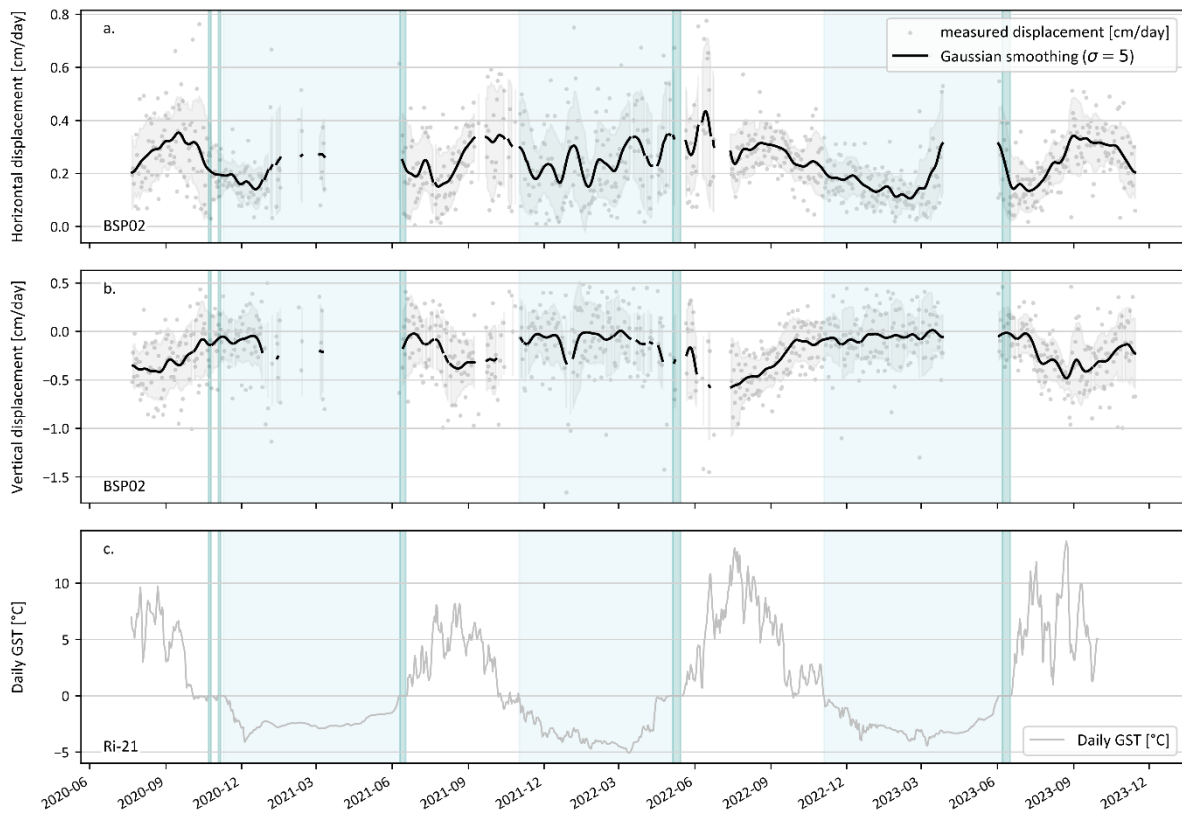


Figure 4.18 : Daily horizontal and vertical surface displacement measured by the permanent dGNSS BSP-02 (a) and (b), respectively. Daily ground surface temperature measured by the logger UTL-21 (Ri-21) (c). The light blue shaded area represents the period when ground surface temperatures are below 0°C for at least 15 days. The dark blue shaded area represents of the zero-curtain period. Discontinuities in the dGNSS data are explained by data gaps caused by the burial of the station by snow or other technical issues in data transfer.

5 Synthesis

Being at the interface between the fields of glaciology, geomorphology, hydrology, paleoclimatology and natural hazard assessment, environments and their associated landforms subject to glacier-permafrost interactions and interrelations reach beyond clear and linear research frontiers. Throughout this thesis, we have underlined the complexity and non-linearity of the processes taking place in these complex interconnected systems. This thesis revolved on the analysis and interpretation of a rich dataset essentially comprising of geodetic, geophysical, and ground surface temperature data, but also direct field observations. This dataset appeared to be essential in creating clarity towards a better understanding of the factors and processes involved in driving the dynamics of complex geomorphological systems where glacier-permafrost interactions occurred or still occur, and to better interpret their climatic, hydrological, and geomorphological significance. This chapter proposes a discussion of the approach on which this thesis was based, as well as the principal findings that emerged from it in a context of process understanding, providing a synoptic overview supported by the current state of knowledge on environments and their associated landforms subject to glacier-permafrost interactions and interrelations.

5.1 Methodological approach

To overcome the shortcomings in the interpretation of observations and results that arise when techniques are applied separately, as each individual method is often ambiguous in determining environmental properties and process understanding, this thesis privileges a multi-method and interdisciplinary approach. This allows for the most comprehensive and holistic understanding of the driving processes contributing to the dynamics of environments and their associated landforms, which are subject to glacier-permafrost interactions and interrelations. The combined analysis of datasets from different methods can nevertheless be a challenging endeavour as a thorough understanding of each individual method, as well as the geomorphological context in which these methods are applied is necessary in order to interpret them to their full potential.

The core results stemming from this thesis are derived from the combined use of geophysical and geodetic techniques as well as ground surface temperature data. More importantly, the approach chosen provided valuable insights on the processes occurring at different spatial and temporal scales within these systems.

The use of terrestrial geodetic surveys (annual¹, seasonal², and continuous³), UAV surveys³, and historical aerial imagery⁴ enabled an in-depth, of both high-temporal and high-spatial resolution, analysis of the general kinematic behaviour of the investigated sites. In general, the large temporal and spatial coverage of the sites constituted key information for the understanding of the processes involved in the kinematic behaviour of the investigated landforms. Moreover, when

¹ Aget, from 2001 to 2020 (continuing annual monitoring)

² Ritord, from 2019 to 2023 and Gruben, from 2012 to 2023 (continuing seasonal monitoring)

³ Ritord, from 2020 to 2023 and Gruben, from 2022 to 2023

⁴ Ritord, from 1961 to 2005

analysed together, the geodetic datasets were quantitatively comparable, providing confidence to their robustness and reliability (Vivero et al., 2022; Wee et al., in prep.). Very high-resolution datasets (e.g. UAV-derived orthoimages and DEMs) have the advantage to be resampled to match the resolution of the historical aerial images. Despite the large spatial coverage provided by both UAV-derived and historical aerial images, the selection of ground control points can be a challenging processing step, in particular in high-mountain environments where stable ground surfaces are limited. At the higher temporal resolution, but limited spatial coverage, permanent GNSS stations provided a continuous (hourly but aggregated to daily) coverage of local coordinates (Cicoira et al., 2022; Wirz et al., 2016). The interpretation of such datasets can be delicate, as it is important to be able to distinguish kinematic signals from noise in the data, in particular at short time scales.

The application of different geophysical techniques allowed the assessment of the internal structure of the investigated landforms, thereby facilitating an improvement of our comprehension of the impact of polythermal alpine glaciers on perennially frozen sediment accumulations. The repetition of historical geoelectrical surveys at Aget and Ritord enabled to capture the evolution of resistivity values along a one-dimensional profile. The comparable shape of the resistivity curves between the initial and repeated measurements provided confidence in the robustness of the datasets. However, the positioning of the repeated profiles in the context of a changing terrain (e.g. modification of the microtopography due to surface displacements) in which the measurements were carried out can influence the measured data and thus compromise the comparison and interpretation of the datasets over time. Electrode contact resistances may vary over time, and thus consistent and reliable estimations of changes in geophysical properties may be hampered. Complementary geophysical surveys provided a more comprehensive image of the subsurface. The heterogeneity of subsurface characteristics and properties facilitated – to a certain extent – the interpretation of the different geophysical signatures of ice in relation to their properties and origins. At Ritord and Gruben, electrical resistivity tomography measurements were conducted on the debris-covered glaciers as a reference for glacier ice resistivity values in order to better constrain the interpretation of the tomograms of the landforms subject to glacier-permafrost interactions. In a similar vein, ground penetrating radar was deployed at Ritord on a glaciectonized frozen landform and on the debris-covered glacier tongue. Despite the ability of solving some of the shortcomings of each method when analysed alone, the joint analysis of complementary geophysical datasets can still present inherent ambiguities as they remain projected modelled distribution of the geophysical properties of the subsurface and necessitate an interpretation of the physical properties of interest (such as ice content) or the nature of the layer boundary.

Despite providing valuable insights and addressing knowledge gaps regarding the processes involved in the dynamics of environments and their associated landforms subject to glacier-permafrost interactions, the approach employed in this thesis has limitations in terms of capturing and understanding the influence of embedded glacier ice within permafrost on the thermal regime of the latter in relation to energy exchanges and thermodynamics. To fulfil this knowledge gap, in-situ ground temperature measurements and deformation data from inclinometer readings (e.g. both from borehole instrumentation) would not only refine the interpretations yielded from geophysical and geodetic datasets, but also provide insights on the impact of buried glacier ice on permafrost creep dynamics.

5.2 Main system components and their associated dynamics

This thesis provides a detailed analysis of the structure and dynamics of Little Ice Age glacier forefields in mountain permafrost environments, focusing on the spatial distribution and post-LIA evolution of their component landforms (Figure 5.1). Based on multi-method investigations across three case-study sites and literature review, systematic features and processes that characterize these complex systems were identified.

A key finding is the consistent presence of glacitected frozen landforms at the margins of LIA glacier forefields. These landforms, expressed as push moraines, reflect past interactions between polythermal glacier advances and pre-existing perennially frozen ground. This suggests that frozen sediment accumulations, possibly rock glaciers, were already present prior to the LIA. The stress exerted by polythermal glacier advances allowed the partial displacement of pre-existing perennially frozen sediment accumulations further towards the margins of their forefields (Bosson et al., 2015; Kunz et al., 2022; Monnier et al., 2014; Ribolini et al., 2010; Serrano and Martín-Moreno, 2018). The former glacier-permafrost interaction phase not only altered the spatial distribution of ground ice and ground surface thermal regime of the investigated landform through the direct material contact with its thermal coupling and mass exchange, but also induced geometrical deformations (changes in the topographic conditions) with related changes in stress transmission and stress fields. Following glacier retreat, back-creeping dynamics tend to dominate these former glacier-permafrost contact zones. This behavior reflects a geometric readjustment to the release of glacial stress, as the landforms gradually re-equilibrate under the combined influence of gravitational and thermal processes. The post-glacial evolution of these landforms is strongly seasonal, partly driven by variations in ground surface temperature. During the summer, vertical displacement intensifies due to the melt of embedded glacier ice, while in winter, surface lowering continues at a slower rate due to sustained viscous permafrost creep. In this colder phase, elevation loss is mainly due to downslope creep toward topographical thalwegs, illustrating how both thermal and mechanical processes contribute to long-term deformation.

Glaciers are still present at Ritord and Gruben in the form of debris-covered glacier tongues and debris-free accumulation areas, the latter occurring only at Gruben. The extensive debris cover on these glacier surfaces can be attributed to the limited efficiency of glacial and fluvio-glacial processes in evacuating sediment in small glacier systems (Maisch et al., 1999). At the termini of these debris-covered glaciers, surface displacement rates decrease markedly due to the reduction in driving stress, which may also contribute to downstream sediment accumulation. Despite clear signs of downwasting, the debris cover plays a critical role in moderating the magnitude of melt rates. In particular, the thickness of the debris layer is a key factor: while thin debris layers can enhance melt by promoting heat transfer to the underlying ice, a sufficiently thick debris cover acts as an insulator and significantly reduces ablation (Reid et al., 2012). This thermal buffering effect explains why coarse and thick debris-laden glacier ice generally melts more slowly than bare-ice surfaces, as near-surface heat is dissipated into the atmosphere before reaching the ice (Nicholson and Benn, 2006; Rounce et al., 2015).

Glacier forefield-connected intact rock glaciers were observed at the margins of the glacier forefields, where surface elevation loss is predominantly governed by internal continuous creep deformation. This process is expressed by relatively constant displacement rates throughout the

year, with only minor seasonal variations. Slight accelerations occur in early summer and early autumn, while modest deceleration is observed during the winter, reflecting seasonal fluctuations in unfrozen water content that influence internal deformation processes. With ongoing climate warming, increasing ground water content, and enhanced creep rates, important structural changes can occur within the rock glacier body. As permafrost degradation progresses (Mollaret et al., 2019b; Noetzli et al., 2024), thermal mechanisms become progressively less dominant, and hydro-mechanical processes begin to govern short-term dynamic variations (Cicoira et al., 2021). Ultimately, these processes may drive the transition of intact active rock glaciers toward an inactive state (Wee and Delaloye, 2022), highlighting a critical phase in the long-term evolution of rock glaciers under changing climatic conditions.

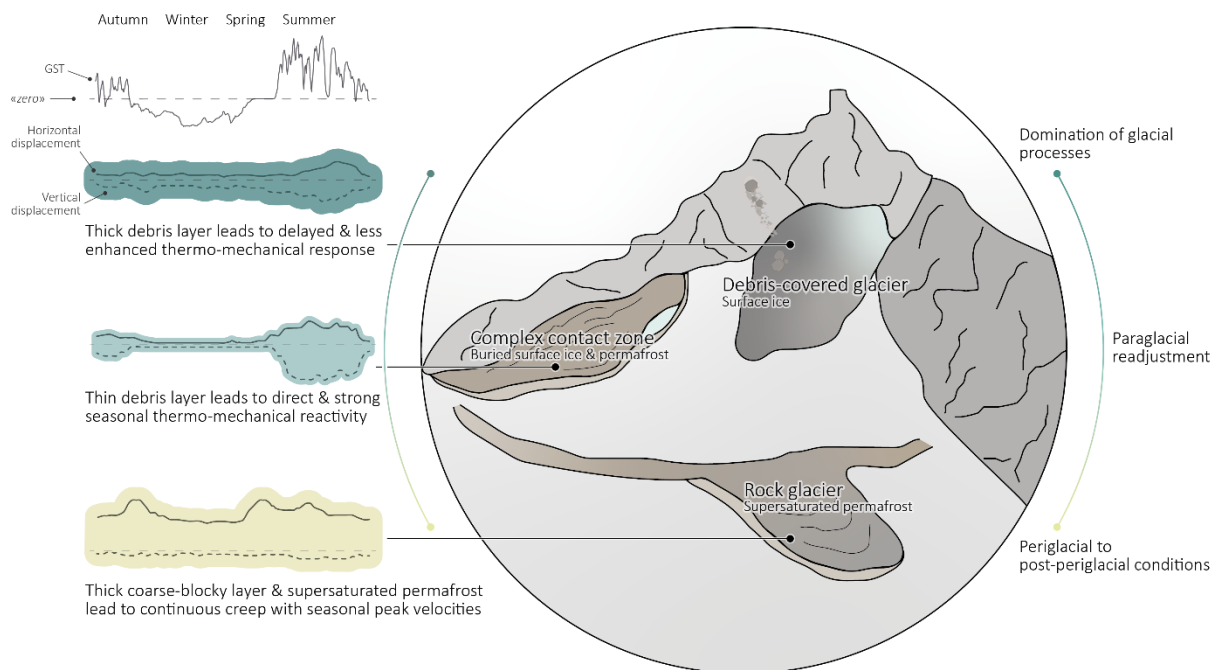


Figure 5.1: Main components of Little Ice Age glacier forefield systems. *The schematic diagram illustrates the contrasting dynamics of the key landforms across different timescales. The right panel depicts the seasonal behavior of the main landforms identified in glacier forefields (debris-covered glaciers, push-moraines, and intact rock glaciers), considering ground ice properties and surface morphology. The left panel represents their long-term evolution in response to a warming climate, highlighting shifts in activity.*

5.3 Internal structure and dynamics

The following sub-chapters provide a synthetic description and discussion of the internal structure of the investigated landforms and its influence on their respective dynamics in relation to different temporal scales.

5.3.1 Glacitected perennally frozen landforms (push-moraines)

Early studies have primarily concentrated on examining thermal conditions and permafrost occurrences in recently exposed glacier forefields situated within the mountain permafrost zone of the Alps (Kneisel, 2003; Reynard et al., 2003). These involved the application of geomorphological mapping, ground surface temperature measurements, and geophysical soundings. The latter largely contributed to address the characterization of the internal structure of the glacitected perennally frozen landforms within these systems. Results from the very few existing studies revealed the presence of sporadic lenticular highly resistive frozen bodies, often found in the proximal side of the investigated landforms (Cusicanqui et al., 2023; Delaloye, 2004; Kunz et al., 2022; Kunz and Kneisel, 2020; Reynard et al., 2003; Ribolini et al., 2010). The geophysical investigations carried out in the scope of this thesis allowed to refine the two-dimensional characterization of the ground ice content at the study sites, from which similar observations were found. Delineated by resistivities often exceeding MΩm ranges, these lenticular subsurface structures point to embedded cold ice of glacial origin. Their spatial extent, depending on various factors varied from one landform to another. For instance, the size, the exerted glacial stress, and consequent extent and imprint of the interacting glacier onto the pre-existing perennally frozen sediment accumulation can potentially influence the distribution of glacier ice masses within the landform. Furthermore, the varying thermal regimes, which are specific to each landform configuration and geomorphological characteristics, can induce different rates of thermal degradation of ground ice.

For instance, the geophysical and ground surface thermal signature observed at Aget suggests that the contact between the glacial ice and permafrost favoured a modified thermal regime of the latter, leading to its advanced thermal degradation. This was also observed in the uppermost section of the former glacier-permafrost contact zone at Gruben. It is likely that the thermal degradation of permafrost could have been induced by the melting of embedded thinner glacier ice lenses due to the thermal energy released by meltwater. Whereas, where glacier ice lenses are more massive, more energy is needed to melt the ice, and the thermal properties of the cold glacier ice bodies contribute to maintaining ice-rich cold permafrost conditions. While in the areas of the landforms that were not directly affected by an interaction with glacier ice, the thermal conditions of permafrost are mainly driven by thermal processes occurring between the atmosphere and the active layer. In addition, it cannot be excluded that embedded glacier ice lenses can impact the thermal regime of *intact* permafrost through lateral energy exchanges.

A clear relation between the internal structure of glacitected frozen landforms and the associated physical processes contributing to surface dynamics was established. It was systematically revealed that enhanced vertical changes occurred in zones underlain by what we interpreted as glacier ice lenses. The observed kinematic behaviour was attributed to thermally-driven ice melt-induced subsidence, given the sensitivity of the phenomenon to air and ground

surface temperature conditions (Figure 5.2). The thickness of the debris layer can likely be considered as a driver of this thermo-mechanical process. In the case of Aget, it was inferred that parts of an ice lens were completely melted during the observation period as the absence of vertical changes was revealed since 2017 in one zone of the GFL. In areas where no glacier ice lenses were detected, surface changes were found to be mainly driven by permafrost creep deformation, and surface elevation changes were attributed to surface flow patterns and seasonal permafrost thaw. In the zones affected by past glacier-permafrost interactions, a back-creeping behaviour was systematically observed, which infers a post-glacial mechanical adjustment to the geometrical deformations and related changes in stress transmission and stress fields induced by the glacier. However, the magnitude of the back-creeping behaviour is highly dependent of the landform's geometry and the extent of the spatial scale at which the pressure of the glacier was transmitted onto the frozen sediment accumulation.

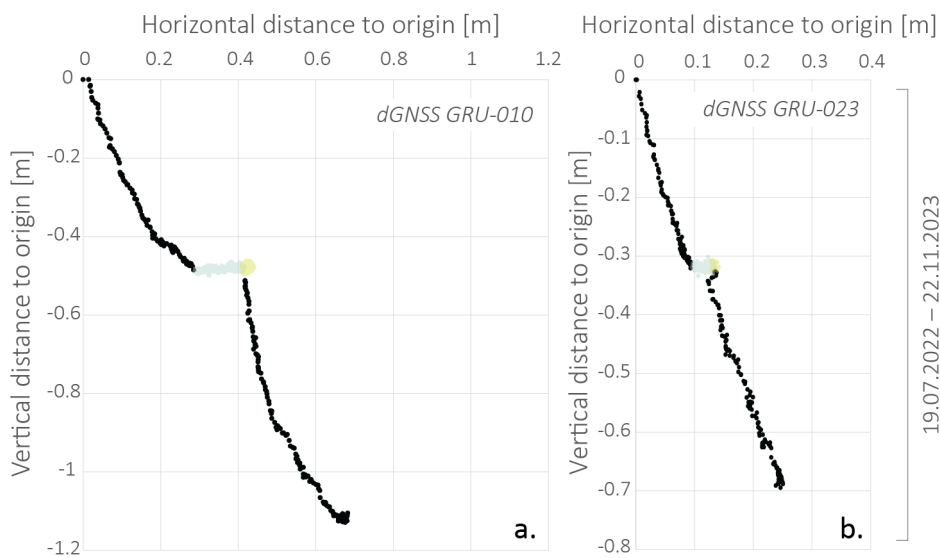


Figure 5.2 : Displacement profiles at the Gruben field site showing relative daily positions measured by permanent dGNSS stations Gru-010 (a) and Gru-023 (b) for the period 19.07.2022 to 22.11.2023. The blue points refer to positions measured during negative ground surface temperatures and the green points refer to positions measured during the zero-curtain period.

5.3.2 Debris-covered glaciers

The characterization of the internal structure of the debris-covered glaciers adjacent to the glacier-affected perennally frozen sediment was investigated with the aim to better constrain our understanding of the kinematic and thermal processes within the glacier forefield systems of Ritord and Gruben. The results from ground penetrating radar measurements conducted on the partly disconnected debris-covered tongue of the *Epée* glacier (in Ritord) indicated the presence of a cold thermal regime. Furthermore, the temperature measurements conducted by Haeberli (1976) on the Gruben glacier also demonstrated the glacier's cold thermal regime. These observations corroborate with observations of glacier systems in similar geographical contexts (Bosson, 2016; Gilbert et al., 2012). The thermal regime of polythermal glaciers in permafrost environments (i.e. cold in their margins and temperate in the centre), likely contributes to their

resilience to the current warming climate, despite their continuing drastic down-wasting. Moreover, their debris-cover thickness is sufficient to reduce the ablation rate of the stagnant terminus part, as near-surface heat transfer is dissipated into the atmosphere before being transferred to the underlying ice surface (Nicholson and Benn, 2006; Rounce et al., 2015). The geoelectrical measurements conducted on the Gruben glacier allowed to estimate its debris-cover thickness to roughly 2-3 m, while ground penetrating radar measurements conducted at Ritord, as well as field observations infer a debris-cover thickness of 1 m. Moreover, lateral outcrops of ice confirm the latter estimation. This difference in debris-cover thickness strongly influences the energy exchanges between the atmosphere and the ice, and consequently ice melt. Continuous geodetic measurements on both debris-covered glaciers enabled to show their varying sensitivity. Similarly to observations made on the Gruben complex contact zone, which is underlain by glacier ice lenses, the kinematic response of the Epée debris-covered glacier to ground surface temperature changes is highly sensitive and ice melt is interrupted as soon as temperatures are negative. Whereas the kinematic signal observed on the Gruben debris-covered glacier indicates a thermal lag, which may be partly attributed to the time for the temperature signal to propagate from the surface to the ice. Moreover, surface displacement rates decrease significantly towards the glacier terminus (Figure 5.3), which can be explained by the reduced driving stress in this area (Cuffey and Paterson, 2010). This effect may be enhanced by the downstream accumulation of sediments.

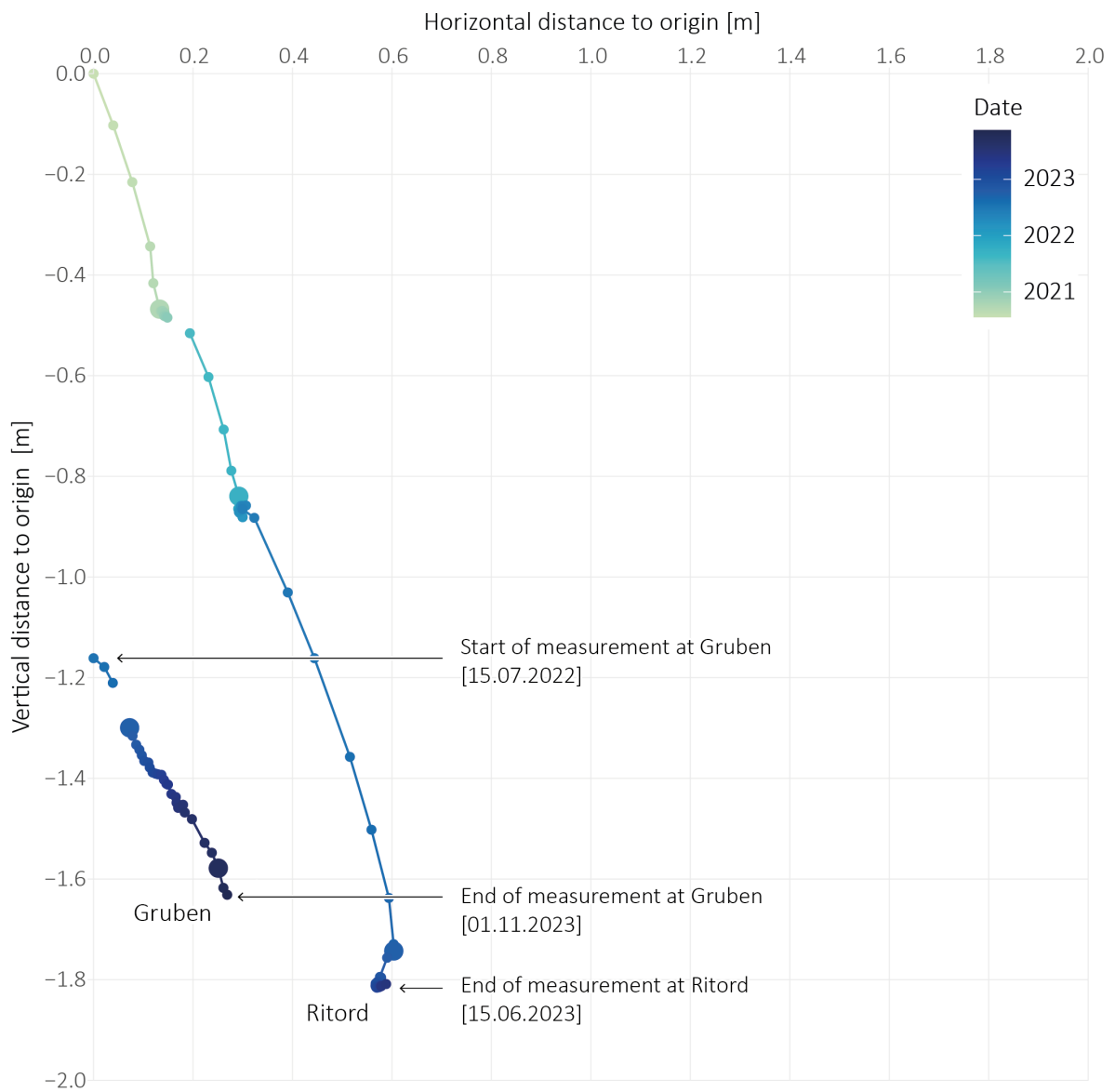


Figure 5.3 : Displacement profiles show relative bi-monthly (15-day interval) positions recorded by permanent dGNSS stations on the debris-covered glaciers of Ritord (20.07.2020–15.06.2023) and Gruben (15.07.2022–01.11.2023). Larger dots indicate the start of each hydrological year (01.10.).

6 Conclusions and outlook

This chapter provides a comprehensive overview of the main research findings of this thesis. It also offers insights into potential avenues for future research on glacier-permafrost interactions, thereby concluding the first part of this thesis, stemming from the work presented in the second part.

6.1 Conclusions

This thesis stemmed from the motivation to foster a better understanding of the morphodynamical response of environments and their associated landforms subject to glacier-permafrost interactions under a transitioning climate and their evolution across different timescales and spatial extents. To this overarching aim, three research questions were addressed within this thesis that allowed the continuation and further development of research on glacier-permafrost interactions in the Alps. A first objective of this thesis was to have a general understanding of the spatial configuration and context in which these systems were found. This was reached with (i) the establishment of non-exhaustive inventory of LIA glacier forefields where kinematically active viscous-creep landforms subject to glacier-permafrost interactions were found, (ii) the characterization of the subsurface geophysical properties at three sites, and (iii) the quantification of ground ice content at one site. A second objective was to gain insights on the influence of subsurface properties on surface changes at different temporal and spatial scales. This was reached with the integrative analysis of a rich and unique long-term time series of geodetic, temperature and geophysical datasets at three different sites in order to estimate the driving processes contributing to surface changes.

The main findings of this thesis can be briefly summarised as follows:

- In this thesis, we gathered and analysed over twenty years of data collected on the Aget glacier forefield, particularly focussing on its actively back-creeping glaciectonized frozen landform (GFL) to understand its recent morphodynamical evolution. Together with geodetic measurements performed on a yearly basis, the geoelectrical surveys carried out in 1998 and repeated in 2017 allowed us to assess the evolution of ground ice within the GFL and its kinematic evolution. *Publication 1* highlights the heterogeneous distribution of the ground ice content throughout the GFL as well as the nonuniform geometrical behaviour of the landform. Climatic signals are highlighted in both the long-term kinematic changes and resistivity changes. The comparison between the historic and repeated geoelectrical surveys revealed a systematic yet varying decrease of measured apparent resistivity of the frozen ground over a nearly twenty-year period, indicating a heterogeneous degradation of permafrost and melt of ground ice in response to increasing ground surface temperatures. Subsidence induced by the melt of excessive ice at the permafrost table was found. In the central zone of the GLF, surface elevation loss appeared to have been mainly the result of a decrease in the thickness of the moving mass due to its extensive flow pattern. Together, these processes contribute to a decrease of the stresses at the shear horizon, progressively driving the landform towards a less dynamic, transitional state of kinematic activity.

- The main findings of this thesis revolve around the application of a multi-method approach which provided new insights on ongoing intra-annual dynamics of the complex ice-rich landforms systems in the Gruben glacier forefield. *Publication II* highlights the relation between the internal structure of the investigated landforms with their physical processes and associated surface dynamics. The magnitude of ice melt-induced subsidence was the greatest where glacier-permafrost interactions occurred, a zone in which isolated remnants of buried surface ice were identified by geophysical investigations. The thickness of the coarse debris layer and the properties of ground ice were found to exert a significant influence on the kinematic response to air and ground temperature changes, with an instant response time. While towards the frontal zone of this glacier forefield-connected rock glacier, where the active layer thickness is greater, permafrost creep deformation, accompanied with seasonal thermal-lag signals was observed. The kinematic signature of these two distinct morphological zones is proof of their geomorphological heritage from the Holocene and LIA and highlights the interrelation between glacial and periglacial processes occurring in the so-called complex contact zone. This underlines the complexity of capturing a complete and thorough understanding of the driving processes contributing to the morphodynamical evolution of such systems. This study also revealed the resilience of the ground ice to a warming atmosphere, in particular in the permafrost of the rock glacier. This was also found for the glacier ice beneath the thickening debris-cover of the Gruben glacier terminus, which is in complete disequilibrium with the current climate.
- The combination of historical and recent high-resolution datasets allowed the analysis of the multi-decadal evolution of the Ritord glacier forefield and of its components across varying temporal and spatial scales in relation to corresponding climatic context. *Publication III* highlights the complexity and heterogeneity of ground ice content and origin within this system, and its varying degrees of sensitivity to the current warming trend.

6.2 Outlook

The research conducted in the scope of this thesis allowed to answer the three main research questions, but also allowed further questions to be raised on the interactions between glaciers and permafrost, and their dynamics. To overcome the remaining open questions and challenges on our understanding of glacier-permafrost interactions and their derived landforms, future studies could address the following research paths:

- Apply and further develop finite-element modelling (FEM) of rock glacier deformation approach by Frehner et al. (2015) to the context of glaciotectonics to better understand the influence of glacier-induced stresses on frozen materials.
- Extend the analysis at the regional scale, but also to other regions worldwide through the use of remote sensing approaches.
- Collect and analyse in-situ information on sites with a similar context to better characterize and develop a detailed typology of the various existing spatial configurations of systems where glacier-permafrost interactions occurred (or still occur).

- Develop a model simulating the thermo-hydro-mechanical evolution of these systems (or perennally frozen creeping landforms in general) in relation to their dynamic response to climate forcing.
- Address the role of ice melt-induced subsidence (input of meltwater and deepening of the active layer) on the energy exchanges within ice-rich permafrost conditions and its influence on the evolution of the thermodynamic regime.
- Pursue the inventorying efforts to better characterize glaciectonized perennally frozen landforms.

7 References

- Amschwand, D., Wicky, J., Scherler, M., Hoelzle, M., Krummenacher, B., Haberkorn, A., Kienholz, C., and Gubler, H.: Sub-surface processes and heat fluxes at coarse-blocky Murtèl rock glacier (Engadine, eastern Swiss Alps), *EGUsphere*, 1–47, <https://doi.org/10.5194/egusphere-2024-172>, 2024.
- Archie, G. E.: The Electrical Resistivity Log as an Aid in Determining Some Reservoir Characteristics, *Trans. AIME*, 146, 54–62, <https://doi.org/10.2118/942054-G>, 1942.
- Arenson, L., Hoelzle, M., and Springman, S.: Borehole deformation measurements and internal structure of some rock glaciers in Switzerland, *Permafr. Periglac. Process.*, 13, 117–135, <https://doi.org/10.1002/ppp.414>, 2002.
- Arenson, L. U. and Springman, S. M.: Mathematical descriptions for the behaviour of ice-rich frozen soils at temperatures close to 0 °C, *Can. Geotech. J.*, 42, 431–442, <https://doi.org/10.1139/t04-109>, 2005.
- Arenson, L. U., Harrington, J. S., Koenig, C. E. M., and Wainstein, P. A.: Mountain Permafrost Hydrology—A Practical Review Following Studies from the Andes, *Geosciences*, 12, 48, <https://doi.org/10.3390/geosciences12020048>, 2022.
- Aschwanden, A. and Blatter, H.: Meltwater production due to strain heating in Storglaciären, Sweden, *J. Geophys. Res. Earth Surf.*, <https://doi.org/10.1029/2005JF000328>, 2005.
- Azócar, G. F. and Brenning, A.: Hydrological and geomorphological significance of rock glaciers in the dry Andes, Chile (27°–33°S), *Permafr. Periglac. Process.*, 21, 42–53, <https://doi.org/10.1002/ppp.669>, 2010.
- Ballantyne, C. K.: *Periglacial Geomorphology*, John Wiley & Sons, 496 pp., 2018.
- Barboux, C., Delaloye, R., and Lambiel, C.: Inventorying slope movements in an Alpine environment using DInSAR: INVENTORYING OF SLOPE MOVEMENTS IN ALPINE ENVIRONMENT USING DInSAR, *Earth Surf. Process. Landf.*, 39, 2087–2099, <https://doi.org/10.1002/esp.3603>, 2014.
- Barsch, D.: Permafrost creep and rockglaciers, *Permafr. Periglac. Process.*, 3, 175–188, <https://doi.org/10.1002/ppp.3430030303>, 1992.
- Bersier, A.: *Les collines de Noville-Chessel, crêtes de poussée glaciaire*, Université, Faculté des sciences, 1954.
- Boeckli, L., Brenning, A., Gruber, S., and Noetzli, J.: Permafrost distribution in the European Alps: calculation and evaluation of an index map and summary statistics, *The Cryosphere*, 6, 807–820, 2012.
- Bosson, J.-B.: *Internal structure, dynamics and genesis of small debris covered glacier systems located in alpine permafrost environments*, University of Lausanne, 2016.

Bosson, J.-B. and Lambiel, C.: Internal Structure and Current Evolution of Very Small Debris-Covered Glacier Systems Located in Alpine Permafrost Environments, *Front. Earth Sci.*, 4, <https://doi.org/10.3389/feart.2016.00039>, 2016.

Bosson, J.-B., Deline, P., Bodin, X., Schoeneich, P., Baron, L., Gardent, M., and Lambiel, C.: The influence of ground ice distribution on geomorphic dynamics since the Little Ice Age in proglacial areas of two cirque glacier systems, *Earth Surf. Process. Landf.*, 40, 666–680, <https://doi.org/10.1002/esp.3666>, 2015.

Brenning, A.: The impact of mining on rock glacier and glaciers: examples from central Chile, in: *The impact of mining on rock glacier and glaciers: examples from central Chile*, University of California Press, 196–205, <https://doi.org/10.1525/9780520934245-015>, 2008.

Buchli, T., Kos, A., Limpach, P., Merz, K., Zhou, X., and Springman, S. M.: Kinematic investigations on the Furggwanhorn Rock Glacier, Switzerland, *Permafr. Periglac. Process.*, 29, 3–20, <https://doi.org/10.1002/ppp.1968>, 2018.

Capt, M., Bosson, J.-B., Fischer, M., Micheletti, N., and Lambiel, C.: Decadal evolution of a very small heavily debris-covered glacier in an Alpine permafrost environment, *J. Glaciol.*, 62, 535–551, <https://doi.org/10.1017/jog.2016.56>, 2016.

Carlé, W.: Das innere Gefüge der Stauch-Endmoränen und seine Bedeutung für die Gliederung des Altmoränengebietes, *Geol. Rundsch.*, 29, 27–51, <https://doi.org/10.1007/BF01767841>, 1938.

Carrivick, J. L. and Heckmann, T.: Short-term geomorphological evolution of proglacial systems, *Geomorphology*, 287, 3–28, <https://doi.org/10.1016/j.geomorph.2017.01.037>, 2017.

Carrivick, J. L., Geilhausen, M., Warburton, J., Dickson, N. E., Carver, S. J., Evans, A. J., and Brown, L. E.: Contemporary geomorphological activity throughout the proglacial area of an alpine catchment, *Geomorphology*, 188, 83–95, <https://doi.org/10.1016/j.geomorph.2012.03.029>, 2013.

Carturan, L., Rastner, P., and Paul, F.: On the disequilibrium response and climate change vulnerability of the mass-balance glaciers in the Alps, *J. Glaciol.*, 66, 1034–1050, <https://doi.org/10.1017/jog.2020.71>, 2020.

Casty, C., Wanner, H., Luterbacher, J., Esper, J., and Böhm, R.: Temperature and precipitation variability in the European Alps since 1500, *Int. J. Climatol.*, 25, 1855–1880, <https://doi.org/10.1002/joc.1216>, 2005.

Cicoira, A., Beutel, J., Faillettaz, J., and Vieli, A.: Water controls the seasonal rhythm of rock glacier flow, *Earth Planet. Sci. Lett.*, 528, 115844, <https://doi.org/10.1016/j.epsl.2019.115844>, 2019.

Cicoira, A., Marcer, M., Gärtner-Roer, I., Bodin, X., Arenson, L. U., and Vieli, A.: A general theory of rock glacier creep based on in-situ and remote sensing observations, *Permafr. Periglac. Process.*, 32, 139–153, <https://doi.org/10.1002/ppp.2090>, 2021.

Cicoira, A., Weber, S., Biri, A., Buchli, B., Delaloye, R., Da Forno, R., Gärtner-Roer, I., Gruber, S., Gsell, T., Hasler, A., Lim, R., Limpach, P., Mayoraz, R., Meyer, M., Noetzli, J., Phillips, M., Pointner, E., Raetzo, H., Scapozza, C., Strozzi, T., Thiele, L., Vieli, A., Vonder Mühl, D., Wirz, V., and Beutel, J.: In situ observations of the Swiss periglacial environment using GNSS instruments, *Earth Syst. Sci. Data*, 14, 5061–5091, <https://doi.org/10.5194/essd-14-5061-2022>, 2022.

Colucci, R. and Guglielmin, M.: Precipitation–temperature changes and evolution of a small glacier in the southeastern European Alps during the last 90 years, *Int. J. Climatol.*, 35, 2783–2797, <https://doi.org/10.1002/joc.4172>, 2015.

Colucci, R. R.: Geomorphic influence on small glacier response to post-Little Ice Age climate warming: Julian Alps, Europe, *Earth Surf. Process. Landf.*, 41, 1227–1240, <https://doi.org/10.1002/esp.3908>, 2016.

Cuffey, K. and Paterson, W. S. B.: *The physics of glaciers*, 4th ed., Butterworth-Heinemann/Elsevier, Burlington, MA, 693 pp., 2010.

Cusicanqui, D., Bodin, X., Duvillard, P.-A., Schoeneich, P., Revil, A., Assier, A., Berthet, J., Peyron, M., Roudnitska, S., and Rabatel, A.: Glacier, permafrost and thermokarst interactions in Alpine terrain: Insights from seven decades of reconstructed dynamics of the Chauvet glacial and periglacial system (Southern French Alps), *Earth Surf. Process. Landf.*, 48, 2595–2612, <https://doi.org/10.1002/esp.5650>, 2023.

Delaloye, R.: Contribution à l'étude du pergélisol de montagne en zone marginale, *GeoFocus.*, University of Fribourg, Fribourg, 244 pp., 2004.

Delaloye, R., Lambiel, C., and Gärtner-Roer, I.: Overview of rock glacier kinematics research in the Swiss Alps, *Geogr. Helvetica*, 65, 135–145, <https://doi.org/10.5194/gh-65-135-2010>, 2010.

Deline, P., Gruber, S., Amann, F., Bodin, X., Delaloye, R., Failletaz, J., Fischer, L., Geertsema, M., Giardino, M., Hasler, A., Kirkbride, M., Krautblatter, M., Magnin, F., McColl, S., Ravanel, L., Schoeneich, P., and Weber, S.: Chapter 15 - Ice loss from glaciers and permafrost and related slope instability in high-mountain regions, in: *Snow and Ice-Related Hazards, Risks, and Disasters (Second Edition)*, edited by: Haeberli, W. and Whiteman, C., Elsevier, 501–540, <https://doi.org/10.1016/B978-0-12-817129-5.00015-9>, 2021.

Draebing, D.: Application of refraction seismics in alpine permafrost studies: A review, *Earth-Sci. Rev.*, 155, 136–152, <https://doi.org/10.1016/j.earscirev.2016.02.006>, 2016.

Eltner, A. and Sofia, G.: Chapter 1 - Structure from motion photogrammetric technique, in: *Developments in Earth Surface Processes*, vol. 23, edited by: Tarolli, P. and Mudd, S. M., Elsevier, 1–24, <https://doi.org/10.1016/B978-0-444-64177-9.00001-1>, 2020.

Etzel Müller, B. and Hagen, J. O.: Glacier-permafrost interaction in Arctic and alpine mountain environments with examples from southern Norway and Svalbard, *Geol. Soc. Lond. Spec. Publ.*, 242, 11–27, <https://doi.org/10.1144/GSL.SP.2005.242.01.02>, 2005.

Etzel Müller, B., Vatne, G., Ødegård, R. S., and Sollid, J. L.: Mass balance and changes of surface slope, crevasse and flow pattern of Erikbreen, northern Spitsbergen: an application of a geographical information system (GIS), *Polar Res.*, 12, 131–146, <https://doi.org/10.3402/polar.v12i2.6709>, 1993.

Evin, M.: Les relations existant entre la moraine de refoulement, le glacier rocheux et le glacier du Petit Age Glaciaire dans le Haut Vallon d'Asti (Queyras, Alpes du Sud, France), *Geogr. Fis. Dinam. Quat*, 15, 101–105, 1992.

Frehner, M., Ling, A. H. M., and Gärtner-Roer, I.: Furrow-and-Ridge Morphology on Rockglaciers Explained by Gravity-Driven Buckle Folding: A Case Study From the Murtèl Rockglacier

(Switzerland): Rockglacier Furrow-and-Ridge Morphology Explained by Buckle Folding, *Permafr. Periglac. Process.*, 26, 57–66, <https://doi.org/10.1002/ppp.1831>, 2015.

Gärtner-Roer, I. and Bast, A.: (Ground) Ice in the Proglacial Zone, in: *Geomorphology of Proglacial Systems*, Springer, 85–98, 2019.

Gärtner-Roer, I., Brunner, N., Delaloye, R., Haeblerli, W., Käab, A., and Thee, P.: Glacier–permafrost relations in a high-mountain environment: 5 decades of kinematic monitoring at the Gruben site, *Swiss Alps, The Cryosphere*, 16, 2083–2101, 2022.

Gilbert, A., Vincent, C., Wagnon, P., Thibert, E., and Rabatel, A.: The influence of snow cover thickness on the thermal regime of Tête Rousse Glacier (Mont Blanc range, 3200 m a.s.l.): Consequences for outburst flood hazards and glacier response to climate change, *J. Geophys. Res. Earth Surf.*, 117, n/a-n/a, <https://doi.org/10.1029/2011JF002258>, 2012.

Glover, P. W. J.: A generalized Archie’s law for n phases, *GEOPHYSICS*, 75, E247–E265, <https://doi.org/10.1190/1.3509781>, 2010.

González Trueba, J. J., Martín Moreno, R., Martínez de Pisón, E., and Serrano, E.: Little Ice Age glaciation and current glaciers in the Iberian Peninsula, 2008.

Grove, A. T.: A brief consideration of climate forcing factors in view of the Holocene glacier record, *Glob. Planet. Change*, 60, 141–147, <https://doi.org/10.1016/j.gloplacha.2006.07.033>, 2008.

Gruber, S.: Derivation and analysis of a high-resolution estimate of global permafrost zonation, *The Cryosphere*, 6, 221–233, <https://doi.org/10.5194/tc-6-221-2012>, 2012.

Haeblerli, W.: Eistemperaturen in den Alpen, *Z. Für Gletscherkunde Glazialgeol.*, XI/2, 203–220, 1976.

Haeblerli, W.: Holocene Push-Moraines in Alpine Permafrost, *Geogr. Ann. Ser. Phys. Geogr.*, 61, 43, <https://doi.org/10.2307/520513>, 1979.

Haeblerli, W.: Modern research perspectives relating to permafrost creep and rock glaciers: a discussion, *Permafr. Periglac. Process.*, 11, 290–293, 2000.

Haeblerli, W. and Burn, C.: Natural hazards in forests: glacier and permafrost effects as related to climate change, *Environ. Change Geomorphic Hazards For.*, 9, <https://doi.org/10.1079/9780851995984.0167>, 2002.

Haeblerli, W. and Gruber, S.: Global Warming and Mountain Permafrost, in: *Permafrost Soils*, vol. 16, edited by: Margesin, R., Springer Berlin Heidelberg, Berlin, Heidelberg, 205–218, https://doi.org/10.1007/978-3-540-69371-0_14, 2009.

Haeblerli, W. and Röthlisberger, H.: Beobachtungen zum Mechanismus und zu den Auswirkungen von Kalbungen am Gruebengletscher (Saastal, Schweiz), *Z. Für Gletscherkunde Glazialgeol.*, 11, 221–228, 1976.

Haeblerli, W. and Vonder Mühl, D.: On the characteristics and possible origins of ice in rock glacier permafrost, *Z. Für Geomorphol. Suppl.*, 43–57, 1996.

Haeblerli, W., Huder, J., Keusen, H., and Pika, J.: Core drilling through rock glacier permafrost, 2, 1988.

Haerberli, W., Hallet, B., Arenson, L., Elconin, R., Humlum, O., Käab, A., Kaufmann, V., Ladanyi, B., Matsuoka, N., Springman, S., and Mühl, D. V.: Permafrost creep and rock glacier dynamics, *Permafr. Periglac. Process.*, 17, 189–214, <https://doi.org/10.1002/ppp.561>, 2006.

Haerberli, W., Arenson, L. U., Wee, J., Hauck, C., and Mölg, N.: Discriminating viscous creep features (rock glaciers) in mountain permafrost from debris-covered glaciers – a commented test at the Gruben and Yerba Loca sites, Swiss Alps and Chilean Andes, *The Cryosphere*, <https://doi.org/10.5194/egusphere-2023-1191>, 2024a.

Haerberli, W., Arenson, L. U., Wee, J., Hauck, C., and Mölg, N.: Discriminating viscous-creep features (rock glaciers) in mountain permafrost from debris-covered glaciers – a commented test at the Gruben and Yerba Loca sites, Swiss Alps and Chilean Andes, *The Cryosphere*, 18, 1669–1683, <https://doi.org/10.5194/tc-18-1669-2024>, 2024b.

Halla, C., Blöthe, J. H., Tapia Baldis, C., Trombotto Liaudat, D., Hilbich, C., Hauck, C., and Schrott, L.: Ice content and interannual water storage changes of an active rock glacier in the dry Andes of Argentina, *The Cryosphere*, 15, 1187–1213, <https://doi.org/10.5194/tc-15-1187-2021>, 2021.

Harris, S. A. and Permafrost Subcommittee, Associate Committee on Geotechnical Research, National Research Council of Canada (Eds.): *Glossary of permafrost and related ground-ice terms*, Ottawa, Ontario, Canada, 156 pp., 1988.

Hauck, C.: *Geophysical methods for detecting permafrost in high mountains*, Doctoral Thesis, ETH Zurich, <https://doi.org/10.3929/ethz-a-004172478>, 2001.

Hauck, C. and Kneisel, C.: *Applied geophysics in periglacial environments*, Cambridge University Press, 2008.

Hauck, C. and Vonder Mühl, D.: Inversion and interpretation of two-dimensional geoelectrical measurements for detecting permafrost in mountainous regions, *Permafr. Periglac. Process.*, 14, 305–318, <https://doi.org/10.1002/ppp.462>, 2003.

Hauck, C., Böttcher, M., and Maurer, H.: A new model for estimating subsurface ice content based on combined electrical and seismic data sets, *The Cryosphere*, 5, 453–468, <https://doi.org/10.5194/tc-5-453-2011>, 2011.

Helfricht, K., Lehning, M., Sailer, R., and Kuhn, M.: Local extremes in the lidar-derived snow cover of alpine glaciers, *Geogr. Ann. Ser. Phys. Geogr.*, 97, 721–736, <https://doi.org/10.1111/geoa.12111>, 2015.

Herring, T., Lewkowicz, A. G., Hauck, C., Hilbich, C., Mollaret, C., Oldenborger, G. A., Uhlemann, S., Farzamian, M., Calmels, F., and Scandroglio, R.: Best practices for using electrical resistivity tomography to investigate permafrost, *Permafr. Periglac. Process.*, 34, 494–512, <https://doi.org/10.1002/ppp.2207>, 2023.

Hilbich, C.: Time-lapse refraction seismic tomography for the detection of ground ice degradation, *The Cryosphere*, 4, 243–259, <https://doi.org/10.5194/tc-4-243-2010>, 2010.

Hock, R., Rasul, G., Adler, C., Cáceres, B., Gruber, S., Hirabayashi, Y., Jackson, M., Käab, A., Kang, S., Kutuzov, S., Milner, A., Molau, U., Morin, S., Orlove, B., and Steltzer, H.: High Mountain Areas, in: *IPCC special report on the ocean and cryosphere in a changing climate*, edited by: Pörtner, H.-O., Roberts, D. C., Masson-Delmotte, V., Tignor, M., Poloczanska, E., Mintenbeck, K., Alegria, A.,

Nicolai, M., Okem, A., Petzold, J., Rama, B., and Weyer, N. M., Cambridge University Press, Cambridge, 131–202, <https://doi.org/10.1017/9781009157964.004>, 2019.

Hoelzle, M., Mittaz, C., Etzelmüller, B., and Haeberli, W.: Surface energy fluxes and distribution models of permafrost in European mountain areas: an overview of current developments: Surface Energy Fluxes, *Permafr. Periglac. Process.*, 12, 53–68, <https://doi.org/10.1002/ppp.385>, 2001.

Hopkins, O. B.: Some Structural Features of the Plains Area of Alberta Caused by Pleistocene Glaciation, *GSA Bull.*, 34, 419–430, <https://doi.org/10.1130/GSAB-34-419>, 1923.

Hoppe, G. and Schytt, F.: Some Observations on Fluted Moraine Surfaces, 12, 1953.

Hugonnet, R., McNabb, R., Berthier, E., Menounos, B., Nuth, C., Girod, L., Farinotti, D., Huss, M., Dussailant, I., Brun, F., and Käab, A.: Accelerated global glacier mass loss in the early twenty-first century, *Nature*, 592, 726–731, <https://doi.org/10.1038/s41586-021-03436-z>, 2021.

Huss, M. and Fischer, M.: Sensitivity of Very Small Glaciers in the Swiss Alps to Future Climate Change, *Front. Earth Sci.*, 4, <https://doi.org/10.3389/feart.2016.00034>, 2016.

Ikeda, A., Matsuoka, N., and Käab, A.: Fast deformation of perennially frozen debris in a warm rock glacier in the Swiss Alps: An effect of liquid water, *J. Geophys. Res.*, 113, <https://doi.org/10.1029/2007JF000859>, 2008.

IPA Action Group RGIK: Guidelines for inventorying rock glaciers, <https://doi.org/10.51363/unifr.srr.2023.002>, 2023.

Irvine-Fynn, T. D. L., Hodson, A. J., Moorman, B. J., Vatne, G., and Hubbard, A. L.: Polythermal Glacier Hydrology: A Review, *Rev. Geophys.*, 49, <https://doi.org/10.1029/2010RG000350>, 2011.

Ivy-Ochs, S., Kerschner, H., Maisch, M., Christl, M., Kubik, P. W., and Schlüchter, C.: Latest Pleistocene and Holocene glacier variations in the European Alps, *Quat. Sci. Rev.*, 28, 2137–2149, <https://doi.org/10.1016/j.quascirev.2009.03.009>, 2009.

Käab, A.: PERMAFROST AND PERIGLACIAL FEATURES | Rock Glaciers and Protalus Forms, in: *Encyclopedia of Quaternary Science (Second Edition)*, edited by: Elias, S. A. and Mock, C. J., Elsevier, Amsterdam, 535–541, <https://doi.org/10.1016/B978-0-444-53643-3.00104-7>, 2013.

Käab, A. and Haeberli, W.: Evolution of a High-Mountain Thermokarst Lake in the Swiss Alps, *Arct. Antarct. Alp. Res.*, 33, 385–390, <https://doi.org/10.1080/15230430.2001.12003445>, 2001.

Käab, A., Haeberli, W., and Gudmundsson, G. H.: Analysing the creep of mountain permafrost using high precision aerial photogrammetry: 25 years of monitoring Gruben rock glacier, Swiss Alps, *Permafr. Periglac. Process.*, 8, 409–426, [https://doi.org/10.1002/\(SICI\)1099-1530\(199710/12\)8:4<409::AID-PPP267>3.0.CO;2-C](https://doi.org/10.1002/(SICI)1099-1530(199710/12)8:4<409::AID-PPP267>3.0.CO;2-C), 1997.

Käab, A., Frauenfelder, R., and Roer, I.: On the response of rockglacier creep to surface temperature increase, *Glob. Planet. Change*, 56, 172–187, <https://doi.org/10.1016/j.gloplacha.2006.07.005>, 2007.

Kälin, M.: The active push moraine of the Thompson Glacier, Axel Heiberg Island, Canadian Arctic Archipelago, Canada, Doctoral Thesis, ETH Zurich, <https://doi.org/10.3929/ethz-a-000088589>, 1971.

Keller, F., Frauenfelder, R., JM, G., Hoelzle, M., Kneisel, C., Lugon, R., Phillips, M., Reynard, E., and Wenker, L.: Permafrost map of Switzerland, 57, 1998.

Kellerer-Pirklbauer, A., Bodin, X., Delaloye, R., Lambiel, C., Gärtner-Roer, I., Bonnefoy-Demongeot, M., Carturan, L., Damm, B., Eulenstein, J., Fischer, A., Hartl, L., Ikeda, A., Kaufmann, V., Krainer, K., Matsuoka, N., Cella, U. M. D., Noetzli, J., Seppi, R., Scapozza, C., Schoeneich, P., Stocker-Waldhuber, M., Thibert, E., and Zumiani, M.: Acceleration and interannual variability of creep rates in mountain permafrost landforms (rock glacier velocities) in the European Alps in 1995–2022, *Environ. Res. Lett.*, 19, 034022, <https://doi.org/10.1088/1748-9326/ad25a4>, 2024.

Kenner, R.: Geomorphological analysis on the interaction of Alpine glaciers and rock glaciers since the Little Ice Age, *Land Degrad. Dev.*, 30, 580–591, <https://doi.org/10.1002/ldr.3238>, 2018.

Kenner, R. and Magnusson, J.: Estimating the Effect of Different Influencing Factors on Rock Glacier Development in Two Regions in the Swiss Alps, *Permafr. Periglac. Process.*, 28, 767–767, <https://doi.org/10.1002/ppp.1959>, 2017.

Kenner, R., Noetzli, J., Hoelzle, M., Raetzo, H., and Phillips, M.: Distinguishing ice-rich and ice-poor permafrost to map ground temperatures and ground ice occurrence in the Swiss Alps, *The Cryosphere*, 13, 1925–1941, <https://doi.org/10.5194/tc-13-1925-2019>, 2019.

King, L., Fisch, W., Haeblerli, W., and Waechter, H.: GLETSCHERKUNDE COMPARISON OF RESISTIVITY AND RADIO-ECHO SOUNDINGS ON ROCK GLACIER PERMAFROST, 77–97, 1987.

Kneisel, C.: Occurrence of surface ice and ground ice/permafrost in recently deglaciated glacier forefields, St. Moritz area, Eastern Swiss Alps, in: *PERMAFROST - Seventh International Conference, Yellowknife (Canada)*, 7, 1998.

Kneisel, C.: Permafrost in recently deglaciated glacier forefields-measurements and observations in the eastern Swiss Alps and northern Sweden, *Z. Für Geomorphol.*, 47, 289–305, 2003.

Kuhn, M.: The mass balance of very small glaciers, *Z. Für Gletscherkunde Glazialgeol.*, 1995.

Kunz, J. and Kneisel, C.: Glacier–Permafrost Interaction at a Thrust Moraine Complex in the Glacier Forefield Muragl, Swiss Alps, *Geosciences*, 10, 205, <https://doi.org/10.3390/geosciences10060205>, 2020.

Kunz, J., Ullmann, T., and Kneisel, C.: Internal structure and recent dynamics of a moraine complex in an alpine glacier forefield revealed by geophysical surveying and Sentinel-1 InSAR time series, *Geomorphology*, 398, 108052, <https://doi.org/10.1016/j.geomorph.2021.108052>, 2022.

Kupsch, W. O.: Ice-Thrust Ridges in Western Canada, *J. Geol.*, 70, 582–594, <https://doi.org/10.1086/626853>, 1962.

Lambiel, C. and Delaloye, R.: Contribution of real-time kinematic GPS in the study of creeping mountain permafrost: examples from the Western Swiss Alps, *Permafr. Periglac. Process.*, 15, 229–241, <https://doi.org/10.1002/ppp.496>, 2004.

Lliboutry, L., Arnao, B. M., Pautre, A., and Schneider, B.: Glaciological Problems Set by the Control of Dangerous Lakes in Cordillera Blanca, Peru. I. Historical Failures of Morainic Dams, their Causes and Prevention, *J. Glaciol.*, 18, 239–254, <https://doi.org/10.3189/S002214300002133X>, 1977.

Loke, M. H.: RES1D ver. 1.0 1-D Resistivity, UP & SIP Inversion and forward modeling, 2001.

Lüthi, M. P.: Little Ice Age climate reconstruction from ensemble reanalysis of Alpine glacier fluctuations, *The Cryosphere*, 8, 639–650, <https://doi.org/10.5194/tc-8-639-2014>, 2014.

Maisch, M.: Die Gletscher der Schweizer Alpen: Gletscherhochstand 1850, aktuelle Vergletscherung, Gletscherschwund-Szenarien, Vdf, Hochschulverlag AG an der ETH, 2000.

Maisch, M., Haeberli, W., Frauenfelder, R., Kääb, A., and Rothenbühler, C.: Lateglacial and Holocene evolution of glaciers and permafrost in the Val Muragl, Upper Engadin, Swiss Alps, in: *Proceedings 8th International Conference on Permafrost*, International Conference on Permafrost, 717–722, 2003.

Mollaret, C., Hilbich, C., Pellet, C., Flores-Orozco, A., Delaloye, R., and Hauck, C.: Mountain permafrost degradation documented through a network of permanent electrical resistivity tomography sites, *The Cryosphere*, 13, 2557–2578, <https://doi.org/10.5194/tc-13-2557-2019>, 2019a.

Mollaret, C., Hilbich, C., Pellet, C., Flores-Orozco, A., Delaloye, R., and Hauck, C.: Mountain permafrost degradation documented through a network of permanent electrical resistivity tomography sites, *The Cryosphere*, 13, 2557–2578, <https://doi.org/10.5194/tc-13-2557-2019>, 2019b.

Mollaret, C., Wagner, F. M., Hilbich, C., Scapozza, C., and Hauck, C.: Petrophysical Joint Inversion Applied to Alpine Permafrost Field Sites to Image Subsurface Ice, Water, Air, and Rock Contents, *Front. Earth Sci.*, 8, <https://doi.org/10.3389/feart.2020.00085>, 2020.

Monnier, S., Kinnard, C., Surazakov, A., and Bossy, W.: Geomorphology, internal structure, and successive development of a glacier foreland in the semiarid Chilean Andes (Cerro Tapado, upper Elqui Valley, 30°08' S., 69°55' W.), *Geomorphology*, 207, 126–140, <https://doi.org/10.1016/j.geomorph.2013.10.031>, 2014.

Navarro, G., Valois, R., MacDonell, S., De Pasquale, G., and Díaz, J. P.: Internal structure and water routing of an ice-debris landform assemblage using multiple geophysical methods in the semiarid Andes, *Front. Earth Sci.*, 11, 1102620, <https://doi.org/10.3389/feart.2023.1102620>, 2023.

Nicholson, L. and Benn, D. I.: Calculating ice melt beneath a debris layer using meteorological data, *J. Glaciol.*, 52, 463–470, <https://doi.org/10.3189/172756506781828584>, 2006.

Noetzli, J., Arenson, L. U., Bast, A., Beutel, J., Delaloye, R., Farinotti, D., Gruber, S., Gubler, H., Haeberli, W., Hasler, A., Hauck, C., Hiller, M., Hoelzle, M., Lambiel, C., Pellet, C., Springman, S. M., Vonder Muehll, D., and Phillips, M.: Best Practice for Measuring Permafrost Temperature in Boreholes Based on the Experience in the Swiss Alps, *Front. Earth Sci.*, 9, <https://doi.org/10.3389/feart.2021.607875>, 2021.

Noetzli, J., Isaksen, K., Barnett, J., Christiansen, H. H., Delaloye, R., Etzelmüller, B., Farinotti, D., Galleman, T., Guglielmin, M., Hauck, C., Hilbich, C., Hoelzle, M., Lambiel, C., Magnin, F., Oliva, M., Paro, L., Pogliotti, P., Riedl, C., Schoeneich, P., Valt, M., Vieli, A., and Phillips, M.: Enhanced warming of European mountain permafrost in the early 21st century, *Nat. Commun.*, 15, 10508, <https://doi.org/10.1038/s41467-024-54831-9>, 2024.

Nussbaumer, S. U., Steinhilber, F., Trachsel, M., Breitenmoser, P., Beer, J., Blass, A., Grosjean, M., Hafner, A., Holzhauser, H., Wanner, H., and Zumbühl, H. J.: Alpine climate during the Holocene: a

comparison between records of glaciers, lake sediments and solar activity, *J. Quat. Sci.*, 26, 703–713, <https://doi.org/10.1002/jqs.1495>, 2011.

Obu, J.: How Much of the Earth's Surface is Underlain by Permafrost?, *J. Geophys. Res. Earth Surf.*, 126, e2021JF006123, <https://doi.org/10.1029/2021JF006123>, 2021.

Oliva, M., Ruiz-Fernández, J., Barriendos, M., Benito, G., Cuadrat, J. M., Domínguez-Castro, F., García-Ruiz, J. M., Giralt, S., Gómez-Ortiz, A., Hernández, A., López-Costas, O., López-Moreno, J. I., López-Sáez, J. A., Martínez-Cortizas, A., Moreno, A., Prohom, M., Saz, M. A., Serrano, E., Tejedor, E., Trigo, R., Valero-Garcés, B., and Vicente-Serrano, S. M.: The Little Ice Age in Iberian mountains, *Earth-Sci. Rev.*, 177, 175–208, <https://doi.org/10.1016/j.earscirev.2017.11.010>, 2018.

Østrem, G.: Ice Melting under a Thin Layer of Moraine, and the Existence of Ice Cores in Moraine Ridges, *Geogr. Ann.*, 41, 228–230, <https://doi.org/10.1080/20014422.1959.11907953>, 1959.

Paul, F. and Bolch, T.: Glacier Changes Since the Little Ice Age, in: *Geomorphology of Proglacial Systems*, edited by: Heckmann, T. and Morche, D., Springer International Publishing, Cham, 23–42, https://doi.org/10.1007/978-3-319-94184-4_2, 2019.

Pellicciotti, F., Stephan, C., Miles, E., Herreid, S., Immerzeel, W. W., and Bolch, T.: Mass-balance changes of the debris-covered glaciers in the Langtang Himal, Nepal, from 1974 to 1999, *J. Glaciol.*, 61, 373–386, <https://doi.org/10.3189/2015JoG13J237>, 2015.

Péwé, T. L.: Alpine Permafrost in the Contiguous United States: A Review, *Arct. Alp. Res.*, 15, 145–156, <https://doi.org/10.1080/00040851.1983.12004339>, 1983.

Pfeffer, W. T., Arendt, A. A., Bliss, A., Bolch, T., Cogley, J. G., Gardner, A. S., Hagen, J.-O., Hock, R., Kaser, G., Kienholz, C., Miles, E. S., Moholdt, G., Mölg, N., Paul, F., Radić, V., Rastner, P., Raup, B. H., Rich, J., Sharp, M. J., and The Randolph Consortium: The Randolph Glacier Inventory: a globally complete inventory of glaciers, *J. Glaciol.*, 60, 537–552, <https://doi.org/10.3189/2014JoG13J176>, 2014.

Reid, T. D., Carenzo, M., Pellicciotti, F., and Brock, B. W.: Including debris cover effects in a distributed model of glacier ablation, *J. Geophys. Res. Atmospheres*, 117, <https://doi.org/10.1029/2012JD017795>, 2012.

Reynard, E., Lambiel, C., Delaloye, R., Devaud, G., Baron, L., Chapellier, D., Marescot, L., and Monnet, R.: Glacier/permafrost relationships in forefields of small glaciers (Swiss Alps), in: *Proceedings 8th international conference on permafrost*, International Conference on Permafrost, Zurich, Switzerland, 947–952, 2003.

Ribolini, A., Chelli, A., Guglielmin, M., and Pappalardo, M.: Relationships between glacier and rock glacier in the Maritime Alps, Schiantala Valley, Italy, *Quat. Res.*, 68, 353–363, <https://doi.org/10.1016/j.yqres.2007.08.004>, 2007.

Ribolini, A., Guglielmin, M., Fabre, D., Bodin, X., Marchisio, M., Sartini, S., Spagnolo, M., and Schoeneich, P.: The internal structure of rock glaciers and recently deglaciated slopes as revealed by geoelectrical tomography: insights on permafrost and recent glacial evolution in the Central and Western Alps (Italy–France), *Quat. Sci. Rev.*, 29, 507–521, <https://doi.org/10.1016/j.quascirev.2009.10.008>, 2010.

Rounce, D. R., Quincey, D. J., and McKinney, D. C.: Debris-covered glacier energy balance model for Imja–Lhotse Shar Glacier in the Everest region of Nepal, *The Cryosphere*, 9, 2295–2310, <https://doi.org/10.5194/tc-9-2295-2015>, 2015.

Rounce, D. R., Hock, R., McNabb, R. W., Millan, R., Sommer, C., Braun, M. H., Malz, P., Maussion, F., Mouginot, J., Seehaus, T. C., and Shean, D. E.: Distributed Global Debris Thickness Estimates Reveal Debris Significantly Impacts Glacier Mass Balance, *Geophys. Res. Lett.*, 48, e2020GL091311, <https://doi.org/10.1029/2020GL091311>, 2021.

Scherler, M., Schneider, S., Hoelzle, M., and Hauck, C.: A two-sided approach to estimate heat transfer processes within the active layer of the Murtèl–Corvatsch rock glacier, *Earth Surf. Dyn.*, 2, 141–154, <https://doi.org/10.5194/esurf-2-141-2014>, 2014.

Scotti, R., Brardinoni, F., and Crosta, G. B.: Post-LIA glacier changes along a latitudinal transect in the Central Italian Alps, *The Cryosphere*, 8, 2235–2252, <https://doi.org/10.5194/tc-8-2235-2014>, 2014.

Serrano, E. and Martín-Moreno, R.: Surge glaciers during the Little Ice Age in the Pyrenees, *Cuad. Investig. Geográfica*, 44, 213, <https://doi.org/10.18172/cig.3399>, 2018.

Snavely, N., Seitz, S. M., and Szeliski, R.: Skeletal graphs for efficient structure from motion, in: 2008 IEEE Conference on Computer Vision and Pattern Recognition, 2008 IEEE Conference on Computer Vision and Pattern Recognition, 1–8, <https://doi.org/10.1109/CVPR.2008.4587678>, 2008.

Staub, B., Lambiel, C., and Delaloye, R.: Rock glacier creep as a thermally-driven phenomenon: A decade of inter-annual observations from the Swiss Alps, 2, 2016.

Streletskiy, D., Noetzli, J., Smith, S. L., Vieira, G., Schoeneich, P., Hrbacek, F., and Irrgang, A. M.: Strategy and Implementation Plan for the Global Terrestrial Network for Permafrost (GTN-P) 2021–2024, <https://doi.org/10.5281/zenodo.6075468>, 2021.

Timur, A.: Velocity of compressional waves in porous media at permafrost temperatures, *GEOPHYSICS*, 33, 584–595, <https://doi.org/10.1190/1.1439954>, 1968.

Vincent, C.: Solving the paradox of the end of the Little Ice Age in the Alps, *Geophys. Res. Lett.*, 32, <https://doi.org/10.1029/2005GL022552>, 2005.

Vivero, S., Bodin, X., Farías-Barahona, D., MacDonell, S., Schaffer, N., Robson, B. A., and Lambiel, C.: Combination of Aerial, Satellite, and UAV Photogrammetry for Quantifying Rock Glacier Kinematics in the Dry Andes of Chile (30°S) Since the 1950s, *Front. Remote Sens.*, 2, <https://doi.org/10.3389/frsen.2021.784015>, 2021.

Vivero, S., Hendrickx, H., Frankl, A., Delaloye, R., and Lambiel, C.: Kinematics and geomorphological changes of a destabilising rock glacier captured from close-range sensing techniques (Tsarmine rock glacier, Western Swiss Alps), *Front. Earth Sci.*, 10, <https://doi.org/10.3389/feart.2022.1017949>, 2022.

Vonder Mühl, D. S.: Geophysikalische Untersuchungen im Permafrost des Oberengadins, ETH Zurich, <https://doi.org/10.3929/ETHZ-A-000891391>, 1993.

Wagner, F. M., Mollaret, C., Günther, T., Kemna, A., and Hauck, C.: Quantitative imaging of water, ice and air in permafrost systems through petrophysical joint inversion of seismic refraction and

electrical resistivity data, *Geophys. J. Int.*, 219, 1866–1875, <https://doi.org/10.1093/gji/ggz402>, 2019.

Waharftig, C. and Cox, A.: ROCK GLACIERS IN THE ALASKA RANGE, *GSA Bull.*, 70, 383–436, [https://doi.org/10.1130/0016-7606\(1959\)70\[383:RGITAR\]2.0.CO;2](https://doi.org/10.1130/0016-7606(1959)70[383:RGITAR]2.0.CO;2), 1959.

Wee, J. and Delaloye, R.: Post-glacial dynamics of an alpine Little Ice Age glacitectonized frozen landform (Aget, western Swiss Alps), *Permafr. Periglac. Process.*, 33, 370–385, <https://doi.org/10.1002/ppp.2158>, 2022.

Wegmann, M., Brönnimann, S., Bhend, J., Franke, J., Folini, D., Wild, M., and Luterbacher, J.: Volcanic Influence on European Summer Precipitation through Monsoons: Possible Cause for “Years without Summer,” <https://doi.org/10.1175/JCLI-D-13-00524.1>, 2014.

Westoby, M. J., Brasington, J., Glasser, N. F., Hambrey, M. J., and Reynolds, J. M.: ‘Structure-from-Motion’ photogrammetry: A low-cost, effective tool for geoscience applications, *Geomorphology*, 179, 300–314, <https://doi.org/10.1016/j.geomorph.2012.08.021>, 2012.

Wicky, J. and Hauck, C.: Air Convection in the Active Layer of Rock Glaciers, *Front. Earth Sci.*, 8, <https://doi.org/10.3389/feart.2020.00335>, 2020.

Wirz, V., Geertsema, M., Gruber, S., and Purves, R. S.: Temporal variability of diverse mountain permafrost slope movements derived from multi-year daily GPS data, Matternal, Switzerland, *Landslides*, 13, 67–83, <https://doi.org/10.1007/s10346-014-0544-3>, 2016.

Zumbühl, H. J., Steiner, D., and Nussbaumer, S. U.: 19th century glacier representations and fluctuations in the central and western European Alps: An interdisciplinary approach, *Glob. Planet. Change*, 60, 42–57, <https://doi.org/10.1016/j.gloplacha.2006.08.005>, 2008.

Part II Research publications

Publication I: Wee and Delaloye (2022), Permafrost and Periglacial Processes

Post-glacial dynamics of an alpine Little Ice Age glacitectonized frozen landform (Aget, western Swiss Alps)

Authors **Julie Wee** and Reynald Delaloye

Journal Permafrost and Periglacial Processes

Year 2022

DOI doi.org/10.1002/ppp.2158

Citation Wee, J. and Delaloye, R.: Post-glacial dynamics of an alpine Little Ice Age glacitectonized frozen landform (Aget, western Swiss Alps), Permafrost and Periglacial Processes, 33, 370–385, <https://doi.org/10.1002/ppp.2158>, 2022.

Short summary

The morphodynamical evolution of a back-creeping glacitectonized frozen landform in the Aget glacier forefield is investigated. Despite the general increase in ground temperatures responsible for the general increase in permafrost creep velocities, some landforms experience behaviours of permafrost creep deceleration. On the basis of long-term time series of ground surface temperature, and in-situ geodetic and geoelectrical measurements, this contribution aims to identify the underlying driving processes responsible for such kinematic behaviour in permafrost creep.

Main findings

- A systematic yet varying decrease of measured apparent resistivity of the frozen ground was unveiled.
- Subsidence induced by the melt of excessive ice at the permafrost table was observed.
- Surface elevation loss appeared to have been mainly the result of a decrease in the thickness of the moving mass due to its extensive flow pattern.
- A probable liquid water-to-ice content ratio increase within the permafrost body and the latter a ground ice melt at the permafrost table, both processes having taken place heterogeneously at the scale of the landform.
- The absence of acceleration of landform motion may indicate that the ongoing degradation is reaching a tipping point at which the driving processes contribute to a decrease of the stresses at the shear horizon contribute to progressively driving the landform towards a transitional state of kinematic activity.

Contribution of the PhD candidate

Design of the study with the contribution of R. Delaloye. Field measurements until 2016 were conducted by the co-author. From 2016 onwards, field investigations were led and conducted by the PhD candidate J. Wee. Preparation, analysis, and interpretation of the data. Preparation of the manuscript and the figures. The co-author contributed to the improvement of the manuscript.

Data availability

Data on rock glacier kinematics and ground surface temperature are on the PERMOS data portal (<https://www.permos.ch/data-portal>). Data from the geophysical measurements are available upon request.

Post-glacial dynamics of an alpine Little Ice Age glacitectonized frozen landform (Aget, western Swiss Alps)

Julie Wee  | Reynald Delaloye

Department of Geosciences, University of Fribourg, Switzerland

CorrespondenceJulie Wee, Department of Geosciences, University of Fribourg, Switzerland.
Email: julie.wee@unifr.ch**Abstract**

Glaciers and frozen-debris landforms have coexisted and episodically or continuously interacted throughout the Holocene at elevations where the climate conditions are cold enough for permafrost to occur. In the European Alps, the Little Ice Age (LIA) characterized the apogee of the last interaction phase. In areas of consecutive post-LIA glacier shrinkage, the geomorphological dominant conditioning of the ongoing paraglacial phase may have transitioned from glacial to periglacial and later even shifted to post-periglacial. Such transitions can be observed through the morphodynamics of glacitectonized frozen landforms (GFLs), which are permafrost-related pre-existing frozen masses of debris deformed (tectonized) by the pressure exerted by an interacting glacier. This contribution aims at evidencing the processes driving the ongoing morphodynamical evolution of an actively back-creeping GFL within the LIA forefield of the Aget glacier on the basis of long-term time series of ground surface temperature, and in-situ geodetic and geoelectrical measurements. Our observations for the last two decades (1998–2020), which have been the warmest since the LIA, reveal a resistivity decrease in the permafrost body and a surface subsidence of up to a few centimeters per year. The former indicate a liquid water-to-ice content ratio increase within the permafrost body and the latter a ground ice melt at the permafrost table, both processes having taken place heterogeneously at the scale of the landform. The absence of acceleration of landform motion during that period despite a probable warming trend of the frozen ground may indicate that the ongoing degradation is reaching a tipping point at which processes related to interparticle friction and thinning of the permafrost body contribute to gradually inactivate the mechanism of permafrost creep.

KEYWORDS

alpine cryosphere, degradation, frozen debris, glaciers, glacitectonized frozen landforms, Little Ice Age, permafrost, Swiss Alps

This is an open access article under the terms of the [Creative Commons Attribution-NonCommercial](https://creativecommons.org/licenses/by-nc/4.0/) License, which permits use, distribution and reproduction in any medium, provided the original work is properly cited and is not used for commercial purposes.
© 2022 The Authors. *Permafrost and Periglacial Processes* published by John Wiley & Sons Ltd.

1 | INTRODUCTION

Under current atmospheric warming, glacial and periglacial alpine environments are undergoing transformations that illustrate a degrading cryosphere.^{1–3} While glacier shrinkage stands among the most evident signs of a transitioning alpine landscape,^{4,5} visible changes in the periglacial belt such as the degradation of permafrost or the melt of ground ice are more subtle,⁶ especially in environments where both glacial and periglacial processes have occurred or still occur simultaneously. From a geomorphological perspective, they constitute complex environments sitting astride the glacial and periglacial domains,^{7,8} whose consecutive response to atmospheric forcing is little known and deserve in-depth investigation.

In alpine regions, glaciers and frozen-debris landforms such as rock glaciers, ice-cored moraines, or any other mass of frozen sediments may have coexisted and episodically or continuously interacted throughout the Holocene at elevations where the climate conditions were cold enough for permafrost to occur.^{7–13} Such interactions occur mostly below the equilibrium line of glaciers and above the lower boundary of permafrost, which depend on both mean annual air temperature and precipitation, as it is the zone where glacier ice can be cold and unconsolidated sediments can be in a perennially frozen state.¹⁴

In the Alps, one can assume that the reasonably small climatic oscillations of the Holocene mean that the lower altitudinal limit of permafrost has not differed significantly from the current one throughout the last 10,000 years or so.¹⁵ During that time and in regions with drier climatic conditions, such as the inner Swiss Alps, the oscillating extent of small glaciers has mostly occurred above the lower limit of the discontinuous permafrost belt. The Little Ice Age (LIA) characterized the apogee of the last interaction phase (ca. 1350–1850 in the Alps¹⁵) during which small polythermal cirque glaciers^{11,16} altered the thermal regime of their forefields and the spatial distribution of pre-existing perennially frozen sediments.^{17,18}

In such a context, the LIA glacier maximal extent delineates what is considered as an LIA glacier forefield. As geomorphological systems, present-day LIA glacier forefields in alpine permafrost environments mainly result from a wide and interlaced spectrum of former and current glacial, periglacial, hydrological, and mass-wasting processes, some of them being specifically paraglacial, that is directly consecutive to glacier retreat.^{19,20} Beside glacier ice masses,²¹ including debris-covered glacier ice and buried dead ice bodies, and glaciogenic debris accumulations such as till and moraines, a glacier forefield system may comprise in particular permafrost-related pre-existing frozen debris masses^{9,14} deformed and displaced by the pressure exerted by an advancing glacier. The landforms resulting from this glacier–permafrost interaction are presently described as glaciectonized frozen landforms (GFLs). Glaciectonic deformation can occur in the presence of an advancing polythermal glacier^{11,22,23} (cold-based at least in its margins) onto frozen debris masses, as the glacier margins bind to the frozen debris and lead to the transmission of glacial stress.²⁴ The ice present in a GFL is either of non-glacial (interstitial ice) or polygenic (mixture of interstitial and sedimentary ice) origin,

whereas embedding of buried glacial (sedimentary) ice from the LIA is mostly to be expected in its proximal (glacier facing) part only.^{23,25}

The former advance of polythermal glaciers during the LIA not only displaced pre-existing frozen debris but also induced a thermal buffer between the atmosphere and the ground surface, consequently altering the pre-existing ground surface thermal regime. Morphological evidence (e.g., fluted moraines) as well as geophysical and kinematic surveys of LIA glacier forefields often indicate that the LIA glacier tongue was mostly temperate, except at its margins, such that the innermost part of such a forefield is frequently deprived of ground ice, even decades after glacier retreat.^{17,26,27} However, in some cases more or less large volumes of glacier ice may persist under a protective layer of debris.²³

The type of geomorphological system investigated here remains poorly known despite growing interest in glacier–permafrost interactions in recent decades. Early studies have mainly focussed on investigating thermal conditions and permafrost occurrences in recently exposed glacier forefields located within the belt of mountain permafrost in the Alps by using geomorphological mapping, ground surface temperature measurements, and geophysical soundings.^{9,17,25–30} New insights into the process of creeping mountain permafrost in glacier forefields resulted from the combination of measured surface displacements and geophysical prospections of the subsurface, enabling previous studies to be extended.^{12,31,32} A deeper understanding of the post-glacial dynamics of LIA alpine glacier forefields and their associated frozen landforms is essential to reconstruct their past and predict their future evolution. Recent efforts towards the further understanding of glacier–permafrost interactions^{23,33–38} still indicate that there is an increasing necessity for the use of high-resolution data, as well as the systematic monitoring of these systems.

Here, the post-glacial dynamics of an LIA alpine glacier forefield and its associated landforms are investigated. The evolution of the extent and properties of ground ice from 1998 to 2017/20 is assessed through the analysis of repeated historical geoelectrical measurements. The kinematic behavior of a mass-wasting GFL is investigated, with an emphasis on the contribution of ice melt-induced subsidence to surface elevation changes, through the combination of the analysis of 20-year of in-situ geodetic and ground surface temperature (GST) monitoring surveys. This study underlines the importance of decadal-scale and multidisciplinary approach in understanding driving processes contributing to surface elevation changes due to ice melt or thawing frozen ground in permafrost-prone alpine LIA glacier forefields and to the dynamics of associated GFLs.

2 | STUDY REGION

Aget, the site investigated in this study, is an LIA glacier forefield system located in the Bagnes valley in the western Swiss Alps (46°00′32″N, 7°14′20″E; 2,850 m a.s.l.) (Figure 1). The area where the Aget glacier developed is dominated by the Grand-Aget (3,133 m a.s.

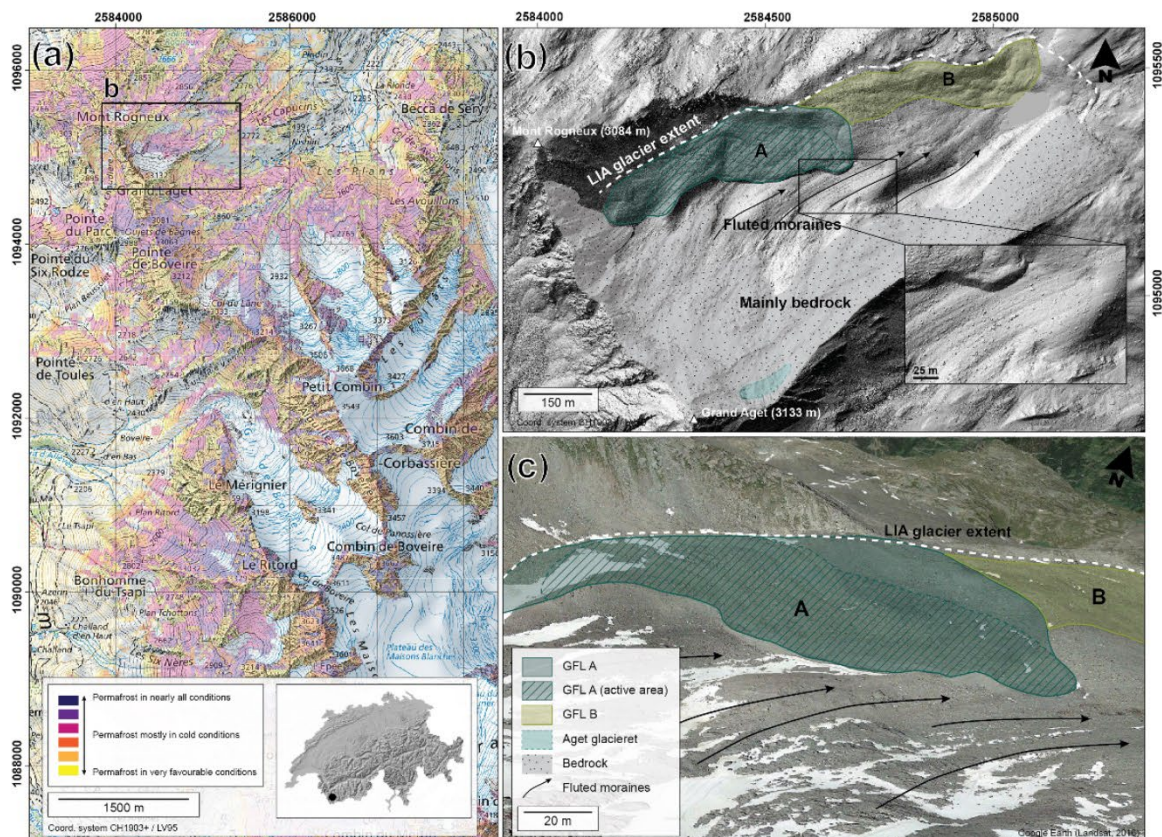


FIGURE 1 General description of the Aget LIA glacier forefield (b, c) and its location within the western Swiss Alps (a) and indicative permafrost distribution (BAFU, 2005). The dark blue polygon represents the investigated GFL A, and the hatched lines highlight its actively back-creeping area. The green polygon represents the no longer active GFL B. The black arrows represent fluted moraines and the LIA extent of the Aget glacier is highlighted by the white dashed lines (base map a: Swisstopo, digital elevation model b: Flotron AG 2019, aerial image c: Google Earth, Landsat 2016) [Colour figure can be viewed at wileyonlinelibrary.com]

l.) and the Mont Rogneux (3,084 m a.s.l.) summits in its uppermost western part and extends northeast down to the LIA frontal moraine at 2,770 m a.s.l.^{15,38} Potential permafrost conditions occur in most of the forefield.^{3,39} During its advance, the LIA glacier was mostly free of debris and temperate at its base as attested by widespread fluted moraines, whereas cold-based conditions were likely towards the glacier margins.^{17,25} Tiny remnants of the glacier were still present in 2020 but occupied less than a hectare at the foot of the Grand-Aget headwall and were entirely covered by a thin layer of debris.

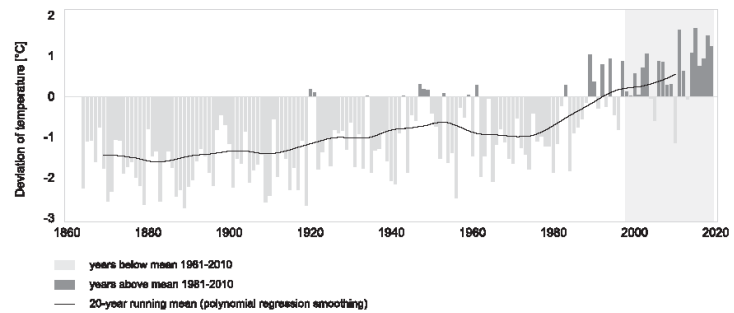
Two GFLs derived from the interaction of the LIA polythermal glacier and pre-existing frozen debris are present in the orographic left, SE-facing side of the glacier forefield (Figure 1b,c). Exploratory electrical resistivity measurements carried out in 1998 attested to the complete degradation of permafrost in a glactectonized landform (GFL B) located in the lower part of the glacier forefield, while in its upper part (GFL A), as well as in the transition zone between GFL A and B, permafrost conditions were revealed and confirmed again in 2017.^{17,25,40} The local occurrence of buried glacier ice cannot be

excluded in GFL A, as indicated by high electrical resistivity values.^{17,25}

Following retreat of the Aget glacier, paraglacial readjustments such as lateral back-creeping (in the direction of the topographic thalweg formerly occupied by the glacier) of GFLs A and B were initiated as indicated by geomorphological evidence of permafrost creep features such as ridges and furrows for the no-longer active GFL B and by in-situ geodetic measurements carried out annually since 2001 for the still active GFL A.³¹ Currently, surface displacements of GFL A range between 10 and 30 cm/year. GST has been monitored at seven locations on GFL A and in the transition zone between GFL A and B since 1998.³

The climate of the study region is predominantly influenced by its mountainous topography and has some inner-alpine continental character.⁴¹ Mean annual precipitation in the region ranges from 1,000 to 1,300 mm/year (MeteoSwiss, 2020). Mean annual air temperature for the period 1981–2010 at 2,850 m a.s.l. can be estimated at -2 to -3°C , as mean annual air temperatures recorded at Grand-St-Bernard

FIGURE 2 Mean annual air temperature based on homogenized data series of two meteorological stations above 2,400 m a.s.l. (GSB, 2,472 m a.s.l.; SAE, 2,502 m a.s.l.). Air temperature deviation from the reference period 1981–2010 of the two same meteorological stations. The period covered by GST monitoring at Aget is highlighted in gray. Adapted from MeteoSwiss (2020)



(GSB; 45°52′08″N, 7°10′14″E; 2472 m a.s.l.) and Sântis (SAE; 47°14′58″N, 9°20′36″E; 2,502 m a.s.l.) meteorological stations are -0.3 and -0.9°C respectively and considering an adiabatic lapse rate of $-0.5^{\circ}\text{C}/100$ m (MeteoSwiss, 2020). Temperatures measured since 1864 at the GSB and SAE meteorological stations show a distinctive warming trend of $1.34 \pm 0.05^{\circ}\text{C}/100$ years, particularly marked by the more recent drastic increase of the 20-year mean by 1.60°C between 1970–1989 and 2000–2019 (Figure 2; MeteoSwiss, 2020).

3 | MATERIALS AND METHODS

3.1 | Geomorphological observations

A preliminary geomorphological analysis was carried out on the basis of historical topographic maps, historical as well as recent high-resolution aerial photographs, and high-resolution digital elevation models (DEMs), allowing to evidence key geomorphological features. Topographic maps (1861 to present) and orthorectified aerial photographs (1946 to 2019) were provided by the Swiss federal institute of topography (Swisstopo) and Flotron AG, while the DEMs were acquired in 2019 by airborne laser scanning (ALS) by Flotron AG.

3.2 | Ground surface temperature measurements

To obtain a quantitative assessment of the thermal state of the ground surface and of the possible occurrence of ground ice close to the subsurface, GST has been measured continuously at a frequency of 2 hr since 1998 at seven locations on GFL A (02–05, 07), above it (06), and in the transition zone to GFL B (01) (Figure 3). From 1998 to 2016, GST data were collected using UTL-1 data loggers (accuracy of $\pm 0.2^{\circ}\text{C}$) and from 2016 to present UTL-3 data loggers have been used (accuracy of $\pm 0.02^{\circ}\text{C}$). Each time series is adjusted to match with the zero-curtain temperature during the snowmelt phase. Each data logger is buried a few decimeters below the ground surface in order to be shielded from direct solar radiation. From the temperature measurements, mean annual ground surface temperature (MAGST), ground freezing index (GFI, i.e., annual sum of negative daily temperatures), and ground thawing index (GTI, i.e., annual sum of positive

daily temperatures), and winter equilibrium temperature (WEqT, i.e., the mean temperature for 30 days before the onset of the snow-melt phase, which is an analog to the bottom temperature of the snowcover [BTS] method) were calculated.^{25,42}

3.3 | Surface displacement measurements and surface elevation changes

Surface displacement velocities have been monitored on GFL A and in the transition zone to GFL B on a yearly basis (late summer) since 2001 and bi-annually (early summer and late summer) from 2004 to 2013, as well as occasionally on GFL B from 2005 to 2013 by differential GNSS survey, according to the measurement set-up described by Lambiel and Delaloye.³¹ Seventy-six marked points are distributed throughout the site, among them three serving as control points on stable bedrock. Horizontal, vertical and total (3D) displacements are calculated between two geodetic surveys with an uncertainty of about 2–3 cm.

According to Lambiel and Delaloye,³¹ it is assumed that a change in elevation over time (Δz) of a point located on a moving mass is, aside any specific tilting of the boulder on which the point is marked, the combination of three main processes: (a) loss in elevation due to the downslope movement, which is assumed to mostly fit with the slope angle topography (Δz_{top}); (b) change in elevation in response to the melting or aggradation of excess ground ice (Δz_{mel}), that is of ice occupying a volume larger than the porosity; and (c) change in elevation due to extending or compressing flow patterns (Δz_{str}). The last can be determined by establishing, for example, a net of triangles between the well-distributed set of points over the surveyed area. The evolution of the surface area of each triangle between two geodetic surveys allows the quantification of a compressing (decrease in surface area) or extending (increase in surface area) flow pattern. The related change in elevation is also dependent on the thickness of the moving mass, which is here unknown, but estimated to 20 ± 5 m in accordance with the terrain morphology and the results of the geoelectrical surveys, and which is typical for an active rock glacier.⁴³ Assuming that the motion observed at the surface is constant down to the shear horizon, an increase (decrease) by 10% of the area implies a subsidence (heave) of 2.0 ± 0.5 m of the surface. Here, the thickness

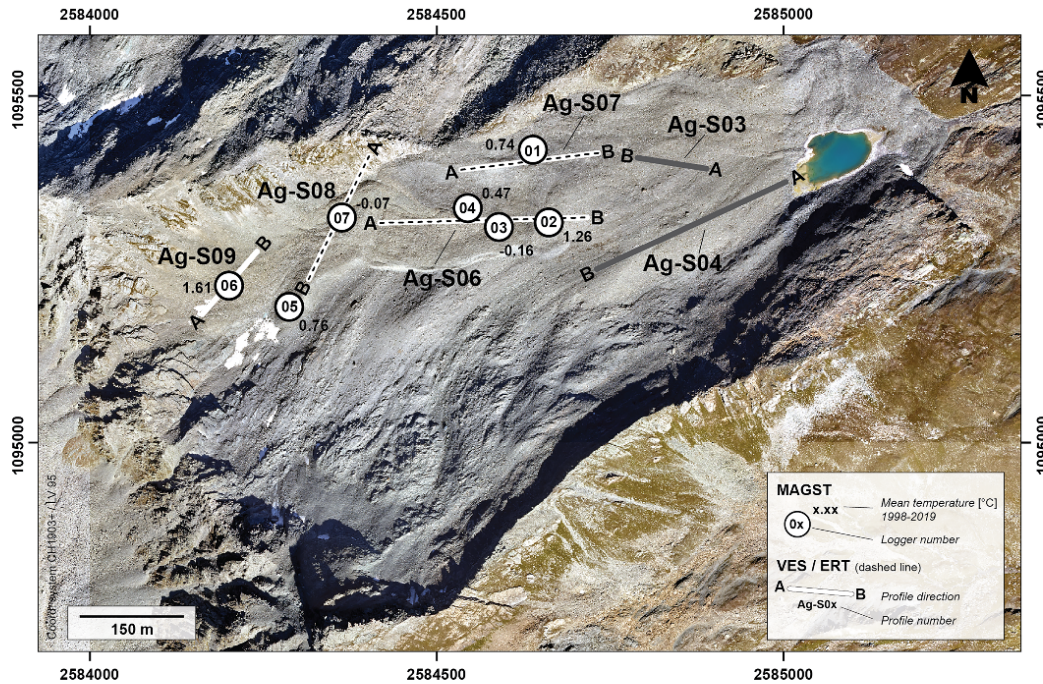


FIGURE 3 Overview of distribution of the GST sensors throughout the site and the location of the geoelectrical profiles. The location of the GST sites is marked by white dots. The geoelectrical profiles at the site are marked by a continuous segment (VES) and by a dashed line (ERT). Profiles marked in white represent permafrost-prone areas, and in gray permafrost-deprived areas (orthorectified aerial image: Flotron AG 2019) [Colour figure can be viewed at wileyonlinelibrary.com]

of the moving mass is set arbitrarily to 20 m throughout most of the GFL and to 15 m where extension is $\geq 5\%$. Fixing the thickness at 15 or 20 m implies a margin of error of the estimated vertical motion rate by 0.05 m per percent of deformation.

From this, the contribution of ice melt-induced subsidence (or ice growth-induced heave) to the vertical component of surface displacement is estimated using the following equation (1):

$$\Delta z_{mel,est} = \Delta xy \times \tan(\alpha_{T0}) - v \times h - \Delta z_{mes} \quad (1)$$

where Δxy is the horizontal surface displacement, α_{T0} is the shear horizon slope angle proxy presumed to be parallel to the surface topography, v is the extension/compression factor, and h is the thickness of the mass in motion (Figure 4). To assess the extent to which the melt of excess ice contributes to surface elevation changes of the GFL, 18 points distributed throughout the actively back-creeping GFL A were selected. The period 2006–2018, during which the observed surface velocity and, thus, the contribution of the downslope mass movement to the vertical component were almost constant, is considered here to estimate the surface subsidence due to ground ice melt in moving areas (Table 1). For the period 2006–2018, the margin of error related to the fixing of thickness at 15 or 20 m is 0.004 m/year per per cent of deformation. Moreover, the uncertainty of the deformation pattern (extension or compression) is estimated to be

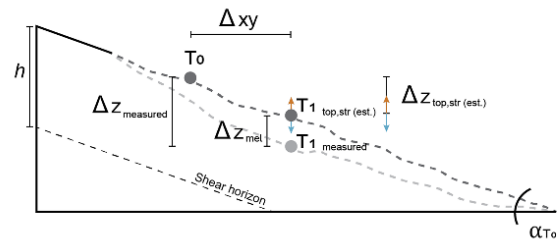


FIGURE 4 Schematic description of the three main processes contributing to change in elevation over time: (a, b) estimated loss in elevation due to the downslope movement, which is assumed to fit with the slope angle topography, and change in elevation due to extending or compressing flow patterns ($\Delta z_{top, str}$); and (c) change in elevation in response to the melting or aggradation of excess ground ice (Δz_{mel}) [Colour figure can be viewed at wileyonlinelibrary.com]

maximally $\pm 1\%$, corresponding to an error in the vertical motion rate of ± 0.016 m/year (± 0.012 m/year) for a thickness of 20 m (15 m).

3.4 | Geoelectrical surveys

Because of contrasting electrical properties between conductive unfrozen sediments and resistive ice, electrical resistivity

TABLE 1 Contribution to the observed change in elevation (ΔZ_{meas}) by the downslope movement (ΔZ_{top}), the extending or compressing flow pattern (ΔZ_{str}), and the melting or aggradation of excess ground ice (ΔZ_{mel}) from 2006 to 2018

Point ID	Slope angle anomaly (°)	ΔZ_{meas} (m)	ΔZ_{top} (m)	ΔZ_{str} (m)	ΔZ_{mel} (m)
Ag-023	-49	-0.65	-0.08	0.76	-1.41
Ag-024	-54	-0.47	-0.05	0.67	-1.14
Ag-101	-6	-1.01	-0.62	-1.06	0.05
Ag-102	-10	-0.49	-0.08	-0.60	0.11
Ag-107	-22	-0.97	-0.17	-0.75	-0.22
Ag-109	-11	-1.00	-0.41	-0.77	-0.22
Ag-110	-3	-0.76	-0.61	-1.05	0.29
Ag-116	-15	-1.45	-0.73	-0.67	-0.77
Ag-118	-21	-1.70	-0.59	-1.19	-0.51
Ag-119	-27	-1.45	-0.43	-1.24	-0.21
Ag-123	-16	-1.78	-0.99	-1.65	-0.14
Ag-124	-15	-2.41	-1.33	-2.29	-0.13
Ag-125	-20	-2.37	-1.10	-2.33	-0.05
Ag-126	-18	-1.81	-0.80	-1.94	0.13
Ag-137	-37	-0.65	-0.15	-0.97	0.32
Ag-139	-41	-1.28	-0.25	-1.34	0.07
Ag-148	-54	-0.97	-0.15	0.17	-1.14
Ag-149	-80	-1.41	-0.01	-0.09	-1.32

The values obtained for ΔZ_{str} are based on a 20-m-thick moving mass. A thickness of 15 m was applied for points located in zones where the deformation is greater than 5%. The slope angle anomaly is the difference between the observed displacement and the topographical slope angle.

measurements allow the distinction between unfrozen material, sub-saturated permafrost, and massive sedimentary ice.^{8,44} Resistivity magnitudes of material vary as a function of lithology, ice content, air/water content, temperature, etc.⁴⁴

An initial geoelectrical campaign was conducted in September 1998 in the Aget glacier forefield, during which nine vertical electrical soundings (VES) were carried out, as well as parametric soundings (unpublished data) to assess the resistivity of the bedrock (2–6 k Ω m) and of unfrozen sediments (1–4 k Ω m).^{17,25} In late August 2017, six of the nine earlier VES were repeated (Figure 3). The same electrode configurations and measuring device (McOhm 2115 A) as the 1998 campaign were applied to the 2017 campaign. Because homogeneous media are rare in a mountainous terrain, both symmetrical Schlumberger and dissymmetrical Hummel arrays were applied to all VES carried out in 1998 and 2017.

The measured apparent resistivity was inverted to obtain the modeled specific resistivity and thickness of each layer. Inversions were carried out with the program RES1D⁴⁵ using the least-squares optimization method.⁴⁶ Because of high root mean square error (RMSE) obtained for the modeled specific resistivity yielded by an oversteepening effect²⁹ in particular, only the measured apparent resistivity values are considered to assess resistivity changes between 1998 and 2017. The calculated change is based on the measured values at AB/2 distances (half the measurement profile length) of 20, 30, and 40 m, corresponding to an investigation depth of about 10–15 m.

In addition to VES, two electrical resistivity tomography (ERT) measurements were performed along the existing profiles used for

VES Ag-S06 and Ag-S08 in late August 2020 and one along VES profile Ag-S07 in mid-August 2021 to image the two-dimensional distribution of the electrical resistivity of the subsurface. The center (O) of a VES fits with position 117.5 m along the corresponding ERT profile. The instrument used for the ERT measurements was a SYSCAL Junior Switch (Iris Instruments, France). Forty-eight electrodes with a 5-m electrode spacing were used and the Wenner-Schlumberger array was applied as it offers a compromise between investigation depth resolution and horizontal resolution.⁴⁴ Topography data of the profiles were extracted from a high-resolution digital elevation model (DEM). The position of the center and the extremities of each profile was measured in situ with a dGPS. The points were then implemented into a GIS to establish the profile. The position of each electrode was calculated and their coordinates (E, N and altitude) were extracted. Inversions were processed with RES2DINV using the least-squares inversion and robust parameters.⁴² Because of resistivity variations near the ground surface, the model refinement parameter was applied. The extended model was applied to limit artifacts at the edges of the model.

4 | RESULTS

4.1 | Geomorphological interpretation of the past and current situation

The Aget LIA glacier forefield system (Figure 5) is bound by an orographic left lateral moraine, terminating downward as a frontal

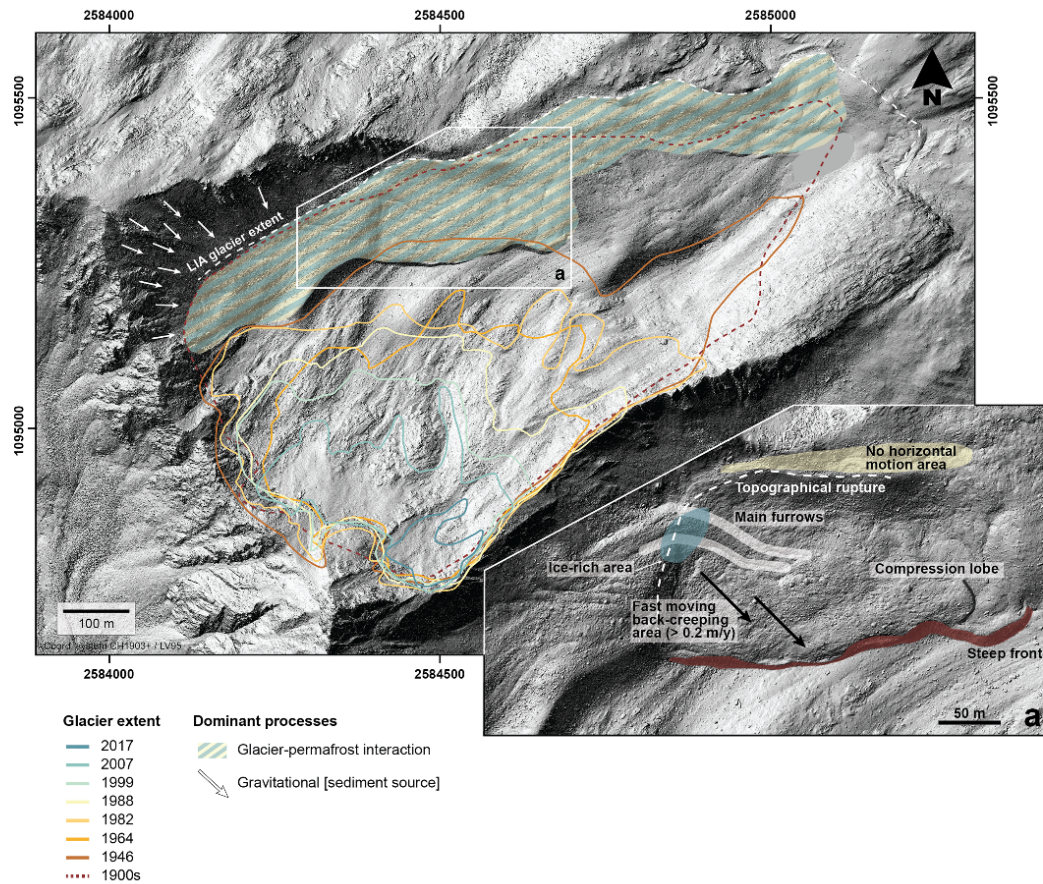


FIGURE 5 Aget glacier forefield. The evolution of the glacier extent from the LIA maximal extent (corresponding to the LIA moraine, ca. 1850) to 2017 is delineated based on geomorphological indicators, historical maps (Dufour and Siegfried), and historical aerial images (Swisstopo). The investigated GFL A is highlighted (white box, a) and its key geomorphological features are described (DEM Flotron AG 2019) [Colour figure can be viewed at wileyonlinelibrary.com]

moraine, which express the historical maximal extent of the glacier around 1850 (e.g., Dufour historical map 1861), inferring that the (cold) glacier margin of the polythermal Aget glacier pushed and (partly) overrode (or superimposed) a pre-existing frozen periglacial landform, which is here recognized as the Aget GFL A–B. According to the Siegfried historical map, around the 1900s GFL A was still glaciated while GFL B was partly deglaciated. It can be assumed that the gradual deglaciation of GFL A was initiated between the 1900s and 1946 as in 1946 only the margins of GFL A remain glaciated, while GFL B was probably completely deglaciated by ca. 1930 or even earlier. Presently, only very small remnants of the Aget glacier are present in the northern flank of the Grand-Aget. Following their respective deglaciation, a permafrost-driven lateral back-creeping motion in the direction of the thalweg was initiated for both GFLs. The lobate structure of GFLs A and B and the observed furrows attest to such kinematic behavior. The subdued topography, smoothed lateral and frontal margins of GFL B, as well as the presence of sparse

vegetation suggest the absence of permafrost and a current state of inactivity. The steep margins and ridge-and-furrow surface topography of GFL A as well as geodetic measurements indicate active motion driven by permafrost creep. Moreover, geoelectrical measurements carried out in 1998 revealed the internal structure of both landforms. Widespread occurrence of ground ice was found in GFL A (Ag-S06 and Ag-S08, Figure 3), while ground ice was sporadic to absent in the transition zone from GFL A to GFL B (Ag-S07 and Ag-S03, Figure 3).^{17,25}

4.2 | Internal structure of GFL A

In its lower section (eastward), the ERT profile Ag-WS06 (Figure 6a) throughout the median to lower zones of GFL A indicates resistivity values ranging between 3 and 10 kΩm, which suggests either an advanced state of degraded permafrost or unfrozen sediments. Under

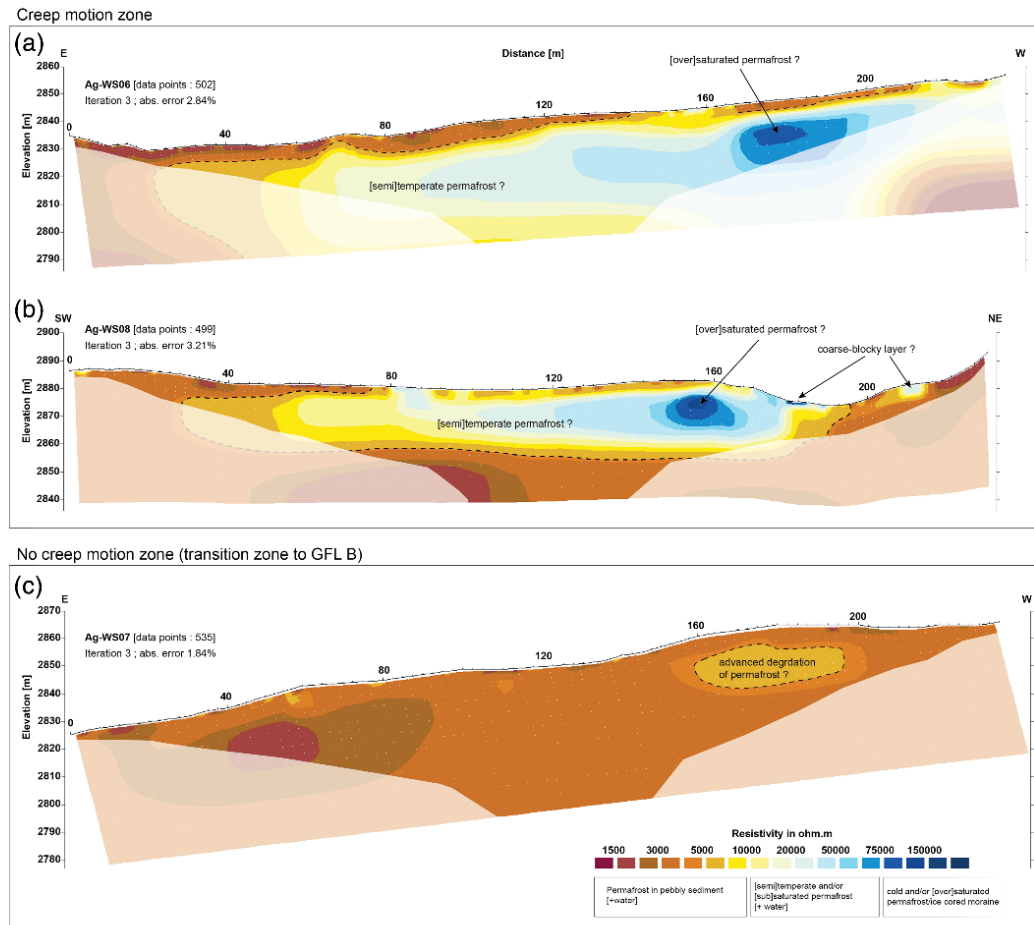


FIGURE 6 ERT profiles Ag-WS06 (a), Ag-WS08 (b), and Ag-WS07 (c). The whited-out sections represent low-confidence data. The dashed line represents the threshold for permafrost occurrence (5 k Ω m). The resistivity scale used in this study and values typical of frozen layers were adapted from Hauck and Kneisel⁴⁴ and Bosson et al.⁸ [Colour figure can be viewed at wileyonlinelibrary.com]

an uppermost layer of roughly 5–8 m, a layer greater than 20 m thick with resistivity ranging between 20 and 50 k Ω m dominates the central section of profile Ag-WS06, suggesting widespread permafrost. A patch with high resistivity values (> 75 k Ω m) is visible at a depth of about 10 m, not fully excluding the presence of remnants of buried sedimentary ice.⁴⁷ Regarding the relatively low resistivity values measured in the southwestern extremity of Ag-WS08 (Figure 6b), similarly as for profile Ag-WS06, they can either be interpreted as degraded permafrost or represent unfrozen debris at shallow depth (between 10 and 30 m along the profile). In the northeastern part of the profile (from 180 m onwards), the overall low resistivities indicate unfrozen material/bedrock outside of the GFL/glacial margin. Deeper than about 5 m, a 10 to 20-m-thick layer with resistivity ranging between 10 and 30 k Ω m indicates widespread permafrost along most of the profile. High resistivity values (75 to > 100 k Ω m) are locally found (patch) in the apparent upslope continuation of the resistive patch

observed in profile Ag-WS06. In the uppermost layer of profile Ag-WS08, which has a thickness of roughly 5 m, isolated more resistive patches are observed, probably indicating a coarse-blocky layer.

For profile Ag-WS07 (Figure 6c), the low resistivity values (< 4 k Ω m) can be interpreted as unfrozen material. Measured values of 5–7 k Ω m in a slightly more resistive patch (between 155 and 195 m) could indicate the occurrence of a frozen body with a high water-to-ice ratio content (highly degraded permafrost).

4.3 | Ground surface temperatures

MAGST for the period 1998–2019 was +0.66°C on average for the seven measurement locations (Figure 7a), ranging between –0.16 and 1.61°C, a spread which appears to be essentially explained by the micro-topoclimatic ground surface conditions at each data logger

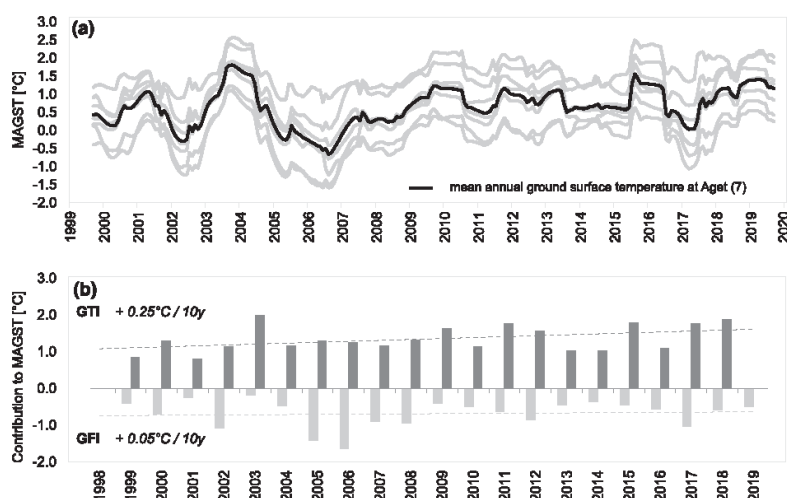


FIGURE 7 Running MAGST measured at Aget (black) averaged from the MAGST of each of the seven temperature loggers on site (light gray) (a) and contribution of the ground thawing index (GTI) and ground freezing index (GFI) to MAGST at Aget on average for all measurement sites (b)

location. The 21-year MAGST development has not differed from what has been observed for other rock glacier and GFL sites in the central and western Swiss Alps.³ A warming of 0.30°C per decade has been recorded at Aget, mainly due to the increase in ground surface temperature in summer (Figure 7b).

The 21-year mean GFI ranged between -186 and $-405^{\circ}\text{C}\cdot\text{day}$ depending on the measurement location. These values are relatively low compared to other permafrost sites in the Swiss Alps.⁴⁸ On average over 21 years, WEqT varies between -0.8 and -1.7°C , indicating the occurrence of deep seasonal freezing at each measurement site but not necessarily the refreezing of the entire active layer down to the permafrost table. GFI and WEqT suggest permafrost conditions almost close to thawing.⁴²

4.4 | Surface displacement measurements and surface elevation changes

In the central zone of GFL A, average surface displacements ranging from 0.15 to 0.30 m/year have been measured from 2001 to 2020, whereas only small surface movements (mainly between < 0.05 and 0.10 m/year) have been observed on the southeastern terminal lobe (Figure 8). The direction of the surface movement follows the slope aspect oriented towards the southeast. The mean slope angle of GFL A is about 15° . The slope angle decreases toward the frontal zone (between 5° and 10°), contributing to decreasing velocities. Close to the uppermost topographical rupture of the back-creeping GFL section, the slope angle gradually changes from 15° to 30° , favouring velocities faster than 0.20 m/year in the area.

Throughout GFL A, mass movement is mainly extending, especially in the uppermost part near the topographical rupture, where values up to $+13\%$ are found over the 19-year observation period (2001–2020). This could imply a decrease in surface elevation of more than 2 m. For the rest of the surface, the extension rate remains

relatively low with values ranging between 0 and $+5\%$ (subsidence of up to 1.0 ± 0.25 m). Compression is restricted to the lowermost frontal zone of GFL A, where the topography flattens and surface displacements are the slowest, and locally at the foot of the topographical rupture in the upper central zone due to some convergence of the flow field. As a geometric response to compressive flow, a relative gain in surface elevation above the initial topography in the order of 0.5 m up to more than 1.0 m on the southeastern front can be expected.

From 2001 to about 2010, the evolution of surface velocities measured at Aget followed the regional trend of creep velocities of six sites in the surrounding Bas-Valais area, in particular the extraordinary high horizontal velocities in 2003 and 2004 (Figure 9, PERMOS, 2020). Since 2006–2010, surface velocities measured at Aget have remained almost stable, contrasting with the significantly increasing regional trend. In 2015, new velocity records were reached at all sites monitored in the Bas-Valais region, surpassing the 2003–2004 peak. At Aget surface velocities increased, in particular in the upper zone of GFL A, but did not approach the peak of the previous decade. While regional mean surface velocities dropped drastically from 2015 to 2017, only a slight decrease of creep velocities was observed at Aget. Since 2018, regional mean creep velocities generally increased to reach a new record in 2020. Velocities measured in the upper zone of GFL A increased as well, but without reaching the previous 2015 peak, while the surface velocities recorded in the median zone remained almost unchanged and in the lower zone continued to decelerate.

4.5 | Contribution of ice melt-induced subsidence to surface elevation changes

Of the 18 selected points, eight express surface elevation change solely due to downslope movement along the topographical slope and

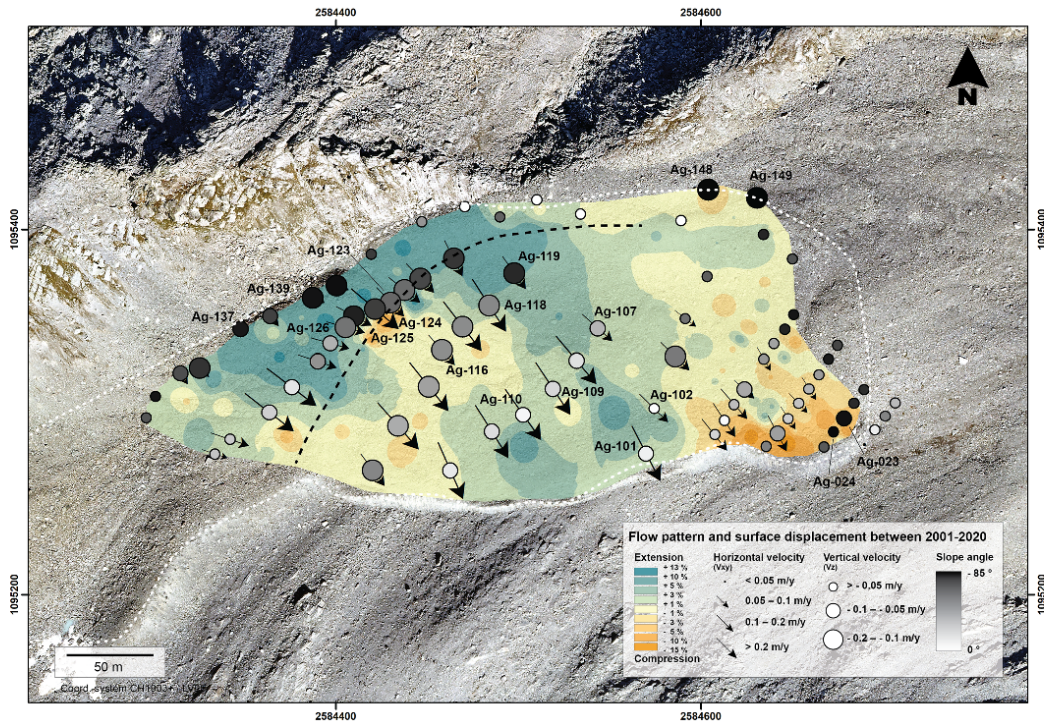


FIGURE 8 Contribution of extensive and compressive flow patterns and surface displacements to thickness variations obtained by an inverse distance weighting (IDW) interpolation. Arrows show the annual horizontal velocity, circles the annual vertical velocity, and the different shades of gray indicate the displacement slope angle of each point. The black dashed line represents the topographical rupture. The white dotted line represents the outline of GFL A [Colour figure can be viewed at wileyonlinelibrary.com]

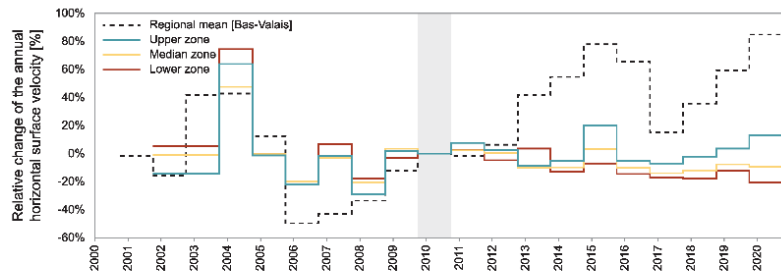


FIGURE 9 Mean annual horizontal surface velocity (%) relative to the reference period 2009–2010 (gray area) of the Aget GFL (subdivided into three zones: upper zone $n = 21$, median zone $n = 28$ and lower zone $n = 25$) from 2001 to 2020 (dashed line) and of six rock glaciers monitored in the Bas-Valais region from 2000 to 2020 derived from terrestrial geodetic surveys (PERMOS, 2020) [Colour figure can be viewed at wileyonlinelibrary.com]

to surface thinning enhanced by an extensive flow pattern⁴⁹ (Table 1). This is observed in the uppermost margins of the GFL where points Ag-137 and Ag-139 are located as well as at the edge of the topographical rupture for points Ag-125 and Ag-126 and also for points Ag-101, Ag-102, Ag-110, and Ag-119 that are situated in an area of extension flow (Figures 8 and 10).

A contribution of ice melt-induced subsidence to surface elevation changes is observed for the 10 other points, but is not uniform throughout the GFL. In the transition zone to GFL B, where almost no horizontal movement occurs, the points Ag-148 and Ag-149 have respectively lost 0.97 m (0.08 m/year) and 1.41 m (0.11 m/year) in surface elevation from 2006 to 2018. Taking into account slight strain

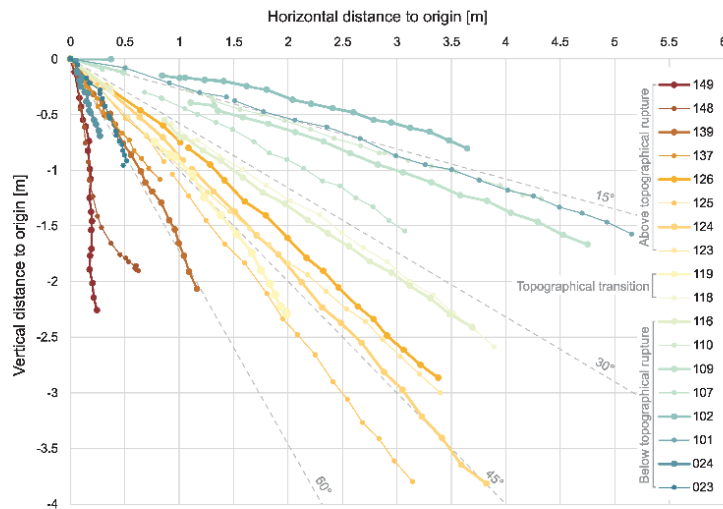


FIGURE 10 Displacement profiles for the period 2001–2020 of selected points distributed throughout the actively back-creeping GFL A [Colour figure can be viewed at wileyonlinelibrary.com]



FIGURE 11 Contribution of GTI to annual vertical displacement for points Ag-107, Ag-118, Ag-124, and Ag-149 from 2006 to 2018. GTI is computed as the average of the seven location measurements in the glacier forefield [Colour figure can be viewed at wileyonlinelibrary.com]

deformation at these two points, a respective subsidence of 1.14 m (0.10 m/year) and 1.32 m (0.11 m/year) is due to the melt of (excess) ice. However, since 2017 almost no surface elevation loss has been measured for point Ag-148. At the edge of the topographical rupture, the elevation loss of points Ag-123 and Ag-124 resulting from the extension flow pattern accounts for 1.66 and 2.27 m, while the vertical loss due to ice melt accounts for 0.13 and 0.14 m (0.01 m/year), respectively. Points Ag-107, Ag-109, Ag-116, and Ag-118 located below the topographical rupture but within the area of extensive flow pattern show a surface elevation loss driven by the extension flow pattern that accounts for 0.74, 0.79, 0.68, and 1.18 m of their total

vertical change, and 0.23 m (0.02 m/year), 0.21 m (0.02 m/year), 0.77 m (0.06 m/year), and 0.51 m (0.04 m/year), respectively, is due to ice melt. At the front of the GFL, points Ag-023 and Ag-024 show surface elevation loss of 0.65 and 0.47 m, driven by a melt rate of excess ice of 0.12 and 0.10 m/year, despite an expected surface elevation gain of 0.84 and 0.72 m due to the compression flow pattern.

To assess the extent to which surface summer heating contributes to the vertical displacement rate of the selected points, annual vertical displacements are compared to the annual GTI. The comparison is performed for the period 2006–2018 during which the annual displacements have been almost constant. For a large majority of the 18 points, despite low significance levels, the vertical displacement tends to depend on the GTI: the warmer the ground surface summer heating, the larger the subsidence (Figure 11). The vertical displacement rate during warmer summers surpasses by up to 0.1 m/year the vertical movement during cooler summers, as illustrated for the selected points in Figure 11.

4.6 | Resistivity changes

The repeated VES in 2017 provided similar shapes of apparent resistivity curves to those obtained in 1998²⁸ on all investigated sites, indicating the robustness of the repeated measurements. However, a significant decrease in resistivity has systematically been observed in layers containing ground ice (Figures 12 and 13).

Profiles Ag-S06 and Ag-S08 were carried out on the actively back-creeping zone of GFL A. The results obtained from the surveys performed using the dissymmetrical Hummel array revealed a clear heterogeneity of the subsurface for both soundings (Figure 12), which are mostly in line with the ERT profiles.

Relatively low apparent resistivity values measured in the uppermost layer of both branches (AC and BC) of sounding Ag-S06 indicate

FIGURE 12 Change in resistivity from 1998 to 2017 of VES Ag-S06 and Ag-S08. Both branches AC and BC (Hummel array) of each profile are presented. The data points (measured ρ_a between 20 and 40 m, distance AB/2 [m]) used to calculate the relative change in apparent resistivity are highlighted by the hatched lines

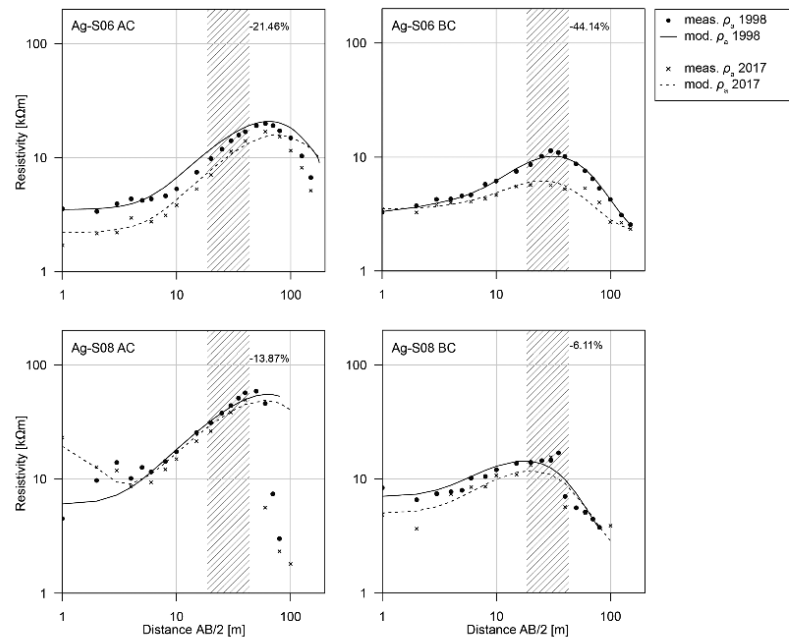
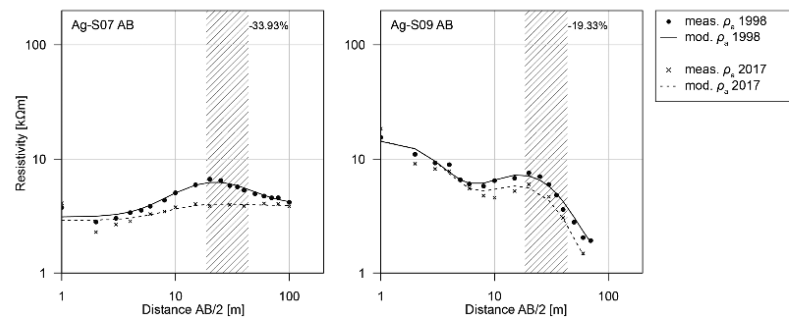


FIGURE 13 Change in resistivity from 1998 to 2017 of VES Ag-S07 and Ag-S09 (Schlumberger array). The data points (measured ρ_a) used to calculate the percentage change in apparent resistivity are highlighted by the hatched lines



the absence of a highly porous uppermost layer, but rather the presence of coarse debris interlaced with fine-grained glaciogenic sediments.⁵⁰ The elongated bell-shaped resistivity curve of branch AC (west) indicates the occurrence of a resistive layer below an estimated depth of 5–6 m, whose apparent resistivity decreased by 21% over 19 years. Resistivity values measured in 2017 for branch BC (east) of sounding Ag-S06 indicate a decrease of the apparent resistivity of the resistive layer of 44%.

A 10- to 20-m-thick and highly resistive (calculated specific resistivity ranging between 200 and 500 kΩm) layer was identified beneath an uppermost layer with an estimated thickness of 3–5 m for branch AC (northeast) of profile Ag-S08. Between 1998 and 2017, the apparent resistivity of the resistive layer decreased by 14%. For branch BC (southwest) of profile Ag-S08, a resistive layer reaching 20–35 kΩm was detected from a depth of roughly 3–4 m. Only a small decrease of 6% in resistivity was observed between 1998 and 2017.

Profile Ag-S07 was performed within the nonmoving part of GFL A while Ag-S09 was carried out upslope of the GFL in an area which has not been covered by the LIA glacier. As the results obtained with the Hummel array reveal a lateral homogeneity of the subsurface for both profiles, resistivities measured with the Schlumberger array are presented here (Figure 13). The elongated bell-shaped resistivity curve of profile Ag-S07 indicates a resistive layer at a depth of 3–4 m, whose resistivity decreased from 12–20 to 6–8 kΩm over a 19-year period, represented by a decrease in the average apparent resistivity at 20–40 m AB/2 by 34%. This corresponds to the zone affected by a significant surface elevation loss, where a more resistive patch (profile Ag-WS07, Figure 6) as well as points Ag-148 and Ag-149 are located (see Figure 8). The high apparent resistivity values measured in the uppermost layer (small electrode spacing) of profile Ag-S09 indicate the presence of a superficial porous layer from which finer sediments have been washed out over time and not replaced by glaciogenic sediments

from the LIA glacier. For increasing electrode spacing, the apparent resistivity first decreases, indicating a 4- to 5-m-thick (active) layer, before increasing and leading to the bell-shaped resistivity curve.⁵⁰ The increase in resistivity indicates the presence of a frozen layer, which is probably permafrost with interstitial ground ice. The specific resistivity of this layer reached 15–20 k Ω m in 1998 and decreased to 14–15 k Ω m in 2017, which is represented by a relative change of the apparent resistivity of –19%.

5 | DISCUSSION

5.1 | Methodological approach

The multimethod approach applied in this study allowed a detailed analysis of the evolution and dynamics of the Aget glacier forefield over the last two decades. Here, the long-term time series of measured ground surface temperatures constitute key information for understanding the ground thermal regime of the site.⁴² Combined with geodetic data, GST data enable assessment of the kinematic response to thermally driven processes occurring at the permafrost table, such as ice melt-induced subsidence.⁵⁰

The repetition of VES allowed the assessment of the evolution of resistivity values along a one-dimensional profile. The similar shape of the resistivity curves for 1998 and 2017 (or measured data point) gave confidence to the robustness of the datasets. However, the positioning of the repeated profiles (electrode configuration) as well as the context of a changing terrain (modification of the microtopography) in which the measurements are carried out yielded a certain margin of error that is not quantifiable.

The application of ERT enabled the delineation of frozen and unfrozen material.^{13,23,24,44} Resistivity values of 3–5 k Ω m could not directly be interpreted as thawing permafrost, because of the lithological composition of the landform having similar resistivity values. The combination of ERT and geodetic data indicated a direct relationship between surface processes and subsurface properties, consequently reducing the above-mentioned ambiguities.

5.2 | Ground temperature evolution

The ground surface thermal evolution observed at Aget (+0.3°C per decade) follows closely the warming trend of about +0.36°C per decade observed on average at various sites in the surrounding region over the last 20 years.^{3,51} The current ground surface conditions (MAGST of +0.66°C) reflect climate conditions that are no longer suitable for permafrost. This disequilibrium sets conditions that are not favorable for the long-term preservation of permafrost at depth. Thawing conditions are likely within the permafrost body as indicated by the relatively high WEqT values, which corroborate with the observed decrease in resistivity values of the frozen ground at depth.

5.3 | Ground ice distribution

Geomorphological indicators within the forefield suggest a former polythermal regime of the LIA Aget glacier. The presence of the GFL A and B complex in the lateral boundaries of the forefield signals the former displacement of frozen sediments by a cold glacier in its margins, while fluted moraines indicate temperate conditions in its central part. In the central section of the former glacier, where the bed topography is relatively flat, it is likely that the ice thickness (about 100 m according to the position of the lateral elevation reached by the glacier) was important enough for pressure and internal friction to yield pressure-melting point temperatures and thus a temperate state of the glacier base. Conversely, towards its margins, the glacier thickness was insufficient to prevent below freezing temperatures penetrating the glacier ice to its base in winter and propagating deeper into the ground, yielding cold englacial and subglacial conditions at the margins.⁵² The temperate subglacial thermal conditions in the center flow line of the glacier allowed basal sliding, and consequently the formation of fluted moraines, while the cold subglacial thermal conditions at the margins of the glacier allowed the preservation of pre-existing frozen sediments (permafrost conditions) and their displacement (GFL build-up). The original position of both GFL A and B at Aget before the LIA is unknown. However, estimating the potential source area of the debris constituting both GFL A and B and with regard to their post-LIA or current flow line, the former is not located upstream of the current locations of GFL A and B. There is no apparent feeding area above GFL B and only a very restricted one above GFL A, which is not adequate for the volume of the latter. Geomorphological indicators (e.g., furrows) suggest that the main sediment source was the southeastern flank of Mont Rogneux and that both frozen debris masses were significantly tectonized and displaced by the LIA glacier advance. The occurrence of fluted moraines or bedrock outcrops in large areas of the LIA glacier forefield shows that the glacier was largely deprived of superficial debris. However, during the interaction phase between the glacier and the pre-existing frozen sediments, it cannot be fully excluded that some debris-covered glacier ice could have been locally embedded within the frozen mass of debris, as high electrical resistivities that could refer to massive ground ice⁴⁴ were locally distinguished by geoelectrical measurements (Figures 6 and 12). The occurrence of relatively deep-seated and resistive (ice-rich) permafrost supports the hypothesis that the sediment masses were already frozen before the LIA glacier advance and are not consecutive to subglacial freezing. The latter process would have only allowed the development of permafrost at shallow depth.

5.4 | Ground ice evolution

Because of the varying ice content within the area of GFL A, the ground ice degradation signal is not uniform.⁶ In the back-creeping part, where interstitial ice is present, the degradation (here, expressed by change in resistivity) is the strongest (Ag-S06 BC, –44% change in ρ_a). Conversely, in the resistive patches of Ag-W06 and Ag-W08,

where an over-saturated ice content is likely to occur, the change in resistivity between 1998 and 2017 is relatively low (Ag-S08 AC, -14% change in ρ_a). As the warming of ground ice induces a relative liquid water-to-ice content ratio increase, a notable decrease in resistivity is expected in interstitial frozen layers as the melt water can fill the pores or build up thin skins at the contact of ice and rock particles. Smaller changes in resistivity in a layer of more massive ice can be explained by its lower capacity for water storage within the frozen ground structure. The rate of change in resistivity lies within the same order of magnitude as those observed on established monitoring sites in the Swiss Alps.³

5.5 | Ground ice melt

Along with resistivity changes, the permafrost degradation is also expressed by geometrical adjustments such as the ice melt-induced subsidence, namely the subsidence observed at the surface caused by the gradual melting of ice related to the porosity of its containing lithic structure. In areas where either the amplitude of the compressive/extensive flow is not pronounced (Ag-116, Ag-148, and Ag-149), or a compressive flow pattern dominates (Ag-023 and Ag-024), the contribution of the melt of excess ice to surface elevation loss has been the highest, ranging between 0.06 and 0.12 m/year. The agreement between the annual subsidence rate observed in these areas with the ground thawing index—the warmer it is, the larger the subsidence is—shows that the melting of excess ground ice is dominantly occurring at the permafrost table and is driven by summer ground surface heating.

In the areas dominated by an extensive flow pattern, the loss in surface elevation is mainly explained by geometric thinning. Nevertheless, the thinning of the moving mass probably favors the deepening of the permafrost table as a thermal response⁴⁹ in which the contribution of ice melt to surface elevation loss observed at Aget has so far been limited (0.01–0.04 m/year) or nonexistent.

The applied method was exploratory and might suffer some deficiencies. However, the order of magnitude of the subsidence rate due to the melting of excess ice estimated on Aget GFL A fits with observations made recently on various rock glaciers in the European Alps.^{51,53,54}

5.6 | Kinematic evolution

From 2001 to 2010, the kinematic behavior of the Aget back-creeping GFL A still fitted with the regional trend of surface velocities observed on other rock glaciers. Since then at least, it has followed an atypical evolution of nonaccelerating surface velocities (Figure 9).³ Combined with ground ice degradation, this behavior indicates a thermo-hydronechanical response to changes in the surface energy balance.⁵⁵ The warming of ground ice induces an increase of the liquid water-to-ice content ratio, which in turn should favor permafrost shearing at depth. An acceleration of the moving mass

should be expected, as regionally observed on many rock glaciers.^{43,55} However, the observations made at Aget show a divergent reaction to warming permafrost conditions, meaning that the surface creep velocities have gradually stopped to accelerate and even started to decrease.

The combined analysis of kinematic, resistivity, and GST data highlights various processes which should contribute to the most recent decelerating kinematic trend of the back-creeping GFL A. Subsidence rates of 0.10–0.12 m/year have been observed in the frontal and northeastern margins of the GFL despite the compressive flow pattern of the former and the absence of horizontal displacement of the latter. This represents about 2 m of thinning in 20 years, or a decrease of about 10% of the GFL thickness above the shear horizon. Along with decreasing resistivity values, this surface lowering indicates the melting of excess ground ice. In this case, the ongoing melt of ground ice leads progressively to a decrease in the thickness of the frozen column above the shear horizon and thus a decrease in the intrapermafrost pore pressure and the driving stress at the shear horizon. An almost similar development has been observed in the last few decades on the Gruben rock glacier.⁵¹ In advanced states of permafrost degradation, as should probably occur at the lowermost section of GFL A, the shear resistance is also expected to increase as interlocking becomes more important,^{43,55} consequently and progressively leading the landform to a state of inactivity. One should note nevertheless that the alteration of the kinematic behavior has been reduced most in the uppermost part of GFL A, where the ground ice content is largest and the permafrost degradation has been less pronounced for the last 20 years, as revealed by the limited resistivity changes at Ag-S06.

In the upper and central areas of the GFL, the kinematic data illustrate a loss of surface elevation essentially driven by a flow pattern of extension explained by a topographical step and the divergent flow at the lateral front of the GFL. The overall thinning of landforms in these areas yields a decrease in stresses exerted at the shear horizon,⁴³ contributing to progressively reduce its kinematic activity. It could be expected that the continuing degradation of permafrost and thinning of the GFL will lead to its transition from a kinematic active to inactive state over the next decades. A similar process should have occurred in GFL B during the first half of the 20th century.

6 | CONCLUSION

This study gathers and analyses over 20 years of data collected on the Aget glacier forefield, particularly focussing on its actively back-creeping GFL to understand its recent morphodynamical evolution. Together with geodetic measurements performed on a yearly basis, the geoelectrical surveys carried out in 1998 and repeated in 2017 allowed us to assess the evolution of ground ice within the GFL and its kinematic evolution.

The comparison between the 1998 and 2017 geoelectrical surveys revealed a systematic yet varying decrease of measured

apparent resistivity of the frozen ground, indicating a heterogeneous degradation of permafrost and melt of ground ice in response to increasing ground surface temperatures. At the margins of the GFL, subsidence induced by the melt of excessive ice at the permafrost table and reaching up to 0.12 m/year was found. In the central zone of the GLF, surface elevation loss appeared to have been mainly the result of a decrease in the thickness of the moving mass due to its extensive flow pattern. Together, these processes contribute to a decrease of the stresses at the shear horizon, progressively driving the landform towards a transitional state of kinematic activity.

The heterogeneous distribution of the ground ice content throughout the GFL as well as the nonuniform geometrical behavior of the landform indicate the complexity and limitations in drawing a complete and thorough understanding of the driving processes contributing to its morphodynamical evolution. However, these first findings highlight the necessity of long-term monitoring and the complementarity of application of different methodological approaches to provide a comprehensive picture of the ongoing changes.

ACKNOWLEDGEMENTS

We thank PERMOS for support with the collection of the GST and GNSS data. Open access funding provided by Universite de Fribourg.

CONFLICT OF INTEREST

The authors declare no conflicts of interest.

AUTHOR CONTRIBUTIONS

JW and RD designed the research. RD conducted field investigations until 2016. JW conducted field investigations since then, prepared data, made all the figures, and wrote the initial version of the paper. RD improved the manuscript.

DATA AVAILABILITY STATEMENT

The data that support the findings of this study are available from the corresponding author upon reasonable request.

ORCID

Julie Wee  <https://orcid.org/0000-0001-7210-793X>

REFERENCES

- Oriove B, Wiegandt E, Luckman BH. *Darkening Peaks: Glacier Retreat, Science, and Society*. Univ of California Press; 2008.
- Sommer C, Malz P, Seehaus TC, Lippel S, Zemp M, Braun MH. Rapid glacier retreat and downwasting throughout the European Alps in the early 21st century. *Nat Commun*. 2020;11(1):1-10. doi:10.1038/s41467-020-16818-0
- PERMOS. In: Noetzi J, Pellet C, Staub B, eds. *Permafrost in Switzerland 2014/2015 to 2017/2018, Glaciological Report Permafrost No. 16-19*. Cryospheric Commission of the Swiss Academy of Sciences; 2019.
- Zemp M, Haeberli W, Hoelzle M, Paul F. Alpine glaciers to disappear within decades? *Geophys Res Lett*. 2006;33(13):1-4. doi:10.1029/2006GL026319
- Fischer M, Huss M, Hoelzle M. Surface elevation and mass changes of all Swiss glaciers 1980-2010. *Cryosphere*. 2015;9(2):525-540. doi:10.5194/tc-9-525-2015
- Mollaret C, Hilbich C, Pellet C, Flores-Orozco A, Delaloye R, Hauck C. Mountain permafrost degradation documented through a network of permanent electrical resistivity tomography sites. *Cryosphere*. 2019;13(10):2557-2578. doi:10.5194/tc-13-2557-2019
- Haeberli W. Investigating glacier-permafrost relationships in high-mountain areas: historical background, selected examples and research needs. *Geol Soc Lond Spec Publ*. 2005;242(1):29-37. doi:10.1144/GSL.SP.2005.242.01.03
- Bosson JB, Deline P, Bodin X, et al. The influence of ground ice distribution on geomorphic dynamics since the Little Ice Age in proglacial areas of two cirque glacier systems. *Earth Surf Process Landf*. 2015;40(5):666-680. doi:10.1002/esp.3666
- Haeberli W. Holocene Push-Moraines in Alpine Permafrost. *Geogr Ann Ser B*. 1979;61(1/2):43-48. doi:10.2307/520513
- Maisch M, Haeberli W, Frauenfelder R, Käab A, Rothenbühler C. Late-glacial and Holocene evolution of glaciers and permafrost in the Val Muragl, Upper Engadin, Swiss Alps. In: *Proceedings 8th International Conference on Permafrost*. Vol 2; 2003:717-722.
- Etzelmüller B, Hagen JO. Glacier-permafrost interaction in Arctic and alpine mountain environments with examples from southern Norway and Svalbard. *Geol Soc Lond Spec Publ*. 2005;242(1):11-27. doi:10.1144/GSL.SP.2005.242.01.02
- Kneisel C, Käab A. Mountain permafrost dynamics within a recently exposed glacier forefield inferred by a combined geomorphological, geophysical and photogrammetrical approach. *Earth Surf Process Landf*. 2007;32(12):1797-1810. doi:10.1002/esp.1488
- Ribolini A, Guglielmin M, Fabre D, et al. The internal structure of rock glaciers and recently deglaciated slopes as revealed by geoelectrical tomography: insights on permafrost and recent glacial evolution in the Central and Western Alps (Italy-France). *Quat Sci Rev*. 2010;29(3-4):507-521. doi:10.1016/j.quascirev.2009.10.008
- Haeberli W. Permafrost-glacier relationships in the Swiss Alps-today and in the past. In: *Proceedings of the Fourth International Conference on Permafrost*. National Academy Press; 1983:415-420.
- Ivy-Ochs S, Kerschner H, Maisch M, Christl M, Kubik PW, Schlüchter C. Latest Pleistocene and Holocene glacier variations in the European Alps. *Quat Sci Rev*. 2009;28(21-22):2137-2149. doi:10.1016/j.quascirev.2009.03.009
- Haeberli W. Mountain permafrost – research frontiers and a special long-term challenge. *Cold Reg Sci Technol*. 2013;96:71-76. doi:10.1016/j.coldregions.2013.02.004
- Reynard E, Lambiel C, Delaloye R, et al. Glacier/permafrost relationships in forefields of small glaciers (Swiss Alps). In: *Proceedings 8th International Conference on Permafrost*. Vol 2; 2003:947-952.
- Kneisel C. Permafrost in recently deglaciated glacier forefields-measurements and observations in the eastern Swiss Alps and northern Sweden. *Z Geomorphol*. 2003;47(3):289-305. doi:10.1127/zfg/47/2003/289
- Slymaker O. Criteria to Distinguish Between Periglacial, Proglacial and Paraglacial Environments. *Quaest Geogr*. 2011;30(1):85-94. doi:10.2478/v10117-011-0008-year
- Carrivick JL, Heckmann T. Short-term geomorphological evolution of proglacial systems. *Geomorphology*. 2017;287:3-28. doi:10.1016/j.geomorph.2017.01.037
- Cogley JG, Hock R, Rasmussen LA, et al. Glossary of glacier mass balance and related terms. *IHP-VII technical documents in hydrology*. 2011:86.
- Haeberli W, Huggel C, Paul F, Zemp M. 13.10 Glacial Responses to Climate Change. *Treat Geomorphol* Elsevier. 2013;152-175. doi:10.1016/B978-0-12-374739-6.00350-X
- Bosson JB, Lambiel C. Internal Structure and Current Evolution of Very Small Debris-Covered Glacier Systems Located in Alpine

- Permafrost Environments. *Front Earth Sci.* 2016;4:1-17. doi:[10.3389/feart.2016.00039](https://doi.org/10.3389/feart.2016.00039)
24. Kunz J, Kneisel C. Glacier–Permafrost Interaction at a Thrust Moraine Complex in the Glacier Forefield Muragl, Swiss Alps. *Geosciences.* 2020;10(6):205. doi:[10.3390/geosciences10060205](https://doi.org/10.3390/geosciences10060205)
 25. Delaloye R. *Contribution à l'étude du pergélisol de montagne en zone marginale.* Vol. 10. GeoFocus. University of Fribourg; 2004.
 26. Evin M. Les relations existant entre la moraine de refoulement, le glacier rocheux et le glacier du Petit Age Glaciaire dans le Haut Vallon d'Asti (Queyras, Alpes du Sud, France). *Geogr Fis Din Quat.* 1992;15: 101-105.
 27. Kneisel C. Occurrence of surface ice and ground ice/permafrost in recently deglaciated glacier forefields, St. Moritz area, Eastern Swiss Alps. In: *PERMAFROST - Seventh International Conference.* Vol 55. Collection Nordicana; 1998:7.
 28. Delaloye R, Devaud G. Permafrost distribution in the proglacial margins of the Challand, Aget and Sanetschhorn Glaciers (Valais, Swiss Alps). *Permafrost distribution in the proglacial margins of the Challand, Aget and Sanetschhorn Glaciers (Valais, Swiss Alps).* Published online 2000:87–96.
 29. Lugon R, Delaloye R, Serrano E, Reynard E, Lambiel C, González-Trueba JJ. Permafrost and Little Ice Age glacier relationships, Posets Massif, Central Pyrenees, Spain. *Permafrost Periglacial Process.* 2004;15(3): 207-220. doi:[10.1002/ppp.494](https://doi.org/10.1002/ppp.494)
 30. Monnier S, Camerlynck C, Rejiba F, Kinnard C, Feuillet T, Dhemaied A. Structure and genesis of the Thabor rock glacier (Northern French Alps) determined from morphological and ground-penetrating radar surveys. *Geomorphology.* 2011;134(3–4):269-279. doi:[10.1016/j.geomorph.2011.07.004](https://doi.org/10.1016/j.geomorph.2011.07.004)
 31. Lambiel C, Delaloye R. Contribution of real-time kinematic GPS in the study of creeping mountain permafrost: examples from the Western Swiss Alps. *Permafrost Periglacial Process.* 2004;15(3):229-241. doi:[10.1002/ppp.496](https://doi.org/10.1002/ppp.496)
 32. Käähb A, Kneisel C. Permafrost creep within a recently deglaciated glacier forefield: Muragl, Swiss Alps. *Permafrost Periglacial Process.* 2006; 17(1):79-85. doi:[10.1002/ppp.540](https://doi.org/10.1002/ppp.540)
 33. Monnier S, Kinnard C. Pluri-decadal (1955–2014) evolution of glacier–rock glacier transitional landforms in the central Andes of Chile (30–33° S). *Earth Surf Dyn.* 2017;5(3):493-509. doi:[10.5194/esurf-5-493-2017](https://doi.org/10.5194/esurf-5-493-2017)
 34. Monnier S, Kinnard C. Reconsidering the glacier to rock glacier transformation problem: New insights from the central Andes of Chile. *Geomorphology.* 2015;238:47-55. doi:[10.1016/j.geomorph.2015.02.025](https://doi.org/10.1016/j.geomorph.2015.02.025)
 35. Kenner R. Geomorphological analysis on the interaction of Alpine glaciers and rock glaciers since the Little Ice Age. *Land Degrad Deve.* 2019;30(5):580-591. doi:[10.1002/dr.3238](https://doi.org/10.1002/dr.3238)
 36. Seppi R, Carturan L, Carton A, et al. Decoupled kinematics of two neighbouring permafrost creeping landforms in the Eastern Italian Alps. *Earth Surf Process Landf.* 2019;44(13):2703-2719. doi:[10.1002/esp.4698](https://doi.org/10.1002/esp.4698)
 37. Seppi R, Zanoner T, Carton A, et al. Current transition from glacial to periglacial processes in the Dolomites (South-Eastern Alps). *Geomorphology.* 2015;228:71-86. doi:[10.1016/j.geomorph.2014.08.025](https://doi.org/10.1016/j.geomorph.2014.08.025)
 38. Gärtner-Roer I, Bast A. (Ground) Ice in the Proglacial Zone. In: *Geomorphology of Proglacial Systems.* Springer; 2019:85-98. doi:[10.1007/978-3-319-94184-4_6](https://doi.org/10.1007/978-3-319-94184-4_6)
 39. Boeckli L, Brenning A, Gruber S, Noetzi J. Permafrost distribution in the European Alps: calculation and evaluation of an index map and summary statistics. *Cryosphere.* 2012;6(4):807-820. doi:[10.5194/tc-6-807-2012](https://doi.org/10.5194/tc-6-807-2012)
 40. Wee J, Delaloye R. Dynamics of the Aget back-creeping push-moraine from 1998 to 2017. In: Deline P, Bodin X, Ravanel L, eds. *5th European Conference on Permafrost, Book of Abstract;* 2018: 543-544.
 41. Werner P. Connaître la nature en Valais-la flore. In: *Pillet, Martigny.-1997. Régression Des Plantes Messicoles En Valais (Alpes Suisses) et Tentatives de Conservation.* Actes Du Colloque Faut-Il Sauver Les Mauvaises Herbes. 1988:43-47.
 42. Haerberli W. Die Basis-Temperatur der winterlichen Schneedecke als möglicher indikator für die Verbreitung von permafrost in den Alpen. *Zeitschrift für Gletscherkunde und Glazialgeologie.* 1973;9(1-2): 221-227.
 43. Cicoira A, Marcer M, Gärtner-Roer I, Bodin X, Arenson LU, Vieli A. A general theory of rock glacier creep based on in-situ and remote sensing observations. *Permafrost Periglacial Process.* 2021;32(1):139-153. doi:[10.1002/ppp.2090](https://doi.org/10.1002/ppp.2090)
 44. Hauck C, Kneisel C. *Applied Geophysics in Periglacial Environments.* Cambridge University Press; 2008. doi:[10.1017/CBO9780511535628](https://doi.org/10.1017/CBO9780511535628)
 45. Loke MH. RES1D ver. 1.0 1-D Resistivity, UP & SIP Inversion and forward modeling. Published online 2001.
 46. Lines LR, Treitel S. A review of least-squares inversion and its application to geophysical problems. *Geophys Prospect.* 1984;32(2):159-186. doi:[10.1111/j.1365-2478.1984.tb00726.x](https://doi.org/10.1111/j.1365-2478.1984.tb00726.x)
 47. Shumskii PA. Principles of Structural Glaciology: The Petrography of Fresh-Water Ice as a Method of Glaciological Investigation; 1964.
 48. PERMOS. In: Noetzi J, Pellet C, eds. *Swiss Permafrost Bulletin 2019/2020.* 2021.
 49. Haerberli W, Vonder Mühl D. On the characteristics and possible origins of ice in rock glacier permafrost. *Zeitschrift Geomorphol Suppl.* 1996;104:43-57.
 50. Delaloye R, Lambiel C. Typology of vertical electrical soundings for permafrost/ground ice investigation in the forefields of small alpine glaciers. In: Hauck C, Kneisel C, eds. *Applied Geophysics in Periglacial Environments.* Cambridge University Press; 2008:101-108. doi:[10.1017/CBO9780511535628.006](https://doi.org/10.1017/CBO9780511535628.006)
 51. Gärtner-Roer I, Brunner N, Delaloye R, Haerberli W, Käähb A, Thee P. Glacier-permafrost relations in a high-mountain environment: 5 decades of kinematic monitoring at the Gruben site, Swiss Alps. *The Cryosphere.* 2021;16(5):1-30.
 52. Gilbert A, Vincent C, Wagnon P, Thibert E, Rabatel A. The influence of snow cover thickness on the thermal regime of Tête Rousse Glacier (Mont Blanc range, 3200 m a.s.l.): Consequences for outburst flood hazards and glacier response to climate change. *J Geophys Res Earth.* 2012;117(F4):n/a-n/a. doi:[10.1029/2011JF002258](https://doi.org/10.1029/2011JF002258)
 53. Cusicanqui D, Rabatel A, Vincent C, Bodin X, Thibert E, Francou B. Interpretation of volume and flux changes of the Laurichard rock glacier between 1952 and 2019, French Alps. *J Geophys Res Earth.* 2021; 126(9):e2021JF006161. doi:[10.1029/2021JF006161](https://doi.org/10.1029/2021JF006161)
 54. Bearzot F, Garzonio R, Di Mauro B, et al. Kinematics of an Alpine rock glacier from multi-temporal UAV surveys and GNSS data. *Geomorphology* Published online. 2022;402:108116. doi:[10.1016/j.geomorph.2022.108116](https://doi.org/10.1016/j.geomorph.2022.108116)
 55. Staub B, Lambiel C, Delaloye R. Rock glacier creep as a thermally-driven phenomenon: A decade of inter-annual observations from the Swiss Alps. Published online 2016:2.

How to cite this article: Wee J, Delaloye R. Post-glacial dynamics of an alpine Little Ice Age glacialized frozen landform (Aget, western Swiss Alps). *Permafrost and Periglacial Process.* 2022;33(4):370-385. doi:[10.1002/ppp.2158](https://doi.org/10.1002/ppp.2158)

Publication II: Wee et al. (2024), The Cryosphere

Characterizing ground ice content and origin to better understand the seasonal surface dynamics of the Gruben rock glacier and the adjacent Gruben debris-covered glacier (southern Swiss Alps)

Authors **Julie Wee**, Sebastián Vivero, Tamara Mathys, Coline Mollaret, Christian Hauck, Christophe Lambiel, Jan Beutel, Wilfried Haerberli

Journal The Cryosphere

Year 2024

DOI doi.org/10.5194/tc-18-5939-2024

Citation Wee, J., Vivero, S., Mathys, T., Mollaret, C., Hauck, C., Lambiel, C., Beutel, J., and Haerberli, W.: Characterizing ground ice content and origin to better understand the seasonal surface dynamics of the Gruben rock glacier and the adjacent Gruben debris-covered glacier (southern Swiss Alps), *The Cryosphere*, 18, 5939–5963, <https://doi.org/10.5194/tc-18-5939-2024>, 2024.

Short summary

The processes governing the seasonal surface dynamics of the Gruben rock glacier, its complex contact zone, and its adjacent debris-covered glacier were investigated. An attempt to discriminate glacial from periglacial processes where glacier-permafrost occurred was initiated as it is assumed that their spatio-temporal patterns of surface change and geophysical signatures are (mostly) different. A multi-method and interdisciplinary approach were applied to grasp a detailed representation of the distribution of ground ice content and origin as well as the seasonal kinematic signal of the investigated landforms.

Main findings

- The magnitude of ice melt-induced subsidence was the highest in the complex contact zone where still existing, isolated remnants of buried surface ice were detected by the geophysical investigations.
- Pronounced surface elevation loss due to extending flow and downslope movement was observed on the glacier forefield-connected rock glacier, which reflects the dominance of permafrost creep deformation.
- The kinematic signature of these two distinct morphological zones attests of their geomorphological heritage from the Holocene and LIA and highlights the interrelationship between glacial and periglacial processes occurring in the so-called complex contact zone.
- The resilience of the ground ice to a warming atmosphere, in particular in the permafrost of the rock glacier was revealed.
- This was also found for the glacier ice beneath the thickening debris-cover of the Gruben glacier terminus, which is in complete disequilibrium with the current climate.

Contribution of the PhD candidate

Designed the research, collected the GST and GNSS data since 2016, planned, coordinated, and participated in the geophysical campaigns, processed and analysed the GST, GNSS data, and the geophysical data. S. Vivero conducted the UAV campaigns and processed the UAV-derived data with the PhD candidate. T. Mathys and C. Mollaret contributed to the development of the PJI code. J. Beutel provided data of one of the permanent GNSS station. C. Hauck and C. Lambiel supervised the study design. W. Haeberli provided his knowledge from earlier studies. Preparation of the manuscript and the figures. All co-authors were involved in the discussion and in the improvement of the manuscript.

Data availability

GST and TGS data are partly available on the PERMOS data portal (<https://www.permos.ch/data-portal>). All other data are available upon request.



Characterizing ground ice content and origin to better understand the seasonal surface dynamics of the Gruben rock glacier and the adjacent Gruben debris-covered glacier (southern Swiss Alps)

Julie Wee¹, Sebastián Vivero¹, Tamara Mathys¹, Coline Mollaret¹, Christian Hauck¹, Christophe Lambiel², Jan Beutel³, and Wilfried Haeblerli⁴

¹Department of Geosciences, University of Fribourg, 1700 Fribourg, Switzerland

²Institute of Earth Surface Dynamics, University of Lausanne, 1015 Lausanne, Switzerland

³Department of Computer Science, University of Innsbruck, 6020 Innsbruck, Austria

⁴Geography Department, University of Zurich, 8057 Zurich, Switzerland

Correspondence: Julie Wee (julie.wee@unifr.ch)

Received: 30 April 2024 – Discussion started: 8 May 2024

Revised: 14 October 2024 – Accepted: 2 November 2024 – Published: 18 December 2024

Abstract. Over the recent years, there have been focused international efforts to coordinate the development and compilation of rock glacier inventories. Nevertheless, in some contexts, identifying and characterizing rock glaciers can be challenging as complex conditions and interactions, such as glacier–rock–glacier interactions, can yield landforms or landform assemblages that are beyond a straightforward interpretation and classification through ordinary visual means alone. To gain a better understanding of the spatial and temporal complexity of the ongoing processes where glacier–permafrost interactions have occurred, the characterization of the subsurface of the Gruben rock glacier and its adjacent complex contact zone with the then more extended Little Ice Age Gruben glacier is quantitatively assessed using a petrophysical joint inversion (PJI) scheme, based on electrical resistivity (ERT) and refraction seismic (RST) data. Surface dynamics are assessed using both in situ and close-range remote sensing techniques to monitor daily and seasonal displacements and to monitor landform-wide surface changes at high spatial resolution, respectively. Both the geophysical and geodetic surveys allowed two zones to be identified: the rock glacier zone and the complex contact zone where both permafrost and embedded surface ice are present. In the complex contact zone extremely high ice contents (estimated up to 85 %) were found. Widespread supersaturated permafrost conditions were found in the rock glacier zone. Surface displacement rates in this zone are typical of permafrost creep

behaviour, with a gradual acceleration in late spring and a gradual deceleration in winter. Moreover, the coherent nature of the rock glacier zone surface deformation contrasts with the back-creeping and slightly chaotic surface deformation of the complex contact zone. Favouring a multi-method approach allowed a detailed representation of the spatial distribution of ground ice content and origin, which enabled us to discriminate glacial from periglacial processes as their spatio-temporal patterns of surface change and geophysical signatures are (mostly) different.

1 Introduction

The high-alpine environment is characterized by glacial and periglacial processes and landforms, which express varying degrees of sensitivity to the current warming trend (Carturan et al., 2020; Cicoira et al., 2021; Huss and Fischer, 2016; Kellerer-Pirklbauer et al., 2024; Mollaret et al., 2019). The dynamic response of these phenomena and landforms to this trend is not uniform in space or in time as the occurrence of ice in high-mountain environments can be found under a wide spectrum of possible conditions, processes, materials, origins, landform settings, and assemblages (Bosson and Lambiel, 2016; Cusicanqui et al., 2023; Monnier et al., 2014; Navarro et al., 2023). For instance, surface ice not only encompasses landforms of glacial origins, such as glaciers,

debris-covered glaciers, or dead-ice masses, but also smaller ice occurrences such as perennial ice patches or glacierets, while various forms of ground ice (also termed subsurface ice) relate to long-term thermal aspects of ice formation and preservation in permafrost conditions. In most contexts, there is a clear differentiation between landforms containing surface ice and those that contain ground ice, as their morphologies and kinematic behaviour are distinctive (Haerberli et al., 2024). However, in environments where glacial and periglacial processes occurred or still occur simultaneously, the typology of the ice content and associated processes of the resulting phenomena and landforms can be delicate to assess as they are the product of complex interconnected glacial and periglacial processes (Monnier et al., 2014; Vivero et al., 2021).

In the Alps, perennially frozen-debris landforms at many sites have coexisted and episodically or continuously interacted with glaciers (Bosson et al., 2015; Haerberli, 2005; Maisch et al., 2003; Ribolini et al., 2010). The Little Ice Age characterized the apogee of the last interaction phase (ca. 1350–1850 in the Alps; Ivy-Ochs et al., 2009) during which small polythermal cirque glaciers (Etzelmüller and Hagen, 2005) altered the thermal regime of their forefields and the spatial distribution of pre-existing perennially frozen sediments (Kneisel and Käab, 2007; Kunz and Kneisel, 2020; Seppi et al., 2019; Wee and Delaloye, 2022).

As geomorphological and glaciological systems, environments in which glacier–permafrost interactions have occurred are the result of a wide and interconnected spectrum of glacial, periglacial, nival, hydrological, gravitational, and mass-wasting processes (Etzelmüller and Hagen, 2005; Ballantyne, 2018). Such interactions give rise to the coexistence of a diverse range of landforms, such as glacio-genic debris, glacier ice masses including debris-covered ice, and buried dead glacier ice, but also thermally controlled (permafrost-related), viscous creeping debris masses (rock glaciers) disturbed and sometimes partly displaced by the loading of glacial stress (glaciotectonic). Besides geometrical alteration, these glaciectonized frozen landforms may encompass sporadic embedding and burial of glacier ice (sedimentary ice) and smaller forms of surface ice into frozen debris.

Post-glacial dynamics of these systems and associated landforms comprise spatio-temporally complex and interlaced glacial, periglacial, paraglacial, hydrological, and mass-wasting processes, whose full understanding requires high-resolution, quantitative, multi-method, and interdisciplinary approaches. Recent studies have manifested a growing interest in investigating these systems to achieve a better understanding of processes resulting from glacier–permafrost interactions (Gärtner-Roer and Bast, 2019; Kenner, 2019; Monnier and Kinnard, 2015; Seppi et al., 2015, 2019). New insights into the latter resulted from in-depth geophysical prospections, high-resolution archival and digital photogrammetry, and systematic kinematic and ground

surface temperature monitoring (Bosson and Lambiel, 2016; Gärtner-Roer et al., 2022; Kunz and Kneisel, 2020; Wee and Delaloye, 2022), which enabled the extension of previous studies on the understanding of glacier–permafrost interactions (Käab et al., 1997; Kneisel and Käab, 2007; Reynard et al., 2003).

In a context of growing interest and effort to coordinate the development of rock glacier inventories as part of large-scale approaches to quantify the impact of climate change on permafrost, such as the Global Terrestrial Network for Permafrost and IPA Action Group Rock Glacier Inventories and Kinematics (IPA Action Group RGIK, 2023; Streletskiy et al., 2021), especially when automated remote sensing approaches are used (Robsons et al., 2020; Sun et al., 2024), confusion and misinterpretations may arise in complex geomorphological settings (Whalley, 2020). This is why there is a necessity for ground truth data to create clarity in order to better interpret and analyse the climatic, hydrological, and geomorphological significance of rock glaciers, in particular where complex geomorphological contexts (e.g. glacier–permafrost interactions) hamper simple and straightforward “either-or” classification (Haerberli et al., 2024).

This contribution aims to understand the extent to which ground ice properties influence the surface dynamics of (a) a rock glacier partially affected by the advance of a glacier during the Little Ice Age and (b) a nearby debris-covered glacier terminus at Gruben (southern Swiss Alps), on the basis of in situ geodetic, close-range remote sensing and geophysical measurements. The extent and properties of ground ice is assessed through the analysis of the combination of refraction seismic and geoelectrical resistivity measurements by applying the petrophysical joint inversion approach (Mollaret et al., 2020; Wagner et al., 2019). The kinematic behaviour of a rock glacier, of a complex contact zone (see Haerberli et al., 2024), and of the adjacent debris-covered glacier is investigated, with an emphasis on the contribution of ice-melt-induced subsidence to surface elevation changes. This is achieved by combining the analysis of seasonal GNSS and uncrewed aerial vehicle (UAV) surveys, as well as continuous time series of displacements from fixed differential global navigation satellite system (dGNSS) stations. This study underlines the importance of a multi-method and multi-disciplinary approach in understanding and discriminating driving processes contributing to the surface dynamics of complex periglacial landforms.

2 Study site

The Gruben site (46°10′22″ N, 7°58′09″ E; Fig. 1) is located in the Saas Valley in the southern Swiss Alps. It is characterized by the rapidly shrinking debris-covered cold tongue of the polythermal Gruben glacier below the western face of the Fletschhorn (3985 m a.s.l.); the continuously advancing, perennially frozen, Gruben glacier-forefield-connected

rock glacier below the south-eastern flank of the Rothorngrat (3104 m a.s.l.); and a complex contact zone of the then more extended Little Ice Age glacier and the rock glacier permafrost (Haerberli et al., 2024). During its Little Ice Age (LIA) maximal extent, the margins of the Gruben polythermal glacier overrode the uppermost zone of the pre-existing Gruben rock glacier (Gärtner-Roer et al., 2022; Kääh et al., 1997), consequently altering the thermal regime, spatial distribution of ground ice, and surface morphology of this zone. The morphological signature of this glacier–permafrost contact and interaction is expressed by glaciotectionics (compressive ridges and furrows perpendicular to the stress exerted by the LIA glacier advance) and thermokarstic features, the latter inferring the presence of buried massive ground ice. Geometrical changes and reoriented stress fields in this zone are expressed by lateral back-creeping (in the direction of the topographic thalweg formerly occupied by the glacier) and enhanced surface elevation changes mainly due to ice-melt-induced subsidence. In contrast to the complex contact zone, the rock glacier displays longitudinal ridges and furrows parallel to its extending flow field. Its kinematic behaviour is rather constant over time (from 1994 to present day) with horizontal surface velocities ranging between 0.3 and 1.0 m yr⁻¹ and mean vertical changes from -0.1 to -0.5 m yr⁻¹ mainly due to the downslope creep movement and permafrost thaw in summer (Gärtner-Roer et al., 2022; Kääh et al., 1997).

The debris-covered glacier tongue of the polythermal Gruben glacier (south-eastern part in Fig. 1) is characterized by a rather chaotic surface morphology; however, a pattern of somewhat subdued transverse ridges and furrows from compressing flow is discernible. Earlier borehole temperature investigations (Haerberli, 1976) revealed ice temperatures of -1 to -2 °C within the tongue of the glacier, which was frozen to its bed at the margins (i.e. cold-based glacier margins) but was temperate at its upglacier base (see Fitzel Müller and Hagen, 2005). Surface elevation changes express strong signs of downwasting: the central zone shows important rates of ice-melt-induced subsidence, gradually decreasing towards the margins, inferring the rapid thinning and vanishing of (cold) glacier ice (Gärtner-Roer et al., 2022).

Winter equilibrium temperature (WEqT; earlier mostly called BTS – bottom temperature of the winter snow cover) values of the measured ground surface temperature at Gruben between 2015 and 2023 are evidence that permafrost is still thermally active – i.e. winter freezing penetrates down to the permafrost table (Gärtner-Roer et al., 2022; Noetzi and Pellet, 2023). However, the mean annual ground surface temperature (MAGST) measured between 2015 and 2023 in this complex contact zone is 0.39 °C, which is significantly (almost 4-fold) colder than the MAGST measured in the rock glacier zone (downslope of the complex contact zone; see Fig. 1), which is 1.27 °C (Fig. 2a). This infers that permafrost conditions at depth are in strong thermal disequilibrium with current thermal conditions at the surface (Noetzi and Pel-

let, 2023). Moreover, an ongoing warming trend of 1.51 °C per decade has been documented on the Gruben rock glacier and complex contact zone, essentially due to summer ground surface warming (Fig. 2b).

Following two lake outburst events in 1968 and 1979, both triggering devastating debris flows down to the main valley, important hazard protection work was carried out, supported by comprehensive field measurements (Kääh and Haerberli et al., 2001; Gärtner-Roer et al., 2022). These integrative glacier and permafrost investigations (Haerberli, 2005) document specific climate-related aspects for the Gruben site, which seem to be quite characteristic for the evolution of cold mountain regions in general. As part of a complex glacier–permafrost system, long-term creep and the advance of perennially frozen-debris masses – here the Gruben rock glacier – represent a comparably stable element with low hazard potential. Much more dynamic and dangerous is the development of lakes in a highly unstable environment of dead ice, locally frozen ground, and thermokarst phenomena (here the various Gruben lakes). Perhaps the most serious and most difficult-to-handle phenomenon is the deep and for very long time periods irreversible warming, degradation, and thaw of perennially frozen rock walls – here especially the north-exposed frozen rock walls south of the glacier, where rockfall and rock avalanche activity increased for decades already. The evolution must be carefully observed, and lake volumes must be kept small in order to avoid dangerous impact and flood waves.

3 Methods

To overcome the limitations in interpreting results that can arise when techniques are applied separately, this study favours a multi-method approach using recent and high-resolution datasets (Fig. 3). The characterization of frozen ground is quantitatively assessed in this study using the newly developed petrophysical joint inversion (PJI) approach (Mollaret et al., 2020; Wagner et al., 2019), based on the application of electrical resistivity tomography and refraction seismic tomography, which have complementary sensitivities to ice-to-water and air phase changes (e.g. Hauck et al., 2011). This novel approach allows not only the quantification of the ice content, but also the quantification of super-saturated conditions using non-invasive geophysical methods. Surface dynamics are assessed through a geodetic approach, which relies on differential global navigation satellite system (dGNSS) observations for high-temporal-resolution and repeated UAV-based imagery acquisition combined with structure-from-motion (SfM) three-dimensional (3D) reconstruction for high-resolution topographic analysis. Lastly, the combination of geodetics and geophysics allows us to link spatially variable ground ice contents with changes over time for different ice origins.

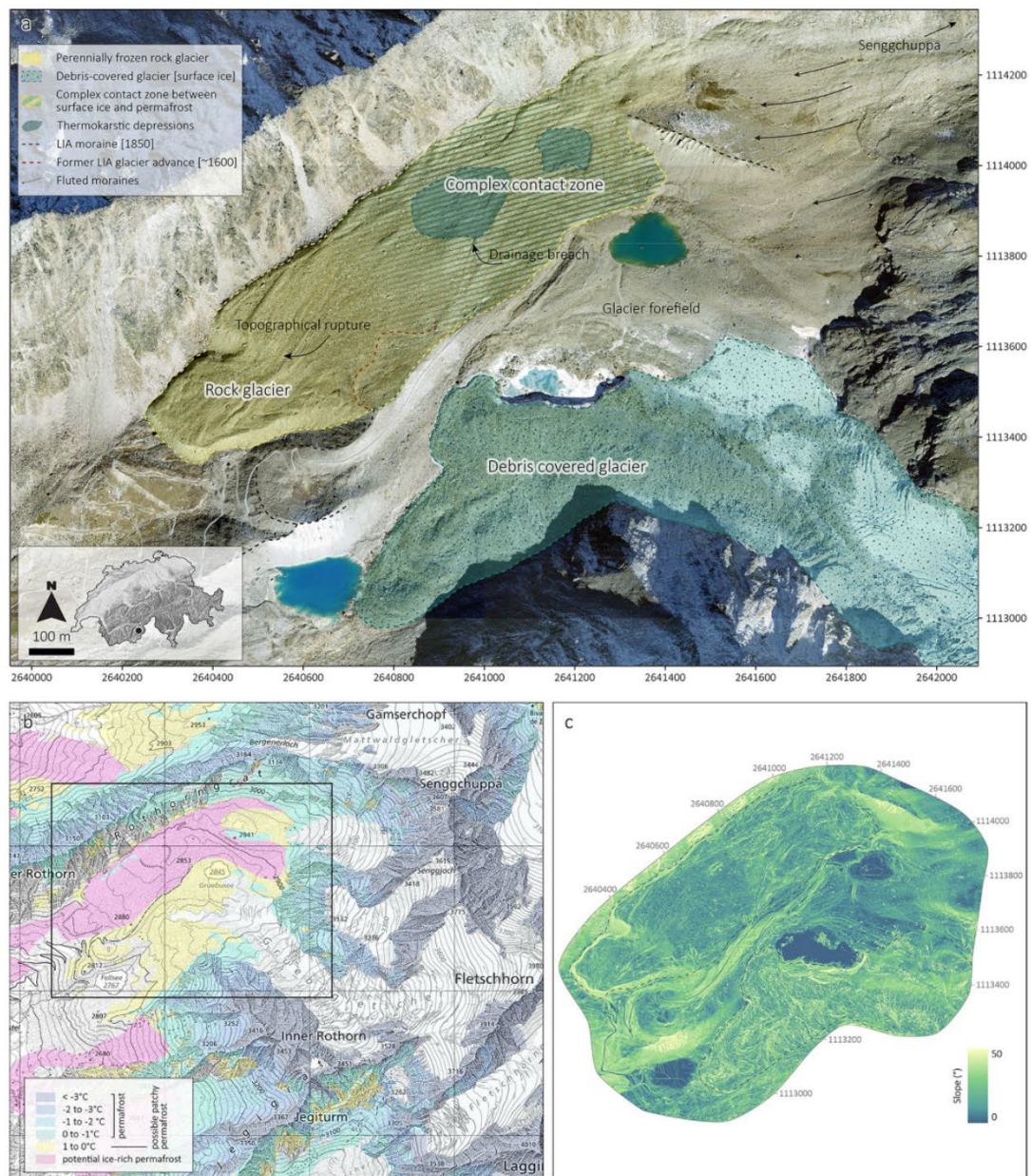


Figure 1. General geomorphological description of the Gruben site (a). The Gruben rock glacier is highlighted by the dashed yellow lines. The complex contact zone is highlighted by alternating dashed yellow and blue lines. The delineation between the rock glacier and the complex contact zone (faded hatched lines) is here not clearly defined but based on geomorphological knowledge and prior studies (Kääb et al., 1997; Gärtner-Roer et al., 2022). The Gruben debris-covered glacier terminus is highlighted in blue. Dashed black lines indicate part of the LIA maximal extent of the Gruben glacier. Dashed red lines indicate a probable, former (~ 1600) LIA glacier advance. Fluted moraines indicate the basal flow direction of the adjacent LIA Senggchuppa glacier. Background: SWISSIMAGE 2017 (swisstopo). Permafrost distribution map (Kenner et al., 2019) of the Gruben area (b) and slope gradient of the study area (c).

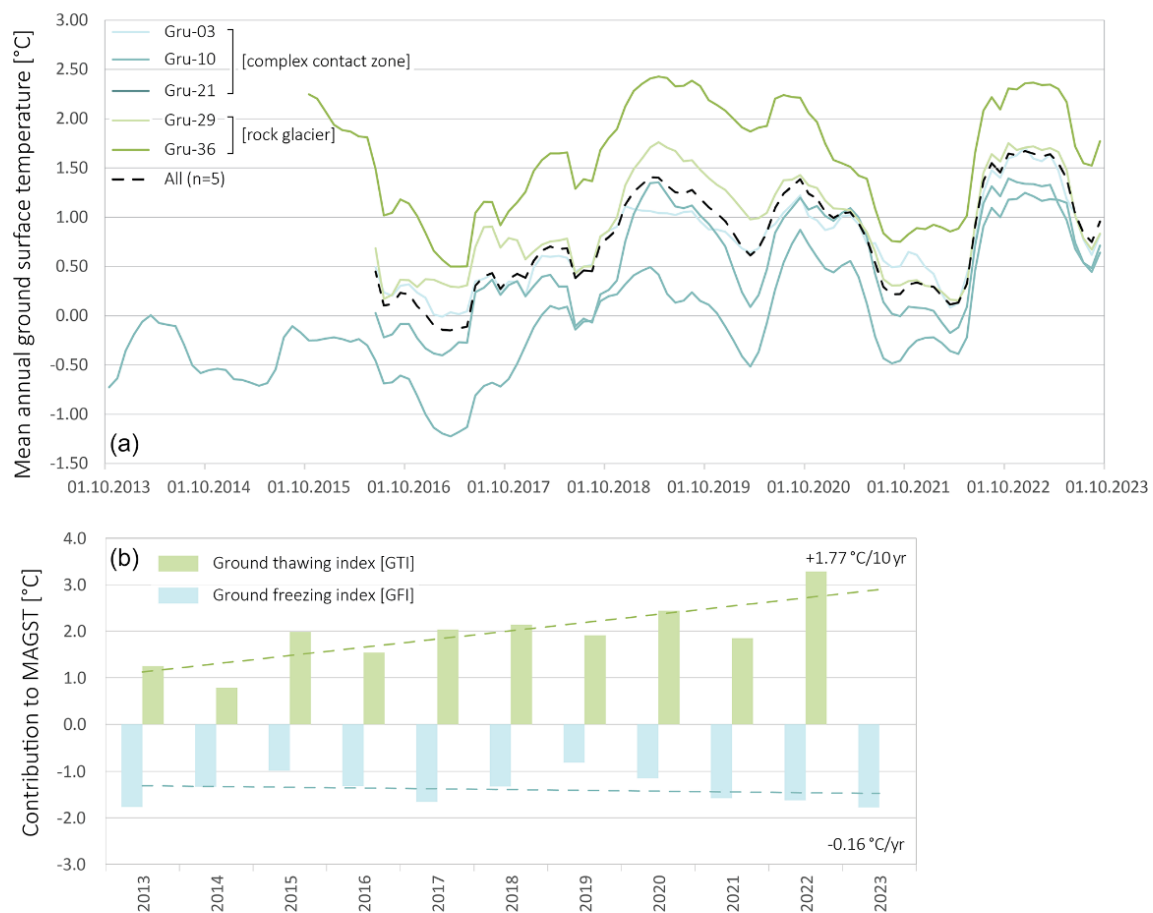


Figure 2. Running MAGST measured on the Gruben rock glacier and complex contact zone (a) and contribution of the ground thawing index (GTI) and ground freezing index (GFI) to the MAGST at Gruben on average (b) (Noetzli and Pellet, 2023).

3.1 Electrical resistivity tomography (ERT)

ERT is a well-established method to image the two-dimensional (2D) distribution of electrical properties of subsurface mountain permafrost and ground ice due to its sensitivity and suitability to distinguish unfrozen material, ice-containing permafrost (excess ice), and massive sedimentary ice due to their contrasting electrical properties (e.g. Haerberli and Vonder Muehll, 1996; Hauck and Kneisel, 2008; Bosson et al., 2015; Halla et al., 2021; Herring et al., 2023).

On the rock glacier and complex contact zone, all ERT profiles were measured between 8–12 August 2022 with a Syscal Pro (Iris Instruments), which can connect to 48 stainless-steel electrodes. A longitudinal profile of 955 m (P00) was achieved by aligning seven consecutive profiles of 235 m (roll-along, with a one-half overlap) with an electrode spacing of 5 m. Along two sections of the profile P00,

two co-located profiles, P00a and P00b (117.5 m each), with 2.5 m electrode spacing were measured to obtain information at a shallower investigation depth. Profiles P00, P00a, and P00b were merged in the data management software Prosys II (Iris Instruments), allowing for a single inversion of all quadrupoles measured along the same line (including both 2.5 and 5 m spacings). On the debris-covered glacier, one profile (P115) with 2.5 m electrode spacing was conducted. All profiles were measured with a Wenner–Schlumberger array configuration. The filtering (i.e. the extermination of bad data points) of the data from all profiles was achieved manually using Res2DInv (Aarhus GeoSoftware). For profiles GRU-P00, GRU-P10, GRU-P23, and GRU-P115, 18 %, 2 %, 6 %, and 14 % of the data points were filtered, respectively. The inversions were carried out using the pyGIMLi-based code (Ruecker et al., 2017).

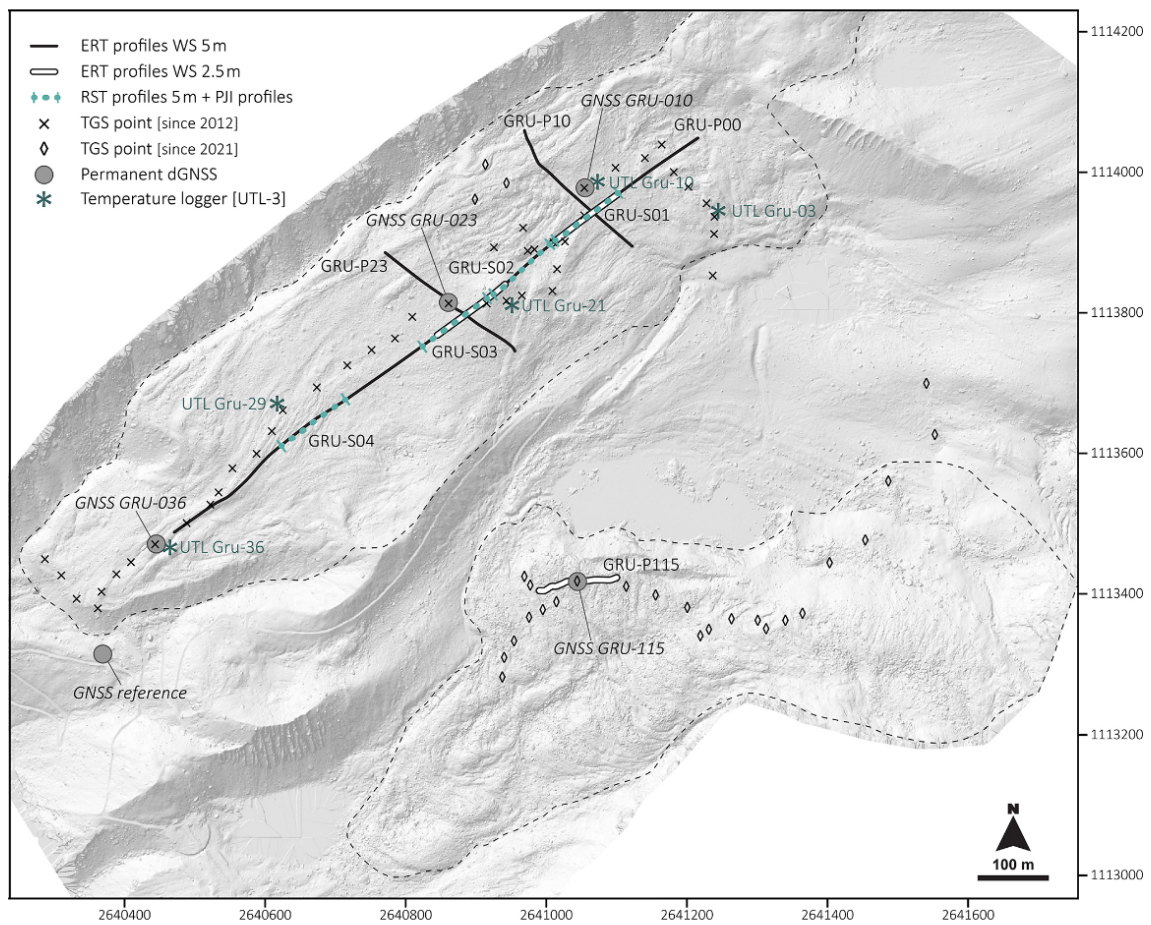


Figure 3. Overview of the distribution of the geodetic survey points (crosses are the points monitored since 2012 and diamonds are the points monitored since 2021) and the location of the four permanent dGNSS stations and the reference station. The location of the electrical resistivity tomography (ERT) and refraction seismic tomography (RST) profiles is also presented. The continuous black line indicates ERT profiles with a 5 m electrode spacing, and the white lines indicate ERT profiles with a 2.5 m electrode spacing (see Sect. 4.1). The distribution of temperature loggers (UTL-3) is also presented. Background: UAV-derived hillshade (6 October 2022).

3.2 Refraction seismic tomography (RST)

RST makes use of the differences in the elastic properties of subsurface materials, such as unfrozen sediments, supersaturated permafrost, and buried surface ice, which are quantified in terms of their different P-wave velocities and their spatial variability. P waves are refracted when they encounter subsurface layers with velocity contrasts and are especially well-suited to delineate quasi-horizontal subsurface layers and to differentiate between air- and ice-filled pore spaces, both of which may exhibit similarly high electrical resistivities (Draebing, 2016; Halla et al., 2021; Hauck, 2001; Hilbich, 2010).

Four RST profiles were measured on co-located lines of the longitudinal ERT profile (P00). A first RST campaign was carried out in mid-August 2022, in the upper glacier-affected zone of the rock glacier (complex contact zone), and a second in mid-August 2023, in the lower glacier-affected zone (complex contact zone) and the rock glacier (see Fig. 3). In both campaigns, a 24-channel Geode instrument (Geometrics) with 24 geophones and a sledgehammer source were used. The 2D data analysis (picking of first breaks) and travel-time analysis were performed using ReflexW (Sandmeier geophysical research).

3.3 Petrophysical joint inversion (PJI)

We apply a PJI approach (Mollaret et al., 2020; Wagner et al., 2019) to jointly invert the measured apparent resistivities and seismic travel times to quantify the volumetric fraction of ice, water, air, and rock contents. Following Mollaret et al. (2020), the PJI approach is based on petrophysical equations that relate bulk electrical resistivities and seismic velocities to the fractions of the four phases in the subsurface, based on the resistivities and P-wave velocities of ice, water, air, and the rock matrix. The sum of all fractions has hereby to adhere to

$$f_r + f_w + f_a + f_i = 1. \quad (1)$$

with the indices r, w, a, and i indicating rock, water, air, and ice, respectively.

The petrophysical equation for P-wave velocities follows the approach of Timur (1968) and Hauck et al. (2011) linking the slowness and volumetric content of the four fractions to the measured bulk slowness as follows:

$$\frac{1}{v_p} = \frac{f_r}{v_r} + \frac{f_w}{v_w} + \frac{f_a}{v_a} + \frac{f_i}{v_i}, \quad (2)$$

with the velocities v_r , v_w , v_a , and v_i for rock, water, air, and ice, respectively.

In Wagner et al. (2019) and in many ERT applications on permafrost, Archie's law (Archie, 1942) is used to link measured resistivity to material properties such as saturation and porosity (see Herring et al., 2023). Archie's law is generally recognized as valid when the electrolytic conduction process is the dominant one. However, this is unlikely to be the case for coarse, blocky materials and supersaturated permafrost conditions, limiting its applicability. Thereby, following Mollaret et al. (2020), the geometric mean model (Eq. 3; Glover, 2010) was applied here instead, as it has the advantage of including all fractions of the four phases (and not only rock and water as in Archie's law), and consequently it yields realistic and well-constrained ice content estimations also in cases where the water content is potentially low (as in rock glaciers; Mollaret et al., 2020):

$$\rho = \rho_r^{f_r} \cdot \rho_w^{f_w} \cdot \rho_a^{f_a} \cdot \rho_i^{f_i}, \quad (3)$$

where ρ_r , ρ_w , ρ_a , and ρ_i are the resistivities for rock, water, air, and ice, respectively.

The results of the PJI depend on different sets of parameters in addition to the measured apparent resistivities and seismic travel times. A range of resistivity [Ωm] and P-wave velocity [m s^{-1}] values was attributed to each of the four phases (ρ_w , ρ_i , ρ_a , ρ_r , v_r , v_i , v_w , v_a). These were based on estimated resistivities and velocities obtained from the ERT and RST datasets as well as on standard ranges found in the literature (Hauck and Kneisel, 2008). A physically plausible range (i.e. 0.2–0.8) of initial porosity ($= 1 - f_r$) values was

prescribed through an iterative process to define the most adequate initial porosity value of each profile, which influences the distribution of the four phases. Regularization parameters for the inversion were attributed according to the suggested values by Mollaret et al. (2020) (see Table 1). Because of the varying sensitivity of the model to prescribed resistivities of the four phases and initial porosity, a looping process was used to systematically test different combinations of parameters (ρ_w , ρ_i , ρ_a , ρ_r , and initial porosity) with different sets of prescribed values (Table 2). The goal was to identify the optimal combination that most closely matched the model's χ^2 , where $\chi^2 = 1$ indicates a perfect fit to the data, given the data error, following the method outlined by Günther and Rucker (2023) and prior site knowledge.

3.4 Differential global navigation satellite system (dGNSS)

Surface velocities of rock glaciers are measured by bi-annual terrestrial geodetic surveys (TGSs) in early and late summer (early July and early October), as well as hourly by permanently installed dGNSS devices. These two complementary approaches allow the seasonal velocity variations to be captured (permanent dGNSS) as well as their spatially distributed annual and intra-annual changes (Noetzi and Pellet, 2023). Moreover, the data derived from these measurements allow the kinematic response to thermally driven processes such as ice-melt-induced subsidence to be calculated (Wee and Delaloye, 2022).

3.4.1 Bi-annual (seasonal) terrestrial geodetic survey (TGS) acquisitions

Surface displacement changes have been monitored on the Gruben rock glacier and complex contact zone bi-annually (early summer and late summer) since 2012, as well as on the Gruben debris-covered glacier since 2021 by differential GNSS surveys with real-time kinematics (RTK) using a Leica Viva GS10 (Leica Geosystems), according to the measurement set-up described by Lambiel and Delaloye (2004). In the scope of this study, measurements from field surveys carried out between 2022 and 2023 in early July and early October are used to distinguish the surface displacements during the longer winter period (approximately 270 ± 5 d) from those occurring during the snow-free summer period (90 ± 5 d). A total of 75 monitoring points are distributed throughout the site, including 46 on the rock glacier and complex contact zone and 24 on the debris-covered glacier as survey points, as well as five control points marked on stable bedrock for quality assessment. Horizontal, vertical, and 3D displacement vectors are calculated between two geodetic surveys with a relative accuracy of about 2–3 cm horizontally and 4–5 cm vertically. On survey dates 6 October 2022 and 3 July 2023, all monitoring points were measured. How-

Table 1. Summary of the applied parameters for each profile. err_U and err_{ρ_a} are the individual inversion errors in both data types, α denotes the smoothness regularization parameter, β corresponds to the volumetric conservation regularization parameter, and $z\text{Weight}$ corresponds to the anisotropic smoothness parameter, used to enhance horizontal or vertical structures (Mollaret et al., 2020).

Parameters	GRU-S01	GRU-S02	GRU-S03	GRU-S04
err_{ρ_a} (%)	0.05	0.06	0.05	0.5
err_U (m s^{-1})	1.5	3	0.3	0.3
α	15	20	20	15
β	10 000	10 000	10 000	10 000
$z\text{Weight}$	0.2	0.1	0.25	0.15

Table 2. Combination of parameters used for the looping process.

ρ_w [Ωm]	ρ_i [Ωm]	ρ_r [Ωm]	ρ_a [Ωm]	φ_{start} [%]
5	1 000 000	10 000	1 000 000	20
50	2 500 000	15 000	10 000 000	30
100	5 000 000	30 000		40
				50
				60
				70
				80

ever, on 7 October 2023, only the monitoring points located on the rock glacier were measured.

From the TGS, we assess the driving processes contributing to surface elevation changes between early October 2022, early July 2023, and early October 2023. This time frame allows seasonal coverage over a year. We hereby assume that the change in elevation (Δz_{meas}) over time is attributed to the combination of three main processes: (a) elevation change due to the downslope movement, following the topographical slope angle (Δz_{topo}); (b) change in elevation due to the melting (Δz_{melt}) or aggradation of excess ground ice, i.e. ice in oversaturated conditions or massive ice lenses; and (c) change in elevation caused by extending or compressing flow patterns (Δz_{flow}) (Bosson and Lambiel, 2016; Haerberli et al., 2006; Lambiel and Delaloye, 2004; Wee and Delaloye, 2022). Here, following Isaksen et al. (2000) and Bosson and Lambiel (2016) the expected vertical position of each block (Δz_{topo}) was calculated from the measured horizontal movement ($\Delta x_{y_{\text{meas}}}$) and the mean topographical slope angle around each block (derived from a resampled 5 m resolution DEM) (Eq. 4).

$$\Delta z_{\text{topo}} = \Delta x_{y_{\text{meas}}} \times \tan(\alpha) \quad (4)$$

The difference between the obtained values of the expected vertical displacement (Δz_{topo}) and the measured vertical movement (Δz_{meas}) provided information related to estimated ice-melt-induced surface elevation changes and flow patterns (calculated $\Delta z_{\text{melt-flow}}$; Eq. 5).

$$\Delta z_{\text{melt-flow}} = \Delta z_{\text{meas}} - \Delta z_{\text{topo}} \quad (5)$$

To assess the seasonality and spatial signature of the driving processes contributing to surface elevation changes, the ratio between the expected summer displacement ($\Delta z_{\text{topo-summer}}$) and the winter displacement ($\Delta z_{\text{topo-winter}}$) was calculated. The ratio between downslope movement and surface lowering ($\Delta z_{\text{topo}}/\Delta z_{\text{melt-flow}}$) was calculated to evaluate the dominant process among the former and the latter. Surface lowering likely due to ice melt is dominant when $\Delta z_{\text{topo}}/\Delta z_{\text{melt-flow}} < 1$, and downslope movement probably enhanced by an extending flow pattern is dominant when $\Delta z_{\text{topo}}/\Delta z_{\text{melt-flow}} > 1$.

3.4.2 Continuous automatic dGNSS acquisitions

Three permanent GNSS stations are installed on the Gruben site: two on the complex contact zone and one on the debris-covered glacier, which have been delivering continuous hourly position measurements since early summer 2022. An additional permanent GNSS station has been installed on stable terrain to provide a reliable reference for the double-difference GNSS post-processing scheme to obtain robust quality-controlled daily positions (Cicoira et al., 2022). The high temporal resolution provided by permanent GNSS instruments enables the computation of monthly to daily displacements (Wirz et al., 2016; Noetzi and Pellet, 2023). However, because of the noise observed in the dataset, which can be caused by stochastic movements of the terrain's surface; by the rotation around the axis of the GNSS mast (which depends on the size of the boulder); and also by various environmental factors such as wind, temperature changes, or snow cover (Cicoira et al., 2022; Wirz et al.,

2014), we apply a simple 15 d running mean to the dataset to filter displacement noise from any displacement signal.

3.5 UAV structure-from-motion (SfM) photogrammetry

To obtain high-resolution orthoimages and digital elevation models (DEMs) for the studied area, UAV surveys were conducted on 6 October 2022, 3 July 2023, and 7 October 2023. These surveys enabled high-spatial-resolution mapping of seasonal (summer and winter) surface displacements at the studied area (Vivero et al., 2022). The UAV surveys employed a DJI Phantom 4 RTK device, equipped with a GNSS antenna with L1 and L2 frequencies, providing real-time kinematics (RTK) differential corrections using a virtual reference station (VRS) based on the automated GNSS (reference stations) network for Switzerland (AGNFS). Flight missions were planned with the built-in DJI GS RTK application. All missions were designed with the same parameters: side and forward overlaps were set to 70 % and 80 %, respectively, and flown at a constant height of 70 m, based on the swissALTI3D DEM loaded in the Terrain Awareness module to cover the entire area of interest. This resulted in approximately 2000 images with a geotagging accuracy between 1–2 cm (horizontally) and 1.5–3 cm (vertically) per survey. The UAV images were processed using the software PIX4Dmapper Pro version 4.7 to derive digital elevation models (DEMs) and orthomosaics, which were sampled at a resolution of 2.5 cm × 2.5 cm.

Surface elevation changes were quantified by differencing the sequential DEMs from each other to obtain a DEM of difference (DoD) for each time interval from 6 October 2022–3 July 2023 and 3 July 2023–7 October 2023. The obtained high-resolution DEMs allowed us to derive the terrain's topography, from which the loss in surface elevation due to downslope movement was calculated (Bosson and Lambiel, 2016; Wee and Delaloye, 2022). Horizontal surface displacements were derived from pairs of the above-mentioned multi-temporal orthoimages of 0.25 m pixel size by applying a normalized cross-correlation (NCC) procedure using the image correlation CIAS software (Debella-Gilo and Käab, 2011; Käab and Vollmer, 2000). The accuracy and quality of the image correlation was evaluated by applying the Helmert transformation based on points placed on stable terrain in the vicinity of the studied landforms. Despite the difficulty of finding stable terrain outside the studied landforms in the surveyed area, 46 (44) stable points were used for the t_1 orthoimage and 44 for the epoch 1 (epoch 2) orthoimage pair. This allowed us to assess scale differences, rotations, or translations (x – y shifts) between two orthoimages (Table 3).

The uncertainties associated with the x and y displacement vectors derived from image-matching in CIAS were assessed using the standard deviations (σ_x and σ_y) of the residuals of the stable points used to assess the orthorectification of each orthoimage and where Δx and Δy are the individual

components of the displacement vector, corrected for any co-registration bias (Redpath et al., 2013).

$$\sigma_d = \sqrt{\left(\frac{\Delta x}{d}\right)^2 \sigma_x^2 + \left(\frac{\Delta y}{d}\right)^2 \sigma_y^2} \quad (6)$$

The variance σ_x and σ_y , which are about equal to the pixel size, indicate the spatial uncertainty that arises from the orthorectification and mosaicking processes, as well as the performance of the automatic image-matching using the NCC function. A confidence interval of 90 % for each displacement vector was calculated (i.e. $1.645 \times \sigma_d$) to define the minimum limit of detection (LoD). The resulting LoD values were converted into metres per year (m yr^{-1}). A GIS filtering of flawed data points (e.g. vectors located on snow patches, vectors pointing upstream) was established in a final step.

3.6 Ground surface temperature

The thermal state of the ground surface and the possible occurrence of ground ice close to the subsurface on the Gruben rock glacier have been assessed through the monitoring of ground surface temperature (GST) at a 2 h frequency since 2013. Three temperature loggers are located in the complex contact zone (Gru-03, Gru-10, Gru-21), and two are located in the rock glacier zone (Gru-29 and Gru-36). From 2013 to 2018, GST data were measured using UTTI-1 data loggers (Geotest AG) with an accuracy of $\pm 0.2^\circ\text{C}$, and from 2018 onwards, UTTI-3 data loggers (Geotest AG) with an accuracy of $\pm 0.02^\circ\text{C}$ were used.

4 Results

4.1 Characterization of the subsurface: conventional ERT

Figure 4 presents the inverted resistivity tomograms for all profiles. Two main zones can be identified from prior geomorphological analysis and interpretation but also from the spatial distribution of resistivity values observed in the longitudinal profile GRU-P00: the rock glacier zone and the complex contact zone (Fig. 4a). In what is here considered as the permafrost zone of the Gruben rock glacier, resistivity values range between 35 and 50 $\text{k}\Omega\text{m}$ in the uppermost 5–7 m, which likely corresponds to the active layer. Below the active layer, a layer with very high resistivity values ranging between 350 and 500 $\text{k}\Omega\text{m}$ dominates the lower section of the profile, suggesting widespread, perennially frozen, ice-supersaturated sediments (excess ice). Resistivity values characterizing perennially frozen ground reach deeper than the penetration depth of the soundings.

In the central part of the profile GRU-P00 (Fig. 4a), between roughly 450 and 650 m, a relatively thin layer of coarse debris of about 2 m, which gradually becomes thinner (supposedly < 1 m), overlays a layer with resistivity values rang-

Table 3. Parameters derived from the Helmert transformation performed in CIAS.

Orthoimage	Points	Scale [m]	Rotation [°]	Shift <i>x</i> [m]	Shift <i>y</i> [m]	σ_x [m]	σ_y [m]
6 October 2022–3 July 2023	46	1.00	359.99	−0.015	−0.007	0.024	0.032
3 July 2023–7 October 2023	44	1.00	359.99	−0.008	0.004	0.031	0.033

ing from 350 to 1000 k Ω m, whose thickness exceeds the penetration depth of the sounding. Local distinct patches of resistivity values of around 2500 k Ω m are corroborated by the transversal profile GRU-P23 that crosses the longitudinal profile at around 500 m (Fig. 4a, e, g). Such extremely high resistivity values suggest the presence of buried surface ice in this zone, as such ice produced by snow accumulation and transformation has been shown to be significantly less conductive than ground ice produced by freezing processes under permafrost conditions. The latter contains more electrically conductive ions through the refreezing of water that has been in contact with rock material (Colombo et al., 2019; Del Siro et al., 2023).

In the uppermost section of the complex contact zone, profiles GRU-S01 and GRU-P10 indicate resistivity values ranging between 350 and 1000 k Ω m under a shallower layer of more conductive glaciogenic fine sediments between 15 and 30 k Ω m (Fig. 4a, c, f). Resistivity values at the north-eastern end of the longitudinal profile (between 900 and 955 m) range from 3 to 10 k Ω m, pointing to unfrozen and ice-free conditions. Similar to the values observed at the uppermost end of the longitudinal profile, towards the outer margins (south-east) of the Gruben rock glacier, both transversal profiles GRU-P10 (Fig. 4f) and GRU-P23 (Fig. 4g) show resistivity values between 3 and 30 k Ω m, which could possibly indicate a high water content.

Profile GRU-P115 is located on the Gruben debris-covered glacier tongue (Fig. 4h). The resistivity values measured in the uppermost 3–4 m of the profile range between 10 and 30 k Ω m. Under this layer of very coarse debris, a highly resistive layer of 1000 to likely >2500 k Ω m is observed, indicating buried surface ice.

4.2 Estimation of ground ice content

Figure 5 shows the estimated ice, water, and rock content distributions along profiles GRU-S01, GRU-S02, GRU-S03, and GRU-S04. Using the full ranges of free parameters (within reasonable physically consistent bounds) shown in Table 2 would yield a wide range of different spatial distributions for the above-mentioned three phases. The parameters selected in Table 4 yield a best-guess estimate for the porosity (or rock fraction) and ice content distribution, informed by prior geomorphological knowledge of the site. The analysis of historical maps and historical aerial images allowed an initial geomorphological interpretation of the study area. For instance, the development of thermokarstic depressions

in the upper area of the Gruben rock glacier (former contact zone) during the 1970s and the documented massive ice outcrops are clear indicators of the near-surface ground ice properties. This allowed us to better constrain the resistivity values for each profile and the rock fraction estimate. The chosen metrics in Table 4 also result in a low χ^2 error, demonstrating a strong agreement with the observed data. A high water-to-ice ratio is observed in the north-eastern section (between 100 and 130 m) of profile GRU-S01 (Fig. 5a), where the terrain surface is characterized by fine-grained glaciogenic sediments (fill), which is where more water capillary action occurs. In contrast, the section between 20 and 75 m, located at the edge of a former thermokarst lake, presents a high ice content. This can be explained by the coarse and blocky terrain surface, which favours the resilience of ground ice (Amschwand et al., 2024). Between 125 and 160 m in profile GRU-S02 (Fig. 5b), where the ice content ranges between 80 %–90 %, almost no water is present, suggesting the presence of embedded, cold surface ice. The minimum ice content is encountered in the thermokarst depression, intersecting the 1995 drainage breach (Kääb et al., 1997), suggesting an alteration of the subsurface thermal regime. Both extremities of profile GRU-S03 contain less ice, which is compensated for by a relatively high rock fraction. High ice contents reaching up to 84 % are locally found in the middle of the profile and are counterbalanced by a relatively porous medium, inferring remnants of massive (possibly surface) ice lenses embedded in the frozen sediments (Fig. 5c).

In contrast to the profiles located in the complex contact zone, the uppermost 5–7 m of profile GRU-S04 within the rock glacier zone displays a well-defined porous (about 40 %–30 %) and coarse debris layer. Below this layer, the maximum ice content is found under supersaturated conditions (Fig. 5d).

4.3 Seasonal surface displacements and surface elevation changes

Figure 6 displays seasonal horizontal surface velocity flow fields of the Gruben rock glacier, complex contact zone, and debris-covered glacier. A coherent, lengthwise-oriented flow field is documented on the Gruben rock glacier downslope of the topographical rupture. Between the latter and the complex contact zone, the measured vector field shows an orientation oblique to the longitudinal surface structures observed on the rock glacier. This flow trajectory may indicate that the influence of the IJA glacier on the creeping permafrost

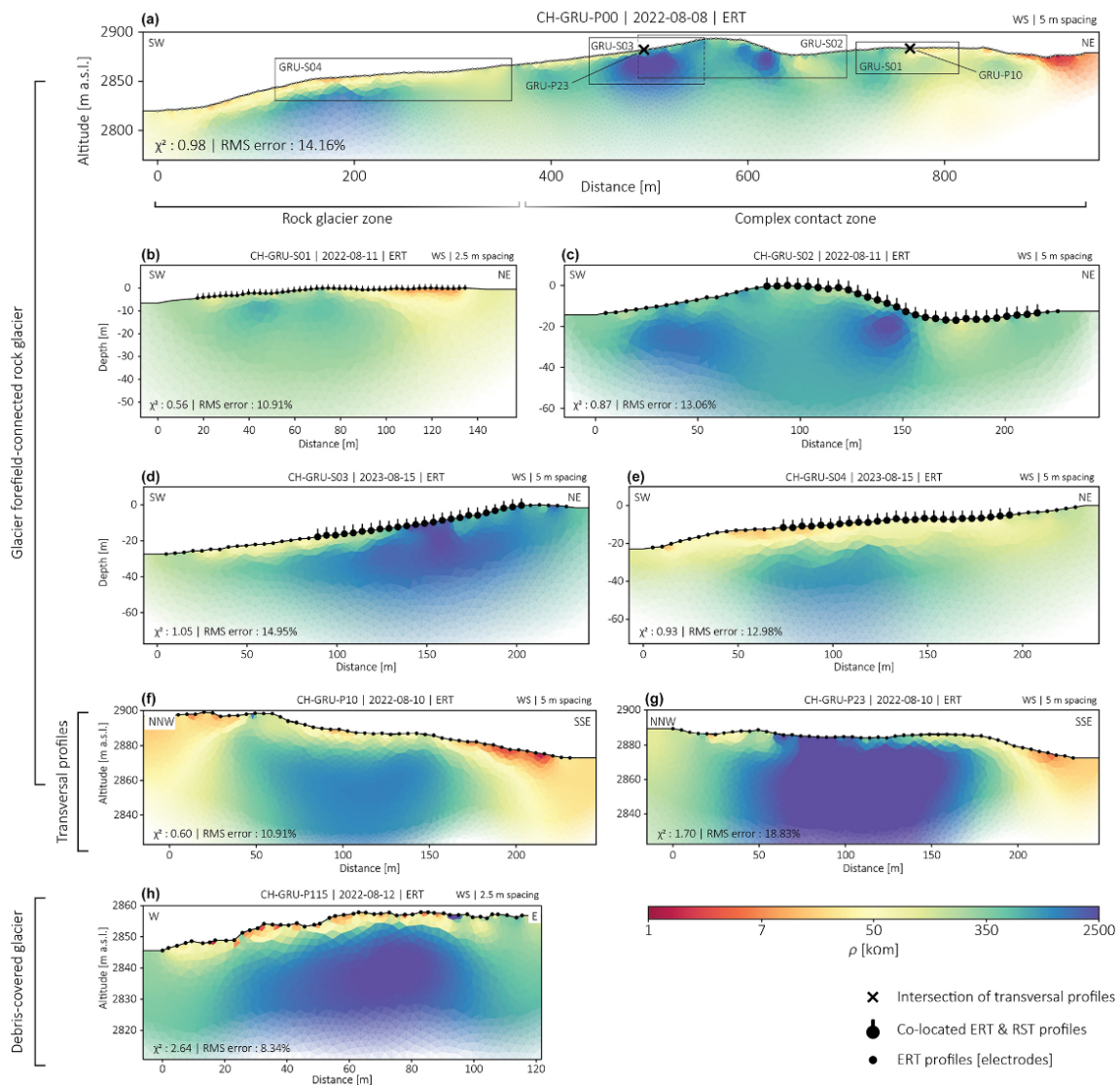


Figure 4. The main longitudinal ERT profile GRU-P00 is presented in the uppermost panel (a). ERT profiles GRU-S01, GRU-S02, GRU-S03, and GRU-S04 are presented in panels (b)–(e) and represent the profiles where both ERT and RST measurements were carried out. The transversal profiles GRU-P10 and GRU-P23 are presented in panels (f)–(g). Profile GRU-P115, carried out on the debris-covered glacier, is presented in panel (h).

extended beyond the former ice margin. In the complex contact zone with the LIA glacier, the flow field is considerably more complex and includes a clear south-east-oriented back-creeping towards the topographic depression of the forefield, previously occupied by the Gruben glacier during the LIA.

During the winter period (6 October 2022–3 July 2023; Fig. 6a), the mean horizontal surface velocity measured in the lower section of the slightly steeper rock glacier zone

(close to the topographical rupture, zone 1) is 0.62 m yr^{-1} , while in the relatively flat complex contact zone (zone 2), the mean horizontal surface velocity is 0.26 m yr^{-1} . Horizontal surface velocities are generally faster during the summer period (Fig. 6b) compared to the winter period, particularly in the uppermost complex contact zone (zone 2), where the mean velocity is 0.52 m yr^{-1} . In the lower section of the rock

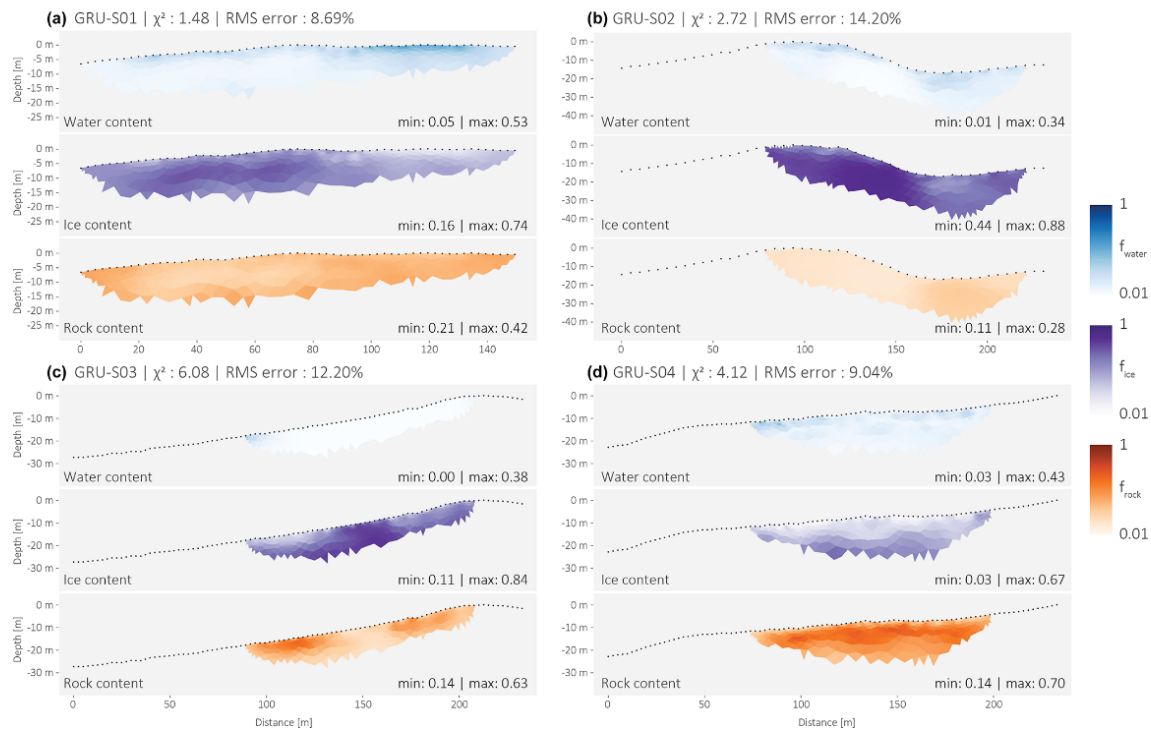


Figure 5. Volumetric fractions of water (f_w), ice (f_i), and rock (f_r) estimated by the petrophysical joint inversion of profiles GRU-S01, GRU-S02, GRU-S03, and GRU-S04.

Table 4. Selected parameters corresponding to low χ^2 and rms error used for the PJI.

Parameters	GRU-S01	GRU-S02	GRU-S03	GRU-S04
ρ_w [Ωm]	50	100	50	5
ρ_i [Ωm]	5 000 000	2 500 000	5 000 000	5 000 000
ρ_r [Ωm]	30 000	30 000	30 000	30 000
ρ_a [Ωm]	1 000 000	10 000 000	10 000 000	1 000 000
φ_{start} [%]	60	80	80	80

glacier (zone 1), the mean summer horizontal surface velocity is 0.92 m yr^{-1} .

The upslope (zone 4; Fig. 6) and downslope (zone 3; Fig. 6) sections of the debris-covered glacier tongue are strikingly distinguishable in terms of flow field direction and velocity. In the uppermost zone, surface displacements are oriented towards the north-west, whereas in the lowermost zone, after the elbow turn, the flow trajectory is more diffuse and is directed towards the south-west. The upper section is characterized by faster velocities than the flatter and decaying frontal zone. The mean horizontal surface velocity observed in the lower zone (zone 3) during the winter period in the lower section is 0.37 m yr^{-1} , while in the upper section (zone 4), the mean velocity is 1.74 m yr^{-1} (Fig. 6a). During the

summer period (Fig. 6b), the lower section's (zone 3) mean velocity is 0.72 m yr^{-1} , and the mean horizontal velocity is 4.19 m yr^{-1} in the upper part (zone 4). The latter is characterized by more chaotic flow fields, which is likely due to differential ablation rates of the glacier in this section caused by an uneven distribution of debris-cover thickness.

Surface elevation changes and horizontal surface velocities presented in Fig. 7 reveal a striking seasonal and spatial signal in terms of the kinematic behaviour of the rock glacier. Flow fields and velocity patterns, together with elevation changes observed on the rock glacier surface, allowed us to highlight the distinction between surface processes occurring in the complex contact zone from processes occurring in the rock glacier zone. UAV-derived elevation changes show

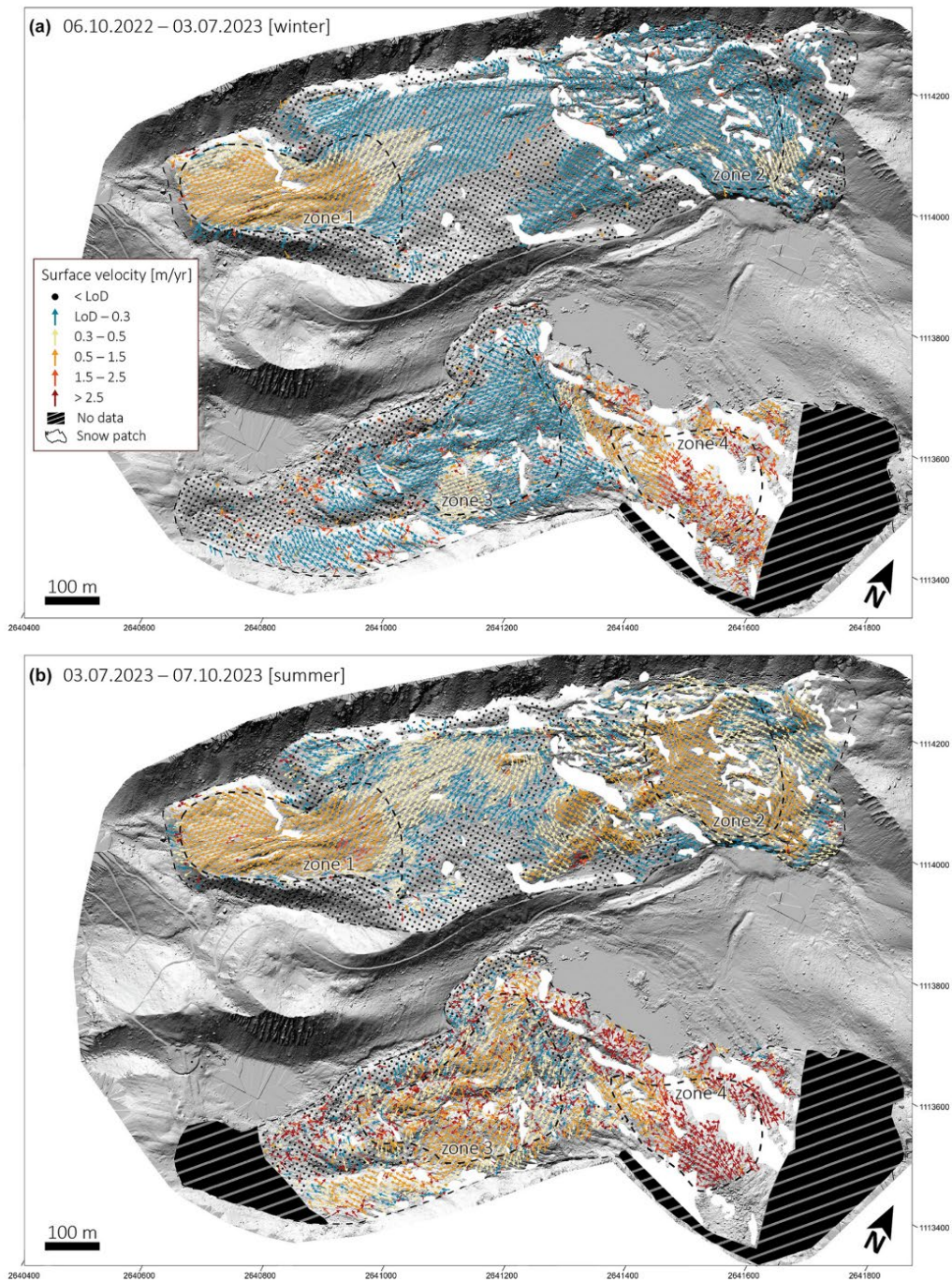


Figure 6. UAV-derived horizontal surface displacements. The winter period (6 October 2022 to 3 July 2023) is presented in panel (a), and the summer period (3 July 2023 to 7 October 2023) is presented in panel (b). The zones (1–4) from which the mean velocities are derived are highlighted by the dashed polygons. Background: UAV-derived hillshade (6 October 2022).

that during the winter period, elevation changes range from -0.05 to -0.20 m in the upper section of the complex contact zone, while in its lower section (east of the thermokarst depression) almost no elevation change is observed. The non-glacier-affected part of the rock glacier illustrates a vertical loss of about -0.20 m during winter, which can largely be explained by the continuous longitudinal stretching of the creeping ice-rich permafrost (Kääb et al., 1997). In summer, a higher vertical decrease of about -0.50 m is evidenced in the uppermost section of the complex contact zone, which largely exceeds the horizontal displacement (as shown in Fig. 7b), inferring ice-melt-induced subsidence. This elevation loss extends downstream to the lower part of the complex contact zone, where the average elevation change reaches -0.35 m. Elevation changes in the rock glacier zone reach -0.20 m, and the general displacement slope angle of the surveyed points largely exceeds the topographical slope angle, evidencing ice melt but also elevation loss due to thinning (extending flow pattern) and downslope movement along the topographical slope. Elevation changes obtained from in situ dGNSS surveys are consistent with the above-mentioned observations and are in agreement with the results previously presented by Gärtner-Roer et al. (2022).

Near the ice-cliff section of the debris-covered glacier terminus, the mean winter (6 October 2022–3 July 2023) surface elevation change is about -0.15 m, while in the margins surface elevation changes are <0.10 m. Summer elevation changes are generally enhanced in this lower section of the debris-covered tongue, ranging from -0.15 to -0.55 m.

The spatio-temporal variation in the surface elevation changes was assessed by calculating the ratio of the expected vertical movement (solely due to the downslope movement) for the summer and winter periods. The results document a strong seasonal and spatial pattern (Fig. 8). In the complex contact zone, the mean ratio between the expected summer vertical displacement and the expected winter vertical displacement is 2.52, which infers that additional processes such as ice-melt-induced subsidence and extending flow contribute dominantly to the elevation loss in this zone, whereas in the rock glacier zone the mean ratio is 1.12, which implies that surface elevation changes are relatively constant throughout the year but are likely slightly enhanced by thaw or melt-induced subsidence or due to the extending flow pattern observed in this area. The ratio between the downslope movement and the additional surface lowering over a year was calculated to determine the weight of the processes contributing to surface elevation loss. Surface lowering most likely due to ice melt dominates in the complex contact zone, with a mean ratio of 0.30. The mean ratio of 5.12 obtained in the rock glacier zone illustrates the predominance of the downslope movement, likely combined with thinning effects from extending flow. Points located in the thermokarst depression showed a less coherent behaviour as their values are relatively heterogeneous.

4.4 Contribution of ground surface temperatures to seasonal surface changes

The potential direct influence of ground surface temperature changes on ice-melt-induced subsidence was assessed through the acquisition of hourly position measurements by permanent dGNSS stations, which were compared to daily GST measurements (Fig. 9). At stations Gru-010 and Gru-023, located in the complex contact zone, vertical surface velocities tend to instantly decelerate once ground surface temperatures are below 0°C and accelerate with a 10 d phase lag following the warming ($>0^{\circ}\text{C}$) of ground surface temperatures. Horizontal surface velocities slightly increase as ground temperatures start to increase (Fig. 9a–b). Displacement profiles of Gru-010 and Gru-023 show the sensitivity of the underlying ground ice to surface temperatures, as summer surface temperatures lead to an enhanced vertical displacement (Fig. 10a–b). Moreover, the displacement angle of about 65° largely exceeds the surface topography (10°), suggesting ice-melt-induced subsidence. The reactivity of surface displacements to the thermal state of the ground surface can likely be attributed to the presence of embedded surface ice buried under a relatively shallow layer of debris, allowing effective direct heat transfer from the atmosphere to the permafrost table (Fig. 4). In contrast to the kinematic behaviour observed in the complex contact zone, the intra-annual variability in vertical and horizontal surface velocities observed at station Gru-036 in the rock glacier zone is more constant throughout the year (Fig. 9c). Peak velocities are reached in early summer, coinciding with the zero-curtain period, and in late autumn. This is explained by a phase lag between the seasonal summer peak in the ground surface temperatures and the surface velocities, which may be partly attributed to the time for the temperature signal to propagate from the surface to the permafrost table (Cicoira et al., 2019; Wirz et al., 2016). The displacement angle of profile Gru-036 (Fig. 10c) follows the topographical slope of 15° , which is in complete accordance with the observations made by Gärtner-Roer et al. (2022). The mere absence of a steeper displacement trajectory during the summer period suggests surface lowering due to downslope movement in a zone where the extending flow pattern is dominant.

5 Discussion

The combination of geophysical datasets with high-spatio-temporal-resolution geodetic measurements and ground surface temperature monitoring allowed a detailed representation of the spatial distribution of ground ice, its properties, and its influence on the kinematic behaviour of the Gruben rock glacier and debris-covered glacier tongue. Here, the analysis of recent and high-resolution geodetic data together with GST data provides key information regarding the kinematic response to thermally driven processes. Moreover, geo-

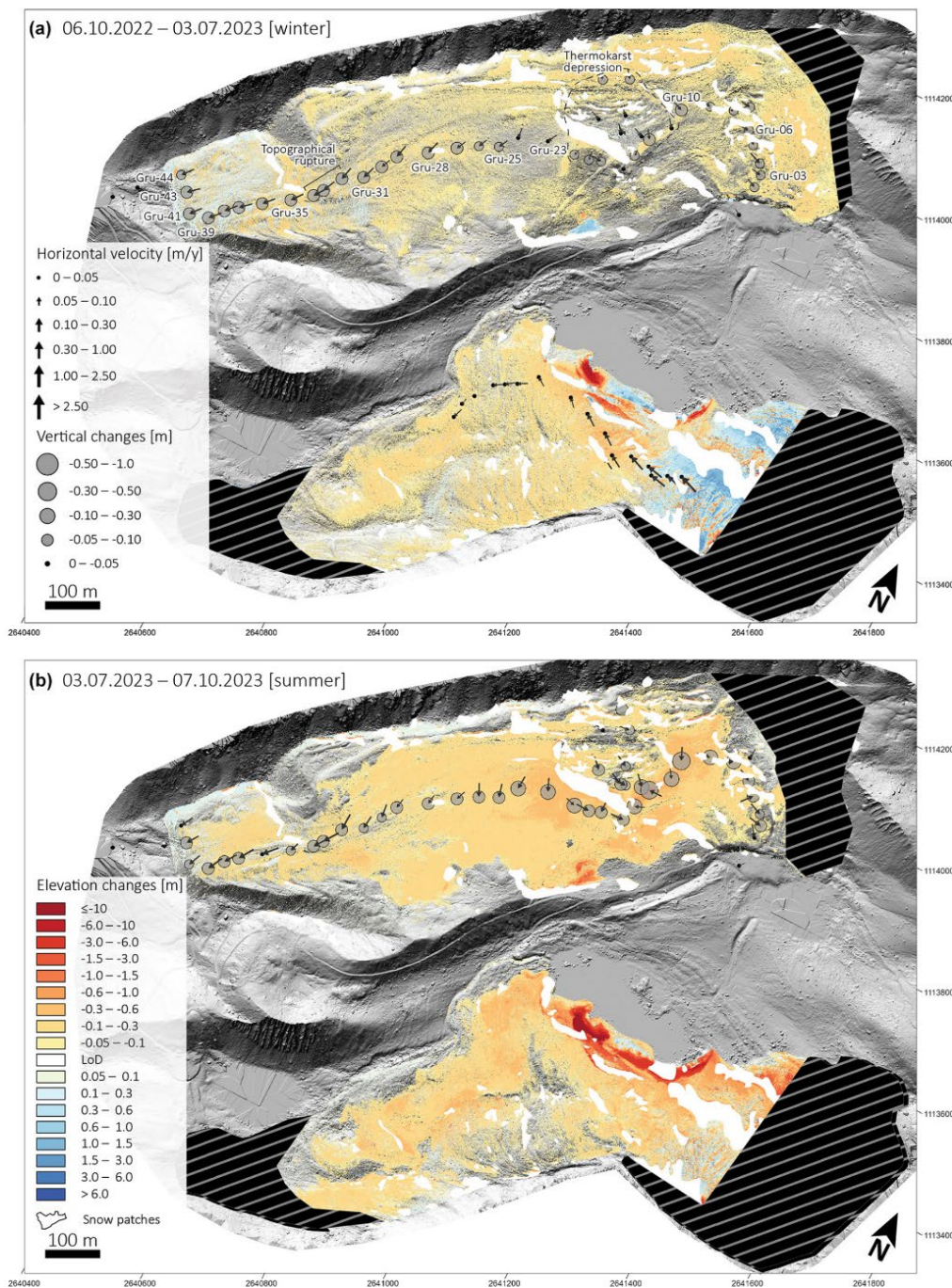


Figure 7. Seasonal elevation changes derived from DoD. Vertical changes and horizontal surface displacements derived from TGS. The measured points are identified by their corresponding number (Gru-xx, only in panel a). The winter period (6 October 2022 to 3 July 2023) is presented in panel (a), and the summer period (3 July 2023 to 7 October 2023) is presented in panel (b). Background: UAV-derived hillshade (6 October 2022).

	Expected Δz_{topo} [m/yr]			Ratio seasonal Δz_{topo}	Calculated $\Delta z_{\text{melt-flow}}$ [m/yr]			Ratio $\Delta z_{\text{topo}}/\Delta z_{\text{melt-flow}}$		
	summer	winter	year		summer	winter	year			
Complex contact zone	Gru-03-06	-0.11	-0.06	-0.07	2.03	-0.43	-0.06	-0.17	0.45	
	Gru-07-11	-0.13	-0.07	-0.08	2.60	-1.09	-0.05	-0.33	0.18	
	Thermokarst depression	-0.19	-0.06	-0.08	3.55	-0.98	0.01	-0.26	0.36	
	Gru-23-27	-0.08	-0.04	0.05	1.91	-0.88	-0.06	-0.28	0.20	
Rock glacier	Gru-28-31	-0.11	-0.11	-0.11	1.02	-0.26	-0.06	-0.11	1.79	
	Topographical rupture	-0.43	-0.36	-0.38	1.18	1.12	-0.31	0.06	-0.04	10.86
	Gru-35-44	-0.23	-0.20	-0.21	1.17	-0.23	-0.02	-0.08	2.71	

Figure 8. The seasonal (summer and winter) and annual expected downslope displacement (solely following the slope angle topography) was calculated for the different zones (see Fig. 7) of the rock glacier and the complex contact zone. The ratio between the summer and winter expected downslope displacement was calculated (ratio seasonal Δz_{topo}). Seasonal and annual surface lowering rates (calculated $\Delta z_{\text{melt-flow}}$) are presented. The main dynamics are represented by the ratio between the annual expected downslope displacement (Δz_{topo}) and the calculated annual surface lowering ($\Delta z_{\text{melt-flow}}$).

electrical and refraction seismic data enabled the characterization of the subsurface, which revealed the influence of ground ice content and properties and the active-layer (or debris-cover) thickness on surface dynamics.

5.1 Evaluation of the geophysical approach

Using several ERT and RST profile lines on the rock glacier and debris-covered glacier, we applied a petrophysical joint inversion (PJI) approach to model the four phase contents of the subsurface, with a focus on the quantification of the ground ice content. Within the PJI, the geometric mean model was employed to link the measured electrical resistivities with the volumetric fractions of each phase, as this approach has yielded well-constrained estimations of ice content and porosity for ice-rich rock glaciers (Mollaret et al., 2020) such as the Gruben rock glacier. As mentioned in Sect. 3.3, different parameters, such as the initial porosity and the resistivity values of the four phases, were tested to build a plausible range of model estimations. It was found that the ground ice estimation is sensitive to the model's initial porosity constraints (Halla et al., 2021; Hilbich et al., 2022; Mollaret et al., 2020), as initial porosities $\geq 60\%$ systematically yielded higher mean ground ice content, which appeared to be the most plausible ice content values according to the model's χ^2 and rms error. The choice of the most

plausible tomograms was determined by considering the final model's best-fit value χ^2 within the region where the model is characterized by high complexity and a low misfit. A sensitivity analysis was performed to better evaluate the reliability of the prescribed parameters and to estimate the range of possible model results from this parameter uncertainty. Figure 11 shows the dependence of (mean) ground ice contents in the different profiles on two of the major influencing parameters in our PJI models: initial porosity φ_{start} and ice resistivity ρ_i . Higher initial porosities ($\varphi_{\text{start}} \geq 0.6$) systematically generated lower χ^2 and rms values (not shown) (Fig. 11). Moreover, we tested the uncertainty range related to the influence of the prescribed water resistivity values ρ_w (5, 50, 100 Ωm ; red circles in Fig. 11) for a fixed set of other parameters. No significant variation in the mean ice content occurs, which reduces the uncertainty in regard to the chosen model. Finally, the choice of the model was also based on geomorphological knowledge and information from geodetic and temperature measurements. In contrast to the strong ambiguity between ice and rock content found in model applications using Archie's law (Hauck et al., 2011; Wagner et al., 2019), the application of the geometric mean model reduces the ice and rock ambiguity as all four phases are constrained by both geophysical datasets (Mollaret et al., 2020). Here, the model enabled better and more realistic estimations of the ice content.

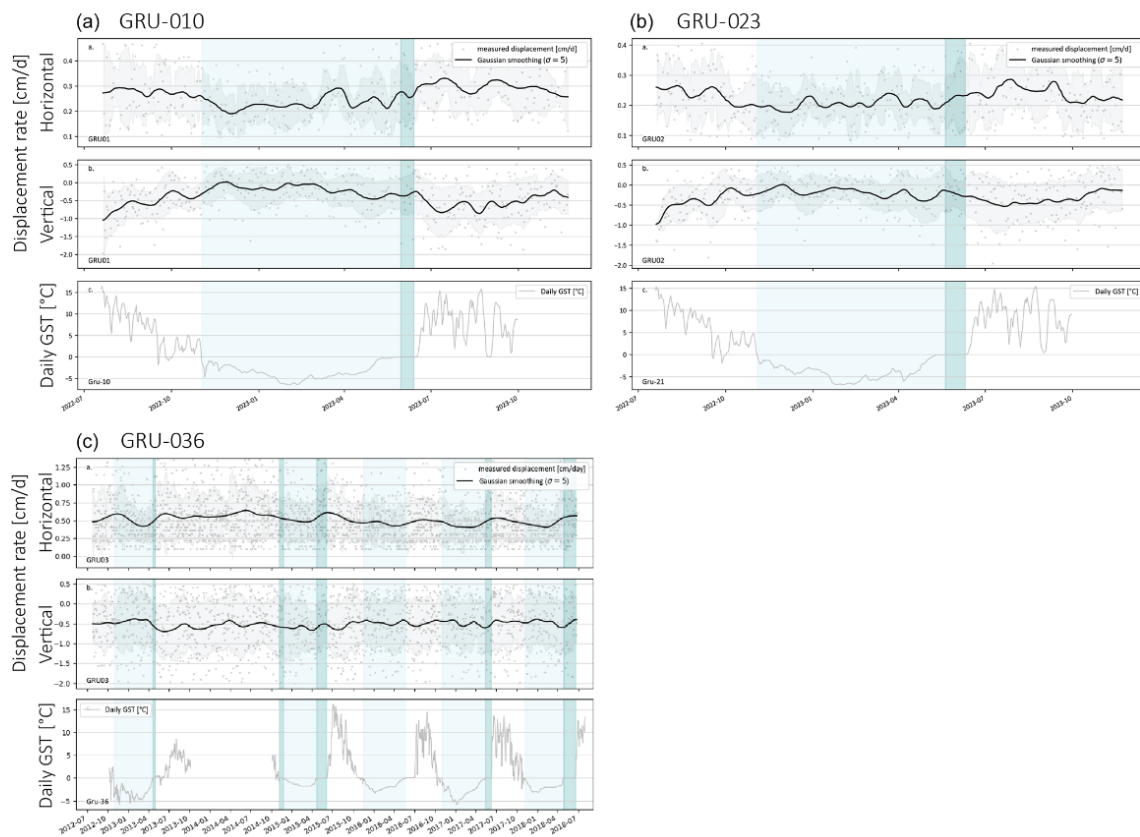


Figure 9. Ground surface temperature and horizontal and vertical velocity time series in the complex contact zones Gru-010 (a) and Gru-023 (b) and in the rock glacier zone Gru-036 (c). The time series recorded by the stations GRU-010 and GRU-023 span July 2022 to early October 2023, whereas the time series recorded by the station GRU-036 spans July 2012 to June 2018. The period highlighted in light blue represents GST below 0 °C, and the period highlighted in dark blue represents the zero-curtain period. Grey points represent the measured data.

The petrophysical joint inversion approach uses the measured apparent resistivities and seismic travel times to image the volumetric fractions of ice, rock, water, and air content. The latter is then re-transformed into P-wave velocity and electrical resistivity tomograms using the same petrophysical Eqs. (1) to (3). Thereby, we additionally assessed the reliability of the model by comparing the conventional, individually inverted ERT and RST tomograms with the PJI-derived (transformed) ERT and RST tomograms (Fig. 12). The same regularization parameters and mesh sizes were used for the individual inversions and for the PJI. All transformed ERT tomograms are qualitatively in good agreement with the conventional ERT tomograms. However, individual information, in particular higher velocities, is not represented in the transformed RST tomograms. Some discrepancies are also observed at the edges of the tomograms (e.g. profile GRU-S04), where the model’s sensitivity to the measured data is inher-

ently lower. The influence of these discrepancies on the overall interpretation remains minimal.

5.2 Geodetic approach

The application of dGNSS and UAV surveys enabled both a high-temporal- and high-spatial-resolution in-depth analysis of the kinematic behaviour of the Gruben rock glacier and debris-covered glacier. The large spatial coverage of the study site allowed us to grasp an overview of the general kinematic behaviour and patterns of both landforms, which are largely comparable to the observations of Kääh et al. (1997) and Gärtner-Roer et al. (2022). The geodetic datasets are quantitatively comparable, providing confidence to their robustness and reliability (Vivero et al., 2022). Despite the large spatial coverage provided by UAV-derived data, the selection of ground control points can be a challenging processing step, in particular in high-mountain environ-

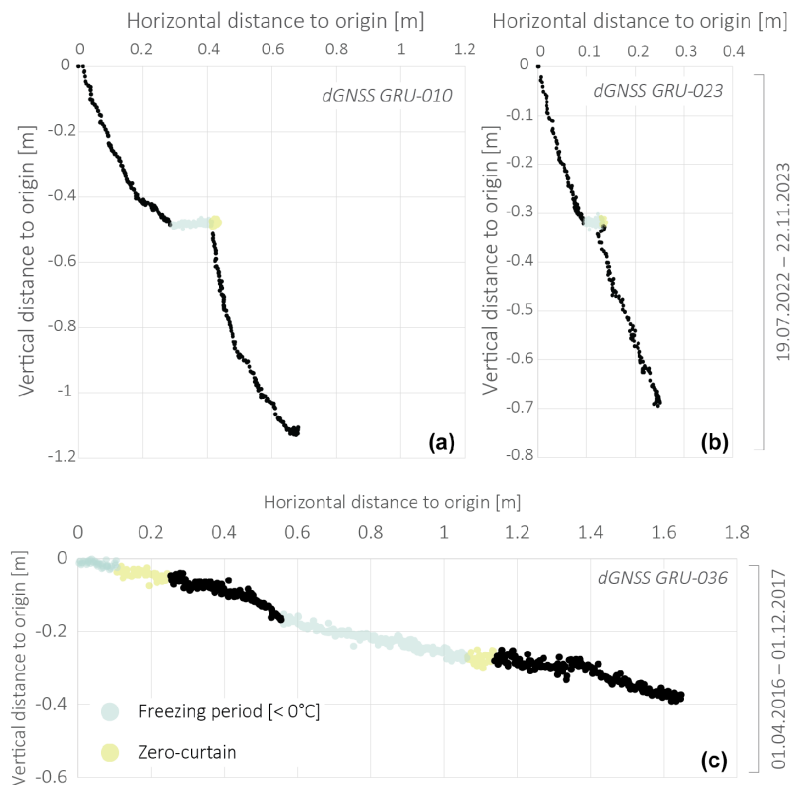


Figure 10. Displacement profiles measured by permanent dGNSS stations Gru-010 (a) and Gru-023 (b) for the period 19 July 2022 to 22 November 2023. The lower graph (c) shows the displacement profile measured by the permanent dGNSS station Gru-036 for the period 1 April 2016 to 1 December 2017.

ments where stable ground surfaces are limited. Furthermore, in this case, the deployment of UAV surveys for kinematic monitoring is limited to snow-free periods. During the early summer survey (3 July 2023), seasonal snow patches were still present on both the rock glacier and the debris-covered glacier and were consequently masked out due to their interference with the image correlation processing applied.

Permanent GNSS stations provided a very high temporal resolution (hourly) of local surface displacements. Here, the use of a reference station mounted on stable ground allowed the accuracy of the measured coordinates to be substantially improved, as each position was corrected in real time relative to the reference station. Despite the noisy dataset, which was filtered by applying a simple 15 d running mean approach, this dataset allowed us to better understand the thermo-mechanical response of the rock glacier and complex contact zone to ground temperature changes in regards to the thickness of the coarse blocky layer above the frozen ground.

5.3 Internal structure and surface dynamics of the Gruben rock glacier and complex contact zone

Despite the lack of a clear surface morphology that would allow a straightforward delineation between the rock glacier and the former glacier–rock-glacier contact zone, the observations made in this study provided key information to better understand the extent of the Gruben LIA glacier on the pre-existing perennally frozen sediments.

Geoelectrical soundings performed between 1979 and 1982 revealed ice-rich permafrost conditions in the downslope section of the rock glacier, here considered as the non-glacier-affected rock glacier zone (King et al., 1987). The results from geoelectrical and refraction seismic data of the present study confirmed the occurrence of a layer of ice-rich permafrost at depth in the frontal zone of the rock glacier and demonstrate the resilience of permafrost to the increasing air temperatures in the past 4 decades. The current conditions infer that the Gruben rock glacier was already under permafrost conditions before the LIA advance of the Gruben glacier. In the upslope section of the rock glacier, geomor-

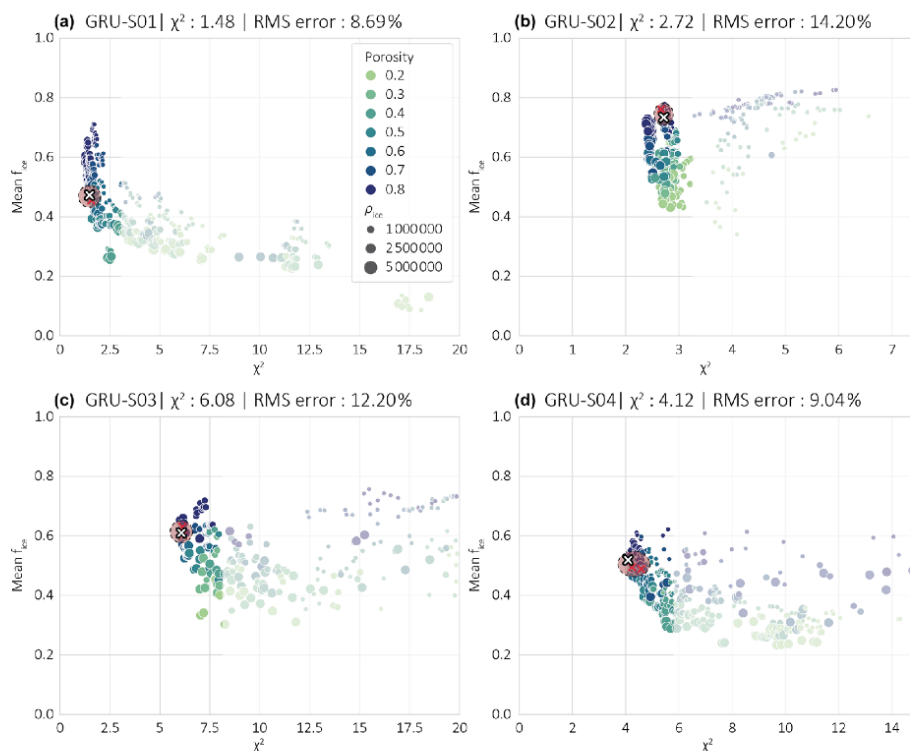


Figure 11. Sensitivity analysis of mean ice content (f_{ice}) for the entire tomogram and model-fit χ^2 to the prescribed porosity and resistivity of ice (ρ_{ice}) for profiles GRU-S01 (a), GRU-S02 (b), GRU-S03 (c), and GRU-S04 (d). χ^2 and rms error indicated in the title correspond to the PJI chosen for interpretation. The white cross represents the chosen model, and the red crosses represent the models with the same set of prescribed parameters aside from ρ_w . The red circle represents the uncertainty range for ρ_w on the estimated mean ice content.

phological indicators attest to a former contact zone between the permafrost of the Gruben rock glacier and the polythermal Gruben glacier during its LIA maximal extent (Kääb et al., 1997; Gärtner-Roer et al., 2022; Haerberli et al., 2024). During the interaction phase between the polythermal glacier and the permafrost of the rock glacier, debris-covered glacier ice was locally embedded within, and primarily on top of, the frozen debris, as evidenced by the geomorphological imprint of thermokarst in the former contact zone but also by the extremely resistive and widespread ground ice content, likely referring to buried cold surface ice.

The spatial distribution of ground ice and its associated properties (embedded cold glacier ice or supersaturated permafrost) within the rock glacier is reflected by the heterogeneous kinematic behaviour of the latter (Bosson and Lambiel, 2016; Cusicanqui et al., 2023; Kunz et al., 2022). The former glacier–permafrost interaction phase not only altered the spatial distribution of ground ice and ground surface thermal regime of the investigated landform through the direct material contact with its thermal coupling and mass exchange, but also induced geometrical deformations (changes

in the topographic conditions) with related changes in stress transmission and stress fields. It is likely that the pressure – and hence the associated stress field reorientation – exerted by the formerly advancing polythermal glacier onto the pre-existing perennially frozen-debris landform was transmitted across extended spatial scales. Deformation may have reached a few tens of metres in depth and over a few hundreds of metres horizontally, meaning that the entire width of the rock glacier was probably impacted.

Figure 13 shows the general extent to which the mechanical behaviour of the rock glacier was influenced by the stresses exerted by the LIA glacier advances. It is likely that down-valley of the topographical rupture, large-scale stress transmission did not occur and the mechanical behaviour (steady-state creep) of the perennially frozen body remained as it was prior to the LIA glacier advance. Coherent flow fields and longitudinal ridges and furrows observed in the downslope section of the rock glacier indicate the gravity and thermally driven internal permafrost creep deformation and extending flow, respectively. However, up-valley of the topographical rupture up to the western bound-

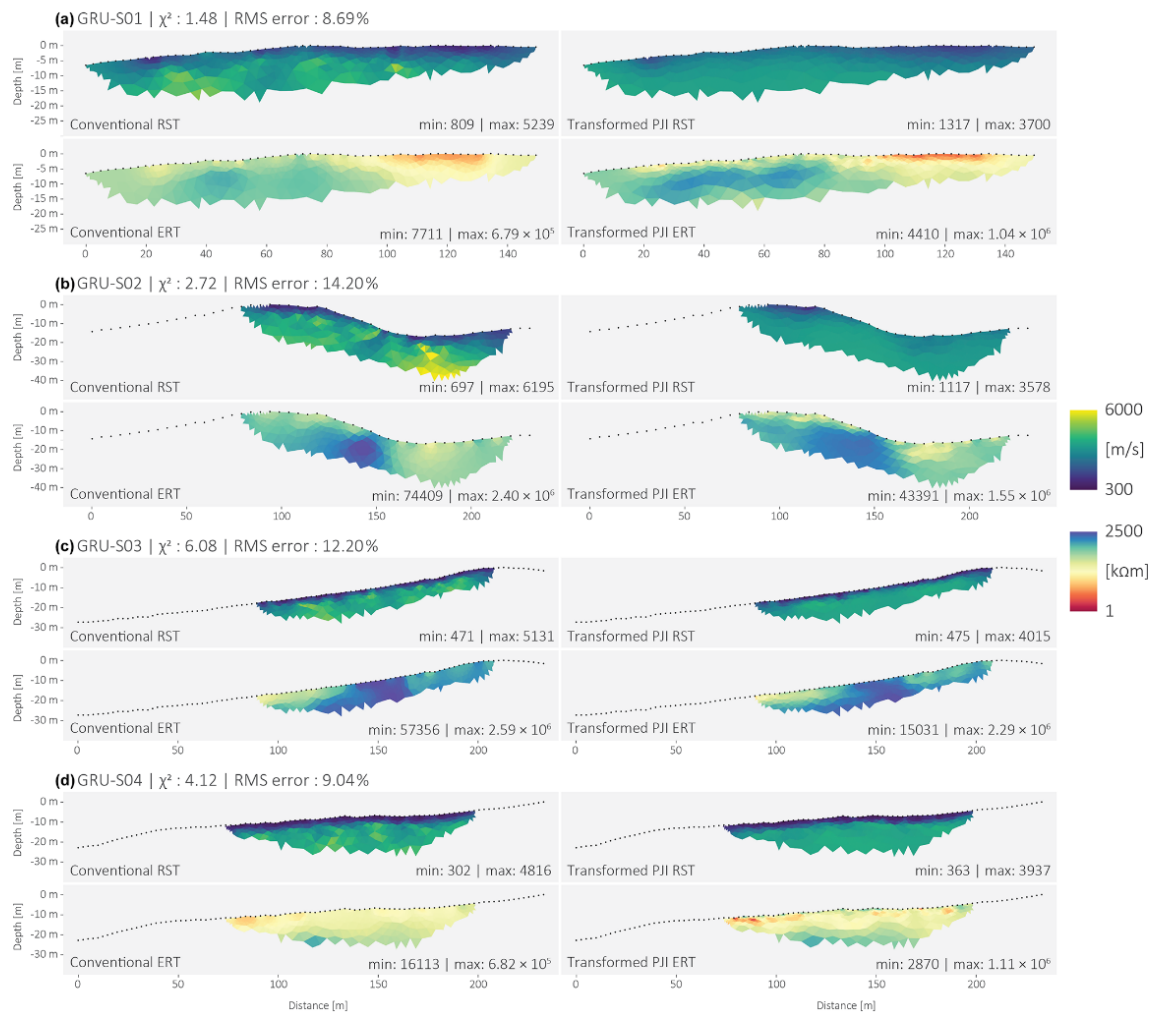


Figure 12. Comparison between the results from the conventional (individual) RST and ERT inversions with the resistivity and P-wave velocity distributions obtained from the PJI using the geometric mean model for resistivity. The electrical resistivity (here in kΩm) is displayed on a logarithmic colour scale.

ary of the thermokarst depression, the stress exerted by the Gruben glacier during its LIA advances probably reached the orographic right side of the rock glacier, causing internal and surface deformation, which could be reflected by the flow trajectories and the compression ridges marked by the dashed dark-red lines. Moreover, a glacier advance prior to the latest 1850 advance (Fig. 13) could have contributed to the mechanical deformation in this zone of the rock glacier. Further up-valley in the complex contact zone, less coherent flow fields, diverging from the down-valley direction towards the glacier forefield, indicate geometrical adjustments following the interaction phase between the Gruben rock glacier and

the debris-covered glacier. A lateral back-creeping motion dominates this former contact zone. However, in the vicinity of the thermokarst depression, the flow pattern becomes locally much less coherent as the topography is relatively chaotic, favouring the stochastic displacement of the blocky surface. Moreover, where ground ice content is widespread within a rock matrix with excess ice, surface lowering is mainly interpreted as the expression of ice melt and thaw subsidence. The magnitude of the latter is highly dependent of the ground ice properties, the surface debris thickness and coarseness, and the temperature of the ground surface. The results from the geodetic and temperature measurements

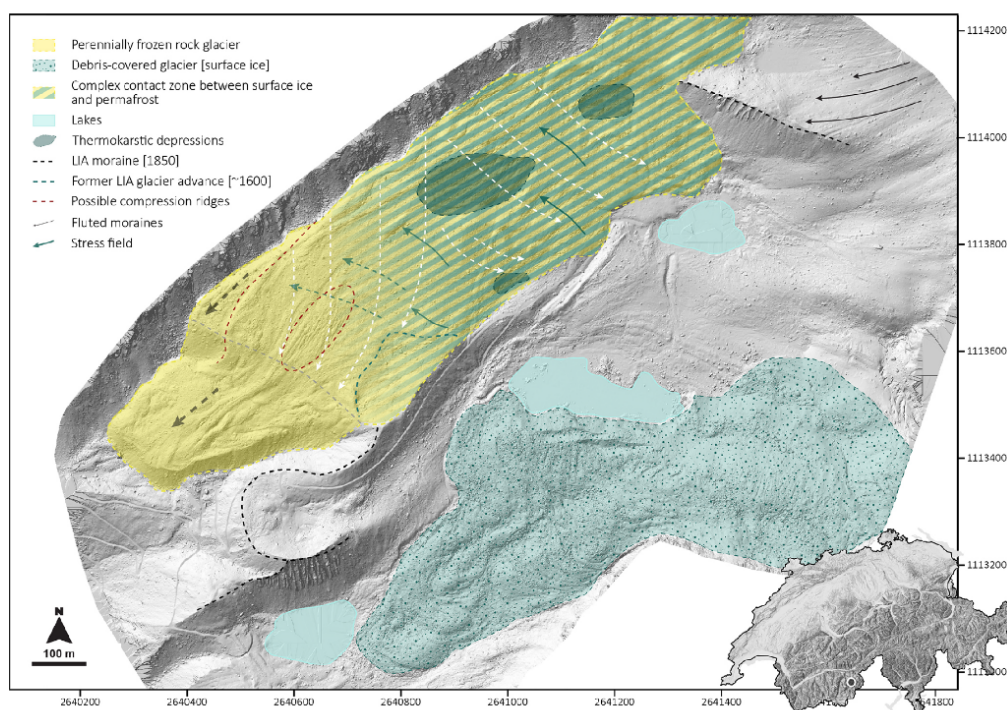


Figure 13. Interpretation of the influence of the LIA glacier–permafrost interaction on the mechanical behaviour of the rock glacier and its adjacent complex contact zone based on the analysis of high-resolution photogrammetry. The dashed black line represents the LIA (1850) moraine and consequently the maximal extent of the Gruben glacier during its LIA apogee. The dashed grey line represents the topographical rupture. The dark blue arrows represent the stress exerted by the glacier onto the rock glacier. The dashed white arrows show the reoriented flow trajectories of the rock glacier and complex contact zone as a response to the stress exerted by the LIA glacier, while the dashed grey arrows show the unchanged flow trajectory of the rock glacier. The dashed blue line shows the probable extent of a prior stage (~1600) of LIA glacier advance. The dashed dark-red line on the orographic right side of the rock glacier and the dashed ellipse show compression ridges likely due to the glacier stress. Background: UAV-derived hillshade (6 October 2022).

show direct and high-magnitude responses of subsidence to summer ground surface heating in the complex contact zone, and the warmest temperatures are hereby associated with the largest subsidence. In this context, this shows that surface lowering is dominated by ice melt, a thermally driven process occurring at the permafrost or ground ice table (Staub et al., 2016; Wee and Delaloye, 2022). On the rock glacier, the loss in elevation appears to be mainly driven by internal continuous creep deformation, as the magnitude of the displacement is rather constant throughout the year, aside from a slight acceleration in early summer and early autumn and a slight deceleration in winter. Ice-melt-induced subsidence appears to be rather ineffective regarding surface lowering; however, the seasonal increase in water content due to snowmelt and permafrost thaw enhances the deformation, suggesting that surface lowering due to a seasonally increased extensive flow pattern cannot be excluded (Cicoira et al., 2019).

5.4 Surface dynamics of the Gruben debris-covered glacier tongue

Surface changes observed on the debris-covered tongue reflect typical processes in response to seasonal variations. However, the magnitude of surface changes observed in the lower section of the Gruben glacier tongue is much smaller than of those observed in the uppermost section of the debris-covered tongue, which is likely due to the thicker debris cover of the latter. The debris-covered glacier terminus, which is still connected to the debris-free active Gruben glacier, documents drastic signs of downwasting. The lowermost section of the debris-covered tongue, on the other hand, shows signs of advanced degradation, in particular in its margins where only very slight surface changes occur (Gärtner-Roer et al., 2022). In addition to the low flow velocities of the tongue's terminus which impede the removal of the debris from the glacier, an important input of debris is provided

from the north-western flank of the Inner Rothorn (Benn et al., 2001; Mölg et al., 2020). In view of the thickness of the debris cover, which reaches up to roughly 5 m (Fig. 4), it cannot be excluded that the latter significantly reduces the ablation rate of the terminus part, as near-surface heat transfer is dissipated into the atmosphere before being transferred to the underlying ice surface (Nicholson and Benn, 2006; Rounce et al., 2015). The heterogeneity of the debris-cover thickness causes differential ablation rates and consequently a rather chaotic debris surface. These differential ablation rates can also eventually lead to the development of ice cliffs (Buri et al., 2016), as is the case at Gruben.

6 Conclusion

The multi-method approach applied in this study provided new insights into ongoing intra-annual and annual dynamics of complex ice-rich landform systems, such as the Gruben rock glacier and Gruben debris-covered glacier. This study has established the relationship between the internal structure of the investigated landforms with their physical processes and associated surface dynamics. The magnitude of ice-melt-induced subsidence was the highest in the complex contact zone where still-existing, isolated remnants of buried surface ice were detected by the geophysical investigations. Pronounced surface elevation loss due to extending flow and downslope movement was observed on the glacier-forefield-connected rock glacier, which reflects the dominance of permafrost creep deformation. The kinematic signature of these two distinct morphological zones attests to the geomorphological heritage from the Holocene and LIA and highlights the interrelationship between glacial and periglacial processes occurring in the so-called complex contact zone. This underlines the complexity in capturing a complete and thorough understanding of the driving processes contributing to the morphodynamical evolution of such systems. This study also revealed the resilience of the ground ice to a warming atmosphere, in particular in the permafrost of the rock glacier. This was also found for the glacier ice beneath the thickening debris cover of the Gruben glacier terminus, which is in complete disequilibrium with the current climate.

Data availability. GST and TCS data are partly available on the PERMOS data portal (<https://doi.org/10.13093/permos-2024-01>, PERMOS, 2024). All other data are available upon request to the corresponding author.

Author contributions. JW designed the research; collected the GST and GNSS data since 2016; planned, coordinated, and participated in the geophysical campaigns; and processed and analysed the GST, GNSS, and geophysical data. SV conducted the UAV campaigns and processed the UAV-derived data with JW. TM and CM contributed to the development of the PJI code. JB provided data of

one of the permanent GNSS stations. CII and CI supervised and contributed to the study design. WH provided his knowledge from earlier studies and local hazard protection work. All authors were involved in the discussion and in the preparation of the manuscript.

Competing interests. At least one of the (co-)authors is a member of the editorial board of *The Cryosphere*. The peer-review process was guided by an independent editor, and the authors also have no other competing interests to declare.

Disclaimer. Publisher's note: Copernicus Publications remains neutral with regard to jurisdictional claims made in the text, published maps, institutional affiliations, or any other geographical representation in this paper. While Copernicus Publications makes every effort to include appropriate place names, the final responsibility lies with the authors.

Acknowledgements. The acquisition of this important dataset would not have been possible without the valuable support and work from colleagues and friends involved in the fieldwork. We are sincerely grateful for the time and effort that you have invested in helping with the data acquisition. We are also thankful for the support that we received from the municipality of Saas-Balen for making the access to Gruben easier. We thank PERMOS for support with the collection of the GST and GNSS data.

Review statement. This paper was edited by Vishnu Nandan and reviewed by Adriano Ribolini and one anonymous referee.

References

- Amschwand, D., Scherler, M., Hoelzle, M., Krummenacher, B., Haberkorn, A., Kienholz, C., and Gubler, H.: Surface heat fluxes at coarse blocky Murtèl rock glacier (Engadine, eastern Swiss Alps). *The Cryosphere*, 18, 2103–2139, <https://doi.org/10.5194/tc-18-2103-2024>, 2024.
- Archie, G. E.: The Electrical Resistivity Log as an Aid in Determining Some Reservoir Characteristics, *Trans. AIME*, 146, 54–62, <https://doi.org/10.2118/942054-G>, 1942.
- Ballantyne, C. K.: *Periglacial Geomorphology*, John Wiley & Sons, 496 pp., 2018.
- Benn, D. I., Wiseman, S., and Hands, K. A.: Growth and drainage of supraglacial lakes on debris-mantled Ngozumpa Glacier, Khumbu Himal, Nepal. *J. Glaciol.*, 47, 626–638, <https://doi.org/10.3189/172756501781831729>, 2001.
- Bosson, J.-B. and Lambiel, C.: Internal Structure and Current Evolution of Very Small Debris-Covered Glacier Systems Located in Alpine Permafrost Environments. *Front. Earth Sci.*, 4, 39, <https://doi.org/10.3389/feart.2016.00039>, 2016.
- Bosson, J.-B., Deline, P., Bodin, X., Schoeneich, P., Baron, L., Gardent, M., and Lambiel, C.: The influence of ground ice distribution on geomorphic dynamics since the Little Ice Age in proglacial areas of two cirque glacier systems. *Earth Surf.*

- Process. Landf., 40, 666–680, <https://doi.org/10.1002/esp.3666>, 2015.
- Buri, P., Pellicciotti, F., Steiner, J. F., Miles, E. S., and Immerzeel, W. W.: A grid-based model of backwasting of supraglacial ice cliffs on debris-covered glaciers, *Ann. Glaciol.*, 57, 199–211, <https://doi.org/10.3189/2016AoG71A059>, 2016.
- Carturan, L., Rastner, P., and Paul, F.: On the disequilibrium response and climate change vulnerability of the mass-balance glaciers in the Alps, *J. Glaciol.*, 66, 1034–1050, <https://doi.org/10.1017/jog.2020.71>, 2020.
- Cicoira, A., Beutel, J., Fäilleltaç, J., and Vieli, A.: Water controls the seasonal rhythm of rock glacier flow, *Earth Planet. Sci. Lett.*, 528, 115844, <https://doi.org/10.1016/j.epsl.2019.115844>, 2019.
- Cicoira, A., Marcer, M., Gärtner-Roer, L., Bodin, X., Arenson, L. U., and Vieli, A.: A general theory of rock glacier creep based on in-situ and remote sensing observations, *Permafrost Periglac. Process.*, 32, 139–153, <https://doi.org/10.1002/ppp.2090>, 2021.
- Cicoira, A., Weber, S., Biri, A., Buchli, B., Delaloye, R., Da Forno, R., Gärtner-Roer, L., Gruber, S., Gsell, T., Hasler, A., Lim, R., Limpach, P., Mayoraz, R., Meyer, M., Noetzi, J., Phillips, M., Pointner, E., Ractzo, H., Scapozza, C., Strozzi, T., Thiele, L., Vieli, A., Vonder Mühll, D., Wirz, V., and Beutel, J.: In situ observations of the Swiss periglacial environment using GNSS instruments, *Earth Syst. Sci. Data*, 14, 5061–5091, <https://doi.org/10.5194/essd-14-5061-2022>, 2022.
- Colombo, N., Salerno, F., Martin, M., Malandrino, M., Giardino, M., Serra, E., Godone, D., Said-Pullicino, D., Pratianni, S., Paro, L., Tartari, G., and Freppaz, M.: Influence of permafrost, rock and ice glaciers on chemistry of high-elevation ponds (NW Italian Alps), *Sci. Total Environ.*, 685, 886–901, <https://doi.org/10.1016/j.scitotenv.2019.06.233>, 2019.
- Cusicanqui, D., Bodin, X., Duvillard, P.-A., Schoeneich, P., Revil, A., Assier, A., Berthet, J., Peyron, M., Roudniiska, S., and Rabatel, A.: Glacier, permafrost and thermokarst interactions in Alpine terrain: Insights from seven decades of reconstructed dynamics of the Chauvet glacial and periglacial system (Southern French Alps), *Earth Surf. Process. Landf.*, 48, 2595–2612, <https://doi.org/10.1002/esp.5650>, 2023.
- Debella-Gilo, M. and Kääh, A.: Sub-pixel precision image matching for measuring surface displacements on mass movements using normalized cross-correlation, *Remote Sens. Environ.*, 115, 130–142, <https://doi.org/10.1016/j.rse.2010.08.012>, 2011.
- Del Siro, C., Scapozza, C., Perga, M.-E., and Lambiel, C.: Investigating the origin of solutes in rock glacier springs in the Swiss Alps: A conceptual model, *Front. Earth Sci.*, 11, 1056305, <https://doi.org/10.3389/feart.2023.1056305>, 2023.
- Dracbing, D.: Application of refraction seismics in alpine permafrost studies: A review, *Earth-Sci. Rev.*, 155, 136–152, <https://doi.org/10.1016/j.earscirev.2016.02.006>, 2016.
- Etzelmüller, B. and Hagen, J. O.: Glacier-permafrost interaction in Arctic and alpine mountain environments with examples from southern Norway and Svalbard, *Geol. Soc. Lond. Spec. Publ.*, 242, 11–27, <https://doi.org/10.1144/GSL.SP.2005.242.01.02>, 2005.
- Gärtner-Roer, I. and Bast, A.: (Ground) Ice in the Proglacial Zone, in: *Geomorphology of Proglacial Systems*, Springer, 85–98, ISBN 978-3-319-94182-0, 2019.
- Gärtner-Roer, L., Brunner, N., Delaloye, R., Haerberli, W., Kääh, A., and Thee, P.: Glacier-permafrost relations in a high-mountain environment: 5 decades of kinematic monitoring at the Gruben site, Swiss Alps, *The Cryosphere*, 16, 2083–2101, <https://doi.org/10.5194/tc-16-2083-2022>, 2022.
- Glover, P. W. J.: A generalized Archie's law for n phases, *Geophysics*, 75, E247–E265, <https://doi.org/10.1190/1.3509781>, 2010.
- Günther, T. and Rücker, C.: Boundless Electrical Resistivity Tomography BERT 2 – the user tutorial, version 2.4.1, <http://www.resistivity.net/download/bert-tutorial.pdf> (last access: 16 December 2024), 2023.
- Haerberli, W.: Eistemperaturen in den Alpen, *Z. Für Gletscherkunde Glazialgeol.*, X/2, 203–220, 1976.
- Haerberli, W.: Investigating glacier-permafrost relationships in high-mountain areas: historical background, selected examples and research needs, *Geol. Soc. Lond. Spec. Publ.*, 242, 29–37, <https://doi.org/10.1144/GSL.SP.2005.242.01.03>, 2005.
- Haerberli, W. and Vonder Mühll, D.: On the characteristics and possible origins of ice in rock glacier permafrost, *Zeitschrift für Geomorphologie*, 43–57, 1996.
- Haerberli, W., Hallet, B., Arenson, L., Elconin, R., Humlum, O., Kääh, A., Kaufmann, V., Ladanyi, B., Matsuoka, N., Springman, S., and Mühll, D. V.: Permafrost creep and rock glacier dynamics, *Permafrost Periglac. Process.*, 17, 189–214, <https://doi.org/10.1002/ppp.561>, 2006.
- Haerberli, W., Arenson, L. U., Wee, J., Hauck, C., and Mölg, N.: Discriminating viscous-creep features (rock glaciers) in mountain permafrost from debris-covered glaciers – a commented test at the Gruben and Yerba Loca sites, Swiss Alps and Chilean Andes, *The Cryosphere*, 18, 1669–1683, <https://doi.org/10.5194/tc-18-1669-2024>, 2024.
- Halla, C., Blöthe, J. H., Tapia Baldis, C., Trombotto Liaudat, D., Hilbich, C., Hauck, C., and Schrott, L.: Ice content and inter-annual water storage changes of an active rock glacier in the dry Andes of Argentina, *The Cryosphere*, 15, 1187–1213, <https://doi.org/10.5194/tc-15-1187-2021>, 2021.
- Hauck, C.: Geophysical methods for detecting permafrost in high mountains, PhD Thesis, ETH Zurich, <https://doi.org/10.3929/ethz-a-004172478>, 2001.
- Hauck, C. and Kneisel, C.: *Applied geophysics in periglacial environments*, Cambridge University Press, ISBN 978-0-521-88966-7, 2008.
- Hauck, C., Böttcher, M., and Maurer, H.: A new model for estimating subsurface ice content based on combined electrical and seismic data sets, *The Cryosphere*, 5, 453–468, <https://doi.org/10.5194/tc-5-453-2011>, 2011.
- Herring, T., Lewkowicz, A. G., Hauck, C., Hilbich, C., Mollaret, C., Oldenborger, G. A., Uhlemann, S., Farzaman, M., Calmels, F., and Scandroglia, R.: Best practices for using electrical resistivity tomography to investigate permafrost, *Permafrost Periglac. Process.*, 34, 494–512, <https://doi.org/10.1002/ppp.2207>, 2023.
- Hilbich, C.: Time-lapse refraction seismic tomography for the detection of ground ice degradation, *The Cryosphere*, 4, 243–259, <https://doi.org/10.5194/tc-4-243-2010>, 2010.
- Hilbich, C., Hauck, C., Mollaret, C., Wainstein, P., and Arenson, L. U.: Towards accurate quantification of ice content in permafrost of the Central Andes – Part 1: Geophysics-based estimates from three different regions, *The Cryosphere*, 16, 1845–1872, <https://doi.org/10.5194/tc-16-1845-2022>, 2022.

- Huss, M. and Fischer, M.: Sensitivity of Very Small Glaciers in the Swiss Alps to Future Climate Change, *Front. Earth Sci.*, 4, 34, <https://doi.org/10.3389/feart.2016.00034>, 2016.
- IPA Action Group RGIG: Guidelines for inventorying rock glaciers, <https://doi.org/10.51363/unifr.srr.2023.002>, 2023.
- Isaksen, K., Ødegård, R. S., Eiken, T., and Sollid, J. L.: Composition, flow and development of two tongue-shaped rock glaciers in the permafrost of Svalbard, *Permafrost Periglac. Process.*, 11, 241–257, [https://doi.org/10.1002/1099-1530\(200007/09\)11:3<241::AID-PPP358>3.0.CO;2-A](https://doi.org/10.1002/1099-1530(200007/09)11:3<241::AID-PPP358>3.0.CO;2-A), 2000.
- Ivy-Ochs, S., Kerschner, H., Maisch, M., Christl, M., Kubik, P. W., and Schlüchter, C.: Latest Pleistocene and Holocene glacier variations in the European Alps, *Quat. Sci. Rev.*, 28, 2137–2149, <https://doi.org/10.1016/j.quascirev.2009.03.009>, 2009.
- Kääb, A. and Haeblerli, W.: Evolution of a high-mountain thermokarst lake in the Swiss Alps, *Arct. Antarct. Alp. Res.*, 33, 385–390, 2001.
- Kääb, A. and Vollmer, M.: Surface Geometry, Thickness Changes and Flow Fields on Creeping Mountain Permafrost: Automatic Extraction by Digital Image Analysis, *Permafrost Periglac. Process.*, 11, 315–326, [https://doi.org/10.1002/1099-1530\(200012\)11:4<315::AID-PPP365>3.0.CO;2-J](https://doi.org/10.1002/1099-1530(200012)11:4<315::AID-PPP365>3.0.CO;2-J), 2000.
- Kääb, A., Haeblerli, W., and Gudmundsson, G. H.: Analysing the creep of mountain permafrost using high precision aerial photogrammetry: 25 years of monitoring Gruben rock glacier, Swiss Alps, *Permafrost Periglac. Process.*, 8, 409–426, [https://doi.org/10.1002/\(SICI\)1099-1530\(199710/12\)8:4<409::AID-PPP267>3.0.CO;2-C](https://doi.org/10.1002/(SICI)1099-1530(199710/12)8:4<409::AID-PPP267>3.0.CO;2-C), 1997.
- Kellerer-Pirklbauer, A., Bodin, X., Delaloye, R., Lambiel, C., Gärtner-Roer, I., Bonnefoy-Demongeot, M., Carturan, L., Damm, B., Eulenstein, J., Fischer, A., Hartl, L., Ikeda, A., Kaufmann, V., Krainer, K., Matsuoka, N., Cella, U. M. D., Noetzi, J., Scoppi, R., Scapozza, C., Schoeneich, P., Stocker-Waldhuber, M., Thibert, E., and Zumbani, M.: Acceleration and interannual variability of creep rates in mountain permafrost landforms (rock glacier velocities) in the European Alps in 1995–2022, *Environ. Res. Lett.*, 19, 034022, <https://doi.org/10.1088/1748-9326/ad25a4>, 2024.
- Kenner, R.: Geomorphological analysis on the interaction of Alpine glaciers and rock glaciers since the Little Ice Age, *Land Degrad. Dev.*, 30, 580–591, <https://doi.org/10.1002/ldr.3238>, 2019.
- Kenner, R., Noetzi, J., Hoelzle, M., Raetz, H., and Phillips, M.: Distinguishing ice-rich and ice-poor permafrost to map ground temperatures and ground ice occurrence in the Swiss Alps, *The Cryosphere*, 13, 1925–1941, <https://doi.org/10.5194/tc-13-1925-2019>, 2019.
- King, L., Fisch, W., Haeblerli, W., and Wächter, H. P.: Comparison of resistivity and radio-echo sounding on rock glacier permafrost, *Z. Für Gletscherkunde Glazialgeol.*, 32, 77–97, 1987.
- Kneisel, C. and Kääb, A.: Mountain permafrost dynamics within a recently exposed glacier forefield inferred by a combined geomorphological, geophysical and photogrammetrical approach, *Earth Surf. Process. Landf.*, 32, 1797–1810, <https://doi.org/10.1002/esp.1488>, 2007.
- Kunz, J. and Kneisel, C.: Glacier–Permafrost Interaction at a Thrust Moraine Complex in the Glacier Forefield Muragl, Swiss Alps, *Geosciences*, 10, 205, <https://doi.org/10.3390/geosciences10060205>, 2020.
- Kunz, J., Ullmann, T., and Kneisel, C.: Internal structure and recent dynamics of a moraine complex in an alpine glacier forefield revealed by geophysical surveying and Sentinel-1 InSAR time series, *Geomorphology*, 398, 108052, <https://doi.org/10.1016/j.geomorph.2021.108052>, 2022.
- Lambiel, C. and Delaloye, R.: Contribution of real-time kinematic GPS in the study of creeping mountain permafrost: examples from the Western Swiss Alps, *Permafrost Periglac. Process.*, 15, 229–241, <https://doi.org/10.1002/ppp.496>, 2004.
- Maisch, M., Haeblerli, W., Frauenfelder, R., Kääb, A., and Rothenbühler, C.: Lateglacial and Holocene evolution of glaciers and permafrost in the Val Muragl, Upper Engadin, Swiss Alps, in: *Proceedings 8th International Conference on Permafrost, International Conference on Permafrost 20–15 July 2003, Zurich, Switzerland*, 717–722, ISBN 90 5809 582 7, 2003.
- Mölg, N., Ferguson, J., Bolch, T., and Vietl, A.: On the influence of debris cover on glacier morphology: How high-relief structures evolve from smooth surfaces, *Geomorphology*, 357, 107092, <https://doi.org/10.1016/j.geomorph.2020.107092>, 2020.
- Mollaret, C., Hilbich, C., Pellet, C., Flores-Orozco, A., Delaloye, R., and Hauck, C.: Mountain permafrost degradation documented through a network of permanent electrical resistivity tomography sites, *The Cryosphere*, 13, 2557–2578, <https://doi.org/10.5194/tc-13-2557-2019>, 2019.
- Mollaret, C., Wagner, R. M., Hilbich, C., Scapozza, C., and Hauck, C.: Petrophysical Joint Inversion Applied to Alpine Permafrost Field Sites to Image Subsurface Ice, *Water, Air, and Rock Contents, Front. Earth Sci.*, 8, 85, <https://doi.org/10.3389/feart.2020.00085>, 2020.
- Monnier, S. and Kinnard, C.: Reconsidering the glacier to rock glacier transformation problem: New insights from the central Andes of Chile, *Geomorphology*, 238, 47–55, <https://doi.org/10.1016/j.geomorph.2015.02.025>, 2015.
- Monnier, S., Kinnard, C., Surazakov, A., and Bossy, W.: Geomorphology, internal structure, and successive development of a glacier foreland in the semiarid Chilean Andes (Cerro Tapado, upper Elqui Valley, 30°08' S., 69°55' W.), *Geomorphology*, 207, 126–140, <https://doi.org/10.1016/j.geomorph.2013.10.031>, 2014.
- Navarro, G., Valois, R., MacDonell, S., De Pasquale, G., and Díaz, J. P.: Internal structure and water routing of an ice-debris landform assemblage using multiple geophysical methods in the semiarid Andes, *Front. Earth Sci.*, 11, 1102620, <https://doi.org/10.3389/feart.2023.1102620>, 2023.
- Nicholson, L. and Benn, D. I.: Calculating ice melt beneath a debris layer using meteorological data, *J. Glaciol.*, 52, 463–470, <https://doi.org/10.3189/172756506781828584>, 2006.
- Noetzi, J. and Pellet, C. (Eds.): PERMOS 2023, Swiss Permafrost Bulletin 2022 (Annual report No. 4 on permafrost observation in the Swiss Alps), Cryospheric Commission of the Swiss Academy of Sciences, <https://doi.org/10.13093/permos-bull-2023>, 2023.
- PERMOS: PERMOS Database, Swiss Permafrost Monitoring Network, Davos and Fribourg, Switzerland [data set], <https://doi.org/10.13093/permos-2024-01>, 2024.
- Redpath, T. A. N., Sirguey, P., Fitzsimons, S. J., and Kääb, A.: Accuracy assessment for mapping glacier flow velocity and detecting flow dynamics from ASTER satellite imagery: Tasman Glacier, New Zealand, *Remote Sens. Environ.*, 133, 90–101, <https://doi.org/10.1016/j.rse.2013.02.008>, 2013.

- Reynard, F., Lambiel, C., Delaloye, R., Devaud, G., Baron, L., Chapellier, D., Marescot, L., and Monnet, R.: Glacier/permafrost relationships in forefields of small glaciers (Swiss Alps), in: Proceedings 8th international conference on permafrost, International Conference on Permafrost, 20–15 July 2003, Zurich, Switzerland, 947–952. ISBN 90 5809 582 7, 2003.
- Ribolini, A., Guglielmin, M., Fabre, D., Bodin, X., Marchisio, M., Sartini, S., Spagnolo, M., and Schoeneich, P.: The internal structure of rock glaciers and recently deglaciated slopes as revealed by geoelectrical tomography: insights on permafrost and recent glacial evolution in the Central and Western Alps (Italy–France). *Quat. Sci. Rev.*, 29, 507–521, <https://doi.org/10.1016/j.quascirev.2009.10.008>, 2010.
- Robson, B. A., Bolch, T., MacDonell, S., Hölbling, D., Rastner, P., and Schaffer, N.: Automated detection of rock glaciers using deep learning and object-based image analysis. *Remote Sens. Environ.*, 250, 112033, <https://doi.org/10.1016/j.rse.2020.112033>, 2020.
- Rounce, D. R., Quincey, D. J., and McKinney, D. C.: Debris-covered glacier energy balance model for Imja–Jhotse Shar Glacier in the Everest region of Nepal. *The Cryosphere*, 9, 2295–2310, <https://doi.org/10.5194/tc-9-2295-2015>, 2015.
- Rücker, C., Günther, T., and Wagner, F. M.: pyGIMLI: An open-source library for modelling and inversion in geophysics. *Comput. Geosci.*, 109, 106–123, <https://doi.org/10.1016/j.cageo.2017.07.011>, 2017.
- Seppi, R., Zanoner, T., Carton, A., Bondesan, A., Francese, R., Carturan, L., Zumiani, M., Giorgi, M., and Ninfo, A.: Current transition from glacial to periglacial processes in the Dolomites (South-Eastern Alps). *Geomorphology*, 228, 71–86, <https://doi.org/10.1016/j.geomorph.2014.08.025>, 2015.
- Seppi, R., Carturan, L., Carton, A., Zanoner, T., Zumiani, M., Ca-zorzi, F., Bertone, A., Baroni, C., and Salvatore, M. C.: Decoupled kinematics of two neighbouring permafrost creeping landforms in the Eastern Italian Alps. *Earth Surf. Process. Landf.*, 44, 2703–2719, <https://doi.org/10.1002/esp.4698>, 2019.
- Staub, B., Lambiel, C., and Delaloye, R.: Rock glacier creep as a thermally-driven phenomenon: A decade of inter-annual observation from the Swiss Alps, XI International Conference on Permafrost – Book of Abstracts, 96–97, <https://doi.org/10.2312/GI/Z.LIS.2016.001>, 2016.
- Streletskiy, D., Noetzi, J., Smith, S. L., Vieira, G., Schoeneich, P., Hrbacek, F., and Irgang, A. M.: Strategy and Implementation Plan for the Global Terrestrial Network for Permafrost (GTN-P) 2021–2024, Zenodo [data set], <https://doi.org/10.5281/zenodo.6075468>, 2021.
- Sun, Z., Hu, Y., Racoviteanu, A., Liu, J., Harrison, S., Wang, X., Cai, J., Guo, X., He, Y., and Yuan, H.: TPRoGI: a comprehensive rock glacier inventory for the Tibetan Plateau using deep learning. *Earth Syst. Sci. Data Discuss.* [preprint], <https://doi.org/10.5194/essd-2024-28>, in review, 2024.
- Timur, A.: Velocity of compressional waves in porous media at permafrost temperatures. *Geophysics*, 33, 584–595, <https://doi.org/10.1190/1.1439954>, 1968.
- Vivero, S., Bodin, X., Farías-Barahona, D., MacDonell, S., Schaffer, N., Robson, B. A., and Lambiel, C.: Combination of Aerial, Satellite, and UAV Photogrammetry for Quantifying Rock Glacier Kinematics in the Dry Andes of Chile (30° S) Since the 1950s. *Front. Remote Sens.*, 2, <https://doi.org/10.3389/frsen.2021.784015>, 2021.
- Vivero, S., Hendrickx, H., Frankl, A., Delaloye, R., and Lambiel, C.: Kinematics and geomorphological changes of a destabilising rock glacier captured from close-range sensing techniques (Tsamine rock glacier, Western Swiss Alps). *Front. Earth Sci.*, 10, 1017949, <https://doi.org/10.3389/feart.2022.1017949>, 2022.
- Wagner, F. M., Mollaret, C., Günther, T., Kemna, A., and Hauck, C.: Quantitative imaging of water, ice and air in permafrost systems through petrophysical joint inversion of seismic refraction and electrical resistivity data. *Geophys. J. Int.*, 219, 1866–1875, <https://doi.org/10.1093/gji/ggz402>, 2019.
- Wee, J. and Delaloye, R.: Post-glacial dynamics of an alpine Little Ice Age glaciectonized frozen landform (Ager, western Swiss Alps). *Permafrost Periglacial Process.*, 33, 370–385, <https://doi.org/10.1002/ppp.2158>, 2022.
- Whalley, W. B.: Gruben glacier and rock glacier. Wallis, Switzerland: glacier ice exposures and their interpretation. *Geogr. Ann. Ser. Phys. Geogr.*, 102, 141–161, <https://doi.org/10.1080/04353676.2020.1765578>, 2020.
- Wirz, V., Beutel, J., Gruber, S., Gubler, S., and Purves, R. S.: Estimating velocity from noisy GPS data for investigating the temporal variability of slope movements. *Nat. Hazards Earth Syst. Sci.*, 14, 2503–2520, <https://doi.org/10.5194/nhess-14-2503-2014>, 2014.
- Wirz, V., Geertsema, M., Gruber, S., and Purves, R. S.: Temporal variability of diverse mountain permafrost slope movements derived from multi-year daily GPS data. Matteredal, Switzerland. *Landslides*, 13, 67–83, <https://doi.org/10.1007/s10346-014-0544-3>, 2016.

Publication III: Wee et al. (in review)

Capturing the multi-decadal evolution of glacier-permafrost interactions in a high-mountain alpine environment (Ritord, western Swiss Alps)

Authors	Julie Wee , Hanne Hendrickx and Sebastián Vivero
Journal	Geomorphology
Year	in review
DOI	doi.org/
Citation	TBD

Short summary

The processes driving surface dynamics in the Ritord Glacier forefield were investigated across multi-decadal to sub-seasonal timescales. To this end, we applied a multi-method approach to capture the evolution of glacier–permafrost interactions in this high-mountain alpine environment. This framework allowed us to assess the system's sensitivity and response to varying climatic conditions over time.

Main findings

- A systematic decrease in apparent resistivity is observed between 1997 and 2020 throughout the glacier forefield, inferring the thermal degradation of ground ice. However, the magnitude of change differs from a landform to another, according to their respective ground ice properties.
- The influence of climatic variation on the dynamics of the landforms within the glacier forefield was highlighted.
- The magnitude of surface changes is significantly influenced by the debris mantle thickness overlaying ground ice (permafrost or glacier ice).
- The different methods provide multiple lines of evidence for different response of the study areas to climate change.

Contribution of the PhD candidate

Designed the research, collected the GST data since 2016. Planned, coordinated, and participated in the geophysical campaigns from 2020 onwards. Initiated the seasonal and continuous TGS monitoring. Collected, processed and analysed the GST, GNSS, and the geophysical data. Prepared the manuscript and the figures. S. Vivero conducted the UAV campaigns and processed the UAV-derived data. H. Hendrickx processed the historical aerial images. All co-authors were involved in the discussion and in the improvement of the manuscript.

Data availability

Datasets are available upon request.

1 Capturing the multi-decadal evolution of glacier-permafrost interactions in a
2 high-alpine environment (Ritord, western Swiss Alps)

3 Julie Wee¹, Hanne Hendrickx² and Sebastián Vivero^{1,3}

4 ¹ Department of Geosciences, University of Fribourg, Chemin du Musée 4, CH-1700 Fribourg (julie.wee@unifr.ch)

5 ² Institute of Photogrammetry and Remote Sensing, Technische Universität Dresden, D-01062 Dresden

6 ³ Laboratory of Catchment Hydrology and Geomorphology, École Polytechnique Fédérale de Lausanne, CH-1951 Sion

7

8 **Abstract**

9

10 This study investigates the multi-decadal evolution of a glacier forefield, post-Little Ice Age (LIA), under
11 permafrost conditions. A multi-method approach based on historical and recent datasets is used to
12 analyse its landform components. The goal is to better understand the complex dynamics of landforms
13 and their interactions in environments shaped by glacial and periglacial processes. This study seeks to
14 foster the use and application of a multi-method approach to capture the multi-decadal evolution of
15 glacier-permafrost interactions in a high-mountain alpine environment. Spatial and temporal surface
16 changes are evaluated on the basis of archive aerial photographs and recent Uncrewed Aerial Vehicle
17 (UAV) surveys, as well as detailed in-situ differential Global Navigation Satellite Systems (dGNSS)
18 measurements. The long-term kinematic evolution of the landforms within the forefield is investigated
19 with an emphasis on the processes contributing to surface lowering. The evolution of the extent and
20 properties of ground ice and debris-covered surface ice is assessed by geophysical surveys and ground
21 surface temperature measurements.

22 Our observations indicate a general down-wasting trend among the investigated landforms, including
23 two perennially frozen back-creeping push moraines, a glacier forefield-connected rock glacier, and a
24 debris-covered glacier tongue. The strongest morphological and surface elevation changes, which are
25 partly due to ice melt-induced subsidence, have been observed in areas where ice of glacier origin is

1

26 present. Furthermore, these changes have been enhanced over the last two decades. A notable decline
27 in resistivity has been documented between earlier (1997) and more recent (2020) geophysical surveys
28 conducted in the push-moraines (-54.02%), the rock glacier rooting zone (-73.71%), and the margins of
29 the debris-covered glacier tongue (-57.69%). This decrease is likely to be the result of an increased
30 water-to-ice ratio due to permafrost degradation, as well as melting and thinning of massive ice from
31 glacial origin. In the debris-covered glacier tongue, resistivity changes are the smallest, which can be
32 attributed to unchanged properties of the cold ice, with the only significant change being its reduced
33 thickness.

34

35 **Keywords:** Permafrost, glacier forefields, Little Ice Age, glacier-permafrost interactions

36 1 Introduction

37

38 High alpine environments are facing substantial modifications in the current context of a changing
39 climate. The increase of temperature initiated at the end of the Little Ice Age (LIA, ca. 1350-1850 in the
40 Alps; (Ivy-Ochs et al., 2009)) has led to a degrading cryosphere partly illustrated by the shrinkage of
41 glaciers (Hock et al., 2019; Hugonnet et al., 2021), gradually exposing their forefields which may be
42 subject to rapid geomorphic activity and evolution (Bosson et al., 2015; Carrivick et al., 2013; Kneisel
43 and Kääh, 2007). In their process of deglaciation, such transitioning environments unravel the
44 geomorphological impact of Holocene and LIA glacier advances on the pre-existing landscape and their
45 consecutive post-glacial response (Betz-Nutz et al., 2023). The geomorphic processes occurring in high-
46 mountain LIA glacier forefield are often conditioned by the former glaciation but can also be influenced
47 by the simultaneous presence of permafrost. Largely governed by glacier-permafrost interactions, the
48 derived landforms present in such geomorphological systems have a distinct morphodynamical
49 signature, which is partly driven by the long-term thermal aspects of ice formation (surface ice of glacial
50 origin or ground ice in permafrost conditions) and preservation. The resilience of ground ice is highly
51 dependent on its properties, the thickness and coarseness of the debris cover, and the ground surface
52 thermal regime (Amschwand et al., 2023; Wee et al., 2024). LIA glacier forefields in which glacier-
53 permafrost interaction occurred or still occur can be considered as cradles to vast, complex, and
54 interconnected spectrum of glacial, periglacial, hydrological, gravitational, and mass-wasting processes,
55 often evidenced by the presence of geomorphologically rich and diverse landform origins,
56 configurations, and assemblages (Haeberli, 2005).

57 In some alpine environments, at altitudes where the topo-climatic conditions allowed for glacier ice to
58 be cold and sediments to be in a perennially frozen state, glaciers and perennially frozen-debris
59 landforms have co-existed and episodically interacted throughout the Holocene, with the LIA being the
60 apogee of the last interaction phase (Etzelmüller and Hagen, 2005; Haeberli, 1983). The advance of LIA
61 polythermal glaciers – often cold-based at their margins (Gilbert et al., 2012) – onto perennially frozen

62 sediments led to their partial displacement by the exerted glacial stress, known as glaciotectionization
63 (Haerberli, 1979; Wee et al., 2024). Often, as a consequence of the transmission of glacier-induced
64 geometrical deformations, isolated embedding and burial of cold glacier ice occurred into the adjacent
65 (glacier facing) flank of the pre-existing frozen debris, contributing to the preservation of glacier ice
66 masses and frozen debris (permafrost-related) in the margins of these forefields. In contrast, their central
67 areas are often occupied by unfrozen glaciogenic sediments such as fluted moraines, which indicate the
68 temperate state of the glaciers in their central zones (Kunz and Kneisel, 2020; Wee and Delaloye, 2022).
69 In some cases, debris-covered glaciers, or debris-covered dead-ice masses are present within the area
70 considered as the LIA glacier forefield, which is here delineated by the LIA glaciers maximal extent.

71 The characterisation of landscapes where glacier-permafrost interactions occurred or still occur and their
72 associated landforms and landform assemblages have been investigated in earlier studies . These
73 investigations primarily addressed the distribution of ground ice and the thermal regimes within these
74 systems. Further efforts towards the understanding of the driving processes contributing to the
75 geomorphological evolution LIA glacier forefields have been undertaken in the recent years through the
76 application of geophysical prospection, geodetic investigations and remote sensing techniques (Bosson
77 et al., 2015; Monnier and Kinnard, 2017; Vivero et al., 2021; Wee and Delaloye, 2022; Gärtner-Roer et
78 al., 2022; Kunz et al., 2022; Cusicanqui et al., 2023; Wee et al., 2024). These recent advances have
79 provided new insights into glacier-permafrost interactions and their associated processes, yet they
80 highlight the ongoing need for further research into this field. In this context, the integration of high-
81 resolution data across varying spatial and temporal scales remains important for enhancing our
82 understanding of the driving processes contributing to the distinctive morphodynamical signature of the
83 different landforms (i.e. push-moraines, glacier forefield-connected rock glaciers, and debris-covered
84 glaciers or dead ice) present within these systems.

85 To better understand the complexity of the post-glacial dynamics of landform assemblages in
86 environments conditioned by glacial and periglacial processes, this contribution investigates the multi-
87 decadal evolution of a LIA glacier forefield in permafrost conditions and its components through a
88 multi-method approach. Spatial and temporal surface changes are evaluated on the basis of historical

89 aerial and recent Uncrewed Aerial Vehicle (UAV) surveys, as well as in-situ geodetic measurements.
90 The long-term kinematic evolution of the landforms within the forefield is investigated with an emphasis
91 on the processes contributing to surface lowering. The evolution of the extent and properties of ground
92 ice and debris-covered surface ice is assessed by geophysical surveys and ground surface temperature
93 measurements. This study seeks to foster the use and application of a multi-method and interdisciplinary
94 approach to capture the multi-decadal evolution of glacier-permafrost interactions in a high-alpine
95 environment.

96

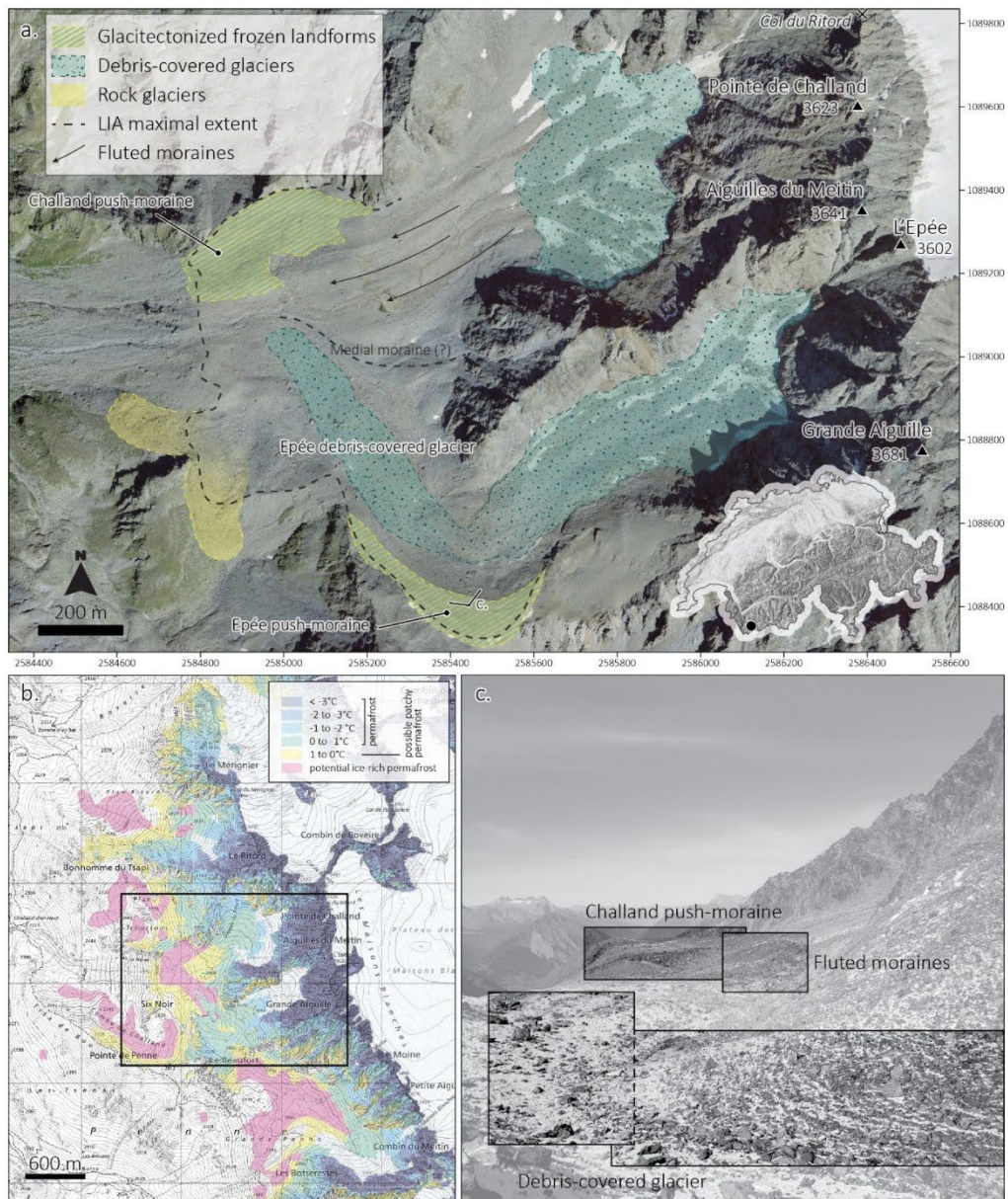
97 2 Study site

98

99 The Ritord site ($45^{\circ}57'10.671''\text{N}$ $7^{\circ}14'46.078''\text{E}$, Figure 1) is located in the Entremont valley in the
100 western Swiss Alps. It is enclosed by the Ritord (3557 m a.s.l.), the Pointe de Challand (3623 m a.s.l.)
101 and the Grande Aiguille (3681 m a.s.l.) summits on its eastern part and its western boundary extends
102 down to the LIA morainic bastion of the Challand and Epée glaciers (2800 m a.s.l.). The study site is
103 characterized by the remnants of the Challand glacieret and the vanishing Epée debris-covered glacier
104 and its adjacent stagnant and partly dynamically disconnected debris-covered tongue (gradually
105 isolating itself from the dynamic glacier system and becoming dead-ice; (Nicholson et al., 2021;
106 Quincey et al., 2009; Thompson et al., 2016)), two perennially frozen back-creeping push-moraines, and
107 two glacier forefield-connected rock glaciers. During its LIA maximal extent, the polythermal debris-
108 covered Epée glacier mainly occupied the southern zone of the study site, while the polythermal debris-
109 free Challand glacier occupied the northern zone of the study area. Here, a medial moraine folded to the
110 north indicates where the two glaciers converged (Figure 1). During their advance, the cold-based
111 margins of both glaciers partly thrust and overrode pre-existing perennially frozen debris landforms
112 occupying the margins of the area. This former glacier-permafrost interaction likely altered the spatial
113 distribution of ground ice, the thermal regime, and the surface morphology of the Challand and Epée

114 glacier forefield, leading to the formation of push-moraines (Delaloye, 2004). Both push-moraines
115 express a morphological signature of glaciotectonics (i.e. compressive ridges and furrows perpendicular
116 to the stress exerted by the LIA advancing glacier) and reveal embedded lenses of massive ice, while
117 the rooting zone of both rock glaciers is characterized by a topographical depression. A clear mechanical
118 response following the shrinkage of both glaciers and consequent release of glacier-induced stress,
119 expressed as back-creeping dominates as the kinematic behaviour of the two push-moraines. The
120 forefield of the Challand glacier is partly occupied by fluted moraines, attesting the glacier lied on water-
121 saturated sediments and was temperate at its base. In contrast to this ice-free zone, the forefield of the
122 Epée debris-covered glacier is occupied by its partly disconnected debris-covered glacier tongue.

123



124

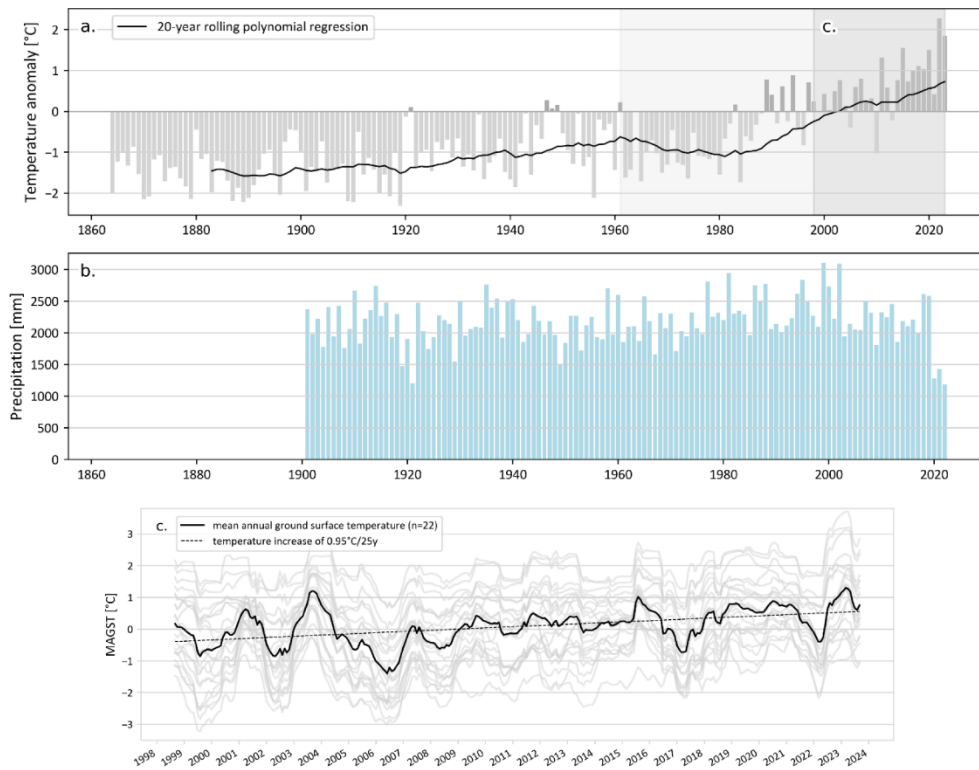
125 Figure 1: General geomorphological description of the Ritord site (a, c) and the general distribution of permafrost and ground
 126 ice (Kenner et al., 2019) in the study area (b). The Ritord glacitected frozen landforms (or push-moraines) are highlighted
 127 by alternating yellow and blue dashed lines. The rock glaciers are highlighted in yellow. The Epée and Challand (-now) debris-
 128 covered glaciers are highlighted in blue. Black dashed lines indicate part of the LIA maximal extent of the Challand and Epée
 129 glaciers. Fluted moraines indicate the flow direction of the Challand debris-free glacier. Location and direction of picture (c)
 130 is marked by a symbol on map (a). Background map (a): SWISSIMAGE 2017 (Swisstopo).

131

132 The climate of the study area is characterised by inner-alpine continental climatic conditions,
133 predominantly influenced by high-relief topography. The mean precipitation for the reference period of
134 1981-2010 measured at the Col du Grand St-Bernard Station (GSB, 2472 m a.s.l.) located at 10 km from
135 the study area is 2368 mm/y (Figure 2b). However, being shielded by the high-mountain topography of
136 the Combins massif, the mean annual precipitation at the study site likely ranges between 1500-1800
137 mm/y (MeteoSwiss, 2024). The mean annual air temperature (MAAT) for the reference period of 1981-
138 2010 measured at the same meteorological station (GSB) is -0.6°C , which infers that at the elevation of
139 the site (around 2800-2900 m a.s.l.), the MAAT, when considering an environmental lapse rate of -
140 0.65°C per 100 m, can be estimated between -2 to -3°C . Temperatures measured since 1864 reveal a
141 clear warming trend of $1.44^{\circ}\text{C}/100$ years, particularly marked by the temperature rise of the last forty
142 years (Figure 2; MeteoSwiss, 2024).

143 The average mean annual ground surface temperature (GST) for the 20 measurements locations is
144 0.08°C , ranging from -1.61°C to 1.98°C (Figure 2c). This spread can be explained mainly by the micro-
145 topo-climatic ground surface conditions at each data logger location, but also by the ground thermal
146 regime, partly governed by the spatial distribution of ground ice along the forefield deposits. Over the
147 measurement period (1997–2023), the mean annual GST experienced an increase of $+0.95^{\circ}\text{C}$ on
148 average.

149



150

151 Figure 2: Deviation of the MAAT from the reference period 1981–2010 based on homogenized data series of the Col du Grand
 152 St-Bernard Swiss National Basic Climatological Network (Swiss NBCN) meteorological station (GSB, 2472 m a.s.l.). (a). The
 153 period covered in this study is highlighted in light grey and the period covered by GST measurements is highlighted in dark
 154 grey (c). Homogenized precipitation measurements since 1901 to 2022 from the GSB station are presented in panel (b). Data
 155 from MeteoSwiss (2024).

156

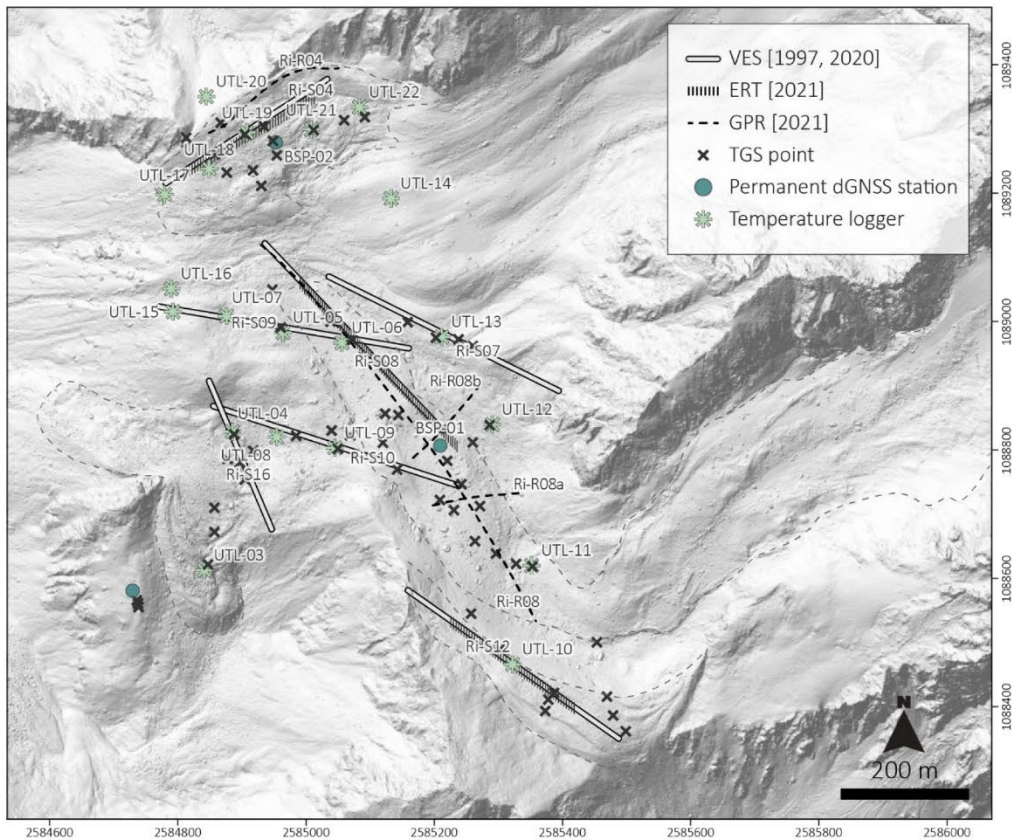
157 3 Methods

158

159 This study applies a multi-method approach, using archival and contemporary high-resolution datasets,
 160 to better analyse and interpret the driving processes behind the long-term geomorphological evolution
 161 of such complex geomorphic systems (Figure 3). The characterisation of the spatial distribution of

162 ground ice is assessed based on the application of electrical resistivity tomography (ERT), which is
163 sensitive to the contrasting electrical properties of conductive unfrozen material and resistive ice, as well
164 as the application of ground penetrating radar (GPR). The evolution of ground ice is estimated through
165 the semi-quantitative comparative analysis of historical and recently repeated vertical electrical
166 soundings (VES). Long-term surface changes are evaluated through archival aerial photogrammetry
167 (1964-2005), UAV-based imagery (2022-2023) and Airborne Laser Scanner (ALS) surveys (2016-
168 2021) for high-resolution topographic analysis. A high-temporal-resolution geodetic approach, based on
169 differential global navigation satellite system (dGNSS) observations, is applied in this study to capture
170 precise surface displacements. Two permanent dGNSS stations were installed, providing daily position
171 measurements, allowing for continuous monitoring of displacement patterns. These high-frequency
172 observations are complemented by a network of well-distributed terrestrial ground survey (TGS) points,
173 which are measured twice a year. The combination of these two datasets enhances the temporal and
174 spatial resolution of our analysis, enabling us to examine both short-term variability and seasonal trends
175 in surface displacement and ground temperature influence.

176



177

178 Figure 3: Overview of the distribution of the different measurements on the Ritord site. The continuous white lines represent
 179 the VES carried out in 1997 and repeated in 2020. The hatched black lines are the ERT profiles co-located to the VES profiles.
 180 The black dashed lines represent the GPR profiles. The black crosses represent the network of TGS points (including the control
 181 points). The blue circles are the permanent dGNSS stations (including the reference station). The light blue asterisks represent
 182 the universal temperature loggers (UTL). Two temperature loggers located on a nearby ridge are not shown on the map. The
 183 grey dashed polygons delineate the investigated landforms. Background: ALS-derived hillshade swissSURFACE3D
 184 (Swisstopo, 2021).

185

186 3.1 Geoelectrical surveys

187 Due to its efficiency and suitability to distinguish contrasting electrical properties between conductive
 188 unfrozen materials, ice-rich sediments, and massive surface ice electrical resistivity measurements are
 189 commonly used for the characterisation of ground ice (Haerberli and Vonder Mühl, 1996; Hauck and

190 Kneisel, 2008; Herring et al., 2023; Kneisel, 2004). In this study, historical and recently repeated VES
191 were used to assess the one-dimensional electrical resistivity changes of the different landforms in the
192 glacier forefield. To complement the single-point, one-dimensional resistivity profiles obtained from
193 VES, ERT measurements were conducted along three existing VES profiles – Ri-S04, Ri-S08, and Ri-
194 S12 – in mid-August 2021. This provided two-dimensional imaging of subsurface electrical properties,
195 offering a more spatially resolved and comprehensive view of internal structures.

196

197 3.1.1 Vertical electrical soundings (VES)

198 Fifteen VES carried out in August-September 1997 allowed to characterise the distribution of ground
199 ice in the debris-covered glacier and Ritord glacier forefield (Delaloye, 2004). In August 2020, seven of
200 the fifteen earlier VES were repeated using the same methodology, measuring device (McOhm 2115
201 resistivity-meter), and electrode configuration as in 1997. The location of the profile were identified
202 based on detailed field descriptions and maps from 1997, which documented the original survey. The
203 symmetrical Schlumberger array was applied to all VES in both campaigns. The measured apparent
204 resistivity values were inverted to determine the thickness and specific resistivity of the layers of a one-
205 dimensional model to produce a model response that best fits the measured values. This approach
206 allowed for a semi-quantitatively comparison between the VES with the ERT data. This was done using
207 the programme RES1D ver. 1.0, where the least-square optimisation method is applied (Loke, 2001).
208 A simple initial model of the subsurface is given, and the optimisation subroutine modifies the thickness
209 and resistivity of the layers in order to reduce the discrepancy between the calculated and measured
210 apparent resistivity values. The measured apparent resistivity values were used for the comparative
211 analysis between the historical and repeated datasets as performed by Wee and Delaloye (2022).

212

213 3.1.2 Electrical resistivity tomography (ERT)

214 In mid-August 2021, the ERT profiles were conducted using a SYSCAL Pro (Iris Instruments), to which
215 48 stainless-steel electrodes can be connected. A 5 m electrode spacing was used for all profiles, which
216 were measured with a Wenner-Schlumberger array configuration. For profiles Ri-S04 and Ri-S12, the
217 ERT measurements were centred at 117.5 meters, aligning with the midpoint of the respective VES
218 profiles. The Ri-S08 profile, a longer ERT line extending 355 meters, was created by combining two
219 235-meter segments with a half-overlap in a roll-along setup. This profile was also co-located with the
220 corresponding VES profile, although with an offset of approximately 60 meters between the centres of
221 the VES and ERT profile. The data from the roll-along Ri-S08 profile was merged using the data
222 management software Prosys II (Iris Instruments) allowing for a single inversion of all quadrupoles
223 along the same line.

224 Data quality assessment was conducted in two stages using RES2DINV (Aarhus GeoSoftware).
225 Initially, outlier removal was performed manually with the “exterminate bad data points” tool.
226 Subsequently, data quality was further evaluated based on RMS error, allowing identification and
227 deletion of points contributing to elevated errors. Overall, the data quality was robust, with only 7% of
228 data points excluded from the inversion. Inversions were then completed using the pyGIMLi-based code
229 (Rücker et al., 2017).

230

231 3.2 Ground penetrating radar (GPR)

232 The GPR method is based on the propagation of high-frequency electromagnetic waves into the ground
233 and their reflection at interfaces between materials with different dielectric permittivity and electrical
234 conductivity (Reynolds, 2011). The GPR wave propagation velocity is determined by the permittivity
235 of the subsurface material, whose values range between 1 (air) and 80 (water). Because of contrasting
236 properties between air, ice, and rock, this method enables the delineation of subsurface layers with
237 velocity contrasts (Forte et al., 2020; Monnier et al., 2008). A longitudinal profile (Ri-R08) and two

238 transversal profiles (Ri-R08a and Ri-R08b) were carried out in mid-April 2021 on the debris-covered
239 tongue of the Epée glacier. A profile (Ri-R04) co-located to the VES and ERT profile Ri-S04 was
240 performed on the Challand push-moraine. A 50 MHz MALÅ Rough Terrain Antenna (MALÅ
241 Geoscience) was used as is it suitable for investigations of deeper structures. The positions of the
242 measurements were simultaneously recorded with a GPS receiver (accuracy of ~5 m). The antenna was
243 dragged over the cold and dry snow-covered surface. Reflection profiles were processed using ReflexW
244 software (Sandmeier geophysical research). Preliminary processing included a static correction of the
245 first arrival time, and a trace enhancement by filtering signal saturation (dewow). The topography data
246 was incorporated and resampled, which allowed the resulting data to be equidistant. A topographic
247 migration was performed. A velocity model was established by attributing propagation velocity values
248 to the debris-cover layer (0.12 m/ns; Degenhardt et al., 2003; Monnier et al., 2008), the ice-core (0.168
249 m/ns; Glen and Paren, 1975), and the bedrock (gneiss, 0.11 m/ns; Reynolds, 2011), and was used to
250 generate a time-to-depth conversion.

251

252 3.3 Archival aerial photogrammetry

253 3.3.1 Data processing

254 The historical aerial images used in this study are part of the database of the Swiss Federal Office of
255 Topography (Swisstopo) which acquired, stored, and scanned the film negatives (Table 1). The aerial
256 images acquired in 1961 and 1964 have a size of 18 cm x 18 cm and were scanned with a resolution of
257 21 μm (1210 dpi). Images of the remaining later periods have a size of 23 cm x 23 cm and were scanned
258 with a resolution of 14 μm (1814 dpi). All images were taken in late summer/early autumn, when snow
259 cover was most likely at a minimum.

260

261 Table 1: Characteristics of the aerial images available from Swisstopo. The epochs highlighted in grey were not used in this
262 study as they yielded bad quality results.

Acquisition date	Lens type	Photogrammetric emulsion	Calibrated focal length (mm)	Number of images used	Quality assessment on stable area compared to SwissSURFSCE3D ALS 2021	
					ME (m)	SDE (m)
20.09.1961	AG 29	b/w	115.26	2	-0.72	1.21
25.08.1964	AG 29	b/w	115.29	2	-0.92	0.89
13.09.1977	15 UAG	b/w	153.02	2	-0.16	0.93
23.08.1982	15/4 UAG	b/w	152.02	2	-1.09	0.46
13.09.1983	15/4 UAG	b/w	153.37	2	-1.15	0.34
07.09.1988	15/4 UAG	b/w	153.37	2	-0.38	0.52
07.10.1995	21/4 NAGA-F	b/w	213.72	2		
02.09.1999	15/4 UAG- S	RGB	152.528	2	-0.49	0.81
09.08.2005	15/4 UAG- S	RGB	152.51	2	0.16	0.79
Average accuracy and precision entire historical image dataset					-0.59	0.74

263 b/w = black and white, RGB = colour (red, green, blue), ME = Mean Error, SDE = Standard Deviation of Error

264

265 For georeferencing the aerial images, twenty ground control points (GCPs) were selected from the
266 swissSURFACE3D ALS survey of 2021, with a planimetric accuracy of 20 cm and an altimetric
267 accuracy of 10 cm (Swisstopo, 2024). The GCPs are distinguishable features that were assumed to be
268 stable over the entire period, such as large boulders on topographic flats and infrastructure.

269 To reconstruct historical digital elevation models (DEMs) and orthomosaics, we applied Structure-from-
270 Motion (SfM) and Multi-View-Stereo (MVS) using commercial software Agisoft Metashape (v 2.0.1).
271 For orienting the multiple epochs of historical aerial photos, we used multi-temporal tie points which
272 can be tracked over several epochs, originally introduced as Time-SIFT method (Feurer and Vinatier,
273 2018), further generalized as the co-alignment method (Blanch et al., 2021; Cook and Dietze, 2019;
274 Hendrickx et al., 2020, 2022) and recently also tested and applied for historical aerial data (Genzano et
275 al., 2024). This way, GCPs are only used in the common SfM project to compute image orientation and

276 camera calibration for all the epochs at once, thus omitting the need for using camera calibration reports.
277 Moreover, the relative accuracy is also improved by the automatic extraction of tie points in stable areas.
278 A sub-pixel reprojection error, indicative of the overall performance of the bundle adjustment, was
279 obtained for the area of interest. The 1995 dataset was omitted due to its low percentage of common tie
280 point (1%). Common tie points of all other epochs averaged 10%, which is sufficient to ensure a
281 common geometry (Cook and Dietze, 2019). After the common tie point reconstruction, dense point
282 clouds were reconstructed for every epoch separately, using high resolution settings with moderate depth
283 filtering (Cusicanqui et al., 2021). These are subsequently used for the creation of DEMs and
284 orthomosaics.

285

286 3.3.2 Quality assessment

287 Quality assessment is done using CloudCompare (v 2.12.4), by performing a change detection on a
288 stable region using the M2C3 plugin (Lague et al., 2013). All epochs are compared to the
289 swissSURFACE3D ALS model and Mean Error (ME) and Standard Deviation of Error (SDE) are
290 evaluated (Table 1). This led to the omission of 1961 and 1997 from further analysis due to their high
291 SDE Subsequently, the Level of Detection (LoD) on 90% significance level can be calculated for every
292 inter epoch comparison via the following formula (Eq. 1):

293

$$\text{LoD}_{90\%} = 1.64 \times \sqrt{\text{SDE}_1^2 + \text{SDE}_2^2} \quad (\text{Eq. 1})$$

294

295 3.4 UAV-SfM photogrammetry

296 Two sets of UAV surveys were conducted at the Ritord site on the 13 of July 2022 and on the 3rd of
297 August 2023 between 12:00 and 15:00 local time. The surveys were carried out using a DJI Phantom 4
298 RTK (P4RTK) quadcopter UAV equipped with a high-quality multi-frequency and multi-system GNSS

299 receiver, achieving centimetre-level accuracy in the geotagging of each image (Taddia et al., 2020). The
300 camera has a resolution of 20 MP and an image size of 5472 x 3648. Flight planning and deployment
301 were performed using the DJI GS RTK application in terrain awareness mode at a nominal height above
302 ground of 85 m. Images were acquired using a nadir camera tilt and a single grid pattern with front and
303 side overlap of 80 and 70%, respectively. Due to the high relief topography of the study sites, the images
304 acquired during the UAV surveys were not strictly nadir to the surface. This camera-surface
305 configuration led to a variable elevation range and nadir/oblique geometry, which contributed to
306 reinforcing the photogrammetric network (Peppia et al., 2019). Camera settings, including white balance,
307 ISO, focus, and aperture, were automatically configured yet maintained consistently for each survey.

308 The initial coordinate and elevation values obtained from the real-time kinematics (RTK) processing of
309 the geotagged images were evaluated, revealing that several images only achieved a float RTK solution
310 with accuracies in the order of 0.5 to 1 m. To enhance this, a post-processing kinematics (PPK) method,
311 using the RTKlib version 2.4.2 software, was employed with the raw GNSS data from the P4RTK, in
312 conjunction with a virtual reference station (VRS) generated from the Automatic GNSS Network for
313 Switzerland (AGNES). The aforementioned procedure yielded enhanced coordinate and elevation
314 accuracy, as evidenced by the generation of fixed PPK solutions with a precision of 1-3 cm.
315 Furthermore, the two surveys were associated with AGNES, resulting in the production of concordant
316 coordinates in terms of the Revised Swiss Reference System (CH1903+LV95).

317 The centimetre-accurate geotagged UAV images were processed using Pix4DMapper version 4.8.4
318 software for automated keypoint feature detection, image matching, and fusion using SfM algorithms
319 (Smith et al., 2016). Initial keypoint processing was performed at full image scale, using an aerial grid
320 model with geometrically verified matching. Optimization of camera calibration parameters from the
321 P4RTK was performed automatically. We then performed point cloud densification at half image scale
322 with three as the minimum number of matches for each point. From these results we generated 3D
323 meshes (visualization of the 3D meshes is available at <https://skfb.ly/p7w6R>) and high-resolution DSMs
324 and orthomosaics with a resolution of 4 cm.

325

326 3.5 Horizontal surface displacements derived from UAV and historical aerial images

327 Horizontal surface displacements were derived from pairs of the above-mentioned multi-temporal
328 orthoimages of 0.5 m pixel size by applying a normalised cross-correlation (NCC) procedure using the
329 image correlation CIAS software (Debella-Gilo and Käab, 2011; Käab and Vollmer, 2000). The
330 accuracy and quality of the image correlation was evaluated by applying the Helmert transformation
331 based on points placed on stable terrain in the vicinity of the studied landforms (Vivero et al., 2022).
332 Despite the difficulty of finding stable terrain outside the studied landforms in the surveyed area,
333 between 20 and 35 check points were used.

334

335 3.6 Terrestrial geodetic surveys (TGS)

336 Surface velocities are measured on a regular basis since 2020. A network of 60 marked boulders and
337 three control points marked on stable bedrock for quality assessment is measured twice a year, in early
338 summer and early autumn, by RTK differential GNSS surveys, following the measurement set-up
339 described by Lambiel and Delaloye (2004). Seasonal horizontal, vertical, and three-dimensional (3D)
340 surface displacement vectors are calculated between two geodetic surveys, from which displacement
341 rates can be derived.

342 In addition to the seasonal in-situ terrestrial geodetic surveys, permanent dGNSS stations installed on
343 the Challand push-moraine and the debris-covered tongue of the Epée glacier yield continuous
344 displacement data for single point locations, allowing to follow the seasonal variations affecting the
345 velocity and surface dynamics of the studied landforms (Beutel et al., 2021; Wirz et al., 2016). Hourly
346 positions are determined in real-time kinematics with a cm-range accuracy based on a continuously
347 operating reference station installed on stable terrain, enabling the differential GNSS measurements of
348 high accuracy. Hourly positions were averaged to obtain daily positions. A Gaussian kernel smoothing
349 approach was applied to the daily positions to reduce noise and improve the data signal quality.

350

351 3.7 Ground surface temperature (GST) measurements

352 The thermal state of the ground surface was quantitatively assessed through the monitoring of GST at a
353 2-hour frequency since 1997 at 20 locations throughout the Ritord site (Figure 3; Delaloye, 2004).
354 Temperature loggers are buried a few decimetres under the ground surface to avoid direct influence of
355 solar radiation. Five temperature loggers were placed on the lateral push-moraines (Ri-18, Ri-19, Ri-20,
356 Ri-21, Ri-22 on the Challand push-moraine and Ri-10 on the Epée push-moraine), two on the debris-
357 covered tongue of the Epée glacier (Ri-06, Ri-11), one on the field of fluted moraines (Ri-14), three on
358 the eastern most margin of the forefield (Ri-15, Ri-16, Ri-17), on the rock glacier and its rooting zone
359 (Ri-03, Ri-04, Ri-08), and five in the margins of the debris-covered tongue of the Epée glacier (Ri-05,
360 Ri-07, Ri-09, Ri-12, Ri-13). From 1997 to 2017, GST data were measured using UTL-1 data loggers
361 (Geotest AG) with an accuracy of $\pm 0.2^{\circ}\text{C}$, and from 2017 onwards, UTL-3 data loggers (Geotest AG)
362 with an accuracy of $\pm 0.02^{\circ}\text{C}$ were used.

363

364 4 Results

365

366 4.1 Contemporary internal structure from ERT and GPR measurements (2021)

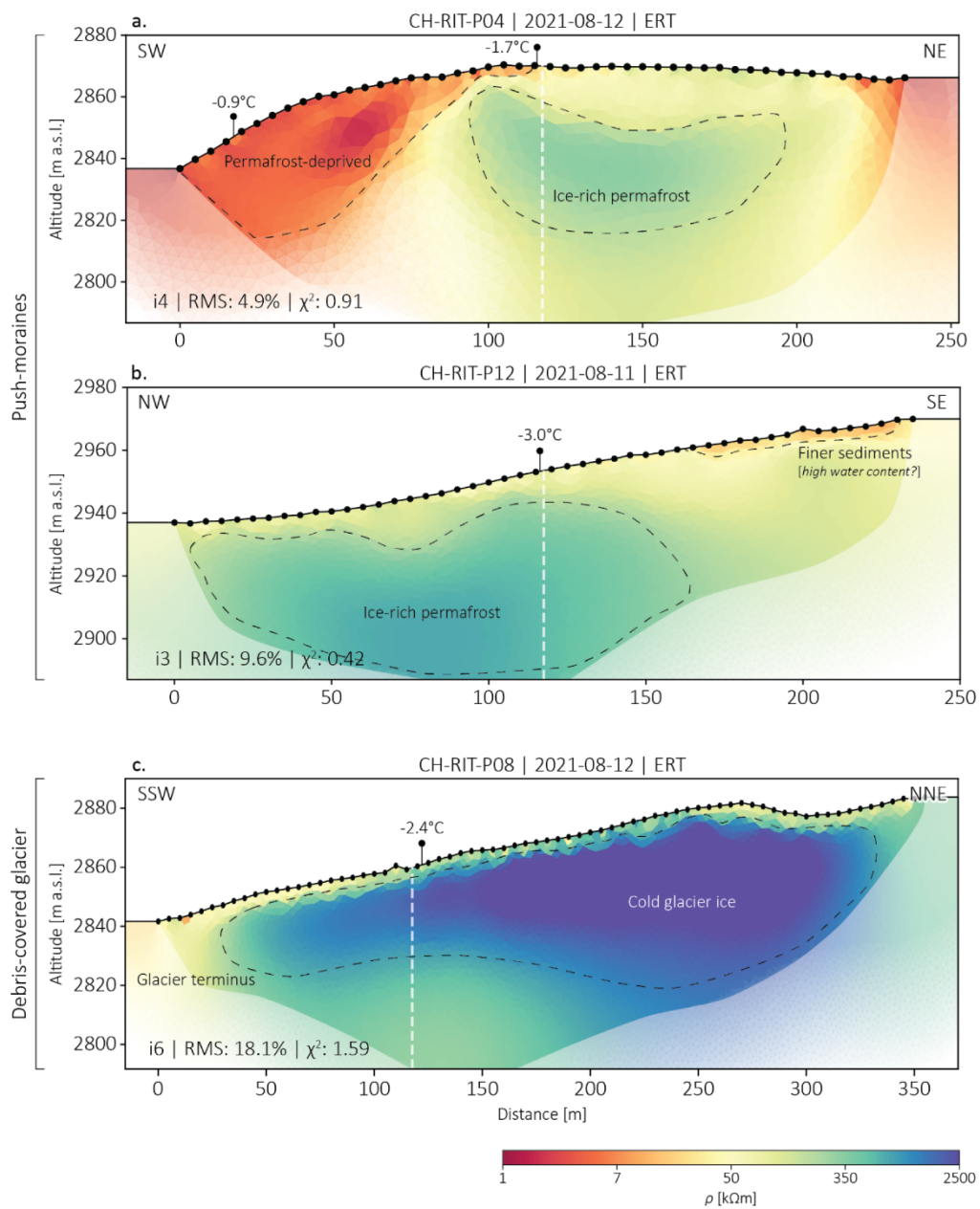
367 The internal structure of the different geomorphic units can be analysed using ERT measurements
368 (Figure 4). Two profiles (RIT-P04 and RIT-P12) were carried out on the lateral push-moraines, and one
369 profile (RIT-P08) was carried out on the debris-covered glacier tongue in the centre of the area of
370 interest. The resistivity values presented in the extremities of profile RIT-P04 (Challand push-moraine,
371 Figure 4a) range between 1 and 5 $\text{k}\Omega\text{m}$, which could possibly point to a relatively high water-to-ice
372 ratio, or a permafrost deprived zone. This is well in accordance with the low winter equilibrium
373 temperature (WEqT) of -0.9°C measured in 2021, which points to the absence of permafrost. In the
374 central part of the same profile, a 20 m thick patch with electrical resistivity values ranging between 200

375 and 350 kΩm is discernible under a more conductive (50 kΩm) 10-15 m layer. The WEqT of -1.7°C
376 measured in 2021 in this area points to ground thermal conditions unfavourable for permafrost
377 occurrence. On the southern part of the glacier forefield, profile RIT-P12 (Epée push-moraine, Figure
378 4b) shows resistivities ranging from 300 to 600 kΩm in its lowermost section (northwest) under a more
379 conductive layer of about 5 m. The WEqT of -3°C measured in 2021 indicates ground thermal conditions
380 favourable for permafrost. Resistivity values gradually decrease towards the upslope section of the
381 profile (southeast), and range between 100 and 300 kΩm. In this same upslope section of the profile,
382 the terrain's surface is characterized by finer grained sediments, which corresponds to a shallow and
383 more conductive layer of about of about 10 kΩm.

384 The ERT profile RIT-P08, which was measured on the Epée debris-covered glacier tongue (Figure 4c),
385 shows electrical resistivity values of around 2500 kΩm in its core, which can be indicative of cold glacier
386 ice. Moreover, the WEqT of -2.4°C points to cold ground thermal conditions. The ERT profile allows
387 the delineation of the debris-covered glacier tongue terminus, as the electrical resistivity values
388 gradually become smaller (down to 20-50 kΩm) towards the southwest downslope section of the profile.
389 A distinct, more conductive uppermost layer is evident and likely corresponds to the debris cover. Based
390 on direct field observations, the thickness of this layer is estimated to be approximately 50-80 cm. The
391 upslope section of the profile indicates electrical resistivity values of about 350 kΩm, which could
392 possibly correspond to a decrease in sensitivity due to geometrical constraints at the edges of the
393 tomogram.

394

395



396

397 Figure 4: ERT profiles carried out on the two push-moraines and the partly disconnected Epée debris-covered glacier (DCG)
 398 tongue. Profile RIT-P04 corresponds to the Challand push-moraine (a), profile RIT-P12 corresponds to the Epée push-moraine
 399 (b), and profile RIT-P08 corresponds to the Epée debris-covered glacier tongue (c). The black dots represent the electrodes.
 400 The white dashed line represents the approximate location of the vertical electrical sounding (c.f. Figure 3). The black pins
 401 represent the location of the GST loggers and the calculated WEqT of 2021.

21

402

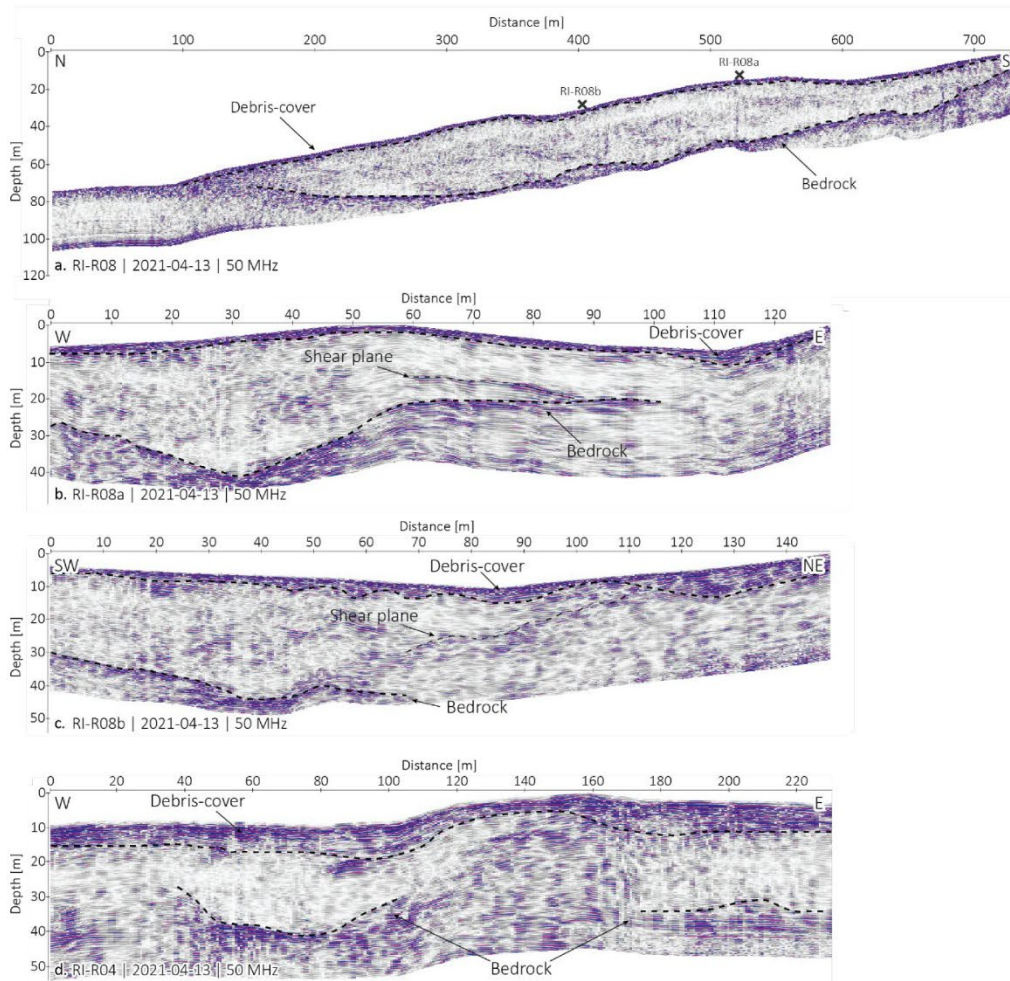
403 The results from the co-located GPR profile RI-R08 (Figure 5a) align closely with the ERT profile RIT-
404 P08 (Figure 4c). In the uppermost layer of the GPR profile RI-R08, a continuous surface-parallel
405 reflector is clearly distinguishable and can be interpreted as the interface between the debris cover of
406 the dynamically disconnected glacier tongue and the underlying ice. This reflection plane is also
407 observed in the cross-profiles Ri-R08a and Ri-R08b, inferring a relatively uniform debris cover
408 thickness across the surveyed area. A second prominent, linear, and continuous reflector was identified,
409 enabling the interpretation of the ice-bedrock interface in profiles RI-R08, RI-R08a, and RI-R08b. This
410 interface is located at a depth of approximately 40 m in the central sections and becomes progressively
411 shallower toward the extremities of both the longitudinal and cross-profiles.

412 The terminus of the debris-covered glacier at around 100 m of the longitudinal profile is characterized
413 by a scattering facies (Figure 5a), which can be associated with a mixture of debris and ice (Forte et al.,
414 2020), and corresponds to lower electrical resistivity values ranging between 100-350 kΩm, as shown
415 in Figure 4c. These lower resistivity values are consistent with the results obtained from the GPR
416 measurements, further supporting the interpretation of reduced ice content in the terminus of the debris-
417 covered glacier tongue. In some areas, the internal structure of the dynamically disconnected debris-
418 covered glacier tongue is characterized by almost transparent facies, which can be interpreted as pure,
419 and often cold, ice. It is also characterized by some internal reflections and scattering, which can be
420 attributed to internal debris or glaciological structures, such as shear planes (Forte et al., 2020;
421 Pettersson, 2005). Similar observations were made for the cross-profiles RI-R08a and RI-S08b (Figure
422 5b-c). However, the lateral boundaries of the dynamically disconnected debris-covered glacier are less
423 evident to delineate in the cross-profiles.

424 Profile RI-R04 (Figure 5d) was carried out parallel to the ERT profile RIT-P04 (Figure 4a) on the
425 Challand push-moraine. A clear surface-parallel reflector is observed at a depth of around 5 m and can
426 be interpreted as the coarse debris active layer. Below this uppermost layer, between 40 m and 100 m,
427 the core of the push-moraine is characterized by a transparent facies, which could be indicative of the

428 presence of an embedded ice lens. A similar signal is distinguishable toward the easternmost end of the
429 profile. The rest of the profile is characterized by scatters, which points to an ice-debris mixture.

430



431

432 Figure 5: GPR profiles carried out on the partly disconnected debris-covered glacier (DCG) tongue (a-c) and the Challand
433 push-moraine (d). RI-R08 corresponds to the longitudinal profile performed on the DCG (a). The cross at around 510 m
434 represents the intersection of the cross-profile RI-R08a (b), and the cross at around 400 m represents the intersection of the
435 cross-profile RI-R08b (c). RI-R04 corresponds to the profile carried out on the Challand push-moraine. Dashed lines mark the
436 main reflectors.

437

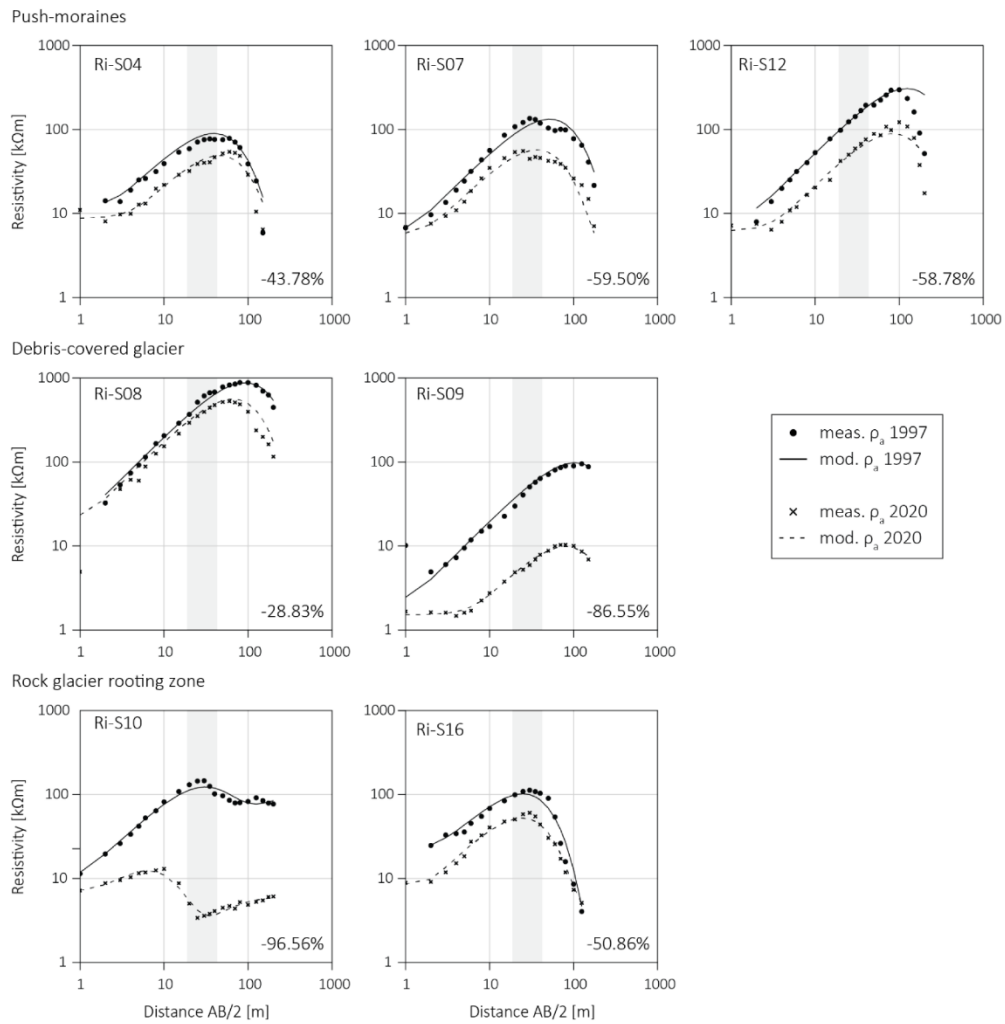
438 4.2 Change in electrical resistivity between 1997 and 2020

439 The seven VES repeated in 2020 yielded coherent apparent resistivity curves, which are similarly shaped
440 to that observed in the historical soundings of 1997 (Figure 6). A decrease in apparent electrical
441 resistivity values was systematically observed at all profiles. The profiles Ri-S04, Ri-S12 and Ri-S07
442 were measured on the two lateral push-moraines and on the medial push-moraine, respectively. The
443 camelback shaped curves of profiles Ri-S04 and Ri-S07, which is much more pronounced for the latter,
444 indicate the presence of an embedded very resistive layer, such as an ice lens, within a less resistive
445 body (Delaloye, 2004), while the steep resistivity curve of profile Ri-S12 indicates the embedding of a
446 thicker resistive layer, such as a massive glacier ice lens. From the resistivity curves of the three profiles,
447 it can be deduced that the resistive core of the push-moraines is underlain by a less resistive layer, which
448 could correspond to the active layer. The change in apparent electrical resistivity for all three profiles
449 seems rather uniform and within a similar range of change. The apparent resistivities of the resistive
450 core of the push-moraines have decrease from 43.73% to 59.50%, which can be explained by the gradual
451 melt and thinning of an embedded more resistive ice layer, but also by the warming and thawing of
452 permafrost.

453 Profiles Ri-S08 and Ri-S09 were carried out along the Epée dynamically disconnected debris-covered
454 glacier tongue and partly across its terminus, respectively. In 1997, very high apparent resistivity values
455 of 750 – 880 k Ω m were recorded at profile Ri-S08 (Delaloye, 2004). These values are likely indicative
456 of cold ice, which is consistent with direct observations of exposed ice in this zone. In contrast, profile
457 Ri-S09, partially crossing the glacier terminus, revealed significantly lower apparent resistivity values
458 of 70–100 k Ω m. This suggests a thinner ice layer, consistent with its proximity to the terminus and the
459 presence of finer sediments that enhance thermal conductivity. At the glacier margins, Ri-S09 showed
460 a striking 86.55% decrease in apparent resistivity, likely driven by accelerated melting of the thinner
461 ice. As the ice-covered surface diminishes, the terrain becomes more water-saturated, further decreasing
462 resistivity. For profile Ri-S08, while ongoing ice melt is evidenced by geodetic measurements, the
463 change in apparent resistivity between 1997 and 2020 is less pronounced. The observed 28.83% decrease

464 is likely due to a reduction in ice volume rather than a fundamental change in the thermal or structural
465 properties of the cold ice, which remains relatively stable despite thinning.

466 The centres of profiles Ri-S10 and Ri-S16 are situated in the rooting zone of the rock glacier, an area
467 likely overridden during the last advance of the Epée debris-covered glacier around 1850. Profile Ri-
468 S10 is located closer to the margins of the debris-covered glacier tongue, while Ri-S16 lies within a
469 topographic depression in the lower part of the rooting zone. In 1997, the vertical electrical profile of
470 Ri-S10 revealed a resistive layer, likely a buried glacier ice lens, at an estimated depth of 4-5 meters
471 (Delaloye, 2004). However, a significant 96.56% decrease in apparent resistivity at Ri-S10 suggests the
472 extensive melting of this resistive layer, with a corresponding increase in water content at depth.
473 However, it remains possible that remnants of ice persist within the layer. In contrast, the apparent
474 resistivity values measured at Ri-S16 are characteristic of a thick, cold layer of frozen sediment, where
475 the presence of embedded glacier ice cannot be entirely ruled out. These observations are consistent
476 with profiles from nearby push moraines, which also suggest the potential presence of embedded ice of
477 glacier origin.



478

479 Figure 6: Change in apparent electrical resistivity between 1997 and 2020 of vertical electrical soundings Ri-S04, Ri-S07, Ri-
 480 S12 (on the northern push-moraine, medial push-moraine and southern push-moraine, respectively), Ri-S08, Ri-S09 (along and
 481 across the debris-covered glacier tongue, respectively), Ri-S10, and Ri-S16 (in the rooting zone of the glacier forefield-
 482 connected rock glacier). The measured apparent resistivity highlighted in grey (between 20 and 40 m, corresponding to an
 483 investigation depth of roughly 10-15 m) were used to calculate the change in resistivity as in Wee and Delaloye (2022).

484

485 4.3 Pluri-decadal surface displacement and elevation change

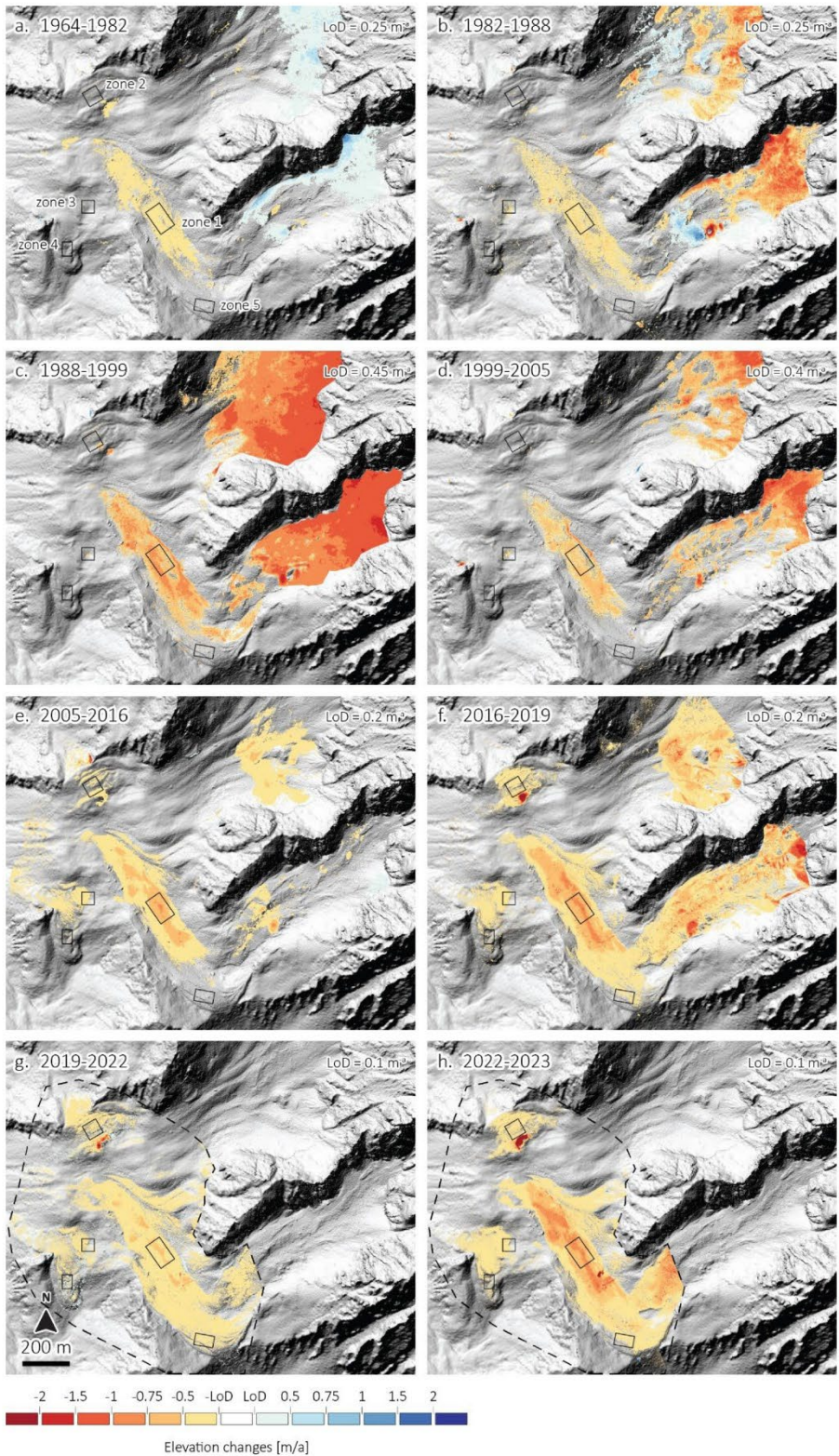
486 Surface elevation changes from 1964 to 2023 could be reconstructed using historical aerial images, UAV
487 data and existing ALS data (Figure 7). These changes reveal spatial and temporal variability across the
488 study area. The primary processes driving these surface elevation changes include: (i) melt-induced
489 subsidence of embedded glacier ice lenses in glacier-affected, perennially frozen landforms (such as
490 push moraines and rock glaciers), as well as in the debris-covered glacier; (ii) thawing of supersaturated
491 permafrost conditions; (iii) downslope displacement; and (iv) thermokarstic erosion.

492 From 1964 to 1982, no significant surface changes occurred in the upper sections of the Challand and
493 Epée glaciers. However, surface gains in the accumulation areas could be attributed to variable snow
494 cover and positive glacier mass balance. In contrast, the debris-covered tongue of the Epée glacier (zone
495 1, Figure 7a) experienced a mean surface lowering of -0.33 m/y. These relatively modest changes likely
496 reflect a colder period, during which ice melt was less pronounced than in the late 1980s. Between 1982
497 and 1988, surface lowering in the debris-covered glacier tongue increased slightly to -0.37 m/y. This
498 trend intensified between 1988 and 1999, with an average surface lowering of -0.74 m/y in the debris-
499 covered tongue. The orographic right lateral margin experienced even greater losses, averaging -0.90
500 m/y, likely due to the development of a lateral gully caused by thermokarstic erosion, as suggested by
501 orthoimages. In subsequent periods, surface lowering remained significant but varied over time.
502 Between 1999 and 2005, the mean surface lowering in the debris-covered glacier tongue was -0.51 m/y,
503 increasing slightly to -0.59 m/y from 2005 to 2016. From 2016 to 2019, the rate rose again to -0.69 m/y.
504 More recent observations reveal fluctuations in the rate of surface lowering. From 2019 to 2022, the
505 mean annual surface lowering slowed to -0.42 m/y. However, between 2022 and 2023, the rate
506 accelerated to -0.71 m/y, reflecting intensification of ice melt in the debris-covered glacier tongue.

507 From 1964 to 1982, surface changes in the Challand push-moraine (zone 2, Figure 7a) were minimal,
508 with a mean surface lowering of -0.16 m/y. Similarly, between 1982 and 1988, surface lowering was
509 negligible at -0.05 m/y. Between 1988 and 1999, a mean surface lowering of -0.17 m/y was observed,
510 followed by a slight increase to -0.22 m/y between 1999 and 2005. From 2005 to 2016, the rate decreased
511 slightly to -0.18 m/y. During this period, and up until 2005, the recorded values remained below the

512 level of detection, indicating very limited surface change. More noticeable surface lowering occurred
513 between 2016 and 2019, with a mean rate of -0.28 m/y. This was followed by a reduction to -0.11 m/y
514 between 2019 and 2022. However, the rate increased again to -0.27 m/y from 2022 to 2023. Significant
515 morphological changes were observed on the inner south-facing flank of the Challand northern push-
516 moraine, where elevation loss reached -3.6 m/y. This pronounced downwasting can be attributed to the
517 melting of an outcropping embedded glacier ice body within the push moraine. By final period
518 investigated, characterized as the 2022-2023 epoch, surface elevation changes on the south-facing flank
519 of the northern push moraine intensified, with rates reaching up to -6 m/y, marking a sharp increase in
520 surface lowering.

521 Prior to the inter-epoch 1988–1999, surface elevation changes in the rock glacier rooting zone (zone 3,
522 Figure 7a) were minimal and remained below the level of detection. However, between 1988 and 1999,
523 a more pronounced mean surface lowering of -0.41 m/y was recorded. This was followed by a decrease
524 to -0.23 m/y from 1999 to 2005. Between 2005 and 2016, surface lowering averaged to -0.20 m/y. From
525 2016 to 2019, the rate remained relatively stable at -0.21 m/y. A notable reduction occurred between
526 2019 and 2022, with the mean surface lowering dropping to -0.09 m/y. However, this trend reversed
527 between 2022 and 2023, as the rate increased to -0.18 m/y.



529 Figure 7: Surface elevation changes in the Ritord glacier forefield, including the Epée debris-covered glacier and the Challand
530 glacier, between 1964 and 2023. The DEMs used to calculate surface elevation changes between 1964 and 2005 are derived
531 from historical aerial images of Swisstopo (a-d). The DEMs used for the more recent years are derived from ALS surveys
532 (2016 and 2019) and UAV-derived datasets (2022-2023). The black dashed polygons in panels g) and h) represent the area
533 covered by the UAV surveys. The black boxes correspond to the areas used to calculate the mean surface elevation changes
534 for the different zones detailed in panel a (zone 1: debris-covered glacier tongue; zone 2: Challand push-moraine; zone 3: rock
535 glacier rooting zone; zone 4: rock glacier; zone 5: Epée push-moraine). Background: swissSURFACE3D (Swisstopo, 2021).

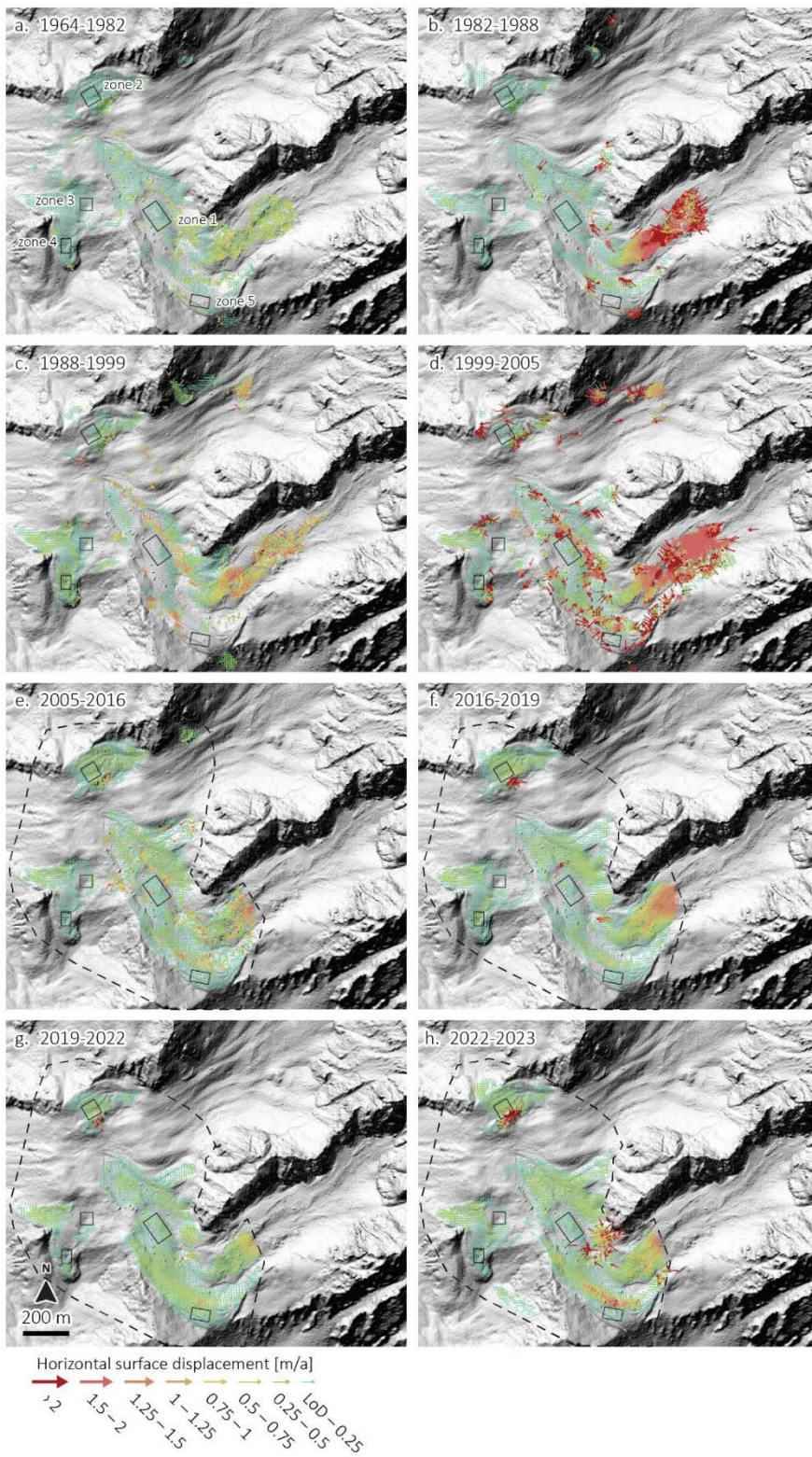
536

537 From 1964 to 1982, horizontal surface velocities on the dynamically disconnected debris-covered
538 glacier tongue were relatively low, averaging 0.08 m/y. A slight increase to 0.14 m/y was observed
539 between 1982 and 1988, likely reflecting the increase of ice flux driven by positive mass balance during
540 this period (Capt et al., 2016). Between 1988 and 1999, velocities decreased again to an average of 0.07
541 m/y, suggesting a period of reduced activity. However, along the orographic right lateral margin of the
542 debris-covered glacier tongue averaged 0.7 m/y, coinciding with the formation of a lateral gully caused
543 by thermokarstic erosion (Figure 8c). This displacement observed in the orographic right margin of the
544 debris-covered tongue further increased to 1.4 m/y between 1999 and 2005, reflecting significant
545 geomorphological adjustments driven by the erosional process (Figure 8d). During this period,
546 horizontal surface velocities increased to 0.17 m/y, possibly indicating a localised geomorphological
547 adjustments consequent to the lateral erosion. In the more recent periods, horizontal surface velocities
548 have stabilized at lower levels. Between 2020 and 2021, velocities averaged 0.08 m/y, decreasing
549 slightly to 0.07 m/y from 2021 to 2022. By 2022–2023, velocities returned to 0.08 m/y, maintaining a
550 consistent trend of minimal displacement. Over the entire study period, horizontal surface displacement
551 on the Epée debris-covered glacier tongue remained relatively stable overall, suggesting its dynamic
552 disconnection from the source area.

553 From 1964 to 1982, horizontal surface velocities on the Challand push-moraine averaged 0.15 m/y,
554 while those on the Epée push moraine were lower at 0.07 m/y. Between 1982 and 1988, both push-
555 moraines experienced an increase in velocities, with the Challand push-moraine reaching 0.19 m/y and
556 the Epée push-moraine rising to 0.16 m/y, potentially in response to slightly warmer conditions. From

557 1988 to 1999, velocities on the Challand push-moraine continued to increase, averaging 0.31 m/y, while
558 the Epée push-moraine exhibited a slight deceleration to 0.14 m/y. Between 1999 and 2005, velocities
559 on the Challand push-moraine increased to 0.44 m/y, whereas the Epée push-moraine experienced a
560 modest increase to 0.15 m/y. In the recent years, horizontal surface velocities derived from terrestrial
561 geodetic surveys were relatively stable, averaging to 0.30 m/y. The displacement flow field showed an
562 accentuated back-creep behaviour at the inner-flanks of both push-moraines.

563 Between 1964 and 1982, horizontal surface velocities averaged 0.19 m/y on the rock glacier and 0.13
564 m/y in its rooting zone. Both areas experienced a reduction in velocities during the period from 1982 to
565 1988, declining to 0.13 m/y and 0.09 m/y, respectively. From 1988 to 1999, velocities increased
566 significantly, reaching 0.29 m/y on the rock glacier and 0.23 m/y in the rooting zone. Between 1999 and
567 2005, the rock glacier recorded its highest velocity at 0.31 m/y, whereas the rooting zone exhibited a
568 marked decrease to 0.09 m/y. The horizontal surface displacement of the rock glacier and its rooting
569 zone were of 0.24 m/y and 0.12 m/y, respectively, between 2020 and 2021. A slight deceleration was
570 observed in 2021–2022, with velocities declining to 0.18 m/y on the rock glacier and 0.07 m/y in the
571 rooting zone. By 2022–2023, velocities reached 0.19 m/y on the rock glacier and 0.12 m/y in the rooting
572 zone.



574 Figure 8: Horizontal surface velocities between 1964 and 2023 at the Ritord glacier forefield, comprising the Challand and
575 Epée glaciers. The orthoimages used to calculate the horizontal surface displacement between 1964 and 2005 are from historical
576 aerial image of Swisstopo (a-e). The orthoimages used for the more recent years are derived from Flotron aerial images (2016
577 and 2019) and UAV-derived images (2022-2023). The black dashed polygons in panels e) to h) represent the area covered by
578 the surveys. The black boxes correspond to the areas used to calculate the mean surface displacements for the different zones
579 (zone 1: debris-covered glacier tongue; zone 2: Challand push-moraine; zone 3: rock glacier rooting zone; zone 4: rock glacier;
580 zone 5: Epée push-moraine; Figure 7a).Background: swissSURFACE3D (Swisstopo, 2021).

581

582 The mean horizontal and vertical velocities of the different zones highlighted in Figures 7 and 8 are
583 presented in Figure 9, covering the period from 1964 to 2023, revealing distinct kinematic signatures of
584 the different landforms. The dynamically disconnected debris-covered glacier tongue shows clear signs
585 of down-wasting, characterized by slow horizontal velocities and pronounced vertical velocities,
586 indicating intensified melt. Glacier-affected landforms in which glacier ice was embedded, such as the
587 lateral push-moraines and the rock glacier rooting zone, generally show more pronounced vertical
588 velocities. This is particularly evident for the Epée push-moraine and the rock glacier rooting zone
589 between 1988 and 1999, in comparison to the rock glacier tongue, which was likely not overlain by the
590 Epée LIA glacier.

591 In the more recent years, from 2020 to 2023, the contrast in kinematic behaviour between glacier-
592 affected landforms and the intact rock glacier has become more pronounced. The intact rock glacier
593 exhibits a morphodynamical signature primarily driven by permafrost creep, while the morphodynamics
594 of the glacier-affected landforms are influenced by both permafrost creep and the melt of embedded
595 glacier ice, especially in the lateral push-moraines.

596



597

598 Figure 9: Mean horizontal (a) and vertical (b) surface velocity of the different landforms present in the Ritord glacier forefield.
 599 Dashed lines represent velocity time series derived from aerial imagery spanning from 1964 to 2022, while continuous lines
 600 correspond to terrestrial geodetic surveys conducted between July 2020 and October 2023. Velocity values for each landform
 601 are calculated based on the data from the zones delineated in Figure 7 and 8.

602

603 4.4 Seasonal and sub-seasonal surface displacement and elevation change

604 The seasonal signal of horizontal and vertical surface displacement rates was assessed through seasonal
 605 TGS measurements (Figure 10). During the summer period (16.07.2020–17.10.2020), vertical velocities
 606 and horizontal surface velocities were generally faster than during the winter period (17.10.2020–
 607 16.07.2021). On the dynamically disconnected debris-covered glacier, the mean summer horizontal
 608 surface velocity was 0.41 m/y and the mean summer vertical velocity was -1.56 m/y, locally reaching
 609 up to -2.74 m/y in the area of strong thermokarstic and gully erosion processes. In contrast, the mean
 610 winter horizontal velocity was 0.06 m/y and the mean winter vertical velocity was 0.03 m/y.

611 The measured vector field on the Challand and Epée push-moraines is oriented perpendicularly to the
 612 compression ridges, a pattern also evident in the vector fields derived from the aerial images. The surface

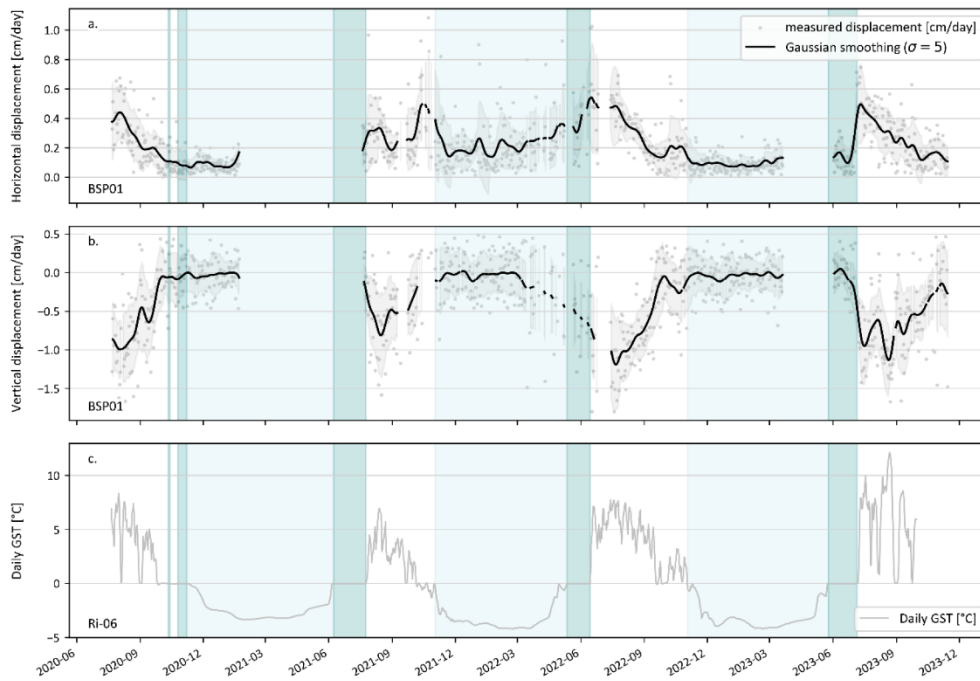
613 morphology, but also this flow trajectory reflects the influence of the Challand and Epée LIA glaciers
614 on these marginal frozen landforms. The Challand push-moraine exhibits a southeast-oriented flow
615 field, while the Epée push-moraine is characterized by a northward-directed flow, both of which display
616 a back-creep movement towards the topographic depression of the forefield, formerly occupied by the
617 Challand and Epée LIA glaciers. During the summer period, on the Challand push-moraine, the mean
618 vertical displacement rate in the zone where embedded glacier ice outcrops and whose extent is
619 suggested by geophysical surveys (Figure 4 and 5) is -0.71 m/y. In contrast, at the margins of the push-
620 moraine, where the embedded glacier ice lens is thought to be absent, the mean vertical displacement
621 rate is significantly lower at -0.17 m/y. During winter, both the ice-rich zone and the margins exhibit a
622 reduced mean vertical displacement rate of -0.03 m/y. Seasonal variations are also evident in horizontal
623 displacement rates. In summer, the mean horizontal displacement reaches 0.82 m/y in the ice-rich zone,
624 while in winter, a slight deceleration occurs, with a mean rate of 0.37 m/y. This seasonal pattern
625 highlights the continuous permafrost back-creep mechanism. During summer, the mean vertical
626 displacement rate on the Epée push-moraine is -0.39 m/y, with the exception of an outlier on the steep
627 inner flank, where displacement reaches -2.15 m/y, likely driven by localized sliding. In winter, vertical
628 displacement slows to -0.05 m/y. Horizontal displacement rates also show seasonal variation, with a
629 mean of 0.30 m/y in summer and a reduced rate of 0.08 m/y in winter.

630 In the formerly glacier-connected rock glacier roots, the mean vertical displacement rate reaches -0.60
631 m/y in summer, likely driven by the melt of a buried ice lens, while in winter, it decreases significantly
632 to -0.03 m/y. Horizontal displacement also varies seasonally, with a mean rate of 0.15 m/y in summer
633 and a slightly lower rate of 0.09 m/y in winter. Downslope from the rooting zone of the rock glacier, the
634 mean vertical displacement rate is -0.38 m/y in summer, decreasing to -0.09 m/y in winter. The mean
635 horizontal displacement rate is higher in summer, with a mean of 0.39 m/y, compared to 0.27 m/y in
636 winter. This seasonal variation in horizontal and vertical displacements suggests that during the summer,
637 warming and thawing of the ice-rich core increase water content within the ice-rich core, leading to
638 faster creep rates. In contrast, during winter, the reduction in ice melt at the permafrost table lowers
639 water availability, resulting in a deceleration of permafrost creep rates.

645 The driving processes contributing to the sub-seasonal horizontal surface displacements and elevation
646 changes were assessed through the comparison of daily position measurements by permanent dGNSS
647 stations with the closest daily ground surface temperature measurements (Figures 11 and 12).

648 The dGNSS station BSP-01 (Figure 11) is located on the partly disconnected debris-covered glacier
649 tongue, where the surface topography is relatively flat. The horizontal surface velocity tends to increase
650 at the end of the zero-curtain period. However, the acceleration phase starts when the ground surface
651 temperatures measured a few hundred metres from the station (still on the debris-covered glacier tongue)
652 gradually increase in late winter – early spring. The inter-annual horizontal velocity is variable as in
653 2021, the peak velocity was reached in autumn, while the 2022 and 2023, the peak velocities were
654 reached in early summer. The vertical velocity systematically reaches its annual peak in summer when
655 the ground surface temperatures are the warmest. The maximal summer vertical velocity ranges between
656 -0.80 cm/day to -1.20 cm/day, which corresponds to a summer (1 July – 1 October) elevation loss of \pm
657 1 m. Both the winter periods 2020-2021 and 2022-2023, when the ground surface temperatures are
658 below 0°C , the horizontal displacement stabilized to ± 0.10 cm/day, while the vertical displacement is
659 close to 0 cm/day. The horizontal displacement during winter period 2021-2022 is characterized by
660 horizontal velocities fluctuating between $\pm 0.18 - 0.24$ cm/day. Similarly to the other winter periods,
661 the vertical displacement during the winter 2021-2022 almost non-existent.

662



663

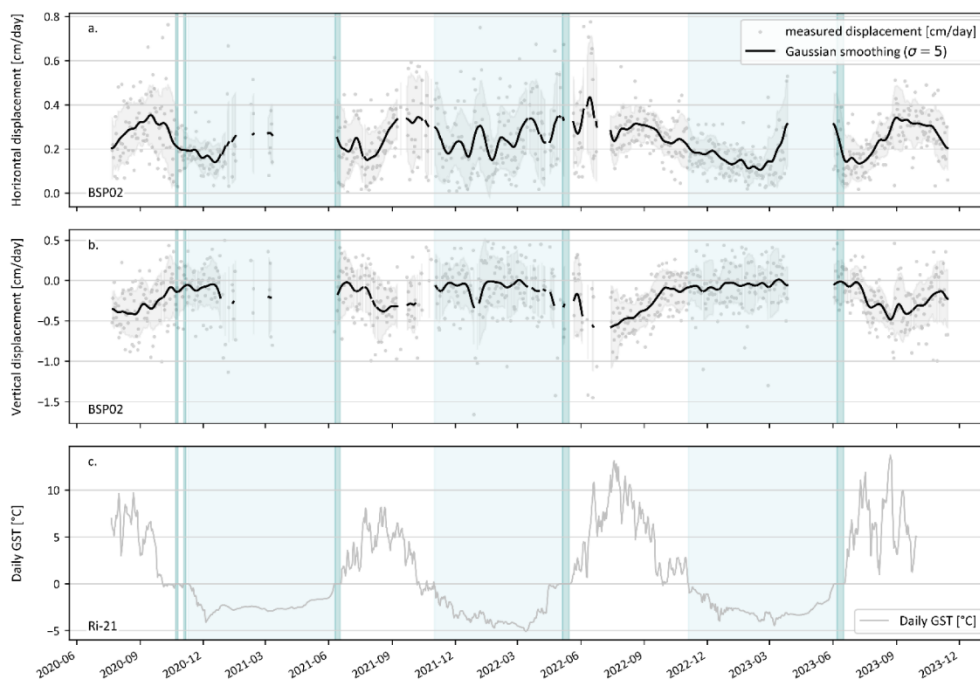
664 Figure 11: Daily horizontal (a) and vertical (b) surface displacement measured by the permanent dGNSS BSP-01. Daily ground
 665 surface temperature measured by the logger UTL-06 (Ri-06) (c). The light blue shaded area represents the period when ground
 666 surface temperatures are below 0°C for at least 20 days. The dark blue shaded area represents of the zero-curtain period.
 667 Discontinuities in the dGNSS data are explained by data gaps caused by the burial of the station by snow or other technical
 668 issues in data transfer.

669

670 The dGNSS station BSP-02 (Figure 12) is located on the Challand push-moraine, where glacier ice is
 671 buried within the frozen landform, and where the kinematic behaviour of the landform is mainly
 672 characterized by back-creep. Horizontal velocities tend to reach their peak in autumn and are around
 673 0.25 - 0.35 cm/day. A peak of 0.45 cm/day in horizontal velocity was reached in early summer 2022,
 674 which was followed by a deceleration in horizontal displacement (0.30 cm/day) towards the end of the
 675 summer. However, the vertical displacement in summer 2022 was more important than in the other
 676 years. This can be explained by the particularly warm ground surface temperatures, which probably
 677 contributed to enhanced ground ice melt-induced subsidence. In winter 2021-2022, the horizontal

678 displacement oscillated between 0.15 and 0.35 cm/day, while the vertical displacement was mainly
679 around 0 cm/day, aside from an event in December where the displacement was -0.35 cm/day. In winter
680 2022-2023, as soon as the ground surface cooling was initiated, the horizontal displacement began to
681 gradually decelerate from early September to early March. Meanwhile, the vertical displacement
682 exhibited a gradual stabilization to 0 cm/day, suggesting a continuous creep behaviour, and an absence
683 of ice melt-induced vertical changes.

684



685

686 Figure 12: Daily horizontal (a) and vertical (b) surface displacement measured by the permanent dGNSS BSP-02. Daily ground
687 surface temperature measured by the logger UTL-21 (Ri-21) (c). The light blue shaded area represents the period when ground
688 surface temperatures are below 0°C for at least 15 days. The dark blue shaded area represents of the zero-curtain period.
689 Discontinuities in the dGNSS data are explained by data gaps caused by the burial of the station by snow or other technical
690 issues in data transfer.

691

692

693

694 5 Discussion

695

696 5.1 Evaluation of the application of a multi-method approach

697 Combining multiple techniques allowed a detailed analysis of the evolution and dynamics of the
698 different landforms present within the Ritord glacier forefield at a varying spatial and temporal
699 resolutions. Moreover, the integrative analysis of all datasets provided key evidence for the
700 understanding of the driving processes contributing to the morphodynamical evolution and signature of
701 the investigated landforms. The use of historical aerial images and UAV-derived images provided a
702 large spatial and temporal coverage of the study area, allowing the analysis of the kinematic evolution
703 at a decadal scale of the glacier forefield. The level of detection (LoD) for surface elevation changes
704 varied between inter-epochs and was likely slightly underestimated. The stable areas used for
705 determining the LoD were outside the study area but in close proximity to it, in locations selected for
706 their high stability and lack of active sedimentary processes or solifluction. While this approach ensured
707 a reliable LoD for the immediate vicinity of these stable areas, it does not account for potentially larger
708 mean errors (ME) and standard deviations of elevation (SDE) in other regions. Furthermore, as the study
709 area for the inter-epoch 1988-1999 is slightly further east and positioned at the edge of the
710 photogrammetric block, where errors are typically more pronounced, this may introduce greater
711 uncertainty in the analysis. It is therefore likely that the actual LoD for this region is higher than the
712 calculated value, which could explain the more pronounced changes in surface elevation calculated for
713 this period.

714 The integration of continuous ground surface temperature time series with in-situ terrestrial geodetic
715 surveys, conducted both seasonally and continuously, enabled a high-temporal resolution kinematic
716 analysis of the dynamically disconnected debris-covered glacier tongue and the Challand push moraine.
717 This comprehensive approach provided valuable insights into the influence of the ground thermal regime

40

718 on the kinematic behaviour of these landforms. Additionally, geophysical measurements enabled the
719 characterisation of the subsurface properties and their impact on surface dynamics. Changes in resistivity
720 further enhanced the understanding of subsurface-surface interactions, revealing processes such as ice-
721 melt-induced subsidence and thermokarstic erosion.

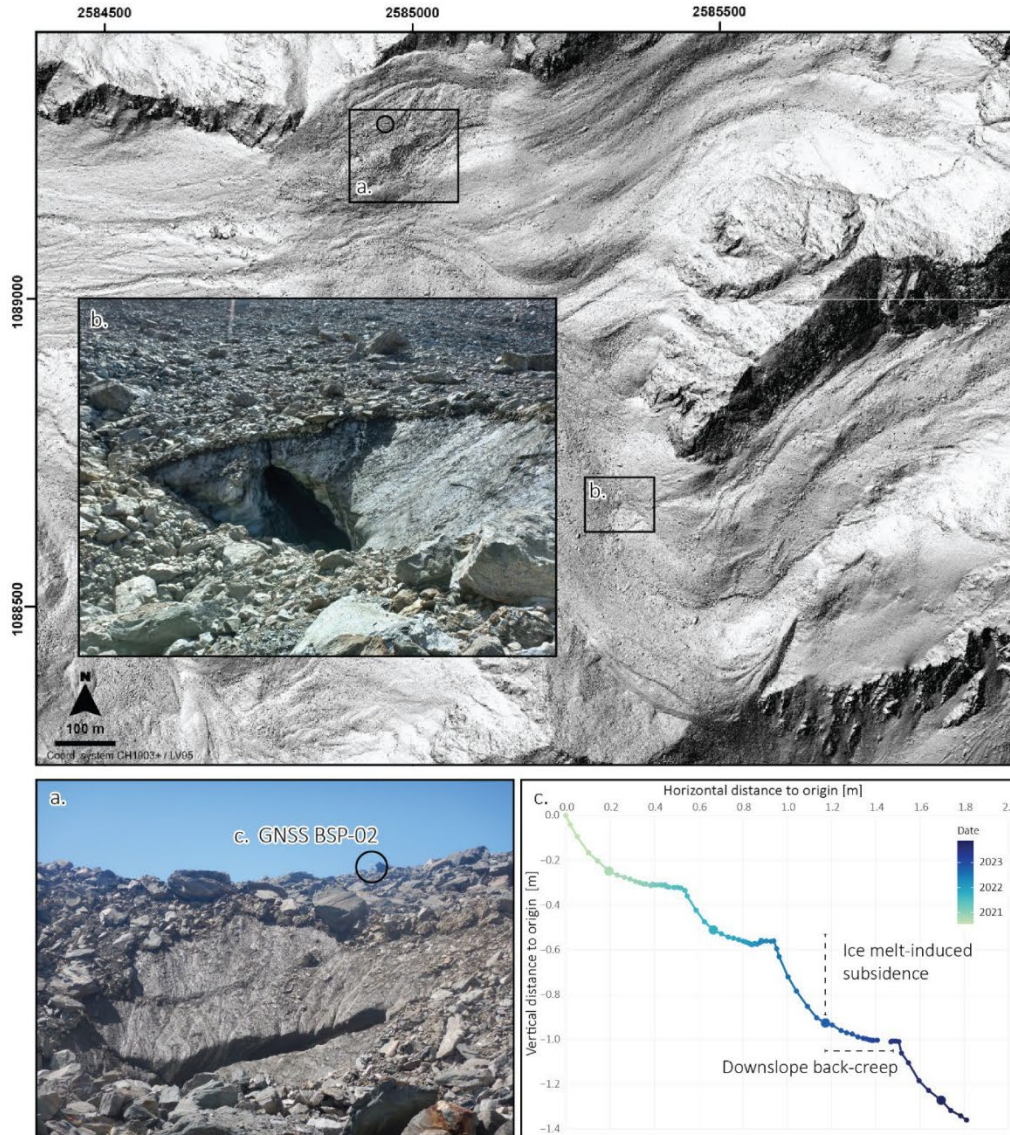
722

723 5.2 Spatial distribution of ground ice and associated surface changes

724 The spatial distribution of ground ice in the Ritord glacier forefield, which includes the adjacent
725 Challand and Epée glaciers, indicates a polythermal regime for both glaciers during the LIA (Delaloye,
726 2004). The fluted moraines and absence of permafrost downstream of the Challand glacier suggest that
727 its base was temperate. In contrast, the presence of lateral push-moraines from both the Challand
728 (northern) and Epée (southern) glaciers, as well as the medial push-moraine, points to the displacement
729 of pre-existing perennially frozen sediments by the cold margins of both glaciers towards the lateral
730 margins of the glacier forefield and the maximal extent of the Challand and Epée glaciers. Similar spatial
731 distribution of ground ice have been documented in alpine LIA glacier forefields within the belt of
732 discontinuous permafrost (Kunz and Kneisel, 2020; Wee et al., 2024).

733 During the interaction between the polythermal glaciers and the permafrost in the existing sediment
734 accumulations, glacier ice was locally embedded within, and primarily on top of, the frozen debris. This
735 is evidenced by a former ice outcrop in the inner flank of the Epée push-moraine (Delaloye, 2004), and
736 by the outcropping of a massive ice lens on the inner flank of the Challand push-moraine (Figure 13a).

737 The embedding of ice lenses also likely occurred in the rooting zone of the rock glacier, as evidenced
738 by the high resistivity values and the pronounced changes in elevation. These changes are probably
739 driven by the melt of an ice lens deposited by the Epée debris-covered glacier. The concave topography
740 of the rooting zone suggests that the Epée debris-covered glacier once extended into this area. Moreover,
741 the current concave shape of the zone indicates that it can no longer feed the rock glacier, highlighting
742 the geomorphological disturbance caused by the glacier's advance (Vivero and Lambiel, 2024).



744

745 Figure 13: Ice outcrops within the Challand (northern) push-moraine and in the lateral margin of the Epéc debris-covered
 746 glacier (a-b). Ice melt subsidence and thermokarstic erosion are evidenced by the permanent dGNSS station BSP-02 (c). Each
 747 plotted marker (point) corresponds to a bi-monthly interval, with the series starting on 21.07.2020 and ending on 15.11.2023
 748 (with a data gap between 15.03.2023 and 01.06.2023). The larger markers indicate the start and end of each hydrological year
 749 (c). Photo credits: Julie Wee, 13.07.2022 (a); Grégoire Seingre, 09.10.2023 (b).

750

751 Ice melt-induced subsidence and thermokarstic erosion can be considered as the driving process
752 contributing to the significant surface lowering observed in this area (Figure 7). Figure 13c highlights
753 the seasonal contribution of surface lowering dominated by ice melt occurring at the interface between
754 the massive ice lens and the debris mantle, but also at the south-facing ice outcrop. The strong
755 downwasting of the exposed ice, is accentuated by the fine-grained sediment deposits likely washed
756 down from the debris mantle, which darken the ice surface (albedo reduction), thus increasing solar
757 radiation absorption and accelerating the melting process (Nicholson and Benn, 2006). The results from
758 the temperature and geodetic measurements (Figure 12 and Figure 13c) show direct and high-magnitude
759 responses of subsidence to summer ground surface heating. Meanwhile, continuous downslope
760 displacement occurs as a result of internal permafrost creep deformation within the permafrost body and
761 at the shear horizon. The horizontal displacement occurring during the winter period, when ground
762 surface temperatures are colder, can be explained by the thermal lag, which may be partly attributed to
763 the time for the temperature signal to propagate from the surface to the ice-rich core.

764 As illustrated by Figure 7, the most dynamic part of the glacier forefield and its adjacent glaciers is
765 characterized by the presence of bare-ice and areas where the debris-cover is relatively thin, such as the
766 central part of the debris-covered glacier tongue of the Epée glacier. In the margins of the latter, surface
767 elevation changes are less significant, as it is probable that in these areas are more heavily debris-covered
768 due to their proximity to headwalls and talus slopes, which supply debris through time (Anderson and
769 Anderson, 2018). This is especially relevant to the eastern side of the Epée debris-covered section, where
770 at least three talus-headwall systems are present. In contrast, the western margin of the Epée debris-
771 covered glacier lacks significant talus, suggesting that the debris in this area is primarily sourced from
772 the lateral and push moraines, which are responsible for transferring debris (van Woerkom et al., 2019).

773

774 5.3 Surface displacement rates and associated dynamics

775 The analysis of horizontal surface velocities allowed to highlight the origin, properties, and spatial
776 distribution of ground ice within the Ritord glacier forefield, but also the temporal variability of the

777 pluri-decadal, as well as the sub-seasonal kinematic behaviour of the different landforms. Important
778 horizontal displacement velocities, due to basal sliding, generally occurred in the steep upslope area of
779 the Epée debris-covered glacier. The horizontal flow fields in this section can be described as exhibiting
780 characteristics of a partly chaotic system, which is likely due to differential ablation rates of the glacier
781 in this section caused by an uneven distribution of debris-cover thickness, as common feature observed
782 elsewhere (Monnier and Kinnard, 2017; Vivero et al., 2021). While surface velocities decrease
783 significantly towards the debris-covered terminus of the Epée glacier, due to the flatter topography and
784 to the reduced driving stress (Capt et al., 2016; Cuffey and Paterson, 2010). This reduction in driving
785 stress can be partly attributed to the 90° (elbow) change in direction of the glacier, the partial and gradual
786 disconnection between the upslope and downslope sections of the glacier, and by the downstream
787 accumulation of sediments, which can increase the compressive flow, contributing to restraining the
788 glacier's motion (Kirkbride and Deline, 2013). The little horizontal motion is captured across the pluri-
789 decadal, seasonal, and sub-seasonal scales (Figures 8, 10 and 11). The annual horizontal displacement
790 rate through ranges around 0.10 to 0.20 m/y, while the winter-seasonal displacement rate is < 0.06 m/y
791 to almost no-motion.

792 Horizontal surface displacement is pronounced on the steep inner flank of both the Challand (northern)
793 and Epée (southern) push moraines. The geometry of the lateral push-moraines is partly due to the
794 pressure exerted by the glaciers during the interaction and glacitectonization phase, and to the
795 subsequent glacier retreat, causing a change in the stress fields, and consequently resulting in the
796 geometric readjustment of the slopes (Haeberli, 1979). The flow fields show a distinct back-creep toward
797 the topographic thalweg previously occupied by the glaciers. In the case of the Challand (northern) push-
798 moraine, horizontal surface velocities on the inner flank – where the ice is exposed – are expected to
799 increase in the future due to accelerated downwasting. This could lead to the formation of a deepening,
800 potentially creating a thermokarstic depression. Alternatively, the area may act as a sediment sink, with
801 debris mantle which is overlaying the melting ice accumulating and filling the depression.

802 The spatial heterogeneity of the horizontal surface displacement rate can be largely attributed to the
803 landform origin and development, as well as the debris coverage and the topographical slope. It was

804 also possible to highlight a seasonal signal in term is surface displacement velocities, which infers that
805 the latter is influenced by thermally-driven processes. This was also shown between 1964 and 1982,
806 which corresponds to a colder period, associated with the advance of some alpine glaciers (Paul et al.,
807 2007). In the case of the Challand and Epée glaciers, it seems that the slight mass gain (Figure 7) was
808 not sufficient enough to contribute to a significant advance of the glaciers. The relatively slower
809 velocities could indicate reduced basal sliding and internal deformation, due to colder temperature.

810 Between 1999 and 2005, horizontal surface displacement highlighted significant geometrical changes
811 in the margins of the debris-covered tongue of the Epée glacier, likely indication its surface loss and the
812 consequent paraglacial readjustments (Deline et al., 2021).

813

814 5.4 Processes contributing to the morphodynamical evolution of the Ritord glacier forefield

815 The observed morphological changes due to surface lowering and geometrical adjustments reflect the
816 long-term, gradual downwasting of various landforms within the glacier forefield. The analysis of
817 resistivity changes between 1997 and 2020 highlights that the magnitude of these changes is strongly
818 influenced by ground ice properties, as well as the thickness and coarseness of the surface debris. Areas
819 that experienced the greatest decrease in electrical resistivity are likely characterized by thin ice lenses
820 buried beneath shallow debris, which accelerates ice melt. In contrast, areas underlain by massive, likely
821 cold glacier ice showed the least resistivity change. However, the overall decrease in resistivity suggests
822 a higher water-to-ice ratio, which could further accelerate the thermal degradation and melting of ground
823 ice. This was revealed by the long-term timeseries of the kinematic behaviour of the glacier-affected
824 landforms, as in the recent years, enhanced vertical displacements were observed.

825

826 6 Conclusion

827 The multi-method approach applied in this study provides a novel contribution to understanding the
828 interactions between permafrost and glacial dynamics, assessing the Ritord glacier forefield's evolution
829 across multiple temporal and spatial scales. By integrating geophysical, geodetic, photogrammetric
830 techniques, and temperature measurements we distinguished between permafrost- and glacial-driven
831 processes, revealing the lasting thermal and mechanical effects of the LIA on current dynamics. High
832 temporal resolution data revealed sub-seasonal kinematic patterns of the debris-covered glacier tongue
833 and push moraine, driven primarily by thermal conditions and surface properties. Historical aerial
834 imagery further highlighted the influence of climatic variations on landform morphodynamics. While
835 similar geomorphic conditions are found at other sites where glacier-permafrost interaction occurred,
836 the extensive and comprehensive dataset from Ritord makes this case study particularly valuable for
837 interpreting dynamics at locations with limited in-situ data. The integration of diverse methods and data
838 enhances our understanding of glacier-permafrost interactions, providing critical insights that can be
839 applied to regions with sparse observational data.

840

841 Acknowledgements

842 The acquisition of this important dataset would not have been possible without the valuable support and
843 work from colleagues and friends involved in the fieldwork. We are sincerely grateful for the time and
844 effort that you have invested in helping with the data acquisition. We would like to thank Christian
845 Hauck, Christophe Lambiel, Marcia Phillips and Isabelle Gärtner-Roer for their insightful comments on
846 the manuscript.

847 CRediT authorship contribution statement

848 Julie Wee: Conceptualization, Data curation, Formal analysis, Investigation, Methodology, Resources,
849 Software, Project administration, Validation, Visualization, Writing – original draft, Writing – review
850 and editing. Hanne Hendrickx: Data curation, Formal analysis, Methodology, Software, Writing –
851 review and editing. Sebastián Vivero: Data curation, Formal analysis, Investigation, Methodology,
852 Software, Writing – review and editing.

853 References

- 854 Amschwand, D., Scherler, M., Hoelzle, M., Krummenacher, B., Haberkorn, A., Kienholz, C., and
855 Gubler, H.: Surface heat fluxes at coarse-blocky Murtèl rock glacier (Engadine, eastern Swiss Alps),
856 EGU sphere, 1–56, <https://doi.org/10.5194/egusphere-2023-2109>, 2023.
- 857 Anderson, L. S. and Anderson, R. S.: Debris thickness patterns on debris-covered glaciers,
858 *Geomorphology*, 311, 1–12, <https://doi.org/10.1016/j.geomorph.2018.03.014>, 2018.
- 859 Betz-Nutz, S., Heckmann, T., Haas, F., and Becht, M.: Development of the morphodynamics on Little
860 Ice Age lateral moraines in 10 glacier forefields of the Eastern Alps since the 1950s, *Earth Surf. Dyn.*,
861 11, 203–226, <https://doi.org/10.5194/esurf-11-203-2023>, 2023.
- 862 Beutel, J., Biri, A., Buchli, B., Cicoira, A., Delaloye, R., Da Forno, R., Gaertner-Roer, I., Gruber, S.,
863 Gsell, T., Hasler, A., Lim, R., Limpach, P., Mayoraz, R., Meyer, M., Noetzli, J., Phillips, M., Pointner,
864 E., Raetzo, H., Scapoza, C., Strozzi, T., Thiele, L., Vieli, A., Vonder Mühl, D., Weber, S., and Wirz,
865 V.: Kinematic observations of the mountain cryosphere using in-situ GNSS instruments, *Cryosphere –*
866 *Permafrost*, <https://doi.org/10.5194/essd-2021-176>, 2021.
- 867 Blanch, X., Eltner, A., Guinau, M., and Abellan, A.: Multi-Epoch and Multi-Imagery (MEMI)
868 Photogrammetric Workflow for Enhanced Change Detection Using Time-Lapse Cameras, *Remote*
869 *Sens.*, 13, 1460, <https://doi.org/10.3390/rs13081460>, 2021.

870 Bosson, J.-B., Deline, P., Bodin, X., Schoeneich, P., Baron, L., Gardent, M., and Lambiel, C.: The
871 influence of ground ice distribution on geomorphic dynamics since the Little Ice Age in proglacial
872 areas of two cirque glacier systems, *Earth Surf. Process. Landf.*, 40, 666–680,
873 <https://doi.org/10.1002/esp.3666>, 2015.

874 Capt, M., Bosson, J.-B., Fischer, M., Micheletti, N., and Lambiel, C.: Decadal evolution of a very
875 small heavily debris-covered glacier in an Alpine permafrost environment, *J. Glaciol.*, 62, 535–551,
876 <https://doi.org/10.1017/jog.2016.56>, 2016.

877 Carrivick, J. L., Geilhausen, M., Warburton, J., Dickson, N. E., Carver, S. J., Evans, A. J., and Brown,
878 L. E.: Contemporary geomorphological activity throughout the proglacial area of an alpine catchment,
879 *Geomorphology*, 188, 83–95, <https://doi.org/10.1016/j.geomorph.2012.03.029>, 2013.

880 Cook, K. L. and Dietze, M.: Short Communication: A simple workflow for robust low-cost UAV-
881 derived change detection without ground control points, *Earth Surf. Dyn.*, 7, 1009–1017,
882 <https://doi.org/10.5194/esurf-7-1009-2019>, 2019.

883 Cuffey, K. and Paterson, W. S. B.: *The physics of glaciers*, 4th ed., Butterworth-Heinemann/Elsevier,
884 Burlington, MA, 693 pp., 2010.

885 Cusicanqui, D., Rabatel, A., Vincent, C., Bodin, X., Thibert, E., and Francou, B.: Interpretation of
886 volume and flux changes of the Laurichard rock glacier between 1952 and 2019, French Alps, *J.*
887 *Geophys. Res. Earth Surf.*, 126, e2021JF006161, 2021.

888 Cusicanqui, D., Bodin, X., Duvillard, P.-A., Schoeneich, P., Revil, A., Assier, A., Berthet, J., Peyron,
889 M., Roudnitska, S., and Rabatel, A.: Glacier, permafrost and thermokarst interactions in Alpine
890 terrain: Insights from seven decades of reconstructed dynamics of the Chauvet glacial and periglacial
891 system (Southern French Alps), *Earth Surf. Process. Landf.*, 48, 2595–2612,
892 <https://doi.org/10.1002/esp.5650>, 2023.

893 Debella-Gilo, M. and Kääb, A.: Sub-pixel precision image matching for measuring surface
894 displacements on mass movements using normalized cross-correlation, *Remote Sens. Environ.*, 115,
895 130–142, <https://doi.org/10.1016/j.rse.2010.08.012>, 2011.

896 Degenhardt, J. J., Giardino, J. R., and Junck, M. B.: GPR survey of a lobate rock glacier in Yankee
897 Boy Basin, Colorado, USA, *Geol. Soc. Lond. Spec. Publ.*, 211, 167–179,
898 <https://doi.org/10.1144/GSL.SP.2001.211.01.14>, 2003.

899 Delaloye, R.: Contribution à l'étude du pergélisol de montagne en zone marginale, *GeoFocus.*,
900 University of Fribourg, Fribourg, 244 pp., 2004.

901 Deline, P., Gruber, S., Amann, F., Bodin, X., Delaloye, R., Failletaz, J., Fischer, L., Geertsema, M.,
902 Giardino, M., Hasler, A., Kirkbride, M., Krautblatter, M., Magnin, F., McColl, S., Ravelin, L.,
903 Schoeneich, P., and Weber, S.: Chapter 15 - Ice loss from glaciers and permafrost and related slope
904 instability in high-mountain regions, in: *Snow and Ice-Related Hazards, Risks, and Disasters (Second*
905 *Edition)*, edited by: Haeberli, W. and Whiteman, C., Elsevier, 501–540, [https://doi.org/10.1016/B978-](https://doi.org/10.1016/B978-0-12-817129-5.00015-9)
906 [0-12-817129-5.00015-9](https://doi.org/10.1016/B978-0-12-817129-5.00015-9), 2021.

907 Etzelmüller, B. and Hagen, J. O.: Glacier-permafrost interaction in Arctic and alpine mountain
908 environments with examples from southern Norway and Svalbard, *Geol. Soc. Lond. Spec. Publ.*, 242,
909 11–27, <https://doi.org/10.1144/GSL.SP.2005.242.01.02>, 2005.

910 Feurer, D. and Vinatier, F.: The Time-SIFT method : detecting 3-D changes from archival
911 photogrammetric analysis with almost exclusively image information, *ISPRS J. Photogramm. Remote*
912 *Sens.*, 146, 495–506, <https://doi.org/10.1016/j.isprsjprs.2018.10.016>, 2018.

913 Forte, E., Santin, I., Colucci, R. R., Dossi, M., Guglielmin, M., Pipan, M., Roncoroni, G., and ?ebre,
914 M.: GPR data analysis for cold and warm ice detection and characterization in polythermal glaciers,
915 in: *18th International Conference on Ground Penetrating Radar*, Golden, Colorado, 14–19 June 2020,
916 Society of Exploration Geophysicists, 69–72, <https://doi.org/10.1190/gpr2020-019.1>, 2020.

917 Gärtner-Roer, I., Brunner, N., Delaloye, R., Haeberli, W., Kääh, A., and Thee, P.: Glacier–permafrost
918 relations in a high-mountain environment: 5 decades of kinematic monitoring at the Gruben site, Swiss
919 Alps, *The Cryosphere*, 16, 2083–2101, 2022.

920 Genzano, N., Fugazza, D., Eskandari, R., and Scaioni, M.: Multitemporal Structure-from-Motion: A
921 Flexible Tool to Cope with Aerial Blocks in Changing Mountain Environment, *Int. Arch.*
922 *Photogramm. Remote Sens. Spat. Inf. Sci.*, XLVIII-2-2024, 99–106, [https://doi.org/10.5194/isprs-](https://doi.org/10.5194/isprs-archives-XLVIII-2-2024-99-2024)
923 [archives-XLVIII-2-2024-99-2024](https://doi.org/10.5194/isprs-archives-XLVIII-2-2024-99-2024), 2024.

924 Gilbert, A., Vincent, C., Wagnon, P., Thibert, E., and Rabatel, A.: The influence of snow cover
925 thickness on the thermal regime of Tête Rousse Glacier (Mont Blanc range, 3200 m a.s.l.):
926 Consequences for outburst flood hazards and glacier response to climate change, *J. Geophys. Res.*
927 *Earth Surf.*, 117, n/a-n/a, <https://doi.org/10.1029/2011JF002258>, 2012.

928 Haeberli, W.: Holocene Push-Moraines in Alpine Permafrost, *Geogr. Ann. Ser. Phys. Geogr.*, 61, 43,
929 <https://doi.org/10.2307/520513>, 1979.

930 Haeberli, W.: Permafrost-glacier relationships in the Swiss Alps-today and in the past, in: *Proceedings*
931 *of the Fourth International Conference on Permafrost, Fourth International Conference on Permafrost.*
932 *July 17-22, Washington DC*, 415–420, 1983.

933 Haeberli, W.: Investigating glacier-permafrost relationships in high-mountain areas: historical
934 background, selected examples and research needs, *Geol. Soc. Lond. Spec. Publ.*, 242, 29–37,
935 <https://doi.org/10.1144/GSL.SP.2005.242.01.03>, 2005.

936 Haeberli, W. and Vonder Mühl, D.: On the characteristics and possible origins of ice in rock glacier
937 permafrost, *Z. Für Geomorphol. Suppl.*, 43–57, 1996.

938 Hauck, C. and Kneisel, C.: *Applied geophysics in periglacial environments*, Cambridge University
939 Press, 2008.

940 Hendrickx, H., De Sloover, L., Stal, C., Delaloye, R., Nyssen, J., and Frankl, A.: Talus slope
941 geomorphology investigated at multiple time scales from high-resolution topographic surveys and
942 historical aerial photographs (Sanetsch Pass, Switzerland), *Earth Surf. Process. Landf.*, 45, 3653–
943 3669, <https://doi.org/10.1002/esp.4989>, 2020.

944 Hendrickx, H., Le Roy, G., Helmstetter, A., Pointner, E., Larose, E., Brillard, L., Nyssen, J.,
945 Delaloye, R., and Frankl, A.: Timing, volume and precursory indicators of rock- and cliff fall on a
946 permafrost mountain ridge (Mattertal, Switzerland), *Earth Surf. Process. Landf.*, 47, 1532–1549,
947 <https://doi.org/10.1002/esp.5333>, 2022.

948 Herring, T., Lewkowicz, A. G., Hauck, C., Hilbich, C., Mollaret, C., Oldenborger, G. A., Uhlemann,
949 S., Farzamian, M., Calmels, F., and Scandroglio, R.: Best practices for using electrical resistivity
950 tomography to investigate permafrost, *Permafr. Periglac. Process.*, 34, 494–512,
951 <https://doi.org/10.1002/ppp.2207>, 2023.

952 Hock, R., Rasul, G., Adler, C., Cáceres, B., Gruber, S., Hirabayashi, Y., Jackson, M., Kääb, A., Kang,
953 S., Kutuzov, S., Milner, A., Molau, U., Morin, S., Orlove, B., and Steltzer, H.: High Mountain Areas,
954 in: *IPCC special report on the ocean and cryosphere in a changing climate*, edited by: Pörtner, H.-O.,
955 Roberts, D. C., Masson-Delmotte, V., Tignor, M., Poloczanska, E., Mintenbeck, K., Alegria, A.,
956 Nicolai, M., Okem, A., Petzold, J., Rama, B., and Weyer, N. M., Cambridge University Press,
957 Cambridge, 131–202, <https://doi.org/10.1017/9781009157964.004>, 2019.

958 Hugonnet, R., McNabb, R., Berthier, E., Menounos, B., Nuth, C., Girod, L., Farinotti, D., Huss, M.,
959 Dussaillant, I., Brun, F., and Kääb, A.: Accelerated global glacier mass loss in the early twenty-first
960 century, *Nature*, 592, 726–731, <https://doi.org/10.1038/s41586-021-03436-z>, 2021.

961 Ivy-Ochs, S., Kerschner, H., Maisch, M., Christl, M., Kubik, P. W., and Schlüchter, C.: Latest
962 Pleistocene and Holocene glacier variations in the European Alps, *Quat. Sci. Rev.*, 28, 2137–2149,
963 <https://doi.org/10.1016/j.quascirev.2009.03.009>, 2009.

964 Kääh, A. and Kneisel, C.: Permafrost creep within a recently deglaciated glacier forefield: Muragl,
965 Swiss Alps, *Permafr. Periglac. Process.*, 17, 79–85, <https://doi.org/10.1002/ppp.540>, 2006.

966 Kääh, A. and Vollmer, M.: Surface Geometry, Thickness Changes and Flow Fields on Creeping
967 Mountain Permafrost: Automatic Extraction by Digital Image Analysis, *Permafr. Periglac. Process.*,
968 11, 315–326, [https://doi.org/10.1002/1099-1530\(200012\)11:4<315::AID-PPP365>3.0.CO;2-J](https://doi.org/10.1002/1099-1530(200012)11:4<315::AID-PPP365>3.0.CO;2-J), 2000.

969 Kääh, A., Haerberli, W., and Gudmundsson, G. H.: Analysing the creep of mountain permafrost using
970 high precision aerial photogrammetry: 25 years of monitoring Gruben rock glacier, Swiss Alps,
971 *Permafr. Periglac. Process.*, 8, 409–426, [https://doi.org/10.1002/\(SICI\)1099-1530\(199710/12\)8:4<409::AID-PPP267>3.0.CO;2-C](https://doi.org/10.1002/(SICI)1099-1530(199710/12)8:4<409::AID-PPP267>3.0.CO;2-C), 1997.

972

973 Kirkbride, M. P. and Deline, P.: The formation of supraglacial debris covers by primary dispersal from
974 transverse englacial debris bands, *Earth Surf. Process. Landf.*, 38, 1779–1792,
975 <https://doi.org/10.1002/esp.3416>, 2013.

976 Kneisel, C.: Occurrence of surface ice and ground ice/permafrost in recently deglaciated glacier
977 forefields, St. Moritz area, Eastern Swiss Alps, in: *PERMAFROST - Seventh International
978 Conference, Yellowknife (Canada)*, 7, 1998.

979 Kneisel, C. and Kääh, A.: Mountain permafrost dynamics within a recently exposed glacier forefield
980 inferred by a combined geomorphological, geophysical and photogrammetrical approach, *Earth Surf.
981 Process. Landf.*, 32, 1797–1810, <https://doi.org/10.1002/esp.1488>, 2007.

982 Kneisel, Chr.: New insights into mountain permafrost occurrence and characteristics in glacier
983 forefields at high altitude through the application of 2D resistivity imaging, *Permafr. Periglac.
984 Process.*, 15, 221–227, <https://doi.org/10.1002/ppp.495>, 2004.

985 Kunz, J. and Kneisel, C.: Glacier–Permafrost Interaction at a Thrust Moraine Complex in the Glacier
986 Forefield Muragl, Swiss Alps, *Geosciences*, 10, 205, <https://doi.org/10.3390/geosciences10060205>,
987 2020.

1060 van Woerkom, T., Steiner, J. F., Kraaijenbrink, P. D. A., Miles, E. S., and Immerzeel, W. W.:
1061 Sediment supply from lateral moraines to a debris-covered glacier in the Himalaya, *Earth Surf. Dyn.*,
1062 7, 411–427, <https://doi.org/10.5194/esurf-7-411-2019>, 2019.

Curriculum vitae

Julie Alexandra Wee

Personal details

Date and place of birth	3 September 1993, Fribourg, Switzerland
Nationality	Swiss
Address	Route Principale 167, CH – 1628 Vuadens, Switzerland
Telephone number	+41 79 538 09 10
E-mail	julie.wee@outlook.com julie.wee@unifr.ch
Languages	French [native], English [native], German [B2], Spanish [B2]

Professional experience

2021 – 2024	Coordinator for school activities, Girls* on Ice Switzerland
2019 – present	Graduate assistant and PhD candidate, Dept. of Geosciences, University of Fribourg
2016 – 2018	Undergraduate assistant, Dept. of Geosciences, University of Fribourg Field work in the Alps and tutoring of Geomorphology and GIS courses

Education

2019 – 2024	Graduate assistant and PhD candidate, Dept. of Geosciences, University of Fribourg Glacier-permafrost interactions and interrelation: dynamics of Little Ice Age glacier forefields in alpine permafrost environments
2016 – 2018	MSc. in Geography, Dept. of Geosciences, University of Fribourg Dynamics in Glaciology and Geomorphology
2015 – 2016	MSc. in Biogeosciences, University of Neuchâtel and University of Lausanne
2012 – 2015	BSc. in Geography, Dept. of Geosciences, University of Fribourg Minor in Biology and Earth Science
2008 – 2011	International Baccalaureate, Internal School Manila, Philippines Main subject Geography and Biology

Teaching activities

2019 – 2022	Mountain Geomorphology, MSc. course, Dept. of Geosciences, University of Fribourg
2019 – 2022	Seminar in Geomorphology, MSc. course, Dept. of Geosciences, University of Fribourg
2016 – 2023	Géomorphologie – Quaternaire, BSc. practical course, Dept. of Geosciences, University of Fribourg
2016 – 2023	Cartographie et Introduction aux SIG, BSc. practical course, Dept. of Geosciences, University of Fribourg
2021	BSc. thesis co-supervision, « <i>Evolution des itinéraires d'alpinisme et de randonnée en haute et moyenne montagne : état des lieux et rôle du climat et des processus géomorphologiques liés</i> »

Outreach activities

2020 – 2022	Board member of Inspiring Girls Expeditions
2019 – 2022	Lead instructor during the Girls* on Ice Switzerland expeditions
2018 – present	Committee member of the Young Swiss Geomorphologists Organisation of excursion and workshops for the Young Geomorphologists
2018 – 2019	Instructor during the Women in Science and Technology [WINS] Organising and leading of day-long stage for a group of female high school students at the University of Fribourg

Side activities

2023	Co-convener at the European Conference on Permafrost
2023	Co-organiser of the European Young Geomorphologists Conference
2020 – present	Co-convener at the Swiss Geoscience Meeting
2018 – present	Committee member of the Swiss Geomorphological Society
2016 – present	Webmaster of the Swiss Geomorphological Society
2016 – present	Jeunesse & Sport Instructor Mountaineering and ski-touring

Skills

Office	Word, Excel, PowerPoint
Programming	Python, R
Software	ArcMap, ArcGIS Pro, QGIS, Agisoft, Pix4D, CIAS, Res1DInv, Res2DInv, ReflexW
Others	Organisation of field work campaigns in technical alpine terrain [geophysics, terrestrial geodetic surveys, installation of measurement stations, etc.]